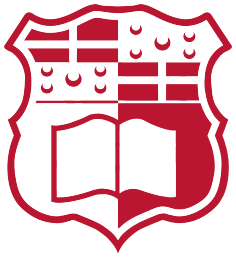

Environmental dose evaluation following the installation of a SPECT/CT scanner in a major public hospital using Monte Carlo simulation

Samuel Grima

Supervised by Mr Sam Agius

Co-supervised by Prof Ing Gianluca Valentino

Department of Medical Physics

Faculty of Health Sciences

University of Malta

September, 2025

A dissertation presented as part-fulfilment of the requirements for the award of the Masters in Medical Physics of the Faculty of Health Sciences of the University of Malta September 2025.

WWW.UM.EDU.MT

First edition, October 15, 2025

L-Università ta' Malta

FACULTY/INSTITUTE/CENTRE/SCHOOL Faculty of Health Sciences

DECLARATIONS BY POSTGRADUATE STUDENTS

(a) Authenticity of Dissertation

I hereby declare that I am the legitimate author of this Dissertation and that it is my original work.

No portion of this work has been submitted in support of an application for another degree or qualification of this or any other university or institution of higher education.

I hold the University of Malta harmless against any third party claims with regard to copyright violation, breach of confidentiality, defamation and any other third party right infringement.

(b) Research Code of Practice and Ethics Review Procedures

I declare that I have abided by the University's Research Ethics Review Procedures. Research Ethics & Data Protection form code FHS-2025-00006.

As a Master's student, as per Regulation 77 of the General Regulations for University Postgraduate Awards 2021, I accept that should my dissertation be awarded a Grade A, it will be made publicly available on the University of Malta Institutional Repository.

Acknowledgements

I would like to open this note of thanks with my supervisor, Mr Sam Agius, for his experienced insight, constant flow of ideas, and our back-and-forth exchanges that made this journey both challenging and enjoyable. Above all, I am grateful to him for trusting me with such an exciting project. My thanks also go to my co-supervisor, Prof. Ing. Gianluca Valentino, for his keen interest in the work and for making sure I had everything I needed to see it through.

A heartfelt thank you also goes to Prof. Carmel J. Caruana and Mr Eric Pace. To me, they represent the spark that lit my curiosity for the Monte Carlo method and its powerful use in the medical physics profession. In particular, I owe much to Mr Pace for planting the idea that has now grown into a path I am excited to follow into the future.

There are then the teams and communities that kept this project running. To the radiography team at MDH's Nuclear Medicine Department, and to Ms Nadine Napoli, thank you for your kind help during data collection. To the IT Department, and especially Ing. Jean-luc Mangion, I am grateful for facilitating access to the cluster server and for guidance in its use, which proved instrumental to the completion of this work. And to the FLUKA user community, thank you for your generosity in sharing knowledge. Your detailed and timely replies ere of great guidance.

Finally, my deepest gratitude goes to the three people who matter most: Ma, Pa, and Martina. My parents have always been my pillars, and my partner, my steadfast anchor throughout this demanding yet deeply rewarding journey. Only a few steps remain as this chapter also draws to a close,

And to everyone else who, in ways big or small, played a part in this project – **thank you**!

Abstract

Background: Accurate shielding design in nuclear medicine requires reliable dose estimates to maintain occupational and public exposures as low as reasonably achievable. Shielding calculations are conventionally performed analytically. A Monte Carlo (MC) approach offers more detailed, site-specific insight but has not yet been systematically applied locally.

Objectives: Acquire proficiency in FLUKA; develop a detailed model of a site-specific SPECT/CT facility; simulate a typical ^{99m}Tc imaging protocol; benchmark the model against experimental data and national dose regulations; extend the framework to ^{177}Lu.

Research Methodology: A hybrid approach combining simulation, experimental measurements, and analytical calculations was adopted. The facility and scanner were modelled based on technical drawings and material data. Ambient dose equivalents were physically measured at multiple locations using thermoluminescent dosimeters exposed to a ^{99m}Tc-injected phantom for model validation. Quantities scored in FLUKA included ambient dose equivalents, fluence distributions, regional energy deposition, and fluence-energy spectra. Dose equivalents were normalised to clinical workloads to derive annual dose estimates.

Results: A high-fidelity MC model of the SPECT/CT facility was successfully developed, simulated and validated. Weighted mean ratios and two-tailed paired t-tests ($n = 11$) showed values of 1.17 ± 0.02 (analytical vs experiment, significant, $p < 0.03$) and 1.20 ± 0.01 (simulation vs experiment, not significant, $p = 0.10$). The ratio findings indicated that the MC method performed at least as well as the analytical approach, while the paired t-test suggested superior performance. Workload-adjusted annual dose equivalents verified compliance of installed shielding with national dose limits and regional energy deposition revealed strong phantom self-absorption (62% for ^{99m}Tc, 87% for ^{177}Lu).

Conclusions and Recommendations: This study introduced and validated an MC facility model for nuclear medicine shielding assessment. Future planning should combine analytical, experimental, and MC methods for accurate, yet time-efficient assessments. Further work should address validation against alternative MC codes, CT source modelling, and dynamic patient and equipment motion.

Keywords: Monte Carlo, SPECT/CT, ambient dose equivalent, radiation shielding, occupational exposure

Contents

List of Definitions

Ambient dose equivalent, $H^*(10)$
An operational quantity defined as the dose equivalent at a depth of 10 mm in the ICRU sphere on the radius opposing the direction of the incident aligned field (International Commission on Radiation Units and Measurements, 1993).

Controlled area
A controlled area established to safeguard individuals from ionising radiation or to limit radioactive contamination, where access is subject to regulatory restrictions (European Union, 2014).

Diagnostic reference levels
For nuclear medicine practices, these refer to typical activity levels administered for standard procedures, based on groups of average-sized patients or standard phantoms, and applicable to broadly defined categories of equipment (European Union, 2014).

Effective half-life
The time required for the activity of a particular radioisotope deposited in a patient to be reduced by half as a result of the combined action of radioactive decay (physical half-life T_p) and biological elimination (biological half-life, T_b), related as (Hacking, 2024),

$$\frac{1}{T_p} + \frac{1}{T_b} = \frac{1}{T_e} \tag{1}$$

Supervised area

A monitored area established for the purpose of radiological protection, but does not require restricted access (European Union, 2014).

Tenth value layer, TVL

The thickness of a material required to reduce the intensity of a beam of ionising radiation to one tenth of its original value, defined as (Podgorsak et al., 2014),

$$\mathrm{TVL} = \frac{1}{\mu} \ln\left(\frac{1}{10}\right), \tag{2}$$

where μ is the linear attenuation coefficient.

Transport threshold

The cut-off energy below which a particle is no longer transported through the geometry and deposits its remaining energy locally in the material, without further tracking of its trajectory. No additional interactions, scattering, or secondary particle generation are simulated for that particle (Parodi et al., 2007).

List of Acronyms

CDF Cumulative Distribution Function

CERN European Organisation for Nuclear Research

CT Computed Tomography

CZT Cadmium Zinc Telluride

DRL Diagnostic Reference Level

HEGP High Energy General Purpose

IAEA International Atomic Energy Agency

ICRP International Commission on Radiological Protection

LEHRS Low Energy High Resolution Sensitivity

LiF:Mg,Cu,P Lithium fluoride doped with magnesium, copper and phosphorus

MC Monte Carlo

MDH Mater Dei Hospital

MPE Medical Physics Expert

NaI(Tl) Thallium-activated Sodium Iodide

NCRP National Council on Radiation Protection and Measurements

NM Nuclear Medicine

PDF Probability Density Function

PET Positron Emission Tomography

PMMA Polymethyl Methacrylate

PMT Photomultiplier Tube

RPC Commission for the Protection from Ionising and Non-Ionising Radiation

RPE Radiation Protection Expert

SPECT Single-Photon Emission Computed Tomography

TLD Thermoluminescent Dosimeter

TVL Tenth Value Layer

List of Figures

List of Tables

1

Introduction to the Study

1.1 | Introduction

This chapter presents the problem statement, background and context, objectives, scope, research methodology summary, ethical considerations, and relevance of the study.

1.2 | Problem statement

A hybrid Single-Photon Emission Computed Tomography (SPECT)/Computed Tomography (CT) system was recently installed at Mater Dei Hospital (MDH), Malta's only public hospital currently providing Nuclear Medicine (NM) services. In accordance with Council Directive 2013/59/Euratom and its Maltese transposition, the Basic Safety Standards for Ionising Radiation Regulations, the Radiation Protection Expert (RPE) is responsible for advising on "plans for new installations and the acceptance into service of new or modified radiation sources in relation to any engineering controls, design features, safety features and warning devices relevant to radiation protection" (European Union, 2014, Art. 82(1)(b); Parliament of Malta, 2018, Reg. 105(2)(d)). This responsibility essentially encompasses the design and verification of the structural shielding of imaging rooms to ensure the safety of radiation workers and the public.

It is common practice, including locally, for pre-installation shielding analysis to rely primarily on analytical calculations. While this approach remains suitable because of its practicality and efficiency, it is subject to uncertainties arising from its reliance on simplified mathematical models. Alternatively, verification of shielding effectiveness through post-installation

dose measurements is labour-intensive and sometimes impractical. More importantly, if discrepancies arise after construction, retrofitting or modifying the shielding can be costly or even unfeasible.

In contrast to analytical approaches, the Monte Carlo (MC) method provides accurate simulations of complex geometry configurations for radiation shielding with high-precision results (Vassiliev, 2017). The central problem is that, aside from the rote use in radiotherapy planning, MC workflows are not yet formally applied in the medical physics and radiation protection professions in Malta, as evidenced by the lack of local literature. Therefore, this study aimed to address that gap by developing and validating a detailed, site-specific MC model of the SPECT/CT installation at the national hospital to demonstrate the added value of integrating MC-based approaches into shielding assessments.

1.3 | Background and context

The accurate estimation of environmental dose distributions is central to effective radiation protection in NM. Traditionally, shielding design has been guided by analytical methods recommended by organisations such as the International Commission on Radiological Protection and the International Atomic Energy Agency (Carlsson & Le Heron, 2014; IAEA, 2018b; ICRP, 2007a). These methods remain the common standard globally (Brígido Flores et al., 2019; Madero Ramirez et al., 2017), particularly in settings with limited access to computational resources. However, analytical models are constrained by simplifying assumptions that limit their ability to account for factors such as complex room geometries and sources distributions. Often, the source is treated as a point emitter with a total disregard of patient self-shielding effects.

The adoption of MC has addressed many of these limitations. They have been applied successfully in a range of contexts, including radiotherapy bunker design (Ibitoye et al., 2022) and cyclotron facility shielding (Infantino et al., 2016). In the latter case, model validation with physical measurements enabled significant optimisation of the shielding design such that it limited radiation leakage out of the bunker.

Despite these advances, applications of MC in SPECT/CT shielding remain underrepresented in the literature. A series of projects conducted annually by the Joint Institute for Nu-

clear Research[1] explore shielding configurations for SPECT and CT using MCNPX and focus on common radionuclides such as ^{99m}Tc and ^{131}I (El-Sadieque, 2022; Soliman, 2024; Tassé, 2025). Although their approach aligns closely with the objectives of this work, given the same modality is considered, their models are generally limited in complexity and not site-specific, and yield only rudimentary results. These restrict their clinical utility and thus, more advanced modelling with realistic geometries and carefully selected physics parameters is necessary to improve predictive accuracy.

1.4 | Objectives of the study

The objectives set for this study were the following:

1. Acquire proficiency in the FLUKA MC code, with a focus on understanding its extent of capabilities, particularly in radiation protection for NM practices.
2. Develop a detailed, high-fidelity model of the SPECT/CT facility at the national hospital that includes the scanner, imaging phantom, shielding barriers, and adjacent rooms and corridors.
3. Simulate the model for a typical NM ^{99m}Tc imaging protocol and validate it against experimental measurements.
4. Apply real-world occupancies and workloads to produce annualised ^{99m}Tc exposure levels and compare with national dose limits and constraints.
5. Apply the model to explore radiation protection considerations for prospective applications of ^{177}Lu.

1.5 | Scope of the study

This study was limited to a General Electric NM/CT 870 DR SPECT/CT system under a fixed patient couch and detector position. A Jaszczak phantom containing ^{99m}Tc was used experimentally, while both ^{99m}Tc and ^{177}Lu were modelled as sources in simulation. To maintain

[1] `https://interest.jinr.ru/index.php?project_id=343`.

focus on areas of greater relevance to NM radiation protection, simulation of the CT source has therefore been excluded in this work.

1.6 | Research methodology

For this work, the FLUKA MC code and its graphical user interface, Flair, were employed. A preliminary study was initially conducted, in which ambient dose equivalent $H^*(10)$ was measured at various distances from a ^{99m}Tc-injected Jaszczak phantom using a set of calibrated Thermoluminescent Dosimeters (TLDs). This setup was subsequently replicated in FLUKA, and the simulated $H^*(10)$ values were benchmarked against the physically measured data to assess model accuracy for the simplified model.

For the main study, the SPECT/CT facility was modelled based on site plan drawings, focusing only on the SPECT/CT room and adjacent areas. The design of the scanner geometry and material composition drew upon multiple sources, such as technical drawings, literature on comparable systems, manufacturer documentation, expert consultations, direct observations, and rationalised assumptions. The ^{99m}Tc-injected Jaszczak phantom was placed on the patient couch and centred between the two gamma detector heads, which were orientated in a vertical H-mode and as close as possible to the phantom. The model was simulated for a total of 9.75×10^{10} primaries on both a personal machine and a high-performance computing cluster for efficiency. Various quantities were scored, including ambient dose equivalent, particle fluence, energy deposition, and energy-fluence spectra, with appropriate normalisation applied.

The same setup was physically reproduced and $H^*(10)$ was measured at various locations using the TLDs. The MC and experimental results were compared to validate the final MC model, and both were further compared against analytically-derived values. Moreover, dose equivalents from the simulation were compared to national dose constraints and limits.

Finally, the setup was adapted to simulate a ^{177}Lu source to assess a subset of the same quantities, with the intention of supporting future radiation protection planning for potential clinical use of ^{177}Lu within the NM department.

1.7 | Ethical considerations

This study did not involve any patients or their associated data. Permission and clearance for the hospital equipment was granted by the Medical Imaging Department, and the MDH data protection officer and CEO. This study has been approved by the University Research Ethics Committee of the University of Malta. These are given in Appendix A.

1.8 | Relevance of the study

The relevance of this study for the various stakeholders is as follows:

The patient, hospital visitors and members of staff: By ensuring that ionising radiation is confined within the SPECT/CT room, personnel in adjacent areas and those waiting nearby are protected from unintended exposures.

The Medical Physics and Radiation Protection professions/practice: For the RPE, the model enables verification that radiation leakage from the SPECT/CT room remains within dose constraints for workers and the public, and provides a framework for assessing shielding requirements in future installations and modifications. For the Medical Physics Expert (MPE), the implemented MC framework can be adapted for patient-specific studies, such as dosimetry and optimisation of imaging protocols.

1.9 | Conclusion

This chapter introduced the study. Chapter two provides a critical literature review, followed by the research methodology in chapter three. Chapter four presents the results, with analysis and discussion in chapter five. Lastly, chapter six summarises the findings, offers recommendations, and suggests future research.

2

Literature Review

2.1 | Introduction

This study focused on the application of the MC method in evaluating radiation exposure around a SPECT/CT scanner for radiation protection purposes. Accordingly, the critical review of the relevant literature commences with an introduction to SPECT/CT. This is followed by discussions on key radiation protection considerations within an NM department. Finally, the MC method for radiation transport was analysed in depth, with particular focus on its theoretical foundations and applications in medical physics and radiation protection. Existing gaps in the field were identified and highlighted throughout the review.

This review was conducted using the electronic databases Google Scholar, PubMed, IOPscience, and University of Malta's HyDi.[2] In searching, the following keywords were used: "Monte Carlo, SPECT/CT, ambient dose equivalent, radiation shielding, occupational exposure." Articles published between 1949[3] and 2025 were selected and analysed based on (1) title, author/s, publication year, (2) aim of study, (3) materials and methods, (4) findings, and (5) strengths and limitations. Additionally, other sources, such as academic textbooks, were consulted, primarily for theoretical background.

[2] `https://hydi.um.edu.mt/`

[3] Works over 20 years old were considered only for historical context or foundational groundwork in the field.

2.2 | The SPECT/CT imaging system

This chapter outlines the operational, technical, and practical aspects of SPECT/CT systems. While the system installed at the hospital is a state-of-the-art SPECT/CT unit, the emphasis here is placed primarily on the SPECT component and the combined system, with only brief reference to CT in isolation. This reflects the scope of this work undertaken, which considers only the SPECT source.

2.2.1 | Principles of SPECT

SPECT is an emission-based, three-dimensional tomographic imaging technique that builds upon the conventional planar scintigraphy technique, and is widely used in NM. It utilises the distribution of radionuclides administered to the patient to produce physiological images of organs and tissues.

2.2.1.1 | Operation and components of a SPECT system

Modern SPECT systems are predominantly based on the Anger, or scintillation, camera design (Peterson and Furenlid, 2011). The components comprising the camera are housed within a detector head. Although specific designs vary across manufacturers and models, most systems follow a similar architecture as illustrated in Figure 2.1.

The imaging process begins when γ-rays emitted from the radiopharmaceutical within the patient exit the body and encounter the collimator. This permits the transmission of photons travelling approximately perpendicular to the detector face while absorbing oblique ones through an array of holes separated by high-density septa, thus, preserving spatial information (Ljungberg, 2021). Two energy-based collimator variants are shown in Figure 2.2: the Low Energy High Resolution Sensitivity (LEHRS) and High Energy General Purpose (HEGP) collimators, used for low-energy (e.g., ^{99m}Tc) and high-energy (e.g., ^{177}Lu) emitters respectively (see § 2.2.1.2), and both of which are parallel-hole designs. While both feature hexagonal holes, they differ in other structural aspects (Table 2.1), which influences detector parameters such as spatial resolution and system sensitivity (General Electric, 2018; Shibutani et al., 2021).

Unattenuated photons interact within the scintillator crystal which emits visible light in response to energy deposition. The crystal is typically a monolithic block of Thallium-activated

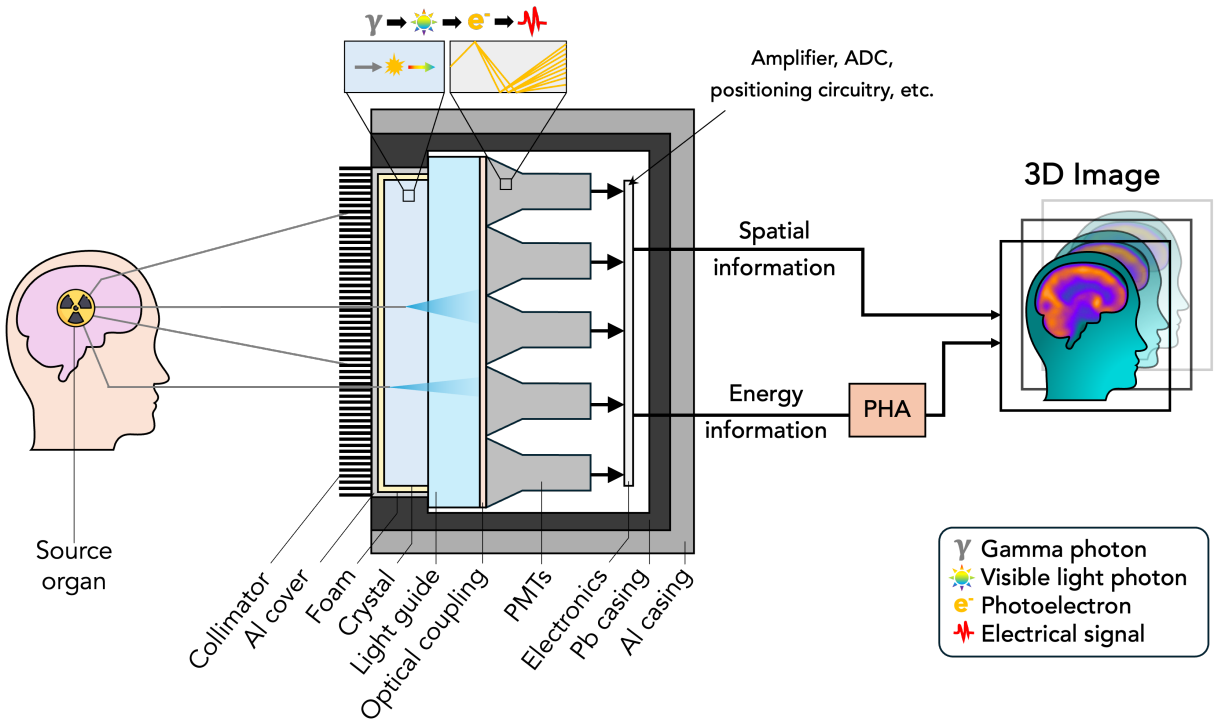

Figure 2.1: A conceptual schematic of scintillation camera technology used in SPECT scanners and the process of generating a three-dimensional image from the source organ. Based on Bouchareb et al. (2024), Cherry et al. (2013) and Rault et al. (2010). ADC = Analogue-to-Digital Converter; Al = Aluminium; Pb = Lead; PHA = Pulse Height Analyser; PMT = Photomultiplier Tube.

Table 2.1: Specification (dimensions) data of the LEHRS and HEGP collimators, obtained from Shibutani et al. (2021) and General Electric (2018), respectively.

Parameter	**LEHRS**	**HEGP**
Septal thickness [mm]	0.13	1.80
Hole diamater [mm]	1.43	4.00
Hole length [mm]	32	66

Sodium Iodide (NaI(Tl)) and is preferred over other materials due to its favourable scintillation properties (Xu et al., 2024). However, its hygroscopic nature necessitates hermetic sealing within an aluminium casing to protect it from moisture-induced degradation (Cherry et al., 2013). Alternative materials such as Cadmium Zinc Telluride (CZT) are increasingly used in modern systems. In fact, the NM/CT 870 scanner present in the hospital supports both detector

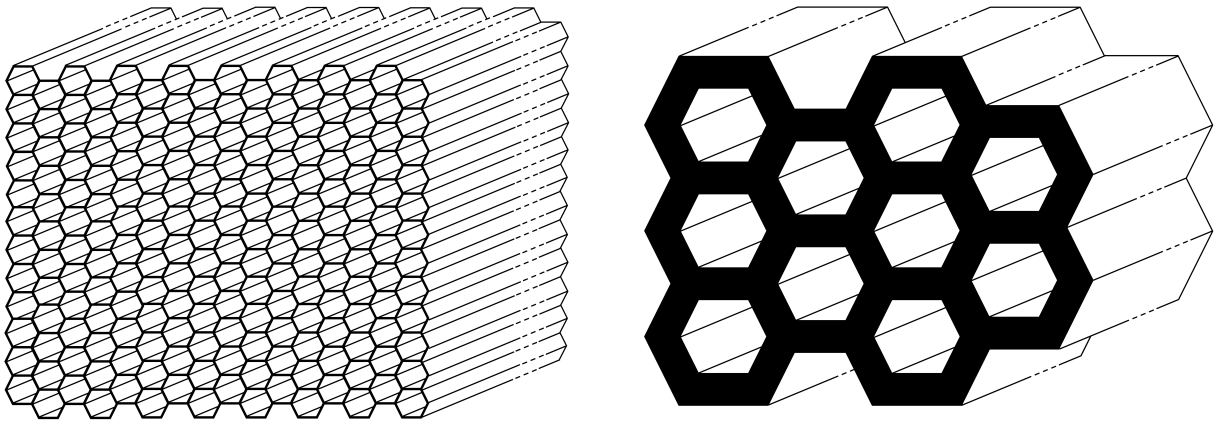

Figure 2.2: A schematic showing sections of the two parallel-hole collimators: LEHRS (left) and HEGP (right). The hole diameter and septal thickness are scaled relative to each other and between the two collimators. The dotted line (- - -) represents the non-true scale of the hole length. Refer to Table 2.1 for exact dimensions. Based on Shibutani et al. (2021) and General Electric (2018) .

types, with the installed model using NaI(Tl).[4]

Between the crystal and the photodetectors lie the light guide and optical coupling, which collectively ensure uniform light distribution, maximise collection efficiency, and minimise reflection losses (Cherry et al., 2013). The light is then detected by an array of Photomultiplier Tubes (PMTs). These convert incident light photons into electrons via the photoelectric effect and then amplify the signal through a series of dynodes (Ljungberg, 2021). The NM/CT 870 DR includes 59 PMTs per head arranged in a hexagonal close-packed geometry (General Electric, 2018).

The resulting signal from the PMTs is further amplified and processed by a positioning circuit to determine spatial and energy information (Saha, 2013). These data are then used to generate an image representing the distribution of radioactivity in the patient.

Lastly, the entire detector assembly is enclosed within a lead casing, which serves to shield the system from external radiation and minimise background noise. An additional outer aluminium layer provides structural support and may offer further shielding for the detector head (Rault et al., 2010).

[4]NM/CT 870 DR.

2.2.1.2 | The source: γ-emitting radionuclides

SPECT radionuclides are γ-emitters such as ^{99m}Tc, ^{123}I, ^{131}I, ^{177}Lu, and ^{201}Tl. Some, including ^{131}I and ^{177}Lu, also emit β particles, making them suitable for theranostic applications (Crișan et al., 2022). Radionuclides may be administered directly, as with ^{131}I, or labelled to pharmaceutical agents that target specific biological sites, such as [^{99m}Tc]-sestamibi and [^{177}Lu]Lu-DOTATATE. Administration routes include intravenous injection, inhalation, or oral ingestion. Properties of the widely used ^{99m}Tc in Malta's NM department and ^{177}Lu, a prospective addition, are summarised in Table 2.2.

Table 2.2: Physical and chemical properties, and applications of the radionuclides ^{99m}Tc and ^{177}Lu. B.R. = Branching Ratio; I.T. = Isomeric Transition; MPI = Myocardial Perfusion Imagin; NET = Neuroendocrine Tumour; PRRT = Peptide Receptor Radionuclide Therapy. Data compiled from the Commission for the Protection from Ionising and Non-Ionising Radiation [RPC] (2022), Crișan et al. (2022), Liu et al. (2021) and Wong et al. (2025).

Property	**Technetium-99m (^{99m}Tc)**	**Lutetium-177 (^{177}Lu)**
Physical half life	6.01 h	6.65 d
Decay mode	I.T.	β^-, γ
Daughter	^{99}Tc	^{177}Hf
Energies (B.R.)	γ 140.5 keV (98.60%) γ 142.6 keV (1.40%)	β^- 134 keV * γ 208.4 keV (10.36%) γ 112.9 keV (6.17%) γ 321.3 keV (0.21%) γ 249.7 keV (0.20%) γ 71.6 keV (0.17%) γ 136.7 keV (0.05%)
Production	Generator (^{99}Mo/^{99m}Tc)	Reactor (via ^{176}Lu or ^{176}Yb)
Chemical form	$^{99m}TcO_4^-$	$^{177}LuCl_3$
Pharmaceuticals†	Sestamibi Tetrofosmin	DOTATATE PSMA-617
Applications†	MPI Bone scintigraphy Renogram Lymphoscintigraphy	NET therapy (PRRT) Prostate cancer therapy Post-treatment imaging

*Average energy.
†Most common

Beyond each radionuclide's physical half-life and photon energies, several other factors influence radiation exposure once administered. One is the biological half-life, which in turn

influences the effective half-life. For example, [^{99m}Tc]-sestamibi's relatively long biological half-life of around 53 h actually reduces the 6 h physical half-life to an effective half-life of 5.4 h, thereby shortening the duration of external exposure (Rizk and Nagalli, 2025).

The type of emission also plays an important role. β particles deposit energy over short distances and are largely self-attenuated within tissue. A useful rule of thumb is that the range in cm of beta particles in tissue does not exceed half their maximum energy in MeV (Holm, 2022). For ^{177}Lu, with $E_{\beta,\max}$~0.5 MeV, this corresponds to a tissue range of about 2.5 mm. In contrast, photons are neutral particles and cause ionisation indirectly through secondary electrons. As a result, photons are generally far more penetrating and contribute significantly to external radiation dose.

Lastly, the administered activity varies depending on the imaging or therapeutic protocol. For example, Malta's Diagnostic Reference Levels (DRLs) recommend 700 MBq for a whole-body bone scan using [^{99m}Tc]-MDP and 185 MBq for post-thyroid ablation imaging with ^{131}I (RPC, 2022). In contrast, therapeutic procedures such as treatment with [^{177}Lu]Lu-DOTATATE may involve activities as high as 7.4 GBq (Ladrière et al., 2023), with clearly greater implications for radiation protection.

2.2.2 | Integration of SPECT and CT in hybrid imaging

One major limitation of stand-alone SPECT imaging is the difficulty in accurately localising radiopharmaceutical uptake, particularly when tumour activity is high, relative to surrounding tissues. This lack of anatomical context makes it challenging to relate functional findings to anatomical structures. To obtain both functional and anatomical information in a single, time-efficient session, SPECT/CT systems were developed (Ljungberg, 2021). Furthermore, the inclusion of CT enables attenuation and scatter correction. This helps mitigate image artefacts caused by photon absorption within the body or scattering outside the detector's field of view (Cherry et al., 2013). Owing to its superior diagnostic accuracy, SPECT/CT is widely employed in applications such as sentinel lymph node mapping, the evaluation of prostate cancer, and the assessment of benign and malignant skeletal conditions.

Modern hybrid SPECT/CT scanners typically consist of a dual-headed SPECT system combined with a multi-slice CT system, both mounted on a common gantry with a patient couch that moves along a shared axis, as seen in Figure 2.3. The SPECT detector heads can be po-

sitioned at various angles, most commonly at 90° (L-mode) or 180° (H-mode), depending on the clinical indication. Scans are generally acquired sequentially, requiring displacement of the patient couch between the CT and SPECT acquisitions to ensure the region of interest is positioned within the appropriate imaging field-of-view. A key practical consideration is the increased physical footprint of hybrid systems, which may pose siting challenges in facilities originally designed for more compact, SPECT-only installations. For example, the NM/CT 870 requires a minimum room size of 6.3 m × 3.7 m (General Electric, 2020).

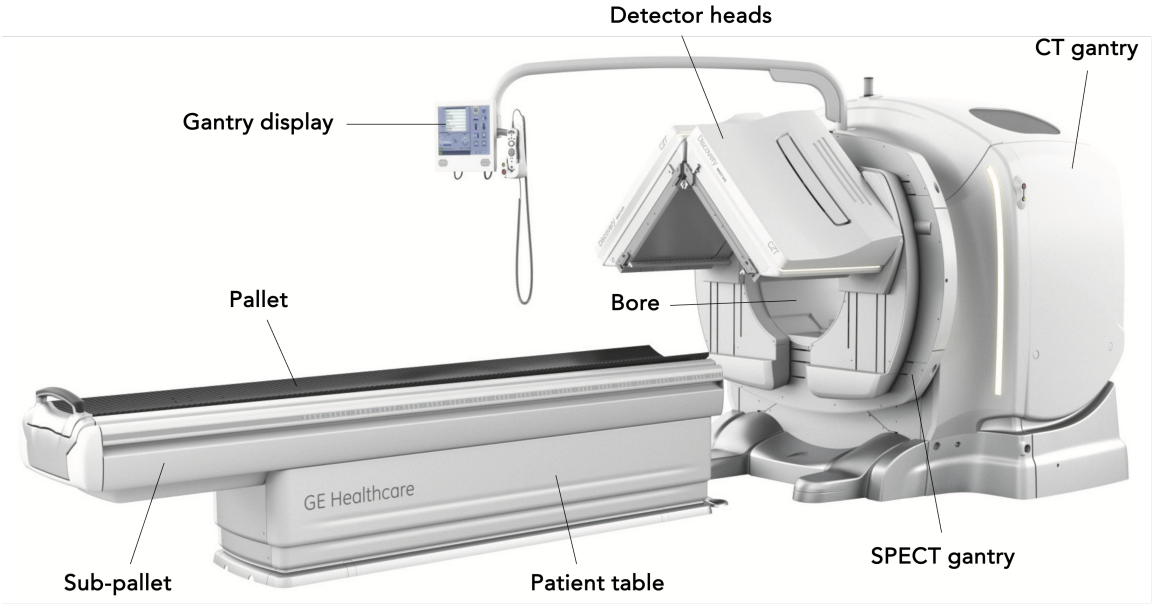

Figure 2.3: Labelled image of General Electric's NM/CT 870 CZT SPECT/CT scanner, a variant of the model installed at Mater Dei Hospital (NM/CT 870 DR), which features CZT detectors in place of the NaI(Tl) scintillation crystal. Figure reproduced from General Electric (2020).

2.2.2.1 | The CT subsystem

Nowadays, the CT component operates as a fully integrated multi-slice diagnostic X-ray system. At its core is the X-ray tube where electrons emitted from a heated cathode are accelerated towards a rotating anode. Their interaction with the anode material produces a useful polychromatic X-ray spectrum, typically ranging from 80 to 140 kVp, depending on the clinical protocol. Opposite the tube is the detector system, composed of scintillator-photodiode arrays that convert incoming X-rays into electrical signals for image reconstruction. Additional essen-

tial subunits include the heat exchanger, the high-voltage generators, and the electronic board (Behling, 2021), as shown in Figure 2.4.

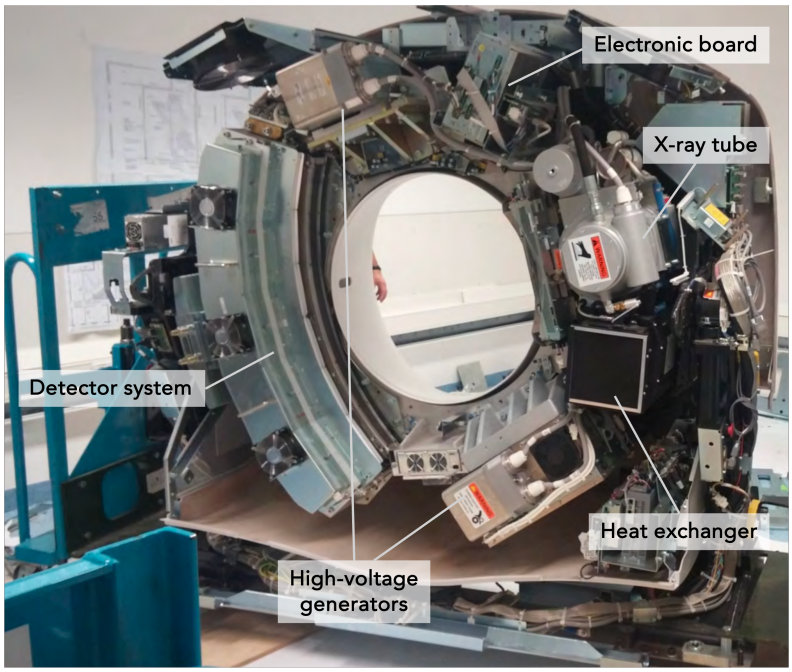

Figure 2.4: Labelled image showing the internal structure of the CT gantry in the NM/CT 870 DR scanner, illustrating the arrangement of key subsystems. Figure reproduced from (General Electric, 2025).

2.3 | Radiation protection in nuclear medicine

Unlike in diagnostic and interventional radiology and radiation oncology, radiation protection in NM presents unique challenges due to the continuous presence of radiation from unsealed "live" sources. Conversely, X-ray tubes and linear accelerators produce radiation only when actively in use and can be switched off. As a result, radiation protection in NM must be integrated into all aspects of daily workflow, and is achieved through one or a combination of the following strategies: reducing exposure time, maximising distance from radiation sources, and using appropriate shielding (Kim, 2018).

2.3.1 | Sources of radiation

At first glance, the main sources of radiation exposure may appear to be the obvious ones: vials, capsules, test sources, and radioisotope generators. In reality, these are typically well-shielded and securely stored, thus posing minimal risk. A far greater concern is the radioactive patient, who, once administered a radiopharmaceutical, becomes a mobile radiation source within the department, including in waiting areas, corridors, and toilets. Marshall et al. (2024) reported that the highest occupational exposure during an entire ^{99m}Tc-MDP bone scintigraphy workflow occurred during patient positioning, with a radiographer receiving an effective dose of 32.03 µSv. This was over ten times the personal dose equivalent of 2.19 µSv received by the radiopharmacist during radiolabelling, quality control, and syringe preparation combined. This underscores that the radioactive patient represents the principal source of occupational exposure in such settings.

Hybrid systems can significantly increase external radiation exposure, particularly when diagnostic CT capabilities are used. Figure 2.5 shows a CT radiation scatter map of the NM/CT 870 DR during a typical scan using a body phantom. This exposure arises primarily from scatter radiation off the patient, rather than directly from the X-ray tube, as most of the primary beam is absorbed within the patient's body. However, the CT component typically operates using low-dose protocols, with patient doses reduced by approximately 20–25% compared to standard diagnostic CT scans (Soo et al., 2019). Moreover, unlike the continuous emission from the SPECT component, CT exposure is pulsed and brief.

2.3.2 | Regulatory requirements for radiation protection

The regulatory framework of radiation protection in NM is governed by a combination of legally binding regulations and internationally recognised standards and guidance documents. The regulations are informed primarily by the recommendations of the ICRP (2007a; 2007b) and the IAEA (2014; 2018a; 2018b; 2018c). At the European level, Directive 2013/59/Euratom establishes the basic safety standards for protection against ionising radiation (European Union, 2014). National regulations transpose this directive into local law and form the legal basis for radiation safety programmes within the NM department (Parliament of Malta, 2018).

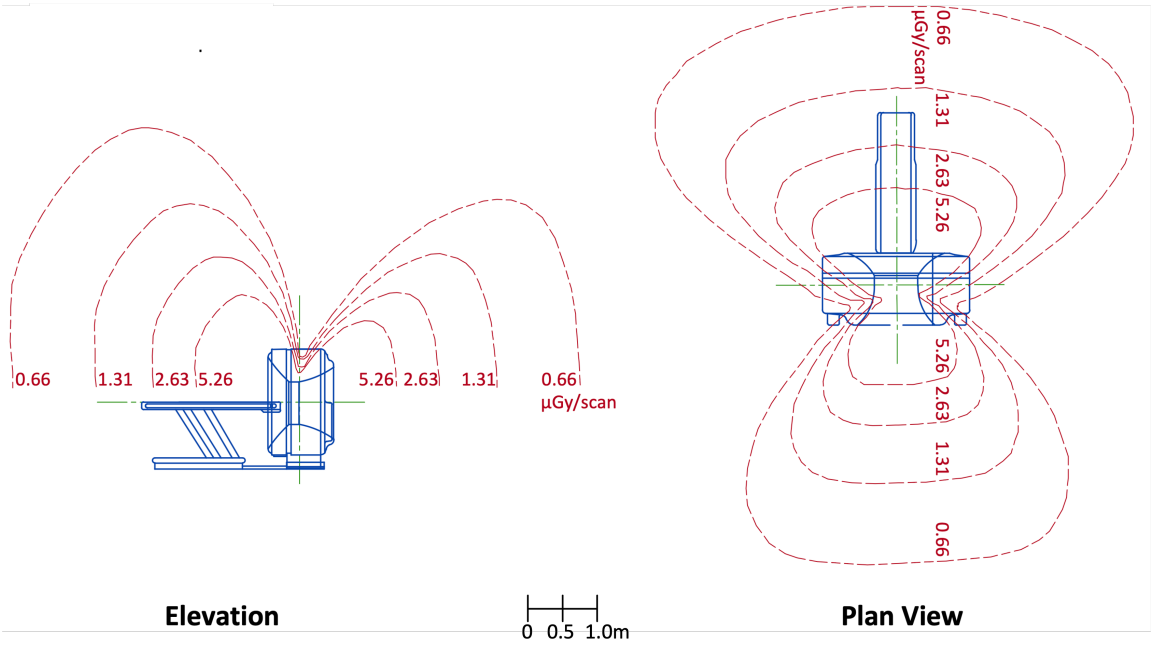

Figure 2.5: Elevation and plan views of scatter dose maps around the Optima CT540 — the CT model integrated into the NM/CT 870 DR system — acquired using a body phantom under typical scan conditions (140 kV; 100 mAs; 1 s; 4 × 5.00 m acquisition). The type of dose is not specified and is referred to only as "CT exposure levels." Figure and data reproduced from General Electric (2024).

2.3.2.1 | Dose limits and constraints

Dose limitation is one of the three key principles of radiation protection, along with justification and optimisation (ICRP, 2007a). Dose limits are legally defined thresholds for the radiation an individual may receive over a specified period and are set to prevent exposure at levels posing unacceptable stochastic or deterministic risks. More stringent than dose limits are dose constraints, which are prospective upper bounds on individual doses used during optimisation to guide protective measures for planned exposures (European Union, 2014). Typically, particularly for occupational exposures, exceeding a dose constraint triggers an internal investigation and reporting, while exceeding a dose limit often requires cessation of work and regulatory intervention. Table 2.3 summarises the applicable dose limits and constraints as adopted in Malta.

Table 2.3: Effective and equivalent annual dose limits and constraints applicable in Malta, based on national implementation of Directive 2013/59/Euratom (European Union, 2014; RPC, 2022). Occupational dose constraints are one third of their respective dose limits.

Type of Limit	**Occupational**		**Public**		**Carers & Comforters**	
	Limit	Constraint	Limit	Constraint	Limit	Constraint
Effective dose	20 mSv*	6 mSv	1 mSv	0.25 mSv	—	1.5 mSv‡
Equivalent dose in:						
Lens of the eye	20 mSv*	6 mSv	15 mSv	—	—	—
Skin†	500 mSv	167 mSv	50 mSv	—	—	—
Hand & feet	500 mSv	167 mSv	—	—	—	—

*Averaged over defined periods of 5 years.
†Average over any area of 1 cm^2.
‡Per five years, not annually.

2.3.3 | Shielding design and planning techniques

Shielding design in NM facilities is well covered by existing guidance documents, especially for Positron Emission Tomography (PET) (IAEA, 2008; Madsen et al., 2006) and cyclotron facilities (Deutsches Institut für Normung, 2003; National Council on Radiation Protection and Measurements [NCRP], 2005). However, documentation specifically addressing SPECT and SPECT/CT shielding remains somewhat scarce. By contrast, CT shielding design is well-standardised (NCRP, 2004), as also reflected in the vendor-issued site installation documentation (Figure 2.5), which provided a dose map for the CT component, but not for SPECT.

2.3.3.1 | Barriers for structural shielding, design and layout

Structural shielding in NM facilities involves strategically placing barriers to attenuate ionising radiation outside the imaging room to acceptably safe levels. This work focuses specifically on the shielding surrounding the SPECT/CT imaging room (Figure 2.6). Lead and concrete are the two most commonly used materials for radiation shielding, with the choice largely depending on factors such as cost, space limitations, and weight limitations on the floor. For example, lead attenuates radiation more effectively than concrete, thus requiring thinner barriers due to its lower Tenth Value Layer (TVL), but comes at a substantially higher cost. Table 2.4 summarises their key properties. In practice, a combination of both materials is often used.

As shown in Figure 2.6, the scanner installed at the hospital is enclosed by four shielded walls. Each wall comprises a succession of the following layers: 24 mm gypsum, a 2 mm lead sheet (up to 2 m height), a 12 mm plywood board, an air gap for services, and another

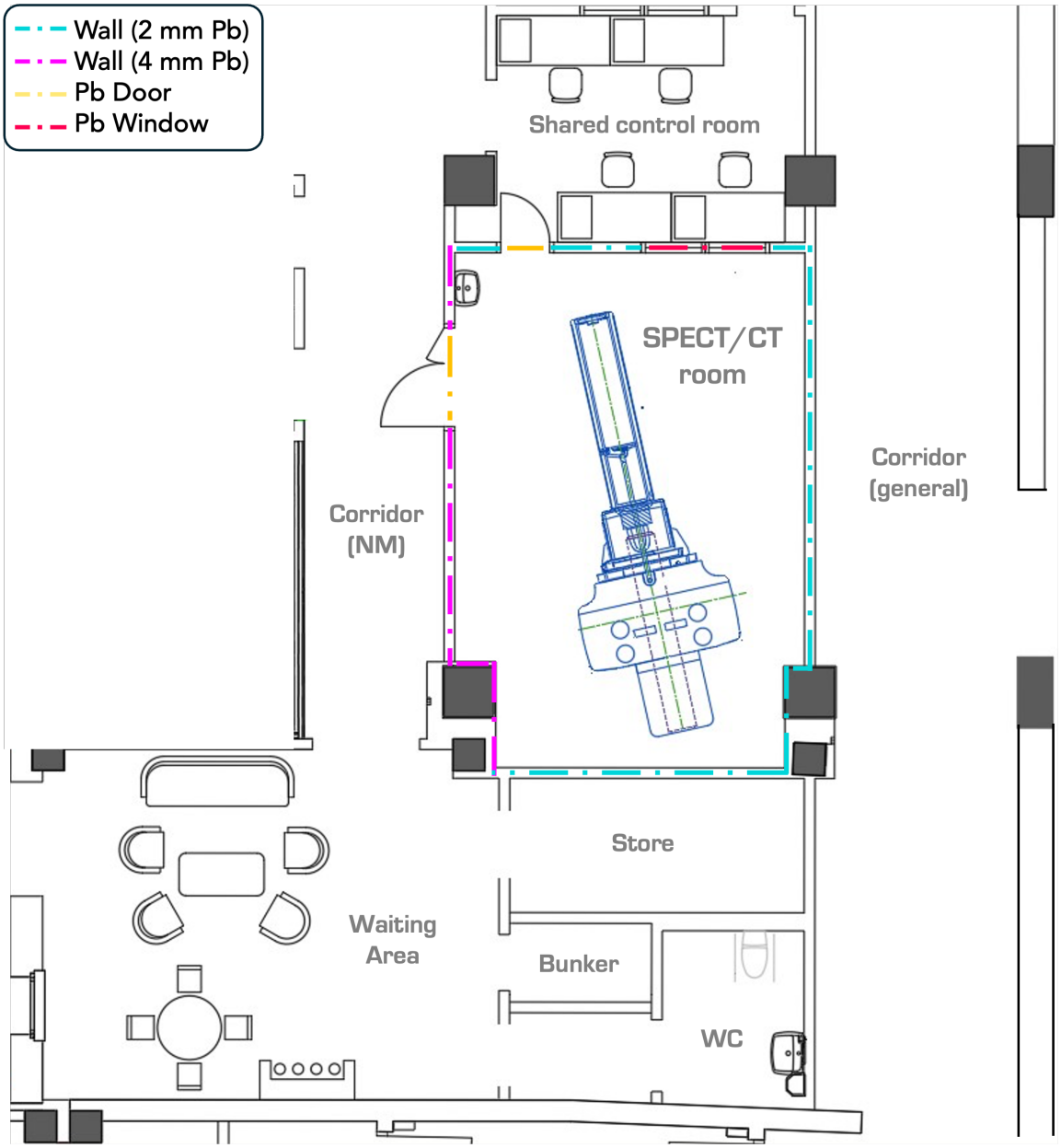

Figure 2.6: Technical layout of the SPECT/CT examination room and its adjoining areas. The original architectural drawing has been lightly modified for visual consistency in this work. Pb = Lead. Reproduced with permission from the hospital's medical imaging department.

12 mm gypsum layer (Figure 2.7a). The west wall uses 4 mm of lead to prevent interference from post-administration PET patients in the adjacent waiting area. Lead sheets are typically overlapped to avoid gaps. Moreover, wall fixtures, like sockets and pipes, have lead backing.

Table 2.4: Properties of lead and concrete as commonly used materials for radiation shielding. Data compiled from Business Insider (2025); Kiran et al. (2015); MaltaToday (n.d.); Oumano et al. (2025).

Property	**Lead**	**Concrete**
Density, ρ [g/cm^3]	11.35	2.30
Effective atomic number, Z_{eff}	82	~14.5
TVL for ^{99m}Tc [mm]	0.87	122
TVL for ^{177}Lu [mm]	1.99	134
Price range per kg [€]	1.60–1.70	0.10–0.20

However, post-construction verification of this is difficult, which highlights the need for an on-site radiation protection expert during installation (European Union, 2014; Salehzahi and Tse, 2020).

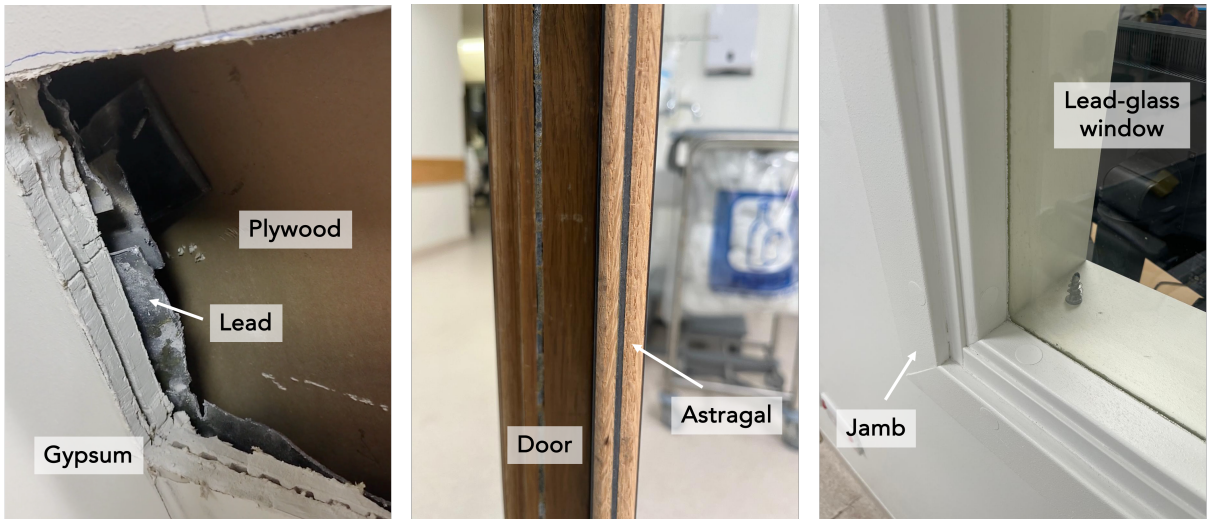

(a) (b) (c)

Figure 2.7: Photographs showing structural shielding elements around the SPECT/CT scanner room: (a) Wall cross-section obtained during construction revealing layers of gypsum, lead and plywood; (b) Lead-lined door with 2 mm lead and an additional 2 mm astragal; (c) Observation window with 2 mm lead-glass, enclosed by a lead-lined jamb.

The west and north walls also contain two 2 mm lead-lined doors (Figure 2.7b) and a 2 mm lead-glass observation window (Figure 2.7c), all surrounded by lead-lined jambs. The main double-leaf door includes a lead-lined astragal to prevent leakage at the central joint. Such practices are standard in radiation protection to eliminate escape paths (Sutton et al., 2012). Lastly, the upper and lower areas are shielded by 50 cm-thick concrete ceiling and floor slabs.

2.3.3.2 | Analytical shielding methods

The analytical approach to shielding design remains the most widely used method (Brígido Flores et al., 2019; Madero Ramirez et al., 2017; Zanzonico et al., 2008). This method uses theoretical formulae with the sole objective of estimating the required barrier thickness for a specific setting. Abdallah (2007) outlines the key defined parameters used in typical shielding calculations. These parameters and any associated assumptions considered are summarised in Table 2.5. From these, the equivalent dose at a point can be derived as,

$$H = \frac{\Gamma \tilde{A}}{d^2} TW. \tag{2.1}$$

To ensure that the equivalent dose H does not exceed the permissible limit P, the required barrier thickness x is calculated using the material's Tenth Value Layer (TVL) through,

$$x = \text{TVL} \cdot \log_{10}\left(\frac{H}{P}\right). \tag{2.2}$$

It must be mentioned that this method works by assuming a point source in air without self-absorption, which justifies the simple inverse-square dependence. This is just one of several underlying assumptions. Attenuation within the scanner and other wall layers is also not considered, which means higher deviations from actual dose values are expected. This leads to potential over-shielding, i.e., higher and unnecessary costs. Moreover, the radionuclide's complex emission spectrum is compressed to an effective photon description via Γ, so weak γ lines are not treated explicitly, and β radiation is generally neglected for room shielding. Lastly, it is not possible to model scatter or complex geometries. In general, these limitations can be accounted for using MC calculations.

2.3.4 | Environmental dose assessment

To verify shielding integrity after installation, an environmental dose assessment may be performed using transmission measurements. These involve comparing unattenuated (no barrier) and attenuated (with barrier) exposure values with a dosimeter (Salehzahi and Tse, 2020), typically calibrated in ambient dose equivalent $H^*(10)$, or its rate. This operational quantity is deliberately defined to exceed the effective dose E, which cannot be measured directly, thus intended to provide a conservative estimate of E (Pelliccioni, 2000; Tajudin, 2020).

Table 2.5: Key parameters used in analytical shielding calculations. Sourced from Abdallah (2007).

Parameter	Definition / Notes
Distance d	The straight-line distance from the radiation source to the point of interest. It appears in the inverse square law component: $$H \propto \frac{1}{d^2}$$
Workload W	The number of patients scanned per day (or week), used to scale the total expected radiation output over time.
Occupancy factor T	A dimensionless value between 0 and 1 representing the fraction of time an area is occupied. E.g., $T = 1$ for control rooms and $T = 0.2$ for corridors.
Administered activity A_0	The initial activity of the radionuclide administered per scan. In practice, **cumulated activity** $\tilde{A}$ can be used in calculations, which accounts for physical decay and represents the total number of disintegrations during the scan period. For a **scan duration** t_s and **decay constant** λ, this is: $$\tilde{A} = \int_0^{t_s} A_0 e^{-\lambda t} dt = \frac{A_0}{\lambda}(1 - e^{-\lambda t_s}) = A_0 \frac{T_p}{\ln 2}\left(1 - e^{-\frac{\ln 2}{T_p} t_s}\right)$$
Gamma constant Γ	A radionuclide-specific constant (in units of mSv/h·MBq, or similar) that relates activity to equivalent dose rate at a distance. It incorporates the photon energy and emission probability.
Uptake factor F_u	Accounts for the biological uptake during waiting time. If no uptake is considered, $F_u = 1$, i.e., neglected.
Decay factor F_d	Represents the decrease in activity due to physical decay during the scan duration. In this work, this factor is absorbed into the definition of A, and thus not applied separately.
Permissible dose P	The annual effective dose constraint for the area being shielded. Controlled areas typically use an occupational limit of 6 mSv/year, but in Malta's NM department, a conservative value of 1 mSv/year is often adopted. Supervised areas follow the public dose limit of 0.25 mSv/year.

Passive monitoring is often done with TLDs (Le et al., 2020; Yin et al., 2021), while survey meters provide real-time spot-checks (Bjerke et al., 2012), or both may be used (Abdallah, 2007). Monitoring is performed near critical boundaries, such as control rooms and entrances, as well as suspected weak spots. This highlights a key advantage over MC simulations, which may not account for unknown weak points like screws within lead sheets or hidden services, especially

if not included in the original technical drawing.

While essential, physical assessment has key limitations, primarily, that it can only be performed post-installation. Moreover, TLD measurements introduce delays due to calibration and processing. Results may vary due to environmental factors, especially from nearby sources such as patients undergoing other scans. These issues are absent or manageable in MC simulations. Nonetheless, physical measurements remain valuable as ground-truth validation data and for refining simulation models, provided they are sufficiently accurate themselves.

2.4 | The Monte Carlo method

There exists a multitude of definitions for the "Monte Carlo method." Originally described by von Neumann, Metropolis and Ulam as “a statistical approach to the study of differential equations” (1949, p.335), it was developed to model neutron behaviour in fissionable materials at Los Alamos. Their key insight was that even deterministic problems could be reformulated probabilistically and solved through random sampling (Allen and Tildesley, 2017). Since then, MC has found applications far beyond physical sciences, in fields like finance, risk analysis, and even computer graphics. For radiation transport, it may be defined as:

A numerical technique that uses random sampling to model complex physical processes that generally lack tractable analytical solutions.

In practice, obtaining a closed-form solution often requires significant simplifications, as it is rarely possible to account for all aspects of a physical problem within an analytical model.

The key word aforesaid is model, which is frequently misunderstood. A physical model is, fundamentally, a system of equations intended to describe a real-world process. The MC method is then applied to this system not to find a closed solution, but to estimate the outcome of interest, which is typically a parameter of a probability distribution, and to quantify the associated statistical uncertainty (Vassiliev, 2017). This leads to a crucial insight in MC methodology: a result without an uncertainty is incomplete and scientifically meaningless. Since the output of an MC simulation is an estimate based on finite sampling, it inherently includes statistical fluctuations. Reporting the estimate without its uncertainty fails to convey

how reliable that result is. This makes uncertainty quantification an inseparable part of any MC-based analysis.

Returning to the distinction between deterministic and stochastic approaches, a widely used example of a deterministic software is MicroShield (Grove Software, 2024). Oliveira and Oliveira (2005) compared it with the MC code MCNP (see § 2.4.3) in a basic shielding setup. Below 500 keV, deviations reached 50% when secondary interactions were included, which is critical given most NM radionuclides emit energies in this range. More crucial, MicroShield supports only simple geometries, making it unsuitable for complex cases like the one in this study.

2.4.1 | Underlying theory of MC

The MC method is based on the use of probability theory and random sampling to model complex physical processes. In radiation transport, MC enables the stochastic simulation of particle interactions with matter to provide detailed insight into various physical quantities that are often impractical or impossible to derive analytically.

2.4.1.1 | The theory of probability

Probability theory underlies the MC method as it provides the mathematical foundation for modelling random processes and interpreting simulation outcomes. The discussion that follows draws substantially on the text from Infantino (2015).

MC techniques often deal with random variables. Let $z(x)$ be a function of a continuous random variable x, which follows a Probability Density Function (PDF) $f(x)$ (Figure 2.8.a). The PDF describes how probability is distributed across values of x and has the following properties:

1. $\int_{-\infty}^{\infty} f(x)\,\mathrm{d}x = 1$
2. $f(x) \geq 0 \quad \forall \quad x \in [a, b]$
3. $P(a \leq x \leq b) = \int_a^b f(x)\,\mathrm{d}x.$

The PDF does not give the probability of a single value of x, but rather the probability that x lies within a small interval $\mathrm{d}x$ around a particular value.

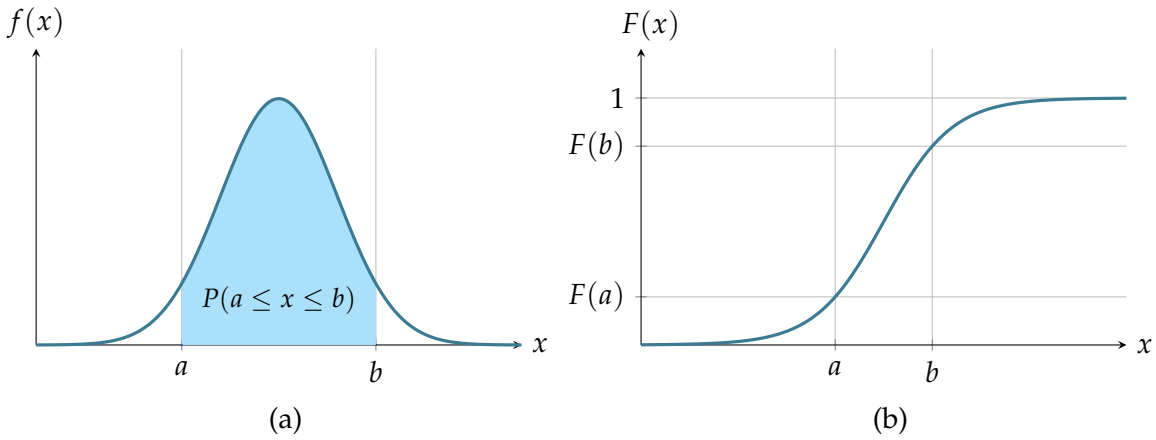

Figure 2.8: (a) Plot of a normal probability density function $f(x)$. The shaded area $P(a \leq x \leq b)$ represents the probability that the variable falls within the interval $[a, b]$; (b) Plot of the corresponding cumulative distribution function $F(x)$, where the same probability is given by the vertical difference $F(b) - F(a)$.

The expected value, or population mean, of $z(x)$ is defined as,

$$\langle z \rangle = \int_a^b z(x) f(x) \, \mathrm{d}x. \tag{2.3}$$

This expression can be difficult or impossible to solve analytically, especially in higher dimensions or when $f(x)$ is complex. MC allows for this expected value to be estimated using random sampling. To estimate $\langle z \rangle$, N values x_i are randomly sampled from the PDF and the sample mean is computed as,

$$\overline{z} \approx \frac{1}{N} \sum_{i=1}^{N} z(x_i). \tag{2.4}$$

This is the MC estimate of the expected value, i.e., an estimate of the true mean $\langle z \rangle$ obtained from a finite number of N samples. In radiation transport jargon, each sample x_i is referred to as a primary or history, and correspond to a simulated particle trajectory. As $N \to \infty$, the sample converges to the true mean,

$$\lim_{N \to \infty} \overline{z} = \langle z \rangle. \tag{2.5}$$

This convergence is guaranteed by the law of large numbers, which is a pillar of the MC method and states that the average of the results will approach the expected value as the number of trials of a random process increases (Grinstead and Snell, 2006).

To quantify the spread or uncertainty in the estimate, the population variance is defined as,

$$\sigma^2(z) = \int_a^b [z(x) - \langle z \rangle]^2 f(x)\, \mathrm{d}x = \langle z^2 \rangle - \langle z \rangle^2 \approx \frac{1}{N} \sum_{i=1}^{N} [z(x_i) - \langle z \rangle]^2. \tag{2.6}$$

In practice, $\langle z \rangle$ is not known, so instead, the sample variance is estimated using,

$$s^2(z) = \frac{1}{N-1} \sum_{i=1}^{N} [z(x_i) - \bar{z}]^2. \tag{2.7}$$

Finally, the result is presented as,

$$\langle z \rangle \approx \bar{z} \pm s(z), \tag{2.8}$$

where $s(z) = \sqrt{s^2(z)}$ is the sample standard deviation. This provides an estimate $\bar{z}$ of the expected value together with an uncertainty $s(z)$, assuming a sufficiently large number of primaries simulated.

2.4.1.2 | Sampling random variables

Having established how an MC estimate is formed, the next natural step is to consider how the random samples x are generated in order to evaluate the estimator. To generate random samples x from a desired PDF, the Cumulative Distribution Function (CDF) is commonly used, and defined as,

$$F(x) = \int_{-\infty}^{x} f(x')\, \mathrm{d}x'. \tag{2.9}$$

The CDF expresses the probability that a random variable takes on a value less than or equal to x and increases monotonically from 0 to 1 (Figure 2.8).

In practice, a random number η is drawn from a uniform distribution over $[0, 1]$, and the corresponding sample is obtained by inverting the CDF, i.e.,

$$x = F^{-1}(\eta). \tag{2.10}$$

This approach is known as inverse transform sampling. Alternative sampling strategies exist, such as the rejection method and von Neumann's method (Vassiliev, 2017), and are used when the CDF cannot be easily inverted. The common goal of these sampling methods is to provide MC simulations with random samples that accurately reflect the target distribution, whether defined by simple analytical functions or user-specified forms (e.g., Gaussian or exponential), or derived from complex physics data libraries (e.g., cross sections, angular distributions or energy spectra).

2.4.1.3 | Pseudorandom number generation

Evidently, random numbers lie at the core of any MC algorithm. However, using truly random numbers would hinder reproducibility and make comparing simulation results difficult. As such, pseudorandom number generators are employed. These produce numbers uniformly distributed in the interval $[0, 1]$ using a deterministic algorithm, such that the same sequence is reproduced whenever the same set of seed values is used. The MC code FLUKA employs the RM64 generator, which is a linear congruential generator that requires 97 seed values (European Organisation for Nuclear Research [CERN], 2024).

2.4.1.4 | Statistical convergence and uncertainty

To achieve low statistical uncertainty, a sufficiently large number of contributions N must reach the estimator (see § 2.4.2). By the central limit theorem, the distribution of the estimator approaches a Gaussian centred on the true expectation value (Grinstead and Snell, 2006), with standard deviation scaling as,

$$\sigma \propto \frac{1}{\sqrt{N}}. \tag{2.11}$$

Thus, reducing uncertainty requires large N, which is computationally expensive. For instance, when particles traverse thick, high-Z materials, their probability of survival, and thus of reaching the estimator, is low, which is compensated for by simulating a large N. Such cases can demand hours or even days of runtime, depending on factors such as geometry and transport thresholds. This limitation is alleviated by the embarrassingly parallel nature of MC algorithms, whereby independent simulation jobs can be executed concurrently on separate processing units, whether on a local workstation, a computing cluster, or both simultaneously (Atanassov et al., 2016) — a scheme adopted in this work. An alternative is the use of variance reduction techniques (Vassiliev, 2017). However, these were not implemented in this work.

2.4.2 | The radiation transport problem

Now that the fundamentals of MC methods have been established, the radiation transport problem can be addressed. This may be described in three stages (CERN, 2024):

- **Radiation source**: The origin of particles in a transport problem, which may include photons, electrons, neutrons, or other particles over a broad energy spectrum. Sources may

be monoenergetic or follow complex energy-angle distributions, and may be isotropic, directional, or spatially structured depending on the physical system modelled.

- **Propagation in matter**: As particles traverse materials of varying composition and geometry, they undergo interactions that alter their energy, direction, or state, and may produce secondary particles. The probability of each interaction is given by its cross section, which depends on factors like particle type, energy, and medium properties (Vassiliev, 2017). For photons, dominant processes in the relevant energy range are the photoelectric effect, Compton scattering, and pair production (Mott and Daniel, 2021b). For electrons, transport is continuous in nature and is dominated by collisional and radiative energy losses through Coulomb interactions (Mott and Daniel, 2021a).

- **Detection**: The measurement of quantities characterising the particle field or its effects, such as energy spectra, deposited dose, and material activation. These quantities are obtained via estimators[5], which are the computational analogues of physical detectors.

In essence, MC radiation transport is the stochastic solution of the Boltzmann transport equation, which describes the statistical behaviour of particles as they traverse and interact with matter (Vassiliev, 2017). The equation incorporates terms for particle streaming, interaction, scattering, absorption, and sources, and is solved by sampling individual particle histories from the underlying probability distributions.

2.4.3 | MC codes: FLUKA and others

Several MC codes exist, each with their own algorithms and domain-specific applications. Table 2.6 summarises the most applicable to the medical physics and radiation protection profession.

Among the codes in Table 2.6, FLUKA (FLUktuierende KAskade in German, "fluctuating cascade") is a general-purpose MC code for particle transport and interaction with matter that covers an extensive range of applications. Founded at CERN, its development places strong emphasis on comprehensive and precise physics models, particularly, its ability to simulate around 60 different particles species over energies ranging from thermal neutrons to cosmic

[5]These are commonly termed *scores* in FLUKA jargon, or *tallies* in other codes such as MCNP.

Table 2.6: Summary of selected MC codes relevant to medical physics and radiation protection. Data compiled from Ahdida et al. (2022), Kawrakow et al. (2000), Ljungberg et al. (1998), Rising et al. (2025), and Strulab et al. (2003).

Code	Particles handled	Energy range	Main applications
MCNP	Neutrons, photons, electrons, etc.	ev–TeV	Shielding, criticality safety, dosimetry
EGS / EGSnrc	Photons, electrons, positrons	keV–GeV	Radiotherapy beam modelling, brachytherapy, detector studies
Geant4 / GATE	Wide range including EM, hadronic, optical	eV–PeV	High-energy physics, space applications, NM imaging (especially PET & SPECT)
SIMIND	Photons	keV–MeV	SPECT imaging research
FLUKA	Photons, electrons, muons, hadrons, heavy ions, etc.	eV–PeV	Shielding, dosimetry, activation, target design, radiotherapy

rays. Moreover, FLUKA can handle very complex geometries using combinatorial geometry, and can operate with minimal user programming required. (Ahdida et al., 2022).

Compared with more specialised codes such as EGS or SIMIND, FLUKA offers a much broader application scope, while for shielding problems it has been shown to deliver results in excellent agreement with experimental benchmarks (Infantino et al., 2016; Romanets et al., 2013). This makes it particularly well-suited to the present study, which, although revolves around modelling a SPECT/CT scanner, its primary focus is on radiation shielding assessment. Also, the availability of Flair (FLUKA Advanced Interface) facilitates an efficient workflow for geometry building and visualising results (Donadon et al., 2024), particularly beneficial for users with limited MC experience.

2.4.4 | Applications of MC in nuclear medicine and radiation protection

The MC method is increasingly regarded as the gold standard for a range of applications across the fields of medical physics and radiation protection due to its negligible cost, absence of patient exposure, and high accuracy in reproducing complex radiation interactions (Sarrut, 2025). However, in Malta, its clinical use is currently limited to a single stage in the radiotherapy pathway, namely treatment planning. This situation is mirrored internationally. Nevertheless, international literature documents its widespread research application, including imaging sys-

tem design, patient dosimetry, treatment planning, and shielding assessment. Representative examples are provided in Table 2.7. With adequate computing resources available at MDH and the University of Malta, and only one relevant Maltese study identified (Bezzina, 2015), there is a strong case for expanding its use nationally within medical physics and radiation protection practices.

Table 2.7: Various works utilising MC simulation in medical physics and radiation protection. CTDI = CT Dose Index; DIR = Diagnostic and Interventional Radiology; RP = Radiation Protection.

Author(s), Year	**Application (incl. validation)**	**Specialty**	**Code**	**Validation**
Abdallah (2007)	Shielding design for PET facility using analytical, experimental and MC approaches to estimate weekly doses and required barrier thickness; comparison of all three approaches.	NM, RP	MCNP	TLD & survey meter measurements (dose type unspecified)
Belinato et al. (2015)	CT dosimetry in PET/CT using anthropomorphic phantoms; included experimental determination of bowtie filter geometry and modelling of X-ray source motion.	DIR, NM	MCNP	Ion chamber CTDI measurements, $CTDI_{100}$
Infantino et al. (2016)	Simulation of different RP aspects in the use of biomedical cyclotrons, including activation of bunker walls.	NM, RP	FLUKA	Experimental neutron dosimetry, $H^*(10)$
Pells et al. (2023)	Model of a SPECT/CT system for quantitative imaging; simulation of projection data, system sensitivity, spatial resolution, and scatter correction methods for different radionuclides and collimators.	NM	GATE	Experimental measurements (various metrics)
Pommranz et al. (2025)	Model replica of a PET/CT scanner for event processing and image reconstruction.	NM	GATE	Experimental measurements (various metrics)
Pretorius et al. (2015)	Modelling of the charge transport within the CZT detectors for a cardiac SPECT system.	NM	SIMIND	Experimental measurements (various metrics)
Rault et al. (2010)	Detailed model of back compartment of gamma camera for improving accuracy in scatter and septal penetration modelling.	NM	GATE	Experimental measurements (various metrics)

Several MC studies have modelled SPECT systems for imaging performance (Pells et al., 2023; Pretorius et al., 2015; Rault et al., 2010), but not for radiation shielding. Moreover, a series of annual student projects (Soliman, 2024; Tassé, 2025) use MCNP to assess lead shielding thickness for a SPECT/CT prototype, where they model SPECT and CT separately with ^{99m}Tc and

^{131}I sources. While relevant in terms of modality, these models are overly simplified and, more critically, lack validation. No comprehensive, site-specific MC shielding study for SPECT/CT exists to date, making the present work unique.

2.5 | Conclusion

Accurate prediction of radiation shielding performance in SPECT/CT is essential for ensuring compliance with radiation protection standards in NM facilities. This chapter has highlighted notable literature gaps, particularly, the absence of detailed, site-specific, and validated MC radiation shielding studies for such systems. The following chapter details the development and validation processes of a realistic model tailored to the facility under investigation.

3

Research Methodology

3.1 | Introduction

In this chapter, the research methodology is presented. This covers the chosen research approach and strategy, data collection techniques, tools and procedures, and data analysis techniques. Notably, the approach in creating the MC model, such as, accurately designing the facility's geometry, setting up the radioisotope source, and selecting the appropriate transport parameters, are explored in great detail and discussed in terms of their implementation in FLUKA through Flair. The validation process is also described. Lastly, the methodological limitations are acknowledged.

3.2 | Research approach

The study relies on outputs from MC simulations, physical experimental measurements, and theory-based analytical calculations, all of which yield data which are measurable, objective and statistical. The nature of these data forms the basis for the choice of a quantitative research approach (Ghanad, 2023). Moreover, data from all three data collection methods are reproducible. Analytical and MC simulations results remain constant for a given set of initial parameters. As for experimental data, while not perfectly reproducible, can achieve a high degree of consistency under controlled conditions, where in this case, variation arises primarily from measurement uncertainties such as reader instability, positioning errors, and variability in TLD chips.

The quantitative approach also facilitates hypothesis testing (Ghanad, 2023). The primary hypothesis formed for this work was whether the MC model could be validated, i.e., whether the simulation results were in agreement with the experimental measurements.

3.3 | Research strategy

The research strategy adopted in this study combines simulation, experimental, and case study approaches, with an overall comparative element. One of the main objectives of this study was to develop an MC model of the scanner and its surroundings, and simulate particle transport using FLUKA. Inherently, this implies a simulation-based research strategy. Moreover, in order to validate the simulation model with empirical data, an experimental strategy was incorporated by conducting TLD measurements. This work also took the form of a case study, as it focused on the installation of a specific SPECT/CT scanner in a single hospital environment, thereby, situating the findings within a real-world context. Lastly, the systematic comparison of simulation, experimental and analytical results enabled the model validation and identification of systematic discrepancies between methods (Sekaran and Bougie, 2016).

Alternative strategies, such as surveys or qualitative interviews, were not applicable, as the research does not involve subjective experiences (Ghanad, 2023). Likewise, a purely observational strategy would have been insufficient, as it would not have provided the quantitative dose estimates required. Instead, the chosen combination of strategies was most appropriate for addressing the research objectives.

3.4 | Data collection technique

Three distinct data collection techniques were employed in this study:

- **Simulation**: Data were obtained through MC simulations in FLUKA. The facility geometry, material compositions, transport parameters, and source characteristics were defined within the code. The simulations produced various numerical outputs including equivalent dose estimates, dose and particle fluence, and energy spectra and deposition.

- **Experimental**: This involved the use of TLDs, which are crystalline materials that, when heated, emit light in proportion to the absorbed radiation dose. The TLDs were placed at predetermined positions within the facility during representative scan conditions and subsequently read out following the appropriate annealing and calibration procedures. This provided empirical dose measurements that enabled direct comparison with the simulated values.
- **Analytical**: Shielding calculations were performed using standard formulae and clinically applied and published reference data. This approach was included to enable further comparison with the other two methods, especially since it is the one routinely used in clinical practice.

3.5 | Data collection tools

The acquisition of data in this study relied on both physical dosimetry instruments and dedicated simulation software. The following outlines each tool used in detail.

3.5.1 | FLUKA and Flair

As previously mentioned, the simulations were performed using FLUKA (v4-4.1) together with Flair (v3.3-1). FLUKA is an MC transport code that executes calculations based on ASCII text-input files (`.inp`), while Flair serves as the graphical user interface for creating and editing input files, constructing and visualising geometries, executing simulations interactively, and inspecting results. Each `.inp` file is organised as a sequence of command lines known as *cards*. Each card contains:

- One keyword
- Six numerical parameters (called `WHATs`)
- One character string (called `SDUM`)

A typical `.inp` file includes the following card sections:

- `General`: Title, default physics setting, and random number initialisation
- `Primary`: Specification of the source term and number of primaries
- `Geometry`: Definition of the model geometry

- `Media`: Definition and assignment of the materials
- `Scoring`: Setup of the estimators (at least one)
- `Transport`, `Biasing`, etc.: Other optional settings

Flair builds upon this structure by generating a `.flair` project from the underlying `.inp`. An example snippet is shown in Figure 3.1. A detailed walk-through of how these elements were implemented in Flair for this work is given in § 3.6.

```
*
******   GENERAL   *****
TITLE
Main Study
*The defaults for precision simulations
DEFAULTS                                                            PRECISIO
*
*
******   PRIMARY   ****
*
*Beam (source) characteristics
*  ISOTOPE = Radioisotope source
BEAM                                                                ISOTOPE
*  Tc-99m
HI-PROPE          43        99        -1
*  Centred within phantom
BEAMPOS   8.80332841   93.3675-1.8712052
*  Within water region of phantom
BEAMPOS           0.      10.8        0.      18.6                  CYLI-VOL
BEAMAXES          0.        0.        1.        0.        1.        0.
*
*
******   GEOMETRY   *****
GEOBEGIN                                                            COMBNAME
    0    0
*Black body container
RPP blkbody    -1400 1300 -600 900 -1450 1100
*Air container
RPP air        -900 800 -100 400 -950 600
*
```

Figure 3.1: Snippet from a FLUKA `.inp` file, specifically, that of the main study. Lines commencing with an asterisk (*) are comments and the rest are commands.

Importantly, the FLUKA code itself undergoes validation after each release using the dedicated FLUKAVAL benchmark suite (Widorski et al., 2023). During the course of this work, updated versions were released (FLUKA v4-5.0; Flair v3.4-4), but upgrades were deliberately avoided to prevent workflow interruption.

3.5.2 | TLD system

Lithium fluoride doped with magnesium, copper and phosphorus (LiF:Mg,Cu,P) was selected as the thermoluminescent material for this study. This choice was preferred over the alternative LiF:Mg,Ti available at the hospital as previous work demonstrated its superior performance (Grima, 2024). In total, 33 LiF:Mg,Cu,P chips were calibrated and of these, 18 were employed

in the pilot study, while the full set was used in the main study. For improved reliability, the TLDs were grouped in threes and placed in thin polyethene pouches (Figure 3.2a).

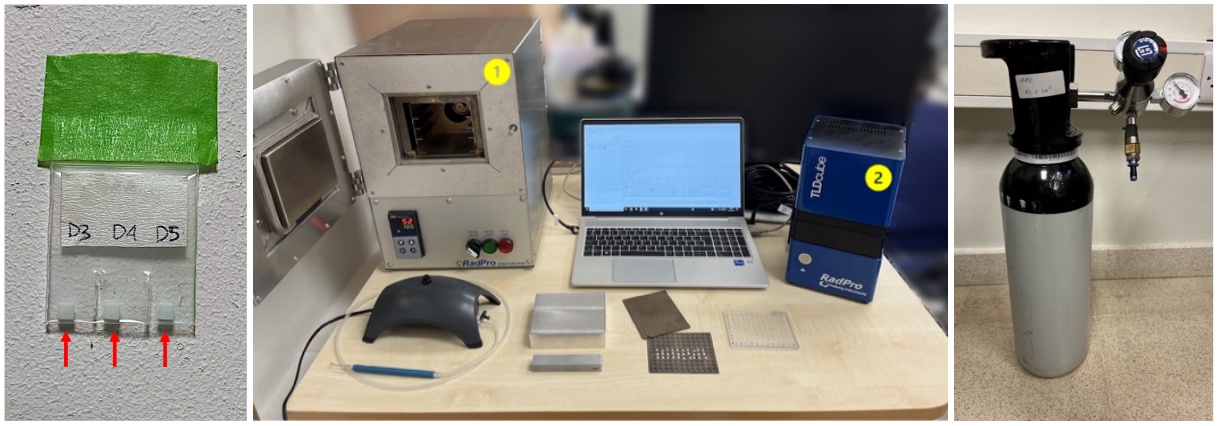

(a) (b) (c)

Figure 3.2: (a) TLDs (marked with red arrows) placed in a polythene pouch. Crystal identifiers 'd3', 'd4', and 'd5' are indicated for the individual TLDs. (b) Workstation setup for annealing and reading the TLDs: (1) TLD Heat (annealing oven) and (2) TLDcube (readout device). The unlabelled equipment is ancillary and thus is not discussed. (c) Nitrogen supply tank with regulator assembly.

TLDs function as part of an integrated dosimetry system rather than as stand-alone dosimeters. Such a system typically comprise an annealing oven, used both to erase residual signals from prior exposures (*pre-irradiation annealing*) and to suppress low-temperature artefacts (*post-irradiation annealing*), together with a reader oven, which detects emitted light photons via a photocathode (Figure 3.2b). In this study, TLD Heat and TLDcube were used and operated with Thermosoft v1.0.7.0 (Könn Thermoprozesstechnik GmbH, Germany) and TLStudio v1.11.2 (Freiberg Instruments GmbH, Germany), respectively. Additionally, nitrogen flushing was employed to improve reader efficiency (Figure 3.2c). The complete system is distributed by RadPro International GmbH (Germany).

3.5.3 | Survey meter

To calibrate the TLDs in terms of $H^*(10)$, a Mini Smart-ION 2120 (Figure 3.3) ionisation chamber–based survey meter (Thermo Fisher Scientific, USA) was employed as it was already calibrated in $H^*(10)$. Its most recent calibration was performed in December 2024 at an accredited calibration laboratory traceable to a primary standards laboratory, thereby ensuring metro-

logical traceability of the TLD measurements. The 2120 model is capable of measuring both instantaneous dose rate and time-integrated dose.

(a) (b)

Figure 3.3: The Mini Smart-ION 2120 survey meter used for this study, showing (a) the display measuring the instantaneous dose rate of $H^*(10)$ in µSv h^{-1}; and (b) the sliding window shield that facilitates the measurement of $H^*(10)$.

3.5.4 | SPECT/CT

The NM/CT 870 DR (General Electric, USA) installed in the NM department was not operated for imaging purposes. It was, however, positioned in the standard bone scintigraphy configuration, with the detectors set in H-mode above and below the patient table, and left in this arrangement for the duration of the main study experimental measurement.

3.5.5 | Source phantom

To emulate the distribution of ^{99m}Tc within a patient, a flanged Jaszczak phantom (Mirion, USA) was used (Figure 3.4). The phantom is constructed from a thick shell of Polymethyl Methacrylate (PMMA), which provides approximate tissue equivalence, and contains removable inserts consisting of cold rods and spheres. For this study, the Jaszczak phantom was filled

with water and known activities of ^{99m}Tc measured using a CRC-55tR dose calibrator (Mirion, USA), and the inserts removed.

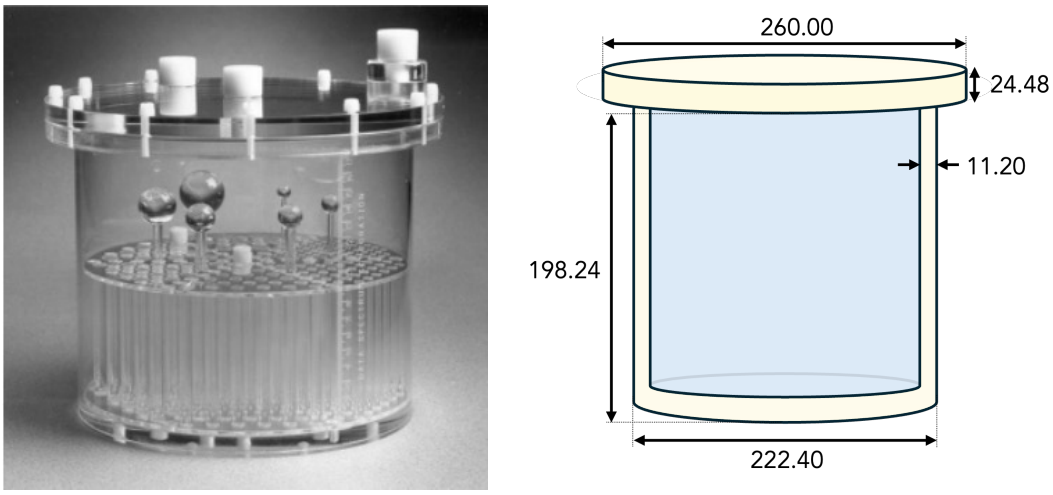

(a) (b)

Figure 3.4: (a) Photograph and (b) schematic drawing of the flanged Jaszczak phantom. Measurements are in millimeters (mm). The schematic drawing is not to scale and not all the measurements are shown. The Jaszczak's rods and shperes are omitted in schematic (b) to reflect the configuration used for this study. (a) is reprinted from ELSE Solutions (n.d.).

3.5.6 | Computational resources

The simulations were executed on a combination of local workstations and a high-performance computing cluster. The local machines were additionally utilised for input preparation and result inspection. The cluster nodes were managed by the Slurm Workload Manager (SchedMD, USA) via custom-written bash scripts and offered parallel processing capabilities that considerably reduced computation times. Table 3.1 summarises the main specifications of each platform.

Two important concepts to discuss are spawns and cycles, which are inherent to FLUKA, but are closely linked to computational resources. A spawn, or job, represents a single independent run executed on a single CPU core. In contrast, a cycle refers to a series of sequential runs on the same core, each with N primaries and a unique random seed. For illustration, running 3 spawns with 5 cycles each produces 15 statistically independent batches of histories. The advantage of this arrangement is that results from all cycles can be combined to reduce statistical

Table 3.1: Specifications of the computational resources used for FLUKA simulations. For the personal laptop, performance (P) and efficiency (E) cores are listed separately. The specifications for the cluster correspond specifically to nodes `ict-d0-01` and `ict-d0-02`. HPC = High-Performance Computing.

	Personal Desktop (custom-built)	**Personal Laptop** (MacBook Pro M3)	**HPC Cluster** (`ict-d0-[01-02]`)
CPU / Chip	Intel Core i5-8600K	Apple M3 Pro	Intel Core i5-10400
Clock Speed	3.60 GHz	4.05 GHz	2.90–4.30 GHz
Cores / Threads	6 cores	11 cores (5P + 6E)	6 cores / 12 threads
RAM	16 GB	18 GB	20 GB
Operating System	Windows v2.0.3	macOS v1.30.0	Ubuntu v22.04.5

uncertainty in less time, provided that multi-core architectures are available. On paper, a total of $6 + 11 + 2(6) = 29$ cores were available for use. However using every core on a machine risks system instability since at least one has to remain free for essential background processes. All simulations were run with the default five cycles per spawn, while the number of spawns varied.

3.6 | Data collection procedure

Data collection in this study followed a sequence of linked stages that combined the three data collection techniques. The workflow illustrated in Figure 3.5 shows how calibration, pilot study, and main study investigations were integrated to produce the final results that eventually led to comparative analyses, annual dose estimates, and the extension to the ^{177}Lu case.

The process commenced with calibration of the TLDs in terms of $H^*(10)$ for ^{99m}Tc exposures. This yielded the calibration factors required for the pilot and main studies in order to convert TLD reader counts into $H^*(10)$ for the TLDs. A full description of the procedure is provided in Appendix B, as its full detail here lies beyond the main focus of this work.

Following calibration, a pilot study was conducted to validate the practicality of a small-scale setup and ensure that the MC implementation was progressing as intended. This was an iterative process, with minor adjustments made to the MC model to improve agreement between simulation and experimental $H^*(10)$ values. For instance, introducing the small gap between the table and the wall, caused by skirting, shifted the phantom away by a few cen-

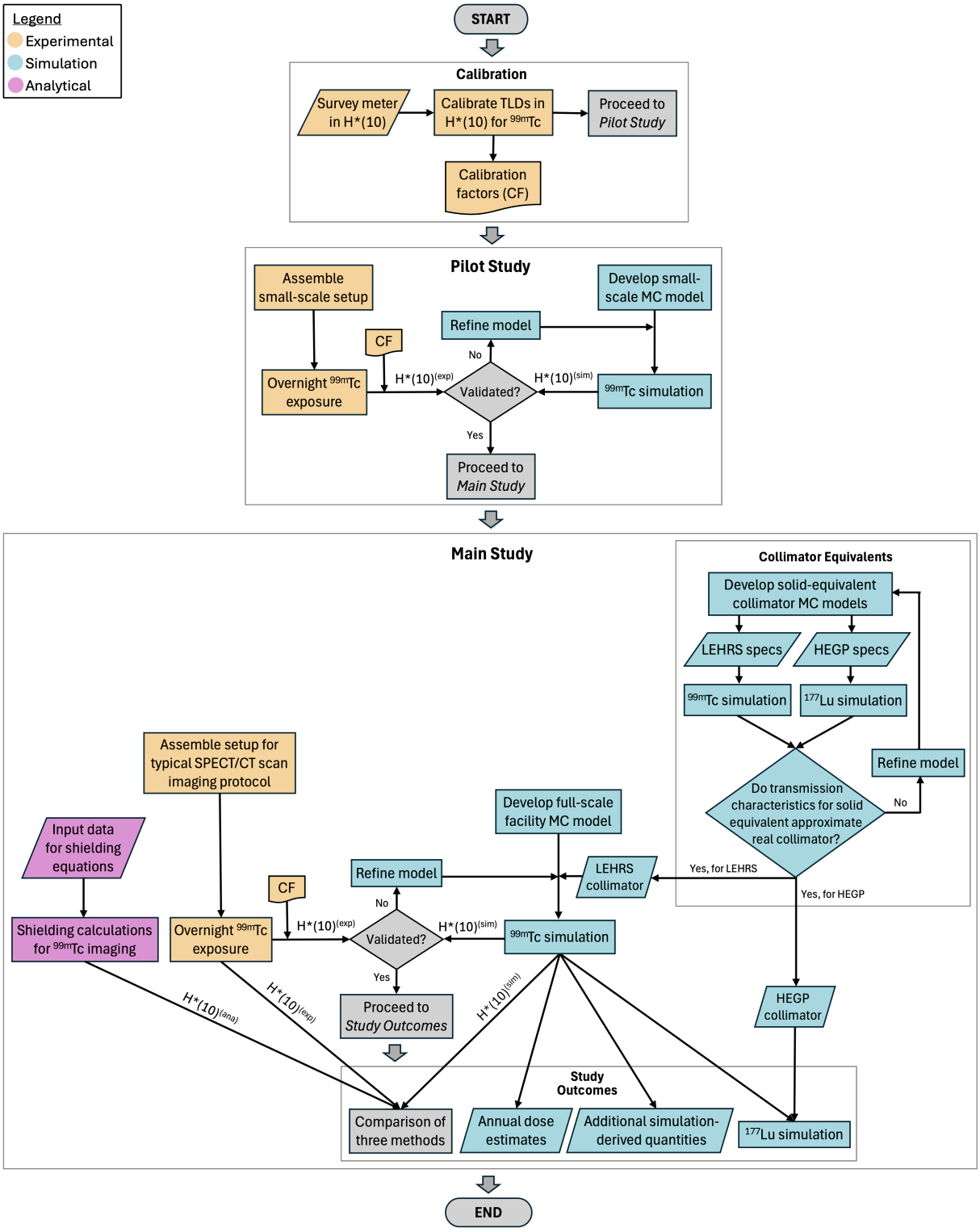

Figure 3.5: Methodological flowchart illustrating the calibration, pilot study, and main study stages of this work. Gold, blue, and purple denote experimental, simulation, and analytical processes, respectively. Grey nodes represent steps that are not specific to a single technique.

timetres and brought the simulated $H^*(10)$ closer to the experimental value.

Lastly, in the main study, a full-scale facility MC model for a typical SPECT/CT imaging protocol was developed. As in the pilot stage, the model was refined iteratively. In parallel, supplementary simulations were carried out to develop LEHRS and HEGP solid-equivalent collimator models. These were designed to reproduce the transmission of the real collimators while reducing modelling complexity. Once the ^{99m}Tc study was validated, experimental, simulation, and analytical $H^*(10)$ results were compared. Moreover, the validated simulation was further extended to derive annual dose estimates, extract additional physical quantities, and form the basis for a ^{177}Lu imaging study.

3.7 | Pilot study

Before undertaking the effortful task of developing the facility-level MC model, a small-scale pilot study using a simple wall set-up (Figure 3.6), related to, but independent of, the full model,[6] was performed to generate $H^*(10)$ values and benchmark it against measurements as a preliminary validation. The aims were to confirm that (i) the FLUKA implementation was progressing in the right direction and (ii) that the experiment-simulation workflow was sound.

For both approaches, the setup consisted of a Jaszczak phantom on a plywood table with six TLDs, grouped in pouches for the analytical method and treated individually for the simulation. The first was positioned 100 cm from the front face of the phantom and the others spaced at 20 cm intervals. The wall layers' configuration mirrored the main study.

3.7.1 | Experimental method

For the pilot study, 18 TLDs were used, grouped in threes within labelled pouches. Further details on the annealing and readout procedures are described in a previous study (Grima, 2024). The phantom was then prepared. Water was partially drained from the phantom to make space for the injection volume of ^{99m}Tc eluate. The activities and timestamps for elution, residual measurement, and phantom placement and removal on the table were recorded as inputs for the simulation phase (see § 3.9.1).

[6] This pilot was not a direct sample of the main study and thus, $H^*(10)$ values were not expected to match the facility model. Accordingly, results are reported in the Results chapter.

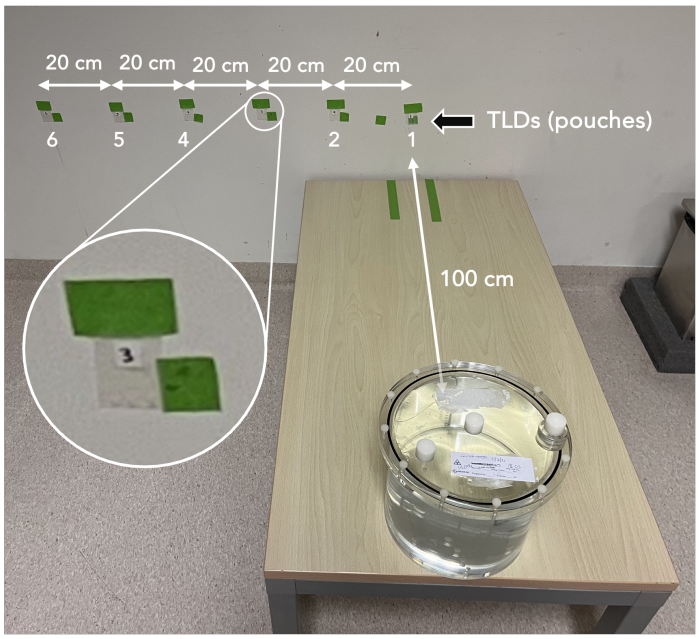

(a)

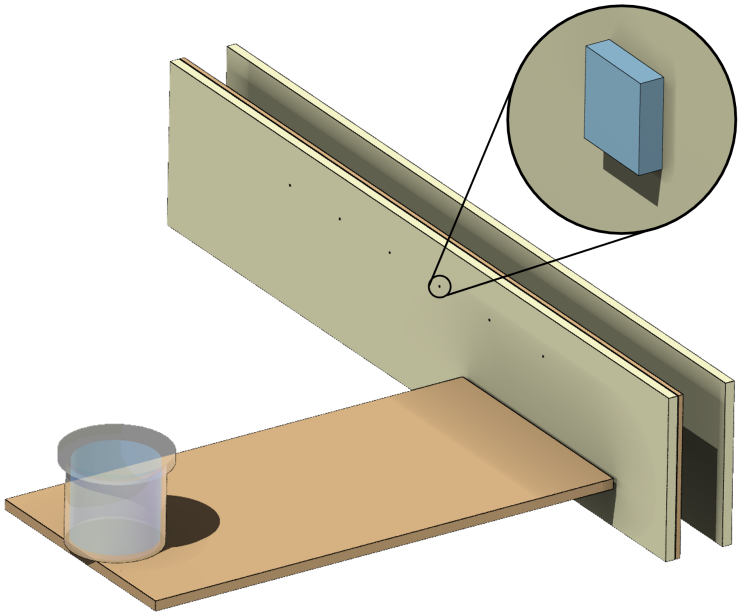

(b)

Figure 3.6: (a) Experimental and (b) MC model setup of the pilot study. The numbers below the TLD pouches, 1–6, in (a) indicate their identifiers. The zoom-ins in show the third (a) TLD pouch and (b) single TLD on the wall, which are at a 40 cm separation from the first pouch/TLD.

Before placing the phantom on the table, the TLD pouches were fixed in their designated positions. These were then irradiated overnight for approximately 19 h, after which the setup was dismantled and the TLDs immediately taken for post-irradiation annealing and readout. The resulting counts were processed with the calibration parameters to yield the $H^*(10)$ values for the experimental phase of the pilot study.

3.7.2 | Simulation method

Since the MC model for the main study built directly on the pilot study, details of the model implementation in Flair are deferred to § 3.8.

Here, the focus is on the number of primaries simulated and the resulting statistical uncertainties. To examine their relationship with run time, several trial runs were performed. These were executed on five out of six cores available on the personal desktop. For each total number of primaries, the simulation run time and the percentage uncertainty of each TLD's $H^*(10)$ value were recorded and plotted, as visualised in Figure 3.7. The run time data were then fitted to generate a predictive equation as function of the total primaries.

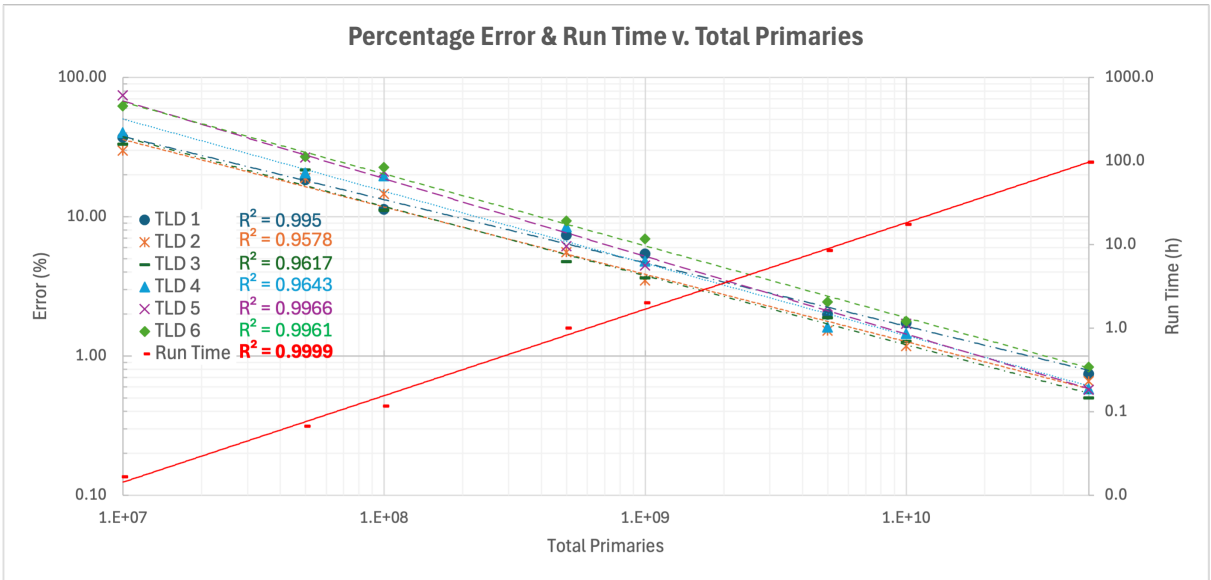

Figure 3.7: Convergence plot for the pilot study showing individual TLD $H^*(10)$ percentage errors and simulation run time as a function of total primaries. Coefficient od determination R^2 values are shown next to each dataset's label. Both axes are logarithmic. Generated using Excel.

Both the error and run time followed power-law behaviour, with errors decreasing and run

time increasing with the number of primaries, as expected. This was supported by coefficient of determination values $R^2 > 0.955$ for all fits. The final primaries-time relationship was:

$$\text{Run time} = 8 \times 10^{-10} \cdot (\text{Primaries})^{1.0353}. \tag{3.1}$$

This trend predicted that achieving $< 1\%$ uncertainties would require 5×10^{10} primaries, corresponding to a run time of 95.4 h. The pilot study was therefore simulated with 5×10^{10} total primaries. The largest observed uncertainty was 0.83% (for TLD 6) with an actual run time of 96.2 h, which was in close agreement with the prediction.

3.8 | Main study

The main study was designed to reproduce a realistic clinical scenario of a patient undergoing a ^{99m}Tc bone scintigraphy scan on a SPECT/CT system. The setup considered all essential components: the phantom positioned on the patient couch with the SPECT detectors in H-mode and in close proximity to the phantom, the scanner itself, and the surrounding shielding structures including walls, doors, the observation window, ceiling, and floor. The TLDs were positioned at selected locations both inside and immediately outside the scanner room to measure $H^*(10)$ at points of occupational and public relevance. This configuration formed the basis for the experimental, simulations, and analytical estimates described in the following subsections. Moreover, another simulation was extended for ^{177}Lu imaging.

3.8.1 | Experimental method

For the experimental method, the same procedure described in the pilot study was followed. The main differences were that a higher activity of ^{99m}Tc and a different exposure time were employed, and all 33 calibrated TLDs (11 pouches) were used instead of a subset.

3.8.2 | Simulation method

To achieve estimates with sufficiently low uncertainty, no trial runs were performed as in the pilot study. Instead, the convergence plot from the pilot study served as a guide for selecting the starting number of primaries. For the main study, simulations were executed using both

the personal desktop and the two cluster nodes on a total of 13 cores. The corresponding total primaries per resource platform and average run times are summarised in Table 3.2. In total, 9.75×10^{10} and 19.50×10^{10} primaries were simulated for ^{99m}Tc and ^{177}Lu, respectively.

Table 3.2: Summary of simulation runs for the main study, showing total primaries handled per resource and average run times for both ^{99m}Tc and ^{177}Lu across the available resources.

Resource	Spawns	^{99m}Tc		^{177}Lu	
		Primaries 10^{10}	Run time h	Primaries 10^{10}	Run time h
Personal desktop	5	3.75	134.75	7.5	122.43
Cluster					
`ict-d0-01`	4	3.0	111.26	6.0	95.81
`ict-d0-02`	4	3.0	111.13	6.0	95.92

3.8.2.1 | Main study `.inp` file

The first section in any FLUKA input file is GENERAL, which typically contains the `TITLE` and `DEFAULTS` cards (Figure 3.8). The latter simplifies input preparation by automatically activating particular physics settings, such as physics models and transport and production thresholds. PRECISIO stands for 'precision' and was selected as it is the recommended option to set for high-precision simulations (CERN, 2020).

Figure 3.8: Flair snippet showing the GENERAL section.

The source was defined in the PRIMARY section (Figure 3.9). By setting the particle type to ISOTOPE in the `BEAM` card, FLUKA was instructed to create a radioisotope source. In this case, ^{99m}Tc was specified in the `HI-PROPE` card by assigning the atomic and mass numbers as 43 and 99, respectively, with the isomeric state indicated by -1.

The `BEAMPOS` cards defined the source position and geometry. The Cartesian coordinates were set such that the source was centred within the phantom and also, to account for the 12° rotational offset of the scanner. The source volume was set as a cylindrical region (CYLI-VOL)

with an outer radius of 10.0 cm, a height of 18.6 cm, and oriented along the Y-axis, with the latter set using the BEAMAXES card.

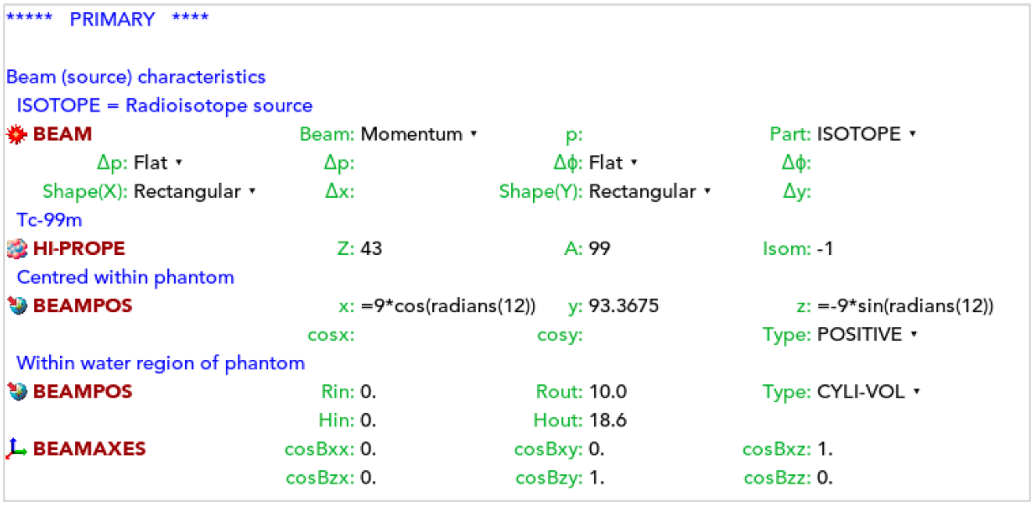

Figure 3.9: Flair snippet showing the source definition in the PRIMARY section.

In FLUKA, geometry is defined using combinatorial geometry. Basic *bodies*, such as planes, cylinders, and quadrics, are combined with Boolean operations (union, intersection, subtraction) to create *zones*. The union of zones in turn creates *regions*, with each assigned a single material.

Figure 3.10 shows an excerpt of the GEOMETRY section to illustrate the typical section structure. For Wall 1 (north of the scanner), multiple infinite YZ-planes at different X-coordinates defined the boundaries: interior surface (W1i), gypsum-lead (W1GL), lead-plywood (W1LP), plywood-air gap (W1PA), air gap-gypsum (W1AG), and exterior surface (W1e). W1GL and W1LP, along with others, were combined to form the lead layer region (W1L), which was defined as the union of four zones (Figure 3.10b). Rather than detailing each body and region, only the key components are discussed here. More comprehensive specifications for each region are detailed in Appendix C.

The modelled SPECT/CT facility extended over the ranges $[X, Y, Z] = [-866{:}734, -50{:}378, -890{:}576]$ cm, with the scanner centre aligned to $X, Z = 0$ and the floor level set at $Y = 0$. All structural components were reproduced in detail as previously outlined in § 2.3.3.1. This included the multi-layered walls, support pillars, lead-lined doors, and the observation lead-glass window. The doors and window were framed with fully lead-lined aluminium jambs,

```
***** GEOMETRY *****
GEOBEGIN                Accuracy:          Option:          Paren:
                        Geometry:          Out:             Fmt: COMBNAME
  Title:
Black body container
RPP blkbody             Xmin: -1400        Xmax: 1300
                        Ymin: -600         Ymax: 900
                        Zmin: -1450        Zmax: 1100
Air container
RPP air                 Xmin: -900         Xmax: 800
                        Ymin: -100         Ymax: 400
                        Zmin: -950         Zmax: 600

---------- FACILITY ----------

Labels follow the notation (mostly):
Char. Idx    Input
1            W = Wall; D = Door; P = Pillar
2 (or 2-3)   Object number (single or double digit)
3-8 (or 4-8) t = top; b = bottom; c = centre; l = left; r = right; a = anterior; p = posterior;
             e = exterior; i = interior;
             G = Gypsum; L = Lead; P = Plywood; A = Air

--- WALLS ---
Wall 1
YZP W1i                 x: 383.5
YZP W1GL                x: 385.9
YZP W1LP                x: 386.1
YZP W1PA                x: 387.3
YZP W1AG                x: 396.6
YZP W1e                 x: 399.0
```

(a)

```
Wall 1 - lead
REGION W1L                          Neigh:
 expr: +W1LP +W4LP +pbt -W1GL -WINDr -floot
     | +W1LP +WINDl +pbt -W1GL -D1re -floot
     | +W1LP +D1le +pbt -W1GL -W2LP -floot
     | +W1LP +WINDr +WINDb -W1GL -WINDl -floot
```

(b)

Figure 3.10: Flair snippet showing the (a) bodies and (b) regions definition parts of the GEOMETRY section.

while the double-leaf door also incorporated a lead-lined astragal. These elements are illustrated in Figure 3.11, with panel (d) providing a perspective view of the scanner room from the west corridor (west wall removed).

Figure 3.12 shows the strategic placement of TLDs around the facility and Table 3.3 details their exact locations. The positions were chosen to focus on areas of interest for shielding evaluation and the heights were selected to approximate the level of a standing adult's waist

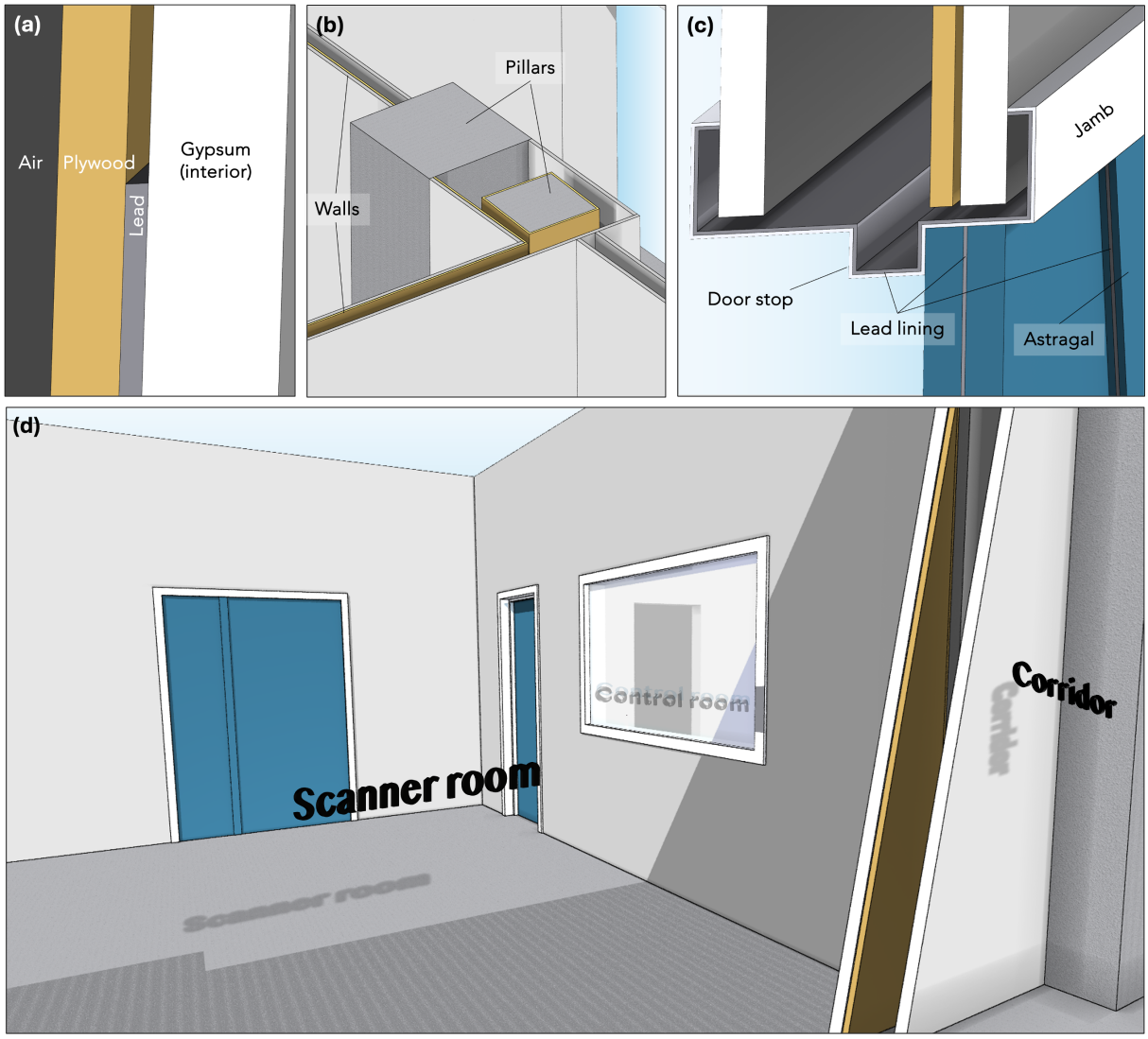

Figure 3.11: Visualisation of key structural elements in the model. (a) Multi-layer wall composition of the scanner room, showing the cut-off of lead at the height of 2 m. (b) View of the south-east support pillars and adjacent bounding walls. (c) Cross-section of the double-leaf door assembly showing the jamb, door stop, astragal, and lead lining. (d) Perspective view into the scanner room, including the two doors and observation window, corridor and control room (the ceiling and the entire scanner are removed on purpose, for clarity).

level. 'C2' was positioned at 150 cm as a storage rack prevented placement at 110 cm. Only one TLD was placed per location rather than three, because, unlike with an experimental setup, virtual detectors are identical and yield consistent responses. This was also the case for the pilot study simulation.

The SPECT/CT scanner was then constructed as three main components:

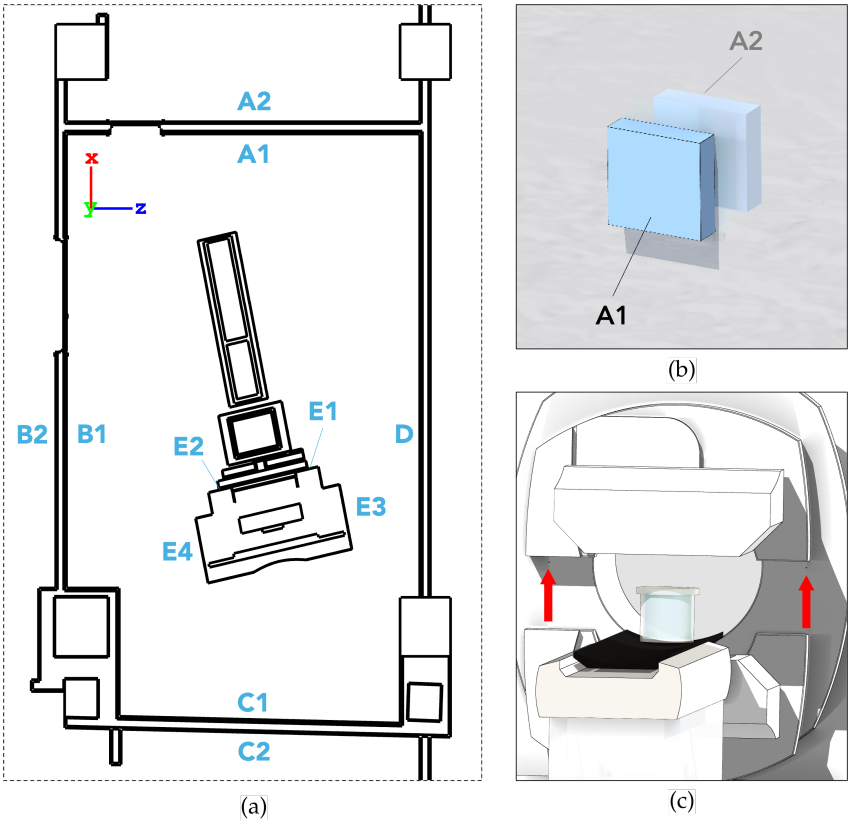

Figure 3.12: (a) Placement of the 11 TLDs around the SPECT/CT facility. Cartesian coordinates are shown at the top left. (b) Close-up on the TLDs 'A1' and 'A2' as seen from the front face of the observation window. (c) Placement of TLDs 'E1' and 'E2' on the front of the SPECT gantry (marked with red arrows).

- **Patient couch**: This consisted of a carbon-fibre table top with an internal foam core and positioned to centre the phantom within the detector field of view. The couch was mounted on a patient table supported by beams enclosed within a protective cover.

- **SPECT system**: The detector heads were modelled in detail as described in § 2.2.1.1 by incorporating all constituent layers in line with the recommendations of Rault et al. (2010). As for the collimators, these were represented as solid air–lead blocks, using the density and elemental compositions established in § 3.8.2.2.

- **CT system**: This included the X-ray tube assembly, heat exchanger, two high-voltage generators, electronic board, and detector system. These units were modelled as basic shapes and oriented following the architecture described by Behling (2021). The tube was parked at the top, facing the centre.

Table 3.3: Cartesian coordinates (X, Y, Z) and placement details of the 11 TLDs modelled for the main study. Coordinates correspond to the centre of each TLD cuboid and are rounded to 1 decimal place.

TLD	X cm	Y cm	Z cm	Details
A1	386.8	110.0	0.0	Observation window, internal
A2	387.0	110.0	0.0	Observation window, external (control room)
B1	0.0	110.0	−263.5	West wall, internal
B2	0.0	110.0	−278.6	West wall, external (NM corridor)
C1	−349.3	110.0	0.0	South wall, internal
C2	−365.7	150.0	−0.4	South wall, external (store room)
D	0.0	110.0	228.0	East wall, internal
E1	−26.8	113.0	60.4	SPECT gantry, left
E2	−49.0	113.0	−44.3	SPECT gantry, right
E3	−93.1	113.0	124.6	CT gantry, left
E4	−135.8	113.0	−76.0	CT gantry, right

The entire scanner was enclosed within a plastic housing. Internal support structures made of steel, aluminium, and composite materials were also taken into account. Lastly, the Jaszczak phantom, which was originally implemented in the pilot study and reused here, was modelled as a cylindrical PMMA shell filled with water and sealed with a PMMA lid. Visuals of the entire SPECT/CT scanner are shown in Figure 3.13

Following region definition, materials were specified in the MEDIA section. Here, elements, predefined compounds, or user-defined mixtures were assigned to each region. Figure 3.14 illustrates the definition of CONCRETE as a mixture of ten elements with a density of 2.3 $\mathrm{g\,cm^{-3}}$ and assigned to the FLOOR, CEILING, and PILLC (pillars) regions.[7] A complete list of region-material assignments is provided in Appendix C.

In the TRANSPORT section, two cards were used: `EMFCUT` and `RADDECAY` (Figure 3.15). The former set the transport threshold to 1 keV for photons and 100 keV for electrons. The electron threshold was kept at its default, as lowering it would have significantly increased computation time while offering negligible benefit since electrons are rapidly absorbed within the phantom. Conversely, the photon threshold was reduced at minimal computational cost due to their uncharged nature. The `RADDECAY` card enabled radioactive decay.

Finally, the detectors were defined in the SCORING section. Figure 3.16 shows the `USRBIN`

[7] CEILING is not explicitly shown, as the region-to-region definition applies to all regions listed between the first (CEILING) and last (PILLC), with CEILING falling within this range.

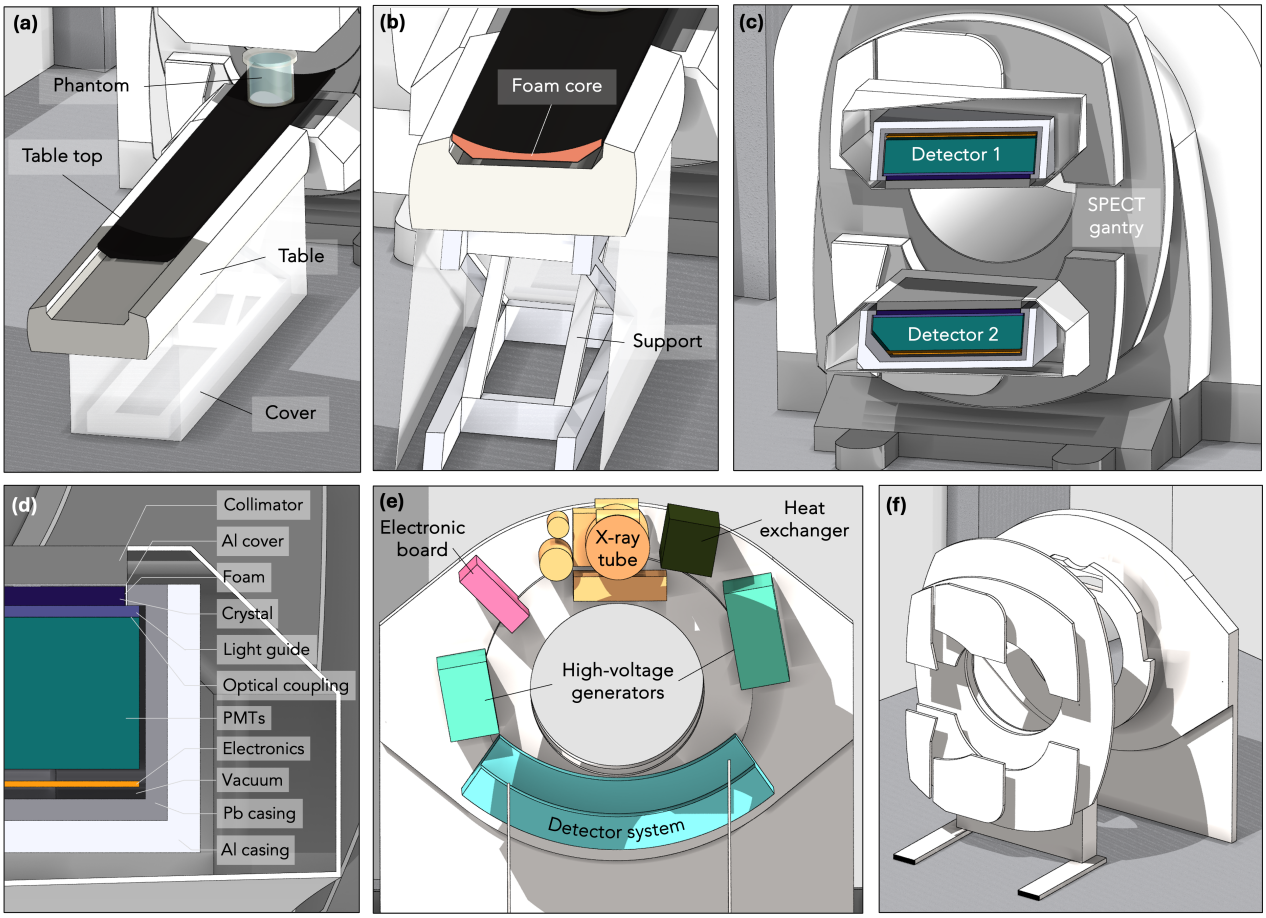

Figure 3.13: Overview of the SPECT/CT scanner model main components. (a) Patient couch setup, also showing the phantom positioned on the table top. (b) Cross-section of the patient couch. (c) Cross-section of the SPECT detector heads and the SPECT gantry. (d) Close-up cross-sectional view of the SPECT detector head layers. (e) Arrangement of the CT components around the gantry with the X-ray tube positioned at the top. (f) View of the gantry's steel support structures. Housing is removed for visual purposes in (e) and (f).

card used to score photon (fluP) and electron (fluE) fluence on 3D Cartesian meshes with specified boundaries and cubic 4 cm bins in all directions. Additional estimators included the $H^*(10)$ distribution, $H^*(10)$ deposited in the TLD regions, energy deposition per region, and energy-particle spectra (using the USRTRACK card) for photons and electrons across selected regions. Fluence was converted to $H^*(10)$ by applying the corresponding conversion factors through the DOSE-EQ option (Pelliccioni, 2000).

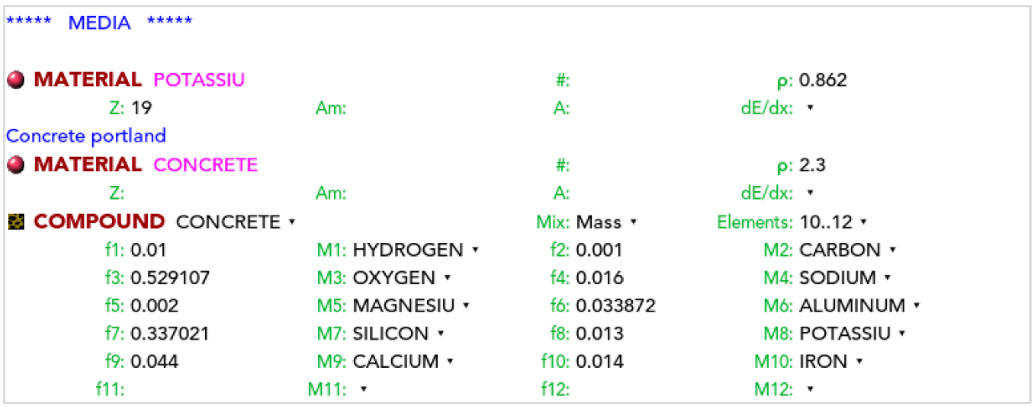

(a)

(b)

Figure 3.14: Flair snippet showing (a) material definition and (b) region-material assignment in the MEDIA section.

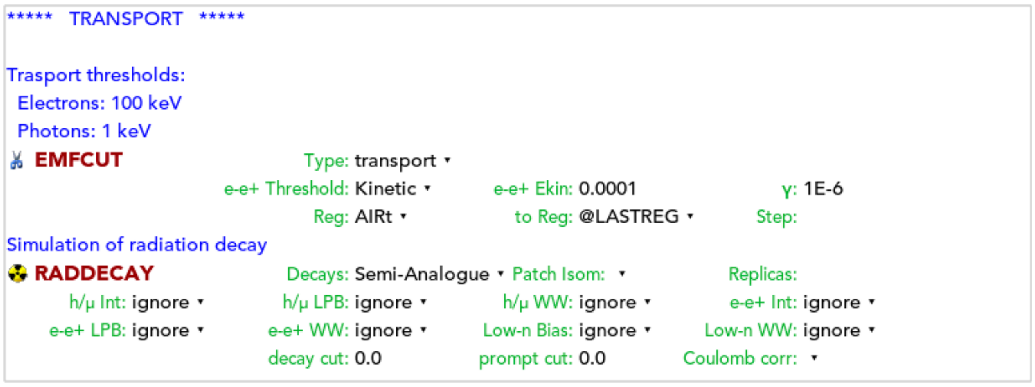

Figure 3.15: Flair snippet showing the TRANSPORT section.

3.8.2.2 | Collimator modelling

The highly intricate geometry of the HEGP, and especially the LEHRS, collimators made direct implementation in Flair impractical and excessively time-consuming. Instead of modelling thousands of individual holes, two solid-block equivalents whose composition was defined as a mixture of air and lead were developed for each variant to reproduce the transmission characteristics of the true collimators.

A $2 \times 2\,\mathrm{cm}^2$ subsection of each collimator was considered for comparison to the real collimators. For reference, even at this reduced scale, the LEHRS required over 3,000 individual region

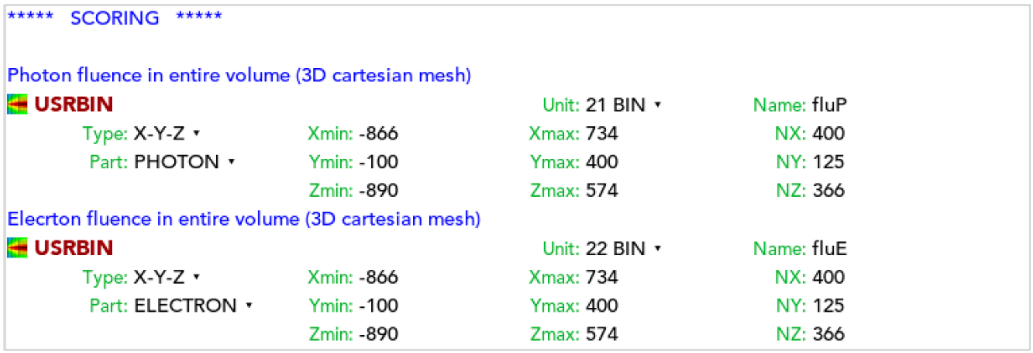

Figure 3.16: Flair snippet showing the SCORING section.

definitions, which would have had to be repeated approximately 550 times more to cover the entire 54.4×40.4 cm^2 area, confirming the impracticality of full hole-by-hole modelling.

Figure 3.17 shows the LEHRS and HEGP collimators alongside a solid-block equivalent. All models were implemented within a 2×2 cm^2 area, however, the true (Holes) collimators (Figures 3.17a,b) were defined to specification, namely septal thickness, hole diameter, and length (see Table 2.1), whereas the bulk (Solid) versions (Figure 3.17c) were represented as $2 \times 2 \times 3.2$ cm^3 lead-air blocks. The LEHRS hole length (3.2 cm) was also applied to the HEGP solid equivalent, despite its true 6.6 cm length, for two reasons: (i) to simplify later substitution of material without redefining geometry in the main facility model, and (ii) to reduce runtime by allowing more photons to reach the posterior detector and thus lowering the number of primaries needed for good statistics. The test setup (Figure 3.17d) involved a water-filled Jaszczak phantom, 50 cm away from the collimator, with fluence detectors before and after to record incident and transmitted particles via `USRTRACK`. Several air-lead mixtures were trialled in this geometry to identify the ratios that best reproduced the transmission of the true collimators. The total number of primaries and run times are listed in Table 3.4. Runs were distributed across available computational platforms, so run times are not directly comparable.

For each energy bin i, the fluence ϕ_i was integrated over its width ΔE_i to give total incident (E_{init}) and transmitted (E_{trans}) energies:

$$E = \sum_i \Delta E_i \, \phi_i. \tag{3.2}$$

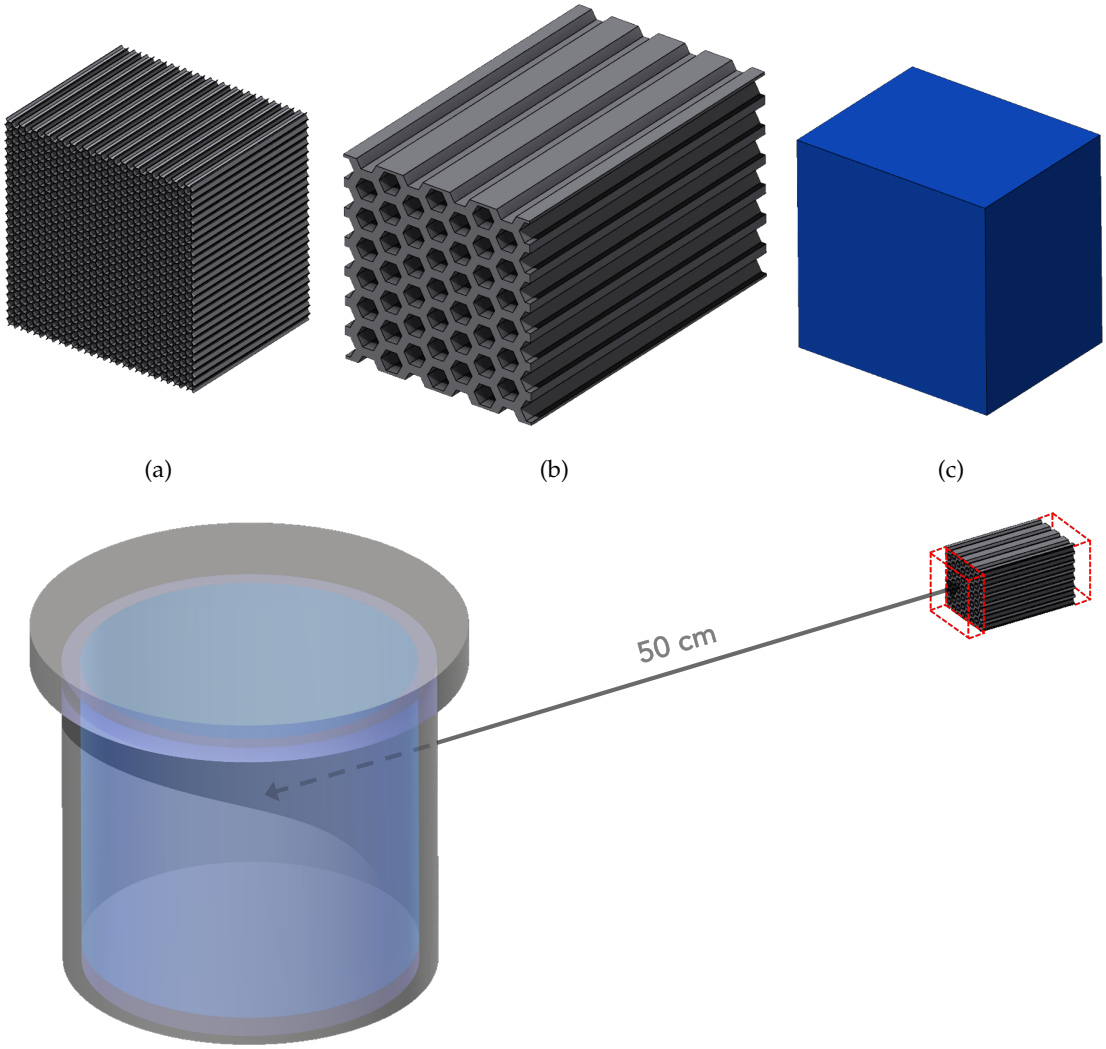

Figure 3.17: (a-c) Collimators as designed in Flair; and (d) the simulation setup with the phantom, [LEHRS] collimator, and detectors (red-outlined boxes). (a) LEHRS collimator; (b) HEGP collimator; (c) solid-equivalent collimator. (a-c) are to scale with one another.

The transmission ratio R and its uncertainty σ_R were then

$$R = \frac{E_{\text{trans}}}{E_{\text{init}}}, \tag{3.3}$$

$$\sigma_R = R\sqrt{\left(\frac{\sigma_{\text{trans}}}{E_{\text{trans}}}\right)^2 + \left(\frac{\sigma_{\text{init}}}{E_{\text{init}}}\right)^2}, \tag{3.4}$$

with σ_{init} and σ_{trans} taken from the relative FLUKA bin errors.

Table 3.4: Summary of simulated collimator configurations for LEHRS and HEGP, showing the total number of primaries simulated and average run times.

Run	**Primaries** 10^9	**Run time** h
LEHRS		
Holes	125.0	84.08
Solid – 98:2	50.0	31.02
Solid – 99:1	50.0	21.02
Solid – 993:7	50.0	21.28
Solid – 995:5	50.0	30.83
Solid – 999:1	50.0	30.82
HEGP		
Holes	12.5	6.01
Solid – 98:2	2.5	1.82
Solid – 985:15	2.9	1.88
Solid – 99:1	2.5	1.32

Table 3.5: Energy transmission results for all collimator settings. Initial E_{init} and transmitted E_{trans} energy totals are in keV (fluence per keV × energy bin width). The transmission ratio R is dimensionless.

Setting	E_{init} keV	E_{trans} keV	R 10^{-3}
LEHRS			
Holes	126 ± 2	1.221 ± 0.093	9.70 ± 0.75
Solid – 98:2	146 ± 3	0.354 ± 0.002	2.42 ± 0.05
Solid – 99:1	150 ± 3	0.981 ± 0.071	6.54 ± 0.49
Solid – 993:7	152 ± 3	1.375 ± 0.072	9.05 ± 0.50
Solid – 995:5	153 ± 3	1.744 ± 0.075	11.38 ± 0.53
Solid – 999:1	157 ± 3	2.932 ± 0.097	18.65 ± 0.70
HEGP			
Holes	30 ± 1	0.260 ± 0.002	8.74 ± 0.43
Solid - 98:2	34 ± 3	0.216 ± 0.005	6.34 ± 0.54
Solid - 985:15	34 ± 3	0.277 ± 0.006	8.03 ± 0.67
Solid - 99:1	35 ± 3	0.377 ± 0.007	10.74 ± 0.87

Table 3.5 summarises the results for all mixtures tested. For the LEHRS, the 993:7 air–lead mixture $R = (9.05 \pm 0.50) \times 10^{-3}$ was in closest agreement with the reference value of $(9.70 \pm 0.75) \times 10^{-3}$. For the HEGP, the 985:15 mixture yielded $R = (8.03 \pm 0.67) \times 10^{-3}$ compared with $(8.74 \pm 0.43) \times 10^{-3}$. Other mixtures deviated more substantially. The validated solid-

block equivalents were therefore defined as air-lead ratios of 993:7 (LEHRS) and 985:15 (HEGP) and used in the ^{99m}Tc and ^{177}Lu facility simulations, respectively.

3.8.3 | Analytical method

The analytical method was based on Equation 2.1 with several adaptations, while still preserving the assumptions delineated immediately thereafter. The gamma constant Γ, was set to 2.24×10^{-5} mSv·h^{-1}·MBq^{-1} (Delacroix et al., 2002), while the cumulative activity $\tilde{A}$ was obtained from the calculation in § 3.9.1. Distances d from the source to TLD was determined accurately using Flair. To account for barrier attenuation for TLDs 'A2', 'B2', and 'C2', the Beer-Lambert law (Cherry et al., 2013) was incorporated, yielding,

$$H = \frac{\Gamma \tilde{A}}{d^2} \cdot e^{-\mu x} \tag{3.5}$$

where μ is the linear attenuation coefficient and x is the thickness of the absorbing material. As is standard in clinical shielding assessments, only the lead layer was considered, with attenuation from other layers neglected. The linear attenuation coefficients were set as $\mu_{\text{Pb}} = 26.25$ cm^{-1} for lead and $\mu_{\text{Pb-glass}} = 11.17$ cm^{-1} for lead glass (for TLD 'A2'), which were derived from the mass attenuation coefficients at 140 keV reported by Hubbell and Seltzer (2004) and scaled by the respective material densities.

3.9 | Data analysis technique

Data analysis was primarily carried out using Python 3.12 on PyCharm 2021.2.2 (JetBrains, Czechia), with additional analyses conducted in Microsoft Excel 16.93.1 (Microsoft, USA). Python was also used to generate all plots. As all analyses and equations are fully described in the text, the scripts are not included in the appendix for brevity. Instead, the complete, version-controlled Python code is available in a public GitHub repository at `https://github.com/weli01/MScProjectPythonScript.git`.

3.9.1 | Phantom activity and time values

To reproduce the acquisition in both the simulation and the analytical approaches, the cumulative activity $\tilde{A}$ over the experimental exposure interval was considered. During the experiment,

key actions were logged along with their corresponding activity and time and are summarised in Table 3.6.

Table 3.6: Activity (MBq) and timing (Day–HH:MM) recorded during the experimental stages of the pilot and main studies. Table and couch refer to the pilot and main studies, respectively.

Action	**Pilot study**		**Main study**	
	Activity MBq	**Time** Day – HH:MM	**Activity** MBq	**Time** Day – HH:MM
Elution measurement	1163.00	1 – 13:05	3080.00	1 – 14:11
Residual measurement	0.04	1 – 13:09	45.50	1 – 14:13
Phantom placed on table/couch	–	1 – 13:18	–	1 – 14:27
Phantom removed from table/couch	–	2 – 08:21	–	2 – 07:29

$\tilde{A}$ was calculated by first determining the activity in the phantom at the time of placement on the couch t_2:

$$A(t_2) = A_0\, e^{-\lambda(t_2-t_0)} - A_{\text{res}}\, e^{-\lambda(t_2-t_1)}, \tag{3.6}$$

where:

- A_0: activity at elution time t_0,
- A_{res}: residual activity at time t_1,
- $\lambda \equiv \frac{\ln 2}{T_{1/2}}$: decay constant of $^{99\text{m}}$Tc.

The total cumulative activity over the exposure period, from phantom placement at t_2 until removal at t_3, was then calculated as,

$$\tilde{A} = \int_{t_2}^{t_3} A(t)\, dt = \frac{A(t_2)}{\lambda}\left(1 - e^{-\lambda(t_3-t_2)}\right), \tag{3.7}$$

yielding $\tilde{A} = 3.1455 \times 10^{13}$ Bq·s for the pilot study and $\tilde{A} = 7.8930 \times 10^{13}$ Bq·s for the main study.

3.9.2 | Normalisation of simulation estimates

Since FLUKA returns estimates per primary particle, all results were normalised by the appropriate scaling factors. In this study, where radioactive decay was simulated, each result was multiplied by the cumulative activity $\tilde{A}$ calculated previously.

In addition, the default output for dose equivalent estimates is expressed in pSv. Therefore, results were further scaled by a factor of 10^{-6} to convert to µSv.

Lastly, for region-based scoring, FLUKA outputs are integrated over the volume ($\times \mathrm{cm}^3$). Accordingly, dose deposition within the TLDs was divided by their volume of $0.32 \times 0.32 \times 0.09 = 9.216 \times 10^{-3}$ cm^3.

3.9.3 | Model validation and comparison of methods

Validation and comparison of the three methods were carried out through a direct comparison of TLD $H^*(10)$ values from the simulation and analytical methods against the experimental measurements, following the approach of Infantino (2015). For each TLD location j, dose values $H^*(10)_j^{(\mathrm{ana})}$, $H^*(10)_j^{(\mathrm{exp})}$, and $H^*(10)_j^{(\mathrm{sim})}$ (in µSv) with associated standard uncertainties $\sigma^*(10)_j^{(\cdot)}$ were obtained from the respective processing pipelines. Agreement was quantified via per-location ratios:

$$R_j^{(\mathrm{ana/exp})} = \frac{H^*(10)_j^{(\mathrm{ana})}}{H^*(10)_j^{(\mathrm{exp})}}, \qquad R_j^{(\mathrm{sim/exp})} = \frac{H^*(10)_j^{(\mathrm{sim})}}{H^*(10)_j^{(\mathrm{exp})}}, \tag{3.8}$$

with uncertainties by standard error propagation:

$$\sigma(R)_j = R_j \cdot \sqrt{\left(\frac{\sigma^*(10)_j^{(1)}}{H^*(10)_j^{(1)}}\right)^2 + \left(\frac{\sigma^*(10)_j^{(2)}}{H^*(10)_j^{(2)}}\right)^2}. \tag{3.9}$$

where superscripts (1) and (2) refer to the appropriate paired values for each ratio.

For comparison of the methods by a single representative value, a weighted mean of each ratio set was computed using:

$$\overline{R}_w = \frac{\sum_j w_j R_j}{\sum_j w_j}, \qquad w_j = \frac{1}{\sigma(R)_j^2}, \tag{3.10}$$

with the standard deviation of the mean as:

$$\sigma(\overline{R}_w) = \sqrt{\frac{1}{\sum_j w_j}}. \tag{3.11}$$

Furthermore, paired two-sided t-tests at the 95% confidence level were conducted to test the null hypothesis that the mean difference between methods is zero:

$$H_0 : \; H^*(10)_j^{(\cdot)} - H^*(10)_j^{(\mathrm{exp})} = 0 \quad \forall j, \tag{3.12}$$

where $H^*(10)_j^{(\cdot)}$ represents the simulated or analytical $H^*(10)$ value and $H^*(10)_j^{(\mathrm{exp})}$ the corresponding experimental measurement for TLD j. The tests also yielded Pearson correlation coefficients.

3.9.4 | Annual doses calculation

Annual doses for the ^{99m}Tc main study simulation were derived by focusing exclusively on TLD positions 'A2', 'B2', and 'C2', as these were located outside the scanner room, where occupational and public dose restrictions are applicable. A representative patient scan, with an administered activity of $A_0 = 500$ MBq and a scan duration of $t_s = 0.5$ h, was assumed. These parameters, along with additional ones described below, reflect the values used in the original shielding calculations performed prior to the installation of the scanner and were therefore adopted for consistency.

For each selected TLD at location j, the per-patient dose equivalent $H^*(10)_j$ was scaled to an annual workload according to:

$$H^*(10)_j^{(\text{annual})} = H^*(10)_j^{(\text{sim})} \times T_j \times W \times 365 \text{ days}, \tag{3.13}$$

where:

- $H^*(10)_j^{(\text{sim})}$: simulated dose at j [mSv],
- T_j: occupancy factor at j ($T_{\text{A2}} = 1$; $T_{\text{B2}} = 0.2$; $T_{\text{C2}} = 0.05$),
- $W = 14$: average daily patient workload.

$H^*(10)_j^{(\text{sim})}$ includes normalisation by TLD volume, unit conversion from pSv to mSv (10^{-9}), and scaling by the cumulative activity $\tilde{A} = 8.7453 \times 10^{11}$ Bq · s corresponding to $A_0 = 500$ MBq and $t_s = 0.5$ h.

Finally, uncertainties were propagated as:

$$\sigma\left(H^*(10)_j^{(\text{annual})}\right) = \frac{H^*(10)_j^{(\text{annual})}}{H^*(10)_j^{(\text{sim})}} \times \sigma\left(H^*(10)_j^{(\text{sim})}\right). \tag{3.14}$$

3.9.5 | FLUKA `.out` file

The standard output file (`.out`) is among one of the files generated after a FLUKA simulation and is particularly useful for investigating results or errors. In this study, it was used to extract two results: (i) dose deposition in each region and (ii) the number of secondary particles generated. While the latter could be read directly from the file, energy deposition required applying Equations 2.4 and 2.7 to estimate both the deposited energy and its associated uncertainty for each region. Both deposited energy and secondary particle counts were expressed as percentages of their respective totals generated in the simulation.

3.10 | Ethical considerations

This study has been approved by the University Research Ethics Committee of the University of Malta (Appendix A).

3.11 | Limitations of the research methodology

This methodology carried certain limitations, some inherent and others due to practical constraints, that should inform subsequent work:

1. Certain facility and scanner geometry was simplified for computational feasibility. Numerous assumptions on component dimensions and material compositions had to be made due to insufficient technical documentation, which potentially introduced deviations from the true setup. A notable example is the definition and orientation of the CT subunits, which could have been positioned at angles different from those modelled.

2. Several structural and non-structural elements were omitted (e.g., external equipment, pipework inside walls, ceiling void components, overlapping shielding, and small electronics). These were excluded either because of their negligible impact on shielding or because sufficient specifications were unavailable.

3. Small structural imperfections, such as cracks, holes, or discontinuities in barriers, were not accounted for, either because they were unknown or not visible during room inspection. Leakage pathways present in reality were therefore absent from the simulations.

4. The simulation used a static geometry, whereas clinical scans involve both couch and detector motion. Moreover, the main study reflects a single standard imaging protocol rather than the full range of clinical procedures. If access to retrospective records of all scan types and their frequencies was available, this could have yielded more representative annual dose estimates. Even so, with such data, realism would remain limited by the use of a simple cylindrical phantom rather than an anthropomorphic model.

5. Although experimental results served as the basis for validating the simulation, they are not absolute ground truth due to unavoidable experimental uncertainties.

6. Despite the use of high primary particle counts to minimise relative errors, some statistical noise remained, particularly in low-fluence regions.

7. Because local data on the number of ^{177}Lu therapy patients, and hence scans, the typical administered activity, and scan durations were unavailable. Any estimate would have relied on literature values that may not reflect national practice. Annual dose calculations were therefore performed only for the ^{99m}Tc case.

3.12 | Conclusion

This chapter provided a comprehensive overview of the research design applied. The following chapter focuses on the study results.

4

Results

4.1 | Introduction

This chapter presents the results of the study. The pilot study is reported first as a small-scale preliminary validation. Following, the facility-level MC model is reviewed as a complete model, after which it is validated through $H^*(10)$ values and the simulation method compared with the experimental and analytical methods. Once validated, annual dose estimates for ^{99m}Tc are presented, followed by various simulation-derived quantities, including for ^{177}Lu. Raw experimental measurements for each individual TLD are provided in Appendix D.

4.2 | Small-scale validation

Table 4.1 lists the ambient dose equivalent $H^*(10)$ for the six wall positions measured during the pilot study, with the same data shown graphically in Figure 4.1. The displayed values are post-processed quantities. For the experimental dataset, calibrated doses were obtained from the TLD readouts: for each set of three TLDs, $H^*(10)^{(\mathrm{exp})}$ is their mean, with the quoted uncertainty given by the sample standard deviation (individual experimental TLD results are given in Table D.2). For the simulation dataset, $H^*(10)^{(\mathrm{sim})}$ corresponds to FLUKA tallies after applying the required normalisation factors, reported together with the simulation's statistical uncertainties. The last column lists the per-position ratio $R^{(\mathrm{sim/exp})}$ of the two methods, with uncertainties obtained by standard propagation from the experimental and simulation terms.

Table 4.1: Numerical pilot study results for ambient dose equivalent $H^*(10)$: experimental $H^*(10)^{(\mathrm{exp})}$, simulation $H^*(10)^{(\mathrm{sim})}$, and their ratio $R^{(\mathrm{sim/exp})}$.

Location	$H^*(10)^{(\mathrm{exp})}$ µSv	$H^*(10)^{(\mathrm{sim})}$ µSv	$R^{(\mathrm{sim/exp})}$
1	164.63 ± 3.74	168.88 ± 1.09	1.03 ± 0.02
2	154.29 ± 3.11	160.26 ± 0.86	1.04 ± 0.02
3	145.02 ± 2.26	144.01 ± 0.81	0.99 ± 0.02
4	122.45 ± 2.07	123.40 ± 0.85	1.01 ± 0.02
5	103.20 ± 3.55	104.04 ± 0.79	1.01 ± 0.04
6	90.77 ± 2.12	87.99 ± 0.80	0.97 ± 0.02

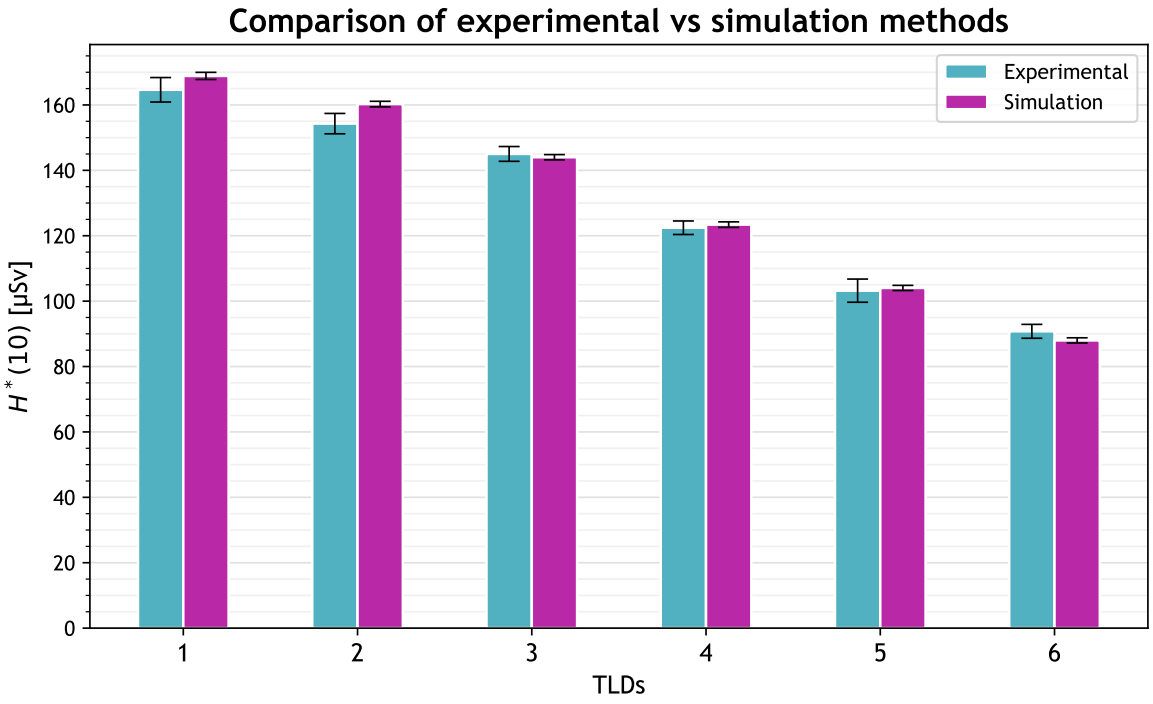

Figure 4.1: Graphical pilot study results for ambient dose equivalent $H^*(10)$ comparing the experimental and simulation results. Error bars show experimental standard deviations and simulation statistical uncertainties. This figure complements Table 4.1.

Table 4.1 shows that $H^*(10)$ decreased monotonically from the closest position, '1', to the furthest, '6', for both methods. The experimental values ranged from 164.63 µSv down to 90.77 µSv, and the simulation values from 168.88 µSv down to 87.99 µSv, with means of 130.06 µSv and 131.43 µSv, respectively. This gave a mean difference of 1.37 µSv. Across all positions, absolute differences between simulation and experiment did not exceed 6 µSv. The largest rela-

tive uncertainty was 3.44% for experimental location '5' and 0.91% for simulation location '6' – almost a fourfold difference.

The ratios $R^{(\mathrm{sim/exp})}$ lay from 0.97 to 1.04, all within $\pm 5\%$ of unity, with a weighted mean of $\overline{R}_w^{(\mathrm{sim/exp})} = 1.01 \pm 0.01$. A two-sided paired t-test (95% confidence) yielded $p = 0.3503$ ($n = 6$, $t_5 = 1.0299$), providing no evidence of a difference between simulation and experimental $H^*(10)$ means ($p > 0.05$). The corresponding Pearson coefficient was $r = 0.9977$.

Figure 4.1 illustrates the two series tracking one another closely across positions '1' to '6' with near-parallel trends and similar magnitudes. In some positions the experimental value exceeded the simulation's and in others, the reverse occurred, with differences remaining small. This pattern was consistent with the weighted mean ratio $\overline{R}_w$ being close to unity.

With an $\overline{R}_w^{(\mathrm{sim/exp})}$ value close to unity and a non-significant paired t-test, the simplified wall set-up was accepted as validated for $H^*(10)$ benchmarking in the pilot configuration.

4.3 | Facility MC model

One of the objectives was to develop an accurate and detailed MC model of the SPECT/CT facility by incorporating all the necessary components. The main individual elements have been described extensively in the Research Methodology. Here, the fully integrated model is presented and visually compared with the real-world facility.

Figure 4.2 presents the complete facility-level FLUKA MC model. Upon comparison to the site's technical drawing (Figure 2.6), it can be observed that all the relevant components were modelled, with the proper doorways put in place and the outline of each room matching the true configuration. The doorways were left open to emulate reality, as these doors are always typically open, except for the scanner room's, hence why they were modelled closed.

Figure 4.3 juxtaposes the SPECT/CT scanner as modelled in Flair (left-hand panels) with the real-life system installed in the facility (right-hand panels) for the main study configuration. The correspondence is evident across various features, particularly, the detector heads in H-mode with comparable head-phantom clearance, patient couch height and tabletop extension, phantom position on the tabletop, gantry housing and support base, and the observation window and door placements relative to the scanner. These snapshots highlight the fidelity of the modelled setup to the real installation.

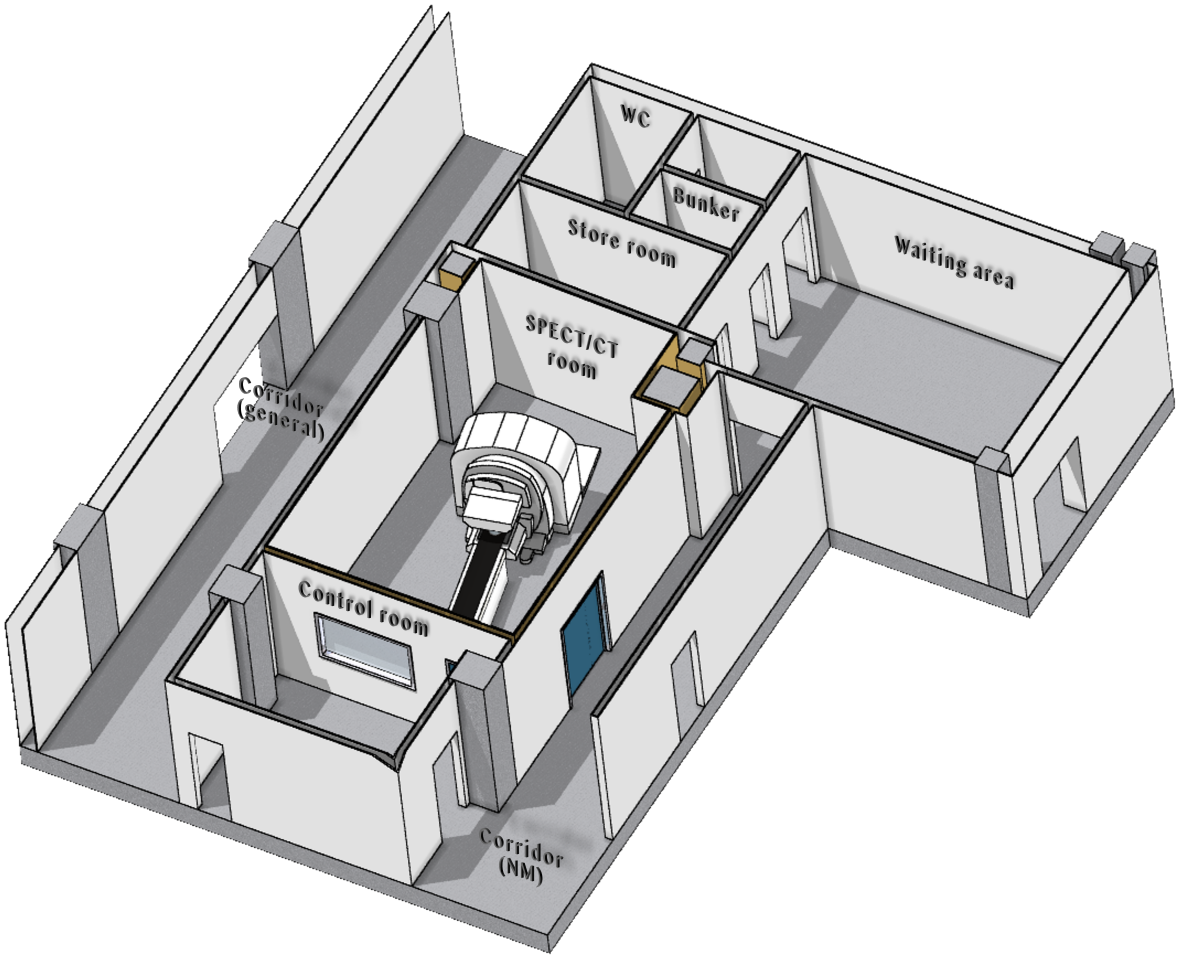

Figure 4.2: Bird's-eye view of the finished facility model in FLUKA with all rooms and areas labelled. The ceiling was intentionally rendered transparent for clarity.

4.4 | Main study validation and comparison of methods

The main study validation method mirrors that of the pilot study, but with the addition of the analytical method to enable a three-way comparison. The post-processed estimates $H^*(10)^{(\mathrm{exp})}$ and $H^*(10)^{(\mathrm{sim})}$ together with the analytical values $H^*(10)^{(\mathrm{ana})}$ are reported in Table 4.2 and plotted in Figure 4.4.

For the main study, $H^*(10)$ values spanned several orders of magnitude. The analytical values ranged from < 0.01 µSv ('C2') to 888.41 ± 17.77 µSv ('E1', 'E2'), the experimental measurements ranged from 0.81 ± 1.67 µSv ('B2') to 765.97 ± 4.55 µSv ('E2'), and the simulation

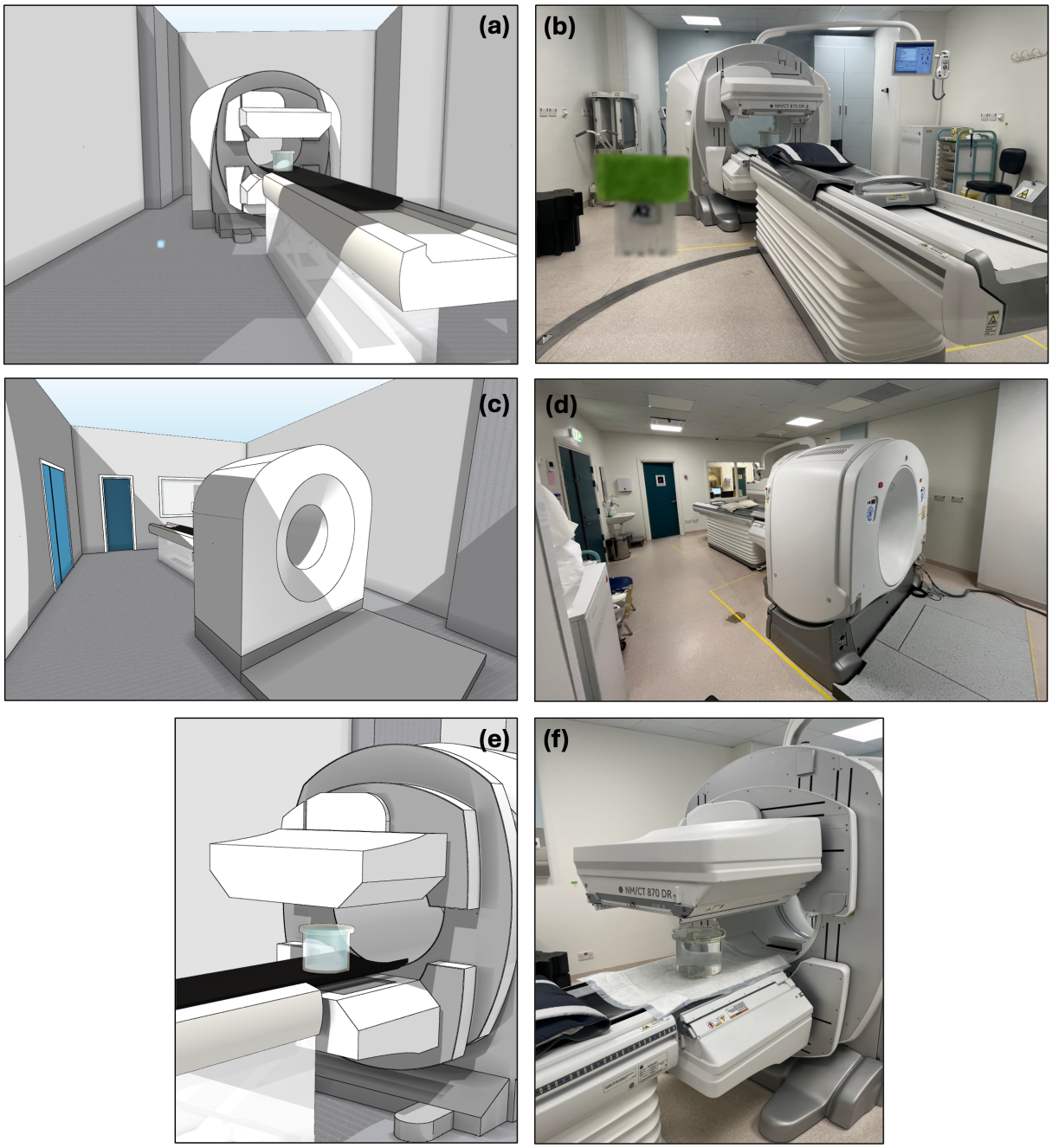

Figure 4.3: Comparison of the virtual model of the NM/CT 870 DR as created on Flair (left-hand panels) and its real-life equivalent (right-hand panels) as was configured for this study: (a,b) taken from the control room and show the 'A1' and 'A2' TLD pouches/individual TLDs attached to the observation window; (c,d) taken from the south-west (back) corner of the room; and (e,f) taken from the side of the scanner showing the phantom setup and detectors orientation. The ceiling was intentionally rendered transparent for clarity. TLD pouch 'E4' is not shown in (d) as the photograph was taken post-study.

Table 4.2: Numerical main-study results for ambient dose equivalent $H^*(10)$: analytical $H^*(10)^{(\mathrm{ana})}$, experimental $H^*(10)^{(\mathrm{exp})}$, simulation $H^*(10)^{(\mathrm{sim})}$, and their ratios $R^{(\mathrm{ana/exp})}$ and $R^{(\mathrm{sim/exp})}$.

Location	$\boldsymbol{H^*(10)^{(\mathrm{ana})}}$ µSv	$\boldsymbol{H^*(10)^{(\mathrm{exp})}}$ µSv	$\boldsymbol{H^*(10)^{(\mathrm{sim})}}$ µSv	$\boldsymbol{R^{(\mathrm{ana/exp})}}$	$\boldsymbol{R^{(\mathrm{sim/exp})}}$
A1	34.31 ± 0.69	29.89 ± 0.65	38.04 ± 0.59	1.18 ± 0.04	1.31 ± 0.04
A2	3.67 ± 0.07	2.81 ± 1.82	3.47 ± 0.16	1.30 ± 0.84	1.23 ± 0.80
B1	71.40 ± 1.43	60.65 ± 1.90	81.63 ± 0.77	1.18 ± 0.04	1.35 ± 0.04
B2	0.33 ± 0.01	0.81 ± 1.67	0.33 ± 0.05	0.41 ± 0.86	0.41 ± 0.84
C1	38.20 ± 0.76	27.44 ± 5.73	27.03 ± 0.39	1.39 ± 0.29	0.99 ± 0.21
C2	< 0.01	1.15 ± 1.52	0.08 ± 0.02	< 0.01	0.07 ± 0.09
D	92.36 ± 1.85	82.02 ± 2.71	102.38 ± 0.75	1.13 ± 0.04	1.25 ± 0.04
E1	888.41 ± 17.77	714.74 ± 36.38	917.09 ± 2.62	1.24 ± 0.07	1.28 ± 0.07
E2	888.41 ± 17.77	765.97 ± 4.55	916.74 ± 2.67	1.16 ± 0.02	1.20 ± 0.01
E3	183.41 ± 3.67	6.91 ± 1.30	11.11 ± 0.28	26.55 ± 5.01	1.61 ± 0.30
E4	183.41 ± 3.67	5.41 ± 1.27	14.45 ± 0.31	33.90 ± 7.99	2.67 ± 0.63

results ranged from 0.08 ± 0.02 µSv ('C2') to 917.09 ± 2.62 µSv ('E2'). Absolute differences from experimental ranged between 0.41 µSv ('C1') and 202.35 µSv ('E1') for simulation, and 0.48 µSv ('B2') to 178.00 µSv ('E4') for analytical. Compared with simulation, 'E4' differed by just 9.04 µSv.

Analytical values were assigned a fixed relative uncertainty of $\pm 2\%$, matching the quoted specification of the CRC-55Rt dose calibrator (Capintec, 2023). Simulation relative uncertainties were generally small ($< 3\%$), whereas the measurements taken behind the walls showed markedly higher uncertainties ('A2': 4.51%, 'B2': 14.96%, 'C2': 29.67%). Experimental uncertainties spanned a wider range and exceeded the simulation at all locations, with the smallest being 0.59% at 'E2' and the largest 206.17% at 'B2', compared with 0.29% and 14.96%, respectively, for the corresponding simulation entries.

Method ratios are given in the last two columns. The simulation-experimental ratios $R^{(\mathrm{sim/exp})}$ ranged from 0.07 ± 0.09 ('C2') to 2.67 ± 0.63 ('E4'), with a mean weighted ratio $\overline{R}_w^{(\mathrm{sim/exp})} = 1.20 \pm 0.01$. The analytical-experimental ratios $R^{(\mathrm{ana/exp})}$ showed a much wider spread, from $<$ 0.01 ('C2') to 33.90 ± 7.99 ('E4'), but with a slightly smaller mean weighted ratio of $\overline{R}_w^{(\mathrm{ana/exp})} = 1.17 \pm 0.02$. Two two-sided paired t-test at the 5% level gave $p = 0.1040$ ($t_5 = 1.7885$) for simulation versus experimental, and $p = 0.0284$ ($t_5 = 2.5599$) for analytical versus experimental. Thus, there was no evidence of a mean difference in the former case ($p > 0.05$) and an evidential difference in the latter ($p < 0.05$). The corresponding Pearson correlation coefficients were

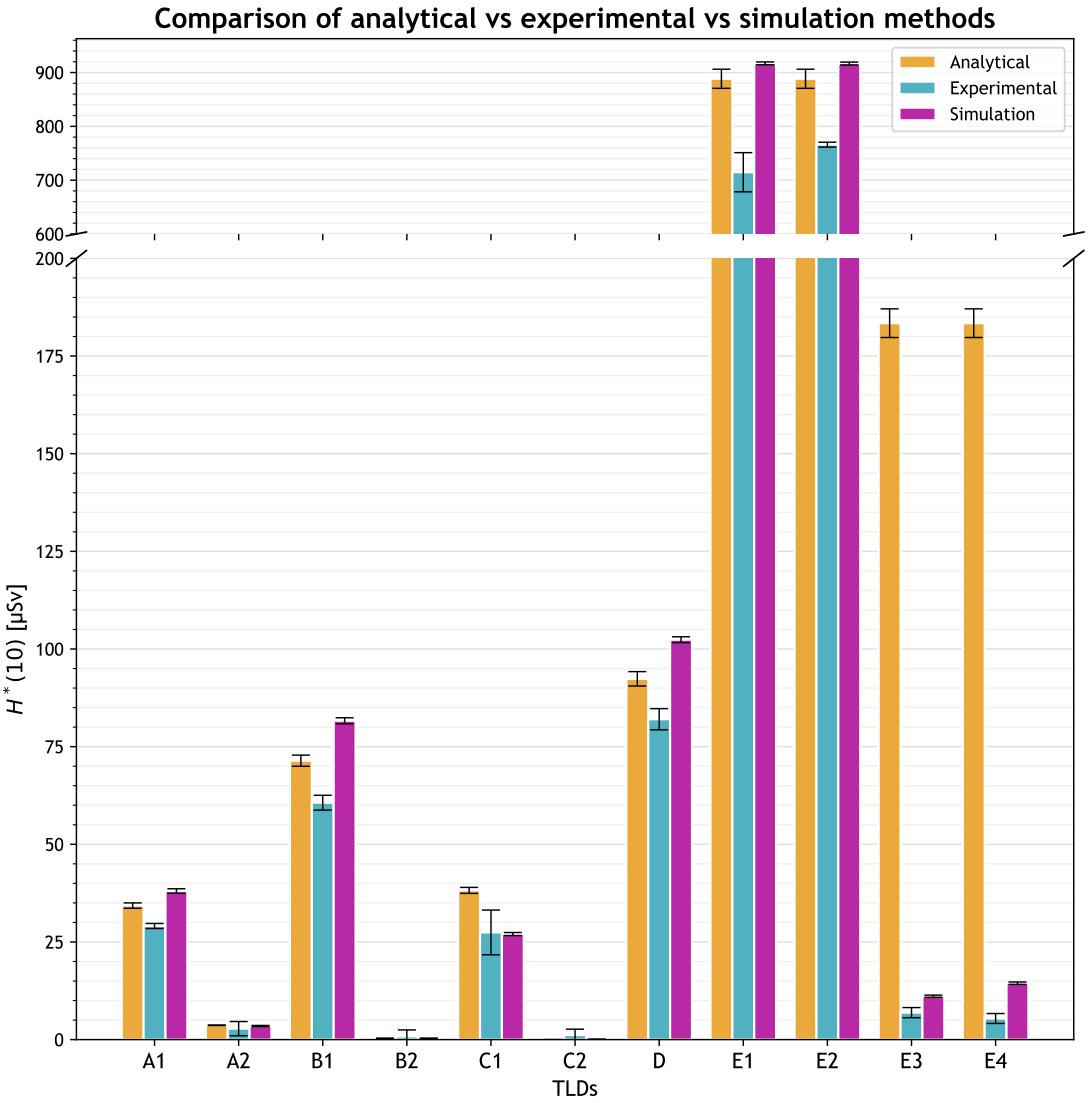

Figure 4.4: Graphical main study results for ambient dose equivalent $H^*(10)$ comparing the analytical, experimental and simulation results. Error bars indicate a constant $\pm 2\%$ uncertainty from dose calibrator accuracy for the analytical results, experimental standard deviations and simulation statistical uncertainties. A break in the ordinate emphasises low-dose regions. This figure complements Table 4.2.

$r = 0.9992$ and $r = 0.9781$, respectively.

Figure 4.4 compares $H^*(10)$ across methods at all TLD locations. All three series consistently peak at 'E1' and 'E2', and are minimal at 'A2', 'B2', and 'C2'. Across the eleven locations, the simulation exceeds the analytical at seven ('A1', 'B1', 'C2', 'D', 'E1', 'E2'), lower at four ('A2', 'C1') and equivalent in one ('B2').

4.5 | ^{99m}Tc annual dose estimates

The annual dose estimates from the simulation for locations 'A2', 'B2' and 'C2' for a representative ^{99m}Tc patient scan, together with their propagated uncertainties, were determined using Equations 3.13 and 3.14, assuming the parameters mentioned thereafter (500 MBq standard activity, 0.5 h scan, 14 patients daily, and the relevant occupancy factors). The results are given in Table 4.3. The dose per patient factors in the activity and scan time only, whereas the annual dose further incorporates the workload and occupancy, with the latter expressed in mSv rather than µSv to facilitate comparison with regulatory dose constraints and limits.

Table 4.3: Simulation-derived per-patient and annual dose estimates for a typical ^{99m}Tc scan in select locations. The uncertainties reflect the simulation's statistical uncertainty for each estimate.

TLD	Location	Occupancy	$H^*(10)$ / patient µSv	$H^*(10)_{\text{annual}}$ mSv year^{-1}
A2	**Control room**	1.00	0.0385 ± 0.0017	0.1965 ± 0.0089
B2	**NM corridor**	0.20	0.0036 ± 0.0005	0.0037 ± 0.0006
C2	**Store room**	0.05	0.0009 ± 0.0003	0.0002 ± 0.0001

4.6 | Simulation-derived quantities

Beyond the facility $H^*(10)$ point measurements from the TLDs, additional quantities were obtained from FLUKA estimators. These are presented next.

4.6.1 | Dose and particle fluence distributions

The following section presents two-dimensional spatial distributions of ambient dose equivalent, and photon and electron fluence obtained from FLUKA `USRBIN` scoring, alongside their relative uncertainty distributions. The maps illustrate selected projections through the facility that highlight the main regions of interest. Only the most relevant views are included here. A more complete set of dose maps along the Y projection is provided in Appendix E.

4.6.1.1 | Ambient dose equivalent

In Figures 4.5–4.7, panel (a) shows the spatial distribution of the annualised ambient dose equivalent $H^*(10)$ (referred to as 'value') at particular planes. These were obtained by scaling each of the `USRBIN` 3D mesh estimates with the cumulative activity and workload parameters for ^{99m}Tc clinical practices defined in § 3.9.4. Superimposed contours denote reference isodose levels at 0.25, 1, 6, and 20 mSv y^{-1}, corresponding to public constraints, public limits, occupational constraints, and occupational limits, respectively. Panel (b) shows the associated relative statistical uncertainty, expressed as a percentage. Similarly, contour lines at 0.1%, 1%, and 10% uncertainty are overlaid to aid interpretation.

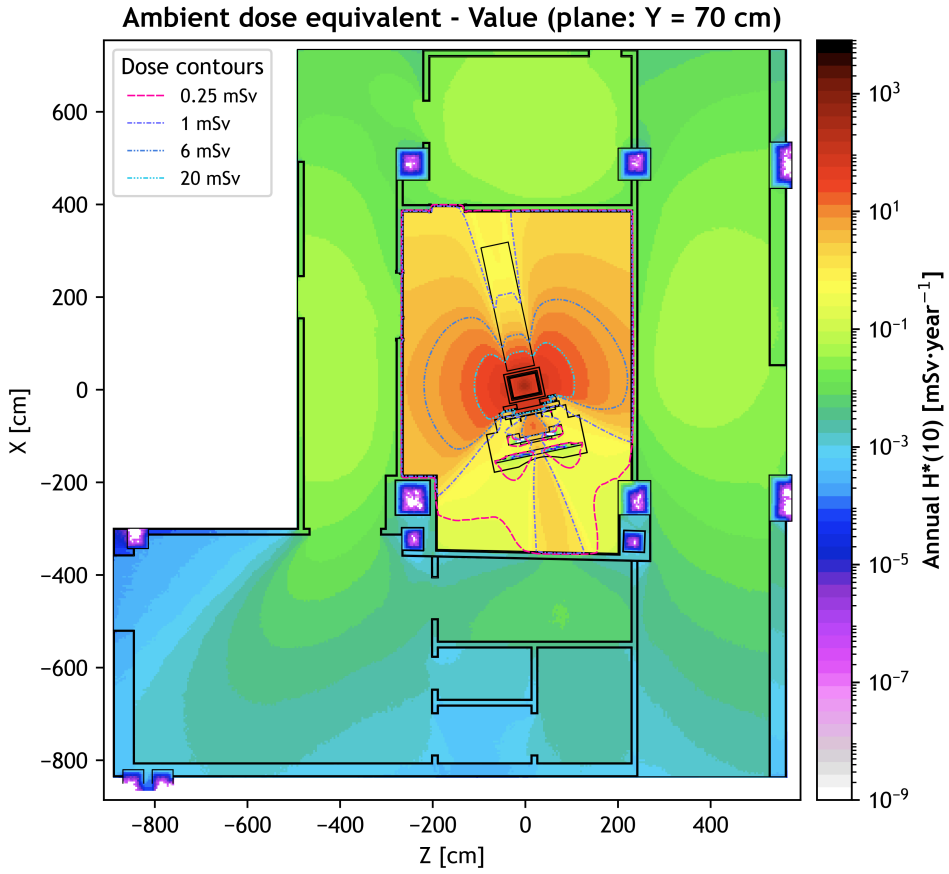

(a)

Figure 4.5: Ambient dose equivalent maps of $H^*(10)$ distribution, shown for the projection at $Y = 70$ cm, corresponding to the average over the slab $Y \in [60, 80]$ cm: (a) Value map of the ambient dose equivalent rate $H^*(10)$, scaled to typical annual workloads for ^{99m}Tc.

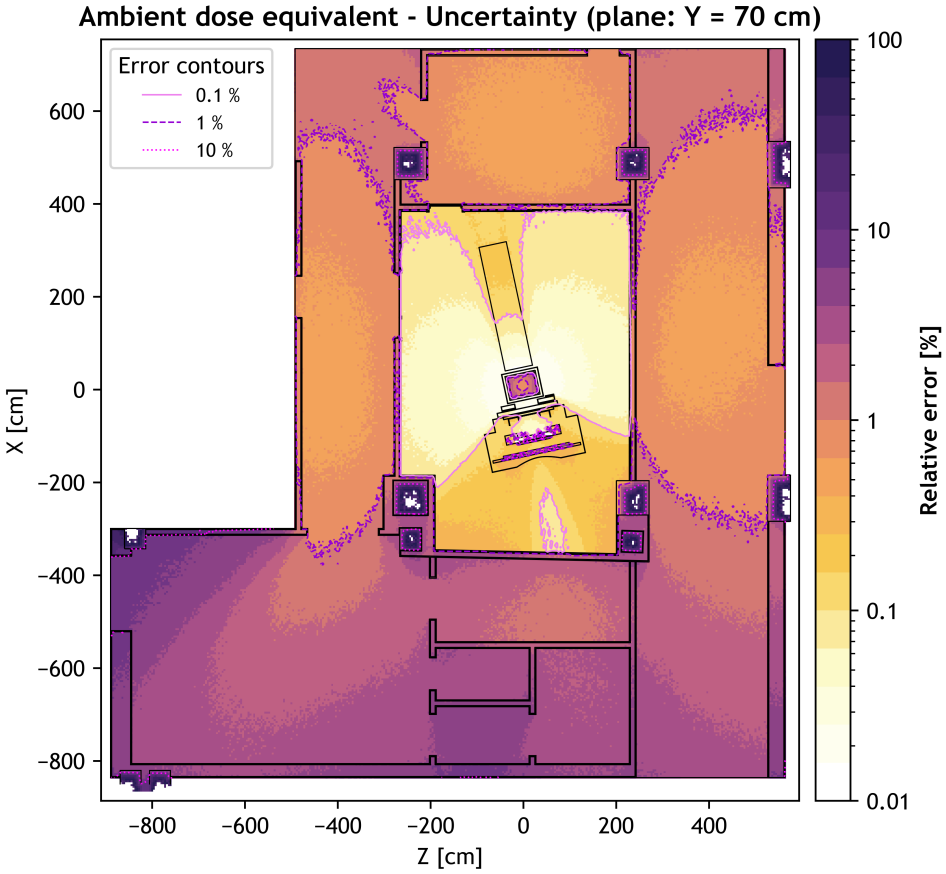

(b)

Figure 4.5 (cont.): Ambient dose equivalent maps of $H^*(10)$ distribution, shown for the projection at $Y = 70$ cm, corresponding to the average over the slab $Y \in [60, 80]$ cm: (b) Relative statistical uncertainty of $H^*(10)$ for the same projection.

For each projection, both the value and the uncertainty represent the average over a ± 10 cm range about the projection level, i.e., the mean within a virtual slab of thickness 20 cm. For example, at $Y = 70$ cm, the value at each (Z, X) coordinate is the mean of the five bins aligned vertically between $Y = 60$ cm and $Y = 80$ cm (since cubic bins of 4 cm side length were used).

4.6.1.2 | Photon and electron fluence

Figure 4.8 shows the photon and electron fluence distributions per (average) disintegration of ^{99m}Tc. For brevity, only the Z projection is presented. Moreover, the maps were obtained using the same slab-averaging approach over a 20 cm thickness as applied for the dose distributions.

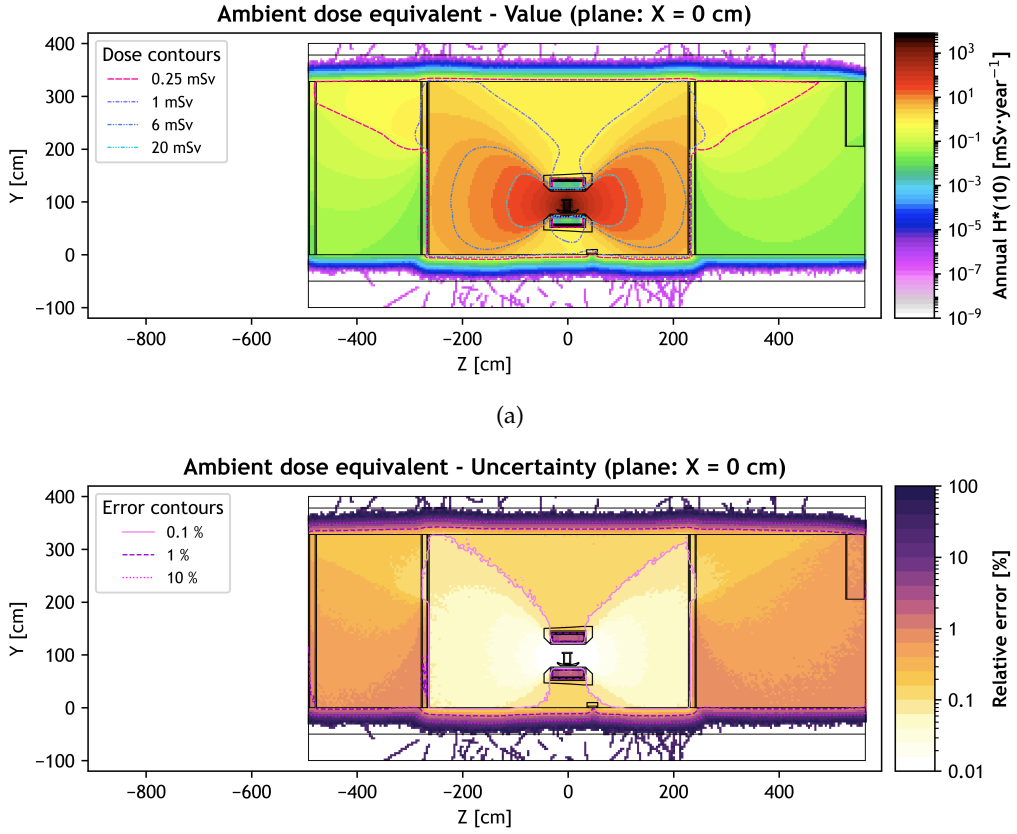

Figure 4.6: Ambient dose equivalent maps of $H^*(10)$ distribution, shown for the projection at $X = 0$ cm, corresponding to the average over the slab $X \in [-10, 10]$ cm: (a) Value map of the ambient dose equivalent rate $H^*(10)$, scaled to typical annual workloads for ^{99m}Tc; (b) Relative statistical uncertainty of $H^*(10)$ for the same projection.

4.6.2 | Energy deposition by region

Energy deposition results were aggregated according to a defined region hierarchy of the model: phantom, scanner, facility, and TLDs. Figures 4.9–4.12 present energy deposition by region in keV, with the corresponding percentage listed beside each bar. The breakdown is shown progressively: first across the top-level regions, then separately for phantom, scanner, and facility components. Error bars are omitted because these were generally $< 1\%$ and would be visually indistinguishable. Similarly, energy uncertainties are not included in the text below. Instead, values and associated uncertainties are fully provided in Appendix F.

The combined energy generated within the model per single disintegration of ^{99m}Tc amounted

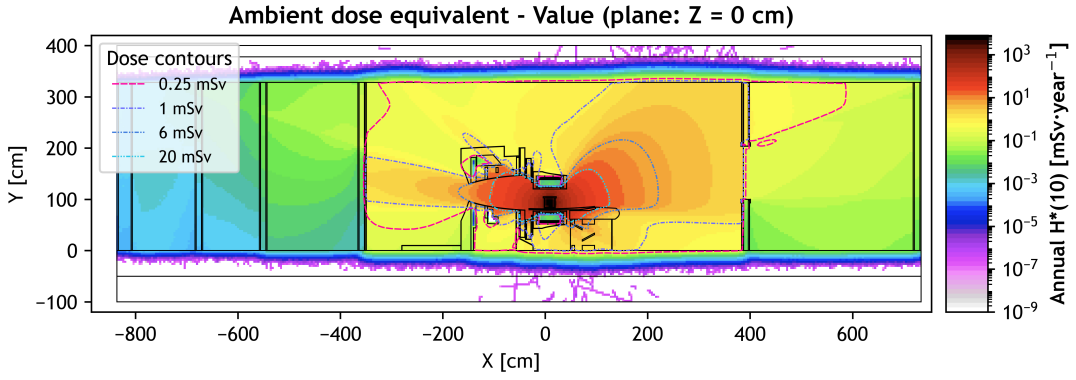

(a)

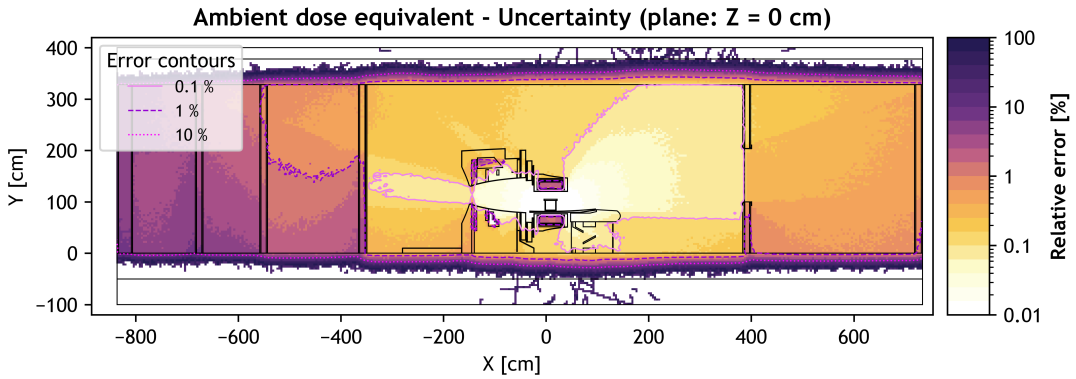

(b)

Figure 4.7: Ambient dose equivalent maps of $H^*(10)$ distribution, shown for the projection at $Z = 0$ cm, corresponding to the average over the slab $Z \in [-10, 10]$ cm: (a) Value map of the ambient dose equivalent rate $H^*(10)$, scaled to typical annual workloads for ^{99m}Tc; (b) Relative statistical uncertainty of $H^*(10)$ for the same projection.

to a total of 224.96 keV. The majority of it was deposited in the phantom, which accounted for 61.75% (138.92 keV) of the total energy (Figure 4.9). The scanner and facility absorbed smaller but comparable fractions of the total, at 20.45% (46.01 keV) and 17.79% (40.02 keV), respectively. Conversely, contributions to the 11 TLD were negligible as they collectively registered below 0.01% ($<$ 1 keV). Breaking down the phantom (Figure 4.10), the water component absorbed 58.36% (131.28 keV) of the total deposited energy, whereas the phantom shell absorbed a smaller fraction of 3.40% (7.65 keV), approximately $1/17$ of the water's deposition. In the scanner (Figure 4.11), the air-lead collimator absorbed the largest share of the deposited energy at nearly 10.58% (23.81 keV). The next most absorbing scanner component were the steel supports

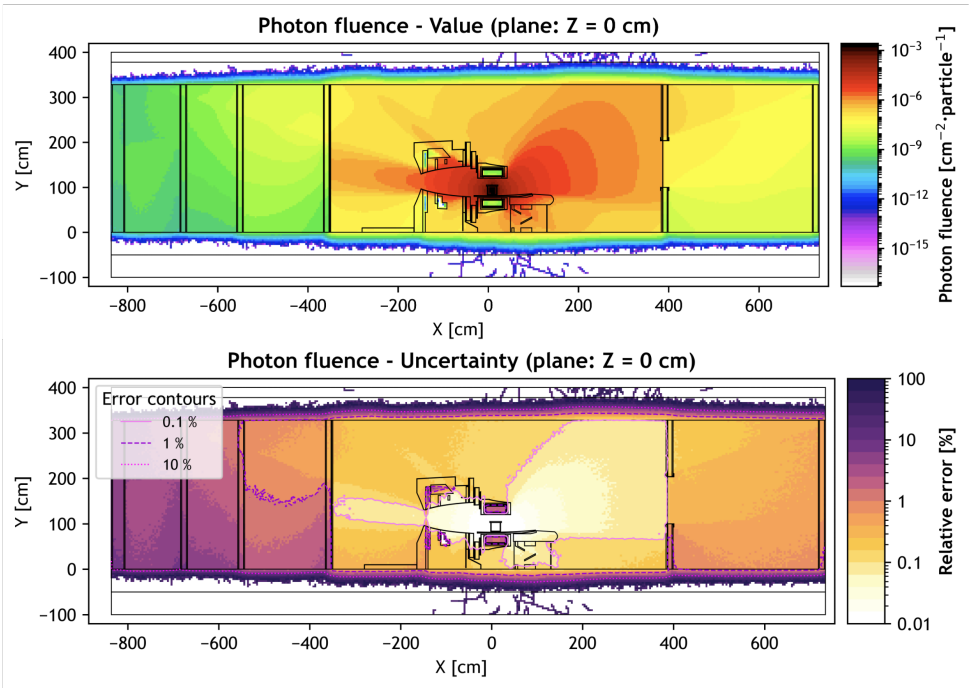

(a)

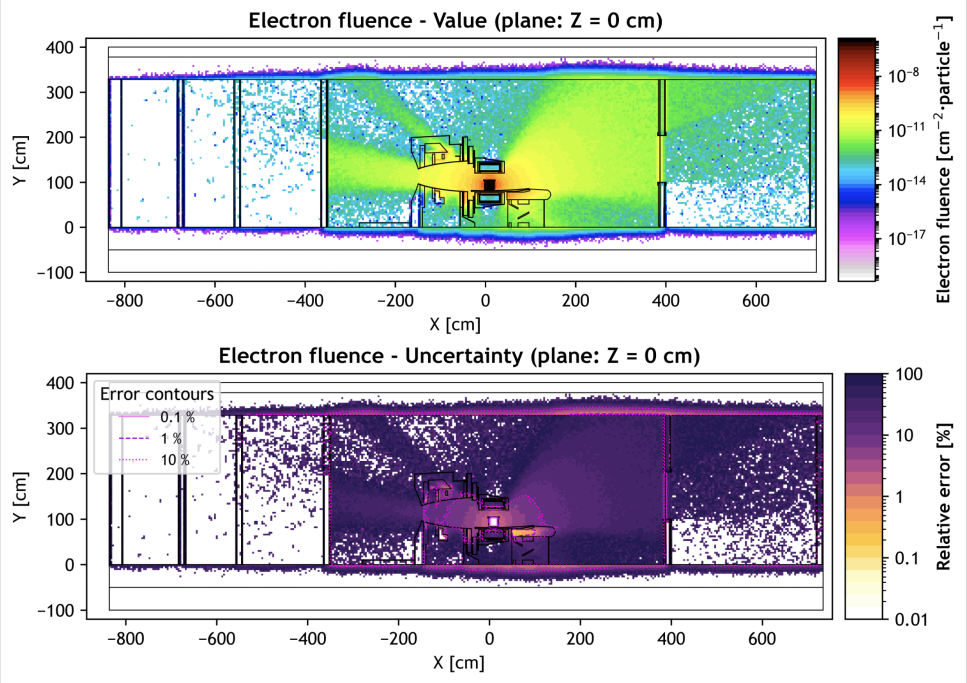

(b)

Figure 4.8: (a) Photon and (b) electron fluence maps for the projection at $Z = 0$ cm, averaged over the slab $Z \in [-10, 10]$ cm. For each particle type, the upper panel shows the fluence distribution per decay (particle), while the lower panel displays the corresponding relative statistical uncertainty.

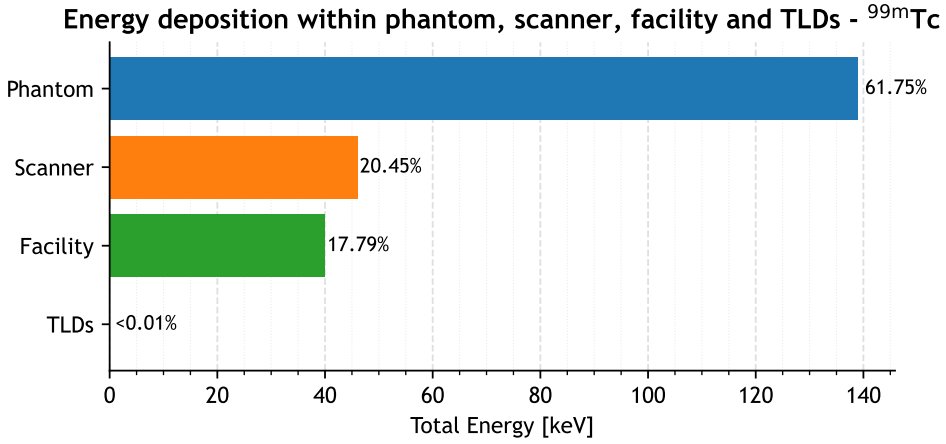

Figure 4.9: Energy deposition, in keV and as a percentage, by region, showing the relative contributions of the phantom, scanner, facility, and TLDs, for the ^{99m}Tc main study simulation.

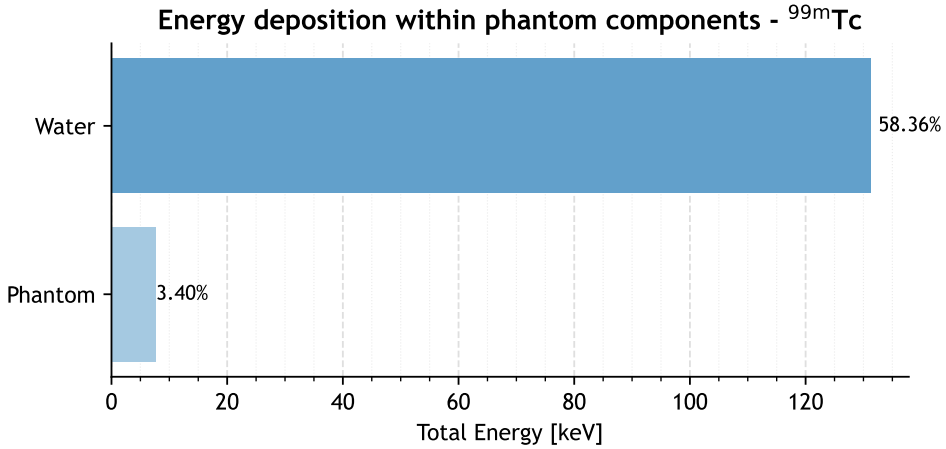

Figure 4.10: Energy deposition, in keV and as a percentage, within the phantom components, separated into water and the phantom shell, for the ^{99m}Tc main study simulation.

at 5.89% (13.24 keV). All the remaining scanner components contributed only marginally, below 1%, with several values close to zero. Lastly, for the facility (Figure 4.12), the ceiling and floor were the largest absorbers of deposited energy, with 2.83% (6.38 keV) and 2.68% (6.02 keV) respectively. The east (wall 4) and west (wall 2) followed closely with `W4L` = 2.09% (4.71 keV), `W4G` = 1.78% (4.01 keV) and `W2L` = 1.92% (4.32 keV), `W2G` = 1.91% (4.31 keV), respectively. Smaller contributions were made from the north and south walls (walls 1 and 3, respectively). The observation window contributed around 0.50%, mostly from the glass itself, while the doors accounted for around 0.85% (door 2) and 0.23% (door 1), mostly from the lead linings.

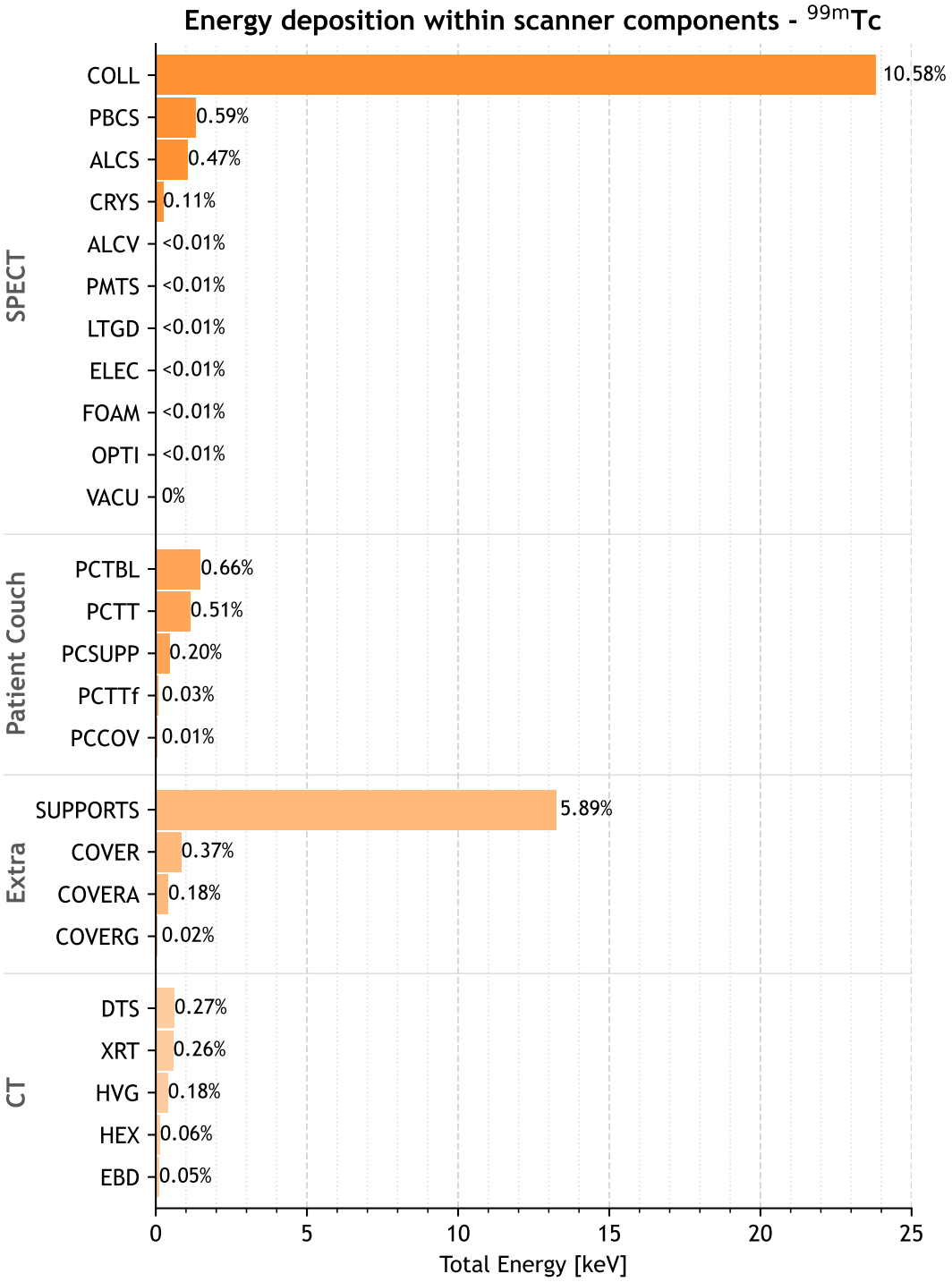

Figure 4.11: Energy deposition, in keV and as a percentage, within the scanner components, including the SPECT system, patient couch, CT unit, and extra components, for the ^{99m}Tc main study simulation.

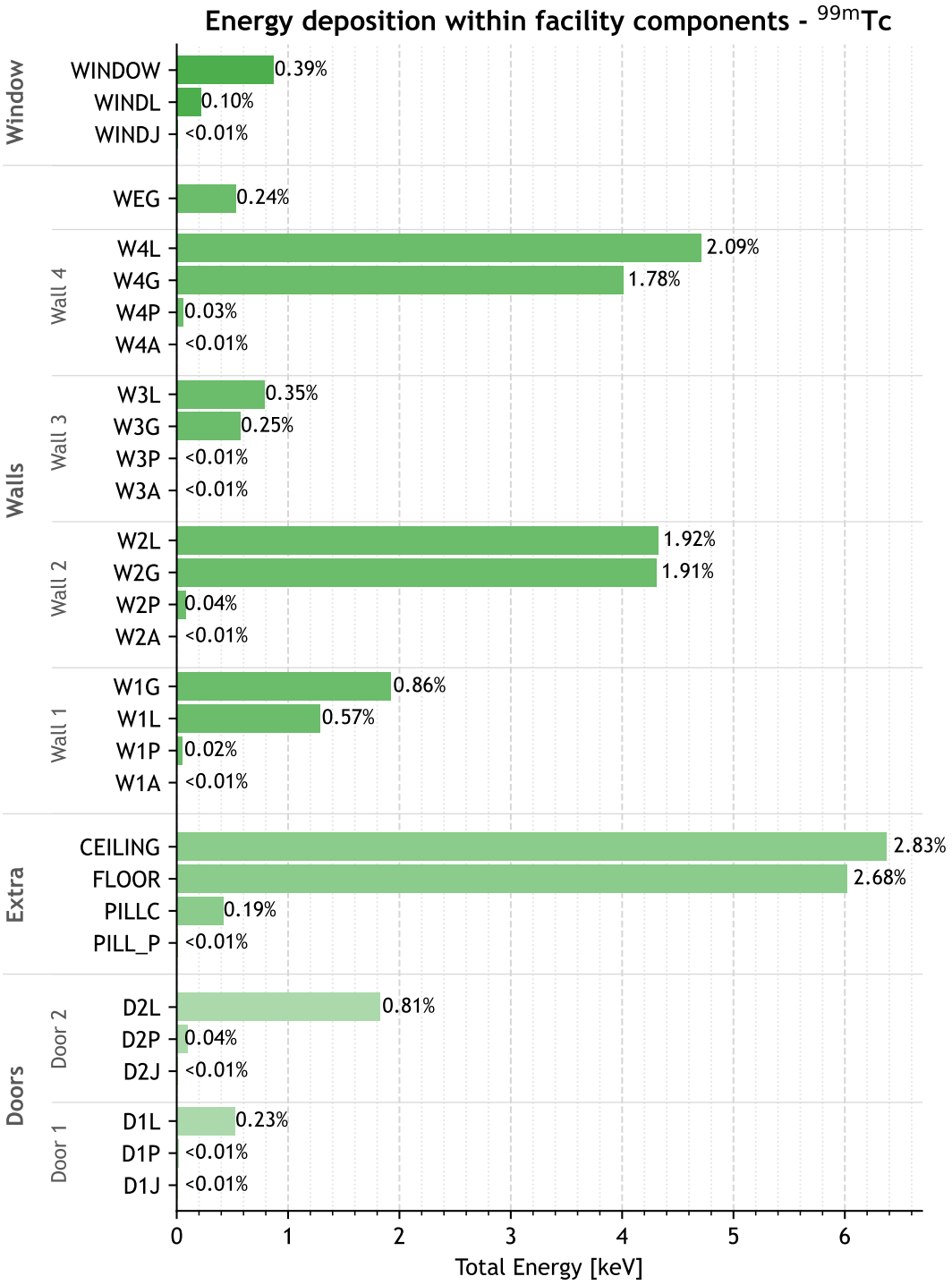

Figure 4.12: Energy deposition, in keV and as a percentage, within the facility components, grouped by windows, walls, doors, and extra structural elements, for the ^{99m}Tc main study simulation.

4.6.3 | Energy–fluence spectra

Figure 4.13 shows fluence-energy spectra scored for photons and electrons in the phantom (water) and in air (room) for a single disintegration of ^{99m}Tc using the `USTRACK` card. For photons, both phantom and air spectra exhibit a pronounced peak around 140 keV. At around 2, 18 and 21 keV, additional minor photon components are visible, though with much smaller magnitudes. For electrons, the spectra commence after the photons', but extend to higher energies. Both electron spectra rises from near zero below ~50 keV and then decreases gradually with increasing energy. In air, there is a marked dip at 140 keV. In general, photons dominated the spectra in both media. However, electrons contributed predominantly within the phantom as they surpassed the photons' magnitude at the 140 keV peak. This was not the case in air. Lastly, both photon and electron fluences were higher in the phantom than in air.

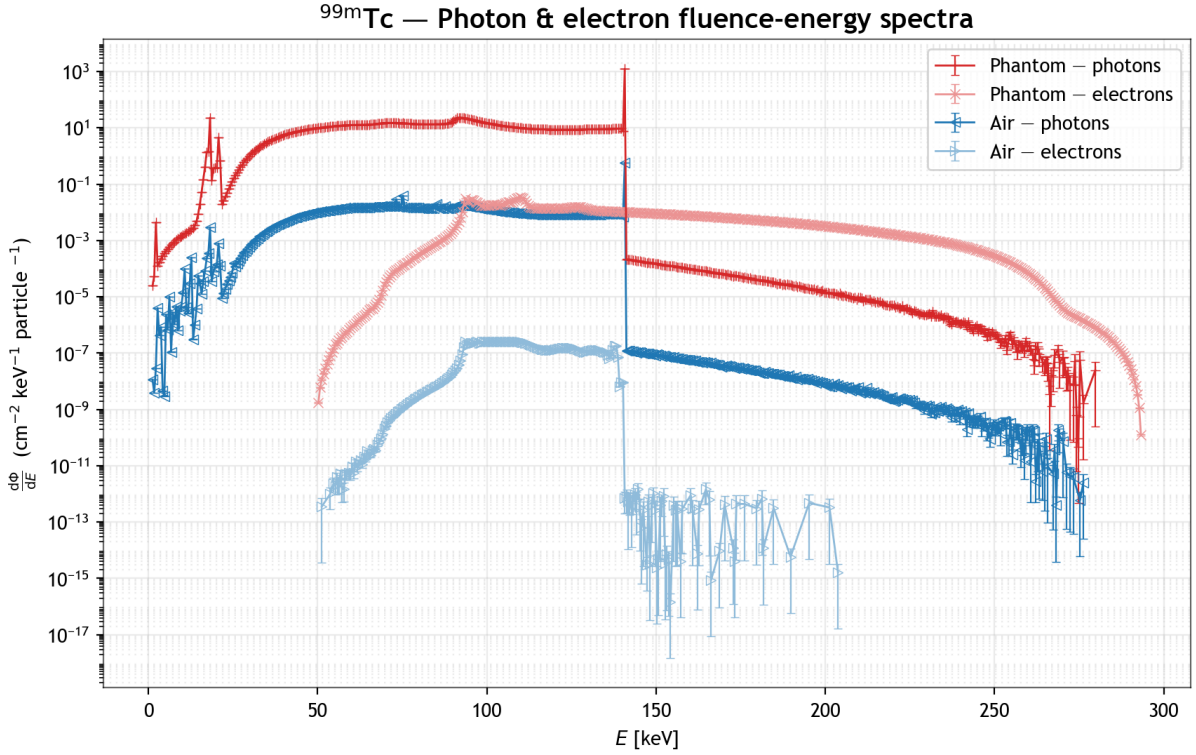

Figure 4.13: Photon and electron spectra of differential fluence $\mathrm{d}\phi/\mathrm{d}E$ against particle energy E scored in the phantom (water) and in air (room), per disintegration of ^{99m}Tc. Error bars are MC uncertainties (1 standard deviation).

4.6.4 | Secondary-particle yields

The final simulation-derived quantity was the yield of secondary particles, as obtained from the `.out` files. On average, per disintegration, secondary electrons were produced in 38.5% of cases, photons in 30.3%, and antineutrinos in 31.2%.

4.7 | Extension to the ^{177}Lu case

The model was also run for ^{177}Lu, generating the same types of outputs as in the previous case. Since some results largely replicated the same spatial patterns they are not reiterated in full. For example, dose and fluence distribution maps displayed the very similar patterns, with variations only in their magnitude, and are therefore omitted from further presentation and discussion. Moreover, given that annual dose estimates were not calculated for ^{177}Lu imaging, there was no basis (nor data) to produce dose distribution maps.

Figure 4.14 summarises the energy deposition across the combined components of the model for ^{177}Lu. The complete dataset is provided in Appendix F. Of the 181.02 keV generated per disintegration, 87.44% (158.28 keV) was deposited in the phantom, with the water compartment alone absorbing 74.52% (134.90 keV), which is nearly three quarters of the total. The remaining proportions across scanner and facility components followed a distribution similar to that obtained for ^{99m}Tc, albeit with reduced contributions in absolute terms due to the generally higher absorption within the phantom. Lastly, although their fraction is modest, the collimators' absorption of 3.58% (6.49 keV) merits mention (from Table F.2).

The photon and electron spectra for ^{177}Lu are shown in Figure 4.15. The photon spectrum displayed several distinct peaks at approximately 8, 55, 63, 72, 113, 208, 250, and 321 keV, each with characteristic relative intensities. The final three peaks were immediately followed by sharp decreases in spectral intensity. As in the ^{99m}Tc case, photons predominated in both media, with the sole exception being within the phantom immediately above the 208 keV photopeak, where the electron spectrum exceeded the photon spectrum. For both particle types, the phantom spectra were higher than those in air across the entire energy range. Lastly, the evaluation of secondary particles indicated that electrons were produced in 49.6% of disintegrations, photons in 10.3%, and antineutrinos in 40.1%.

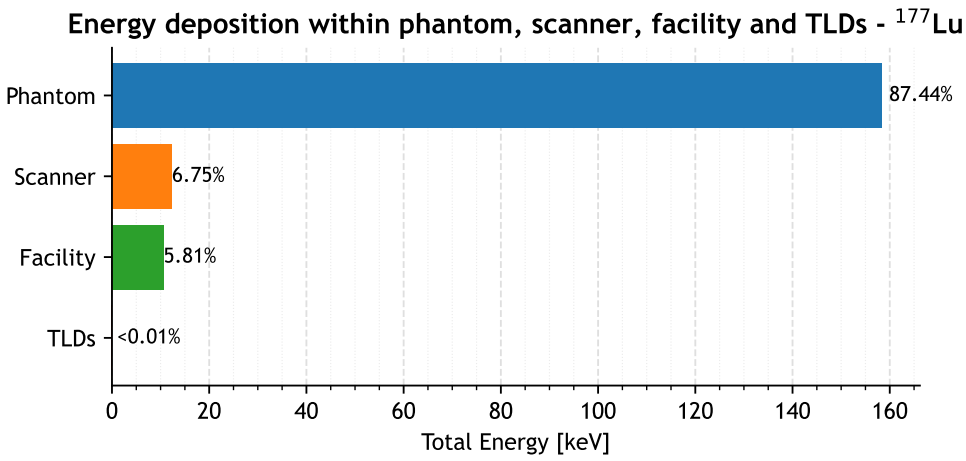

Figure 4.14: Percentage energy deposition by region, showing the relative contributions of the phantom, scanner, facility, and TLDs, for the ^{177}Lu main study simulation.

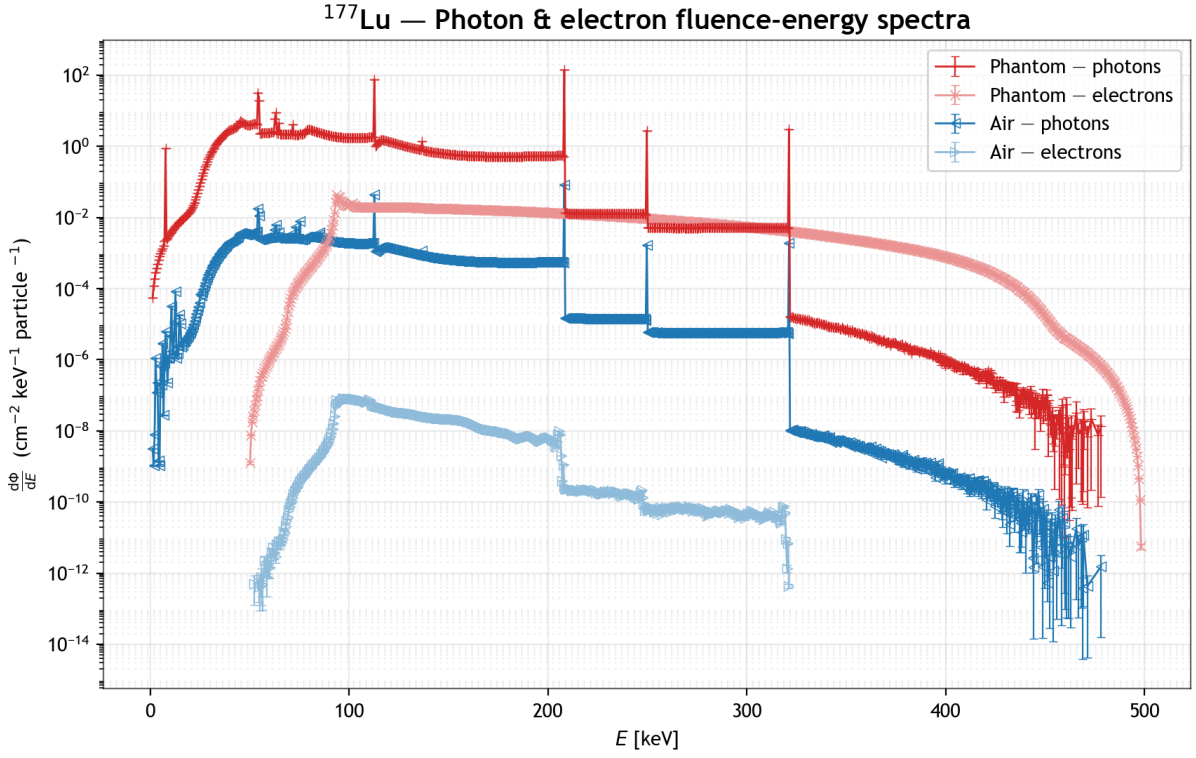

Figure 4.15: Photon and electron spectra of differential fluence $\mathrm{d}\phi/\mathrm{d}E$ against particle energy E scored in the phantom (water) and in air (room), per disintegration of ^{177}Lu. Error bars are MC uncertainties (1 standard deviation).

4.8 | Conclusion

This chapter has provided a systematic presentation of all outputs generated in the study together with their detailed analysis. The following chapter turns to a discussion of the implications of these findings.

5

Discussion

5.1 | Introduction

This work investigated the use of the MC method for shielding assessment in NM practice by developing and validating a detailed FLUKA model of a clinical SPECT/CT facility. The approach combined a small-scale pilot study with a facility-scale model benchmarked against experimental TLD measurements and also compared with analytical estimates, and was applied primarily to the case of ^{99m}Tc with an extension to ^{177}Lu. This chapter interprets these results in the context of the study's objectives and, where possible, in relation to published literature. A critical appraisal of the study's overall strengths and limitations is also provided.

5.2 | Validation of the MC models

Validation should sit at the heart of any MC model. As Infantino (2015) emphasises, "the result of a simulation has a physical meaning only if the model has been validated against experimental measurements or theoretical calculations in well-known problems in which an exact analytical solution can be evaluated" (p. 36). Pells et al. (2023) further emphasise that validation reflects the specific state of both the system and the simulation code, and must therefore be repeated whenever either changes. On this basis, validation was set as a central objective of the present work. A two-step strategy was adopted, where first, a small-scale pilot study provided initial benchmarking, after which validation was extended to the full facility model.

In both stages, validation was carried out using $H^*(10)$ as it represented the primary quantity of interest in this study.

5.2.1 | Pilot study as an initial benchmark

The simplified wall-phantom configuration produced simulation and experimental $H^*(10)$ values that agreed to within a few percent ($< \pm 5\%$) across all six TLD positions. The weighted mean ratio of $\overline{R}_w^{(\mathrm{sim/exp})} = 1.01 \pm 0.01$ indicated that the FLUKA implementation replicated the physical setup with high accuracy. This near-unity ratio had two important implications. First, it confirmed that the modelling procedure was being implemented correctly in FLUKA. This marked an important step in meeting the first objective of this work, which was to acquire proficiency in the MC code FLUKA. Secondly, the slight tendency for the simulation to overestimate the measured experimental values provided an early indication of the bias subsequently observed in the facility-scale study.

Statistical analysis reinforced the two methods' agreement. The paired t-test with $p = 0.3503$ provided no evidence of a systematic difference between simulation and experiment, while the Pearson correlation coefficient of $r = 0.9977$ demonstrated an almost perfect linear relationship across the TLD positions. Together, these metrics showed that the two datasets not only had comparable means but also tracked one another closely across spatial variations. In practical terms, this suggests that the simulation was not simply reproducing average dose levels by chance, but reliably captured the spatial dose gradient from positions '1' through '6'.

The small-scale pilot study also validated the experimental methodology itself. The agreement with simulation values confirmed that the calibration of the TLD system, which required careful determination of various correction factors, was sound. This provided confidence that the TLDs could serve as a reliable benchmark for the main facility study. In this way, the pilot served as a two-sided validation: it established confidence both in the FLUKA model and in the experimental system.

5.2.2 | Facility-level SPECT/CT model

With the preliminary model validated, construction of the complete facility-level SPECT/CT model could confidently be undertaken, fulfilling the objective of developing a high-fidelity

FLUKA representation of the facility. Here, the model's fidelity did not only depend on accurate geometry and material assignment. but also on the physics setup chosen. Validation therefore addressed the complete model.

5.2.2.1 | Model geometry fidelity

The geometry achieved a close correspondence with the real-life SPECT/CT facility, as evidenced by various model visualisations and comparisons with their physical equivalents (Figures 3.11, 3.13, 4.2, 4.3). Its construction relied on accurate specifications wherever available and informed estimates where data were lacking. Special care was taken in the modelling of the scanner to include the relevant elements, such as the collimators, detector heads, couch, and housing. As for the facility, one of the adjustments that became essential in early testing was door and window joint treatment. Initially, their junctions with surrounding walls were represented by gypsum finishes, but dose leakage streaks appeared on the resulting distribution maps. The addition of lead-lined jambs and more accurate modelling of the double-leaf door with a lead-lined astragal eliminated these artifacts and improved the geometry to be closer to the actual installation. In addition to the scanner room proper, corridors and surrounding rooms were added to facilitate dose pathway measurements beyond the immediate clinical area. This is a feature often absent in simpler shielding assessment methods.

Nevertheless, some simplifications were unavoidable. Fine structural details such as ceiling voids, fixtures, penetrations, and scanner electronics were omitted. Moreover, the phantom was static with no detector or couch motion. These choices limited model fidelity but were necessary for computational feasibility. Thus, in general, the model was balanced in terms of detail and practicality as it provided a facility-scale model that could be used for benchmarking and dose assessment and visually recreated the main features of the real installation (Figure 4.3).

5.2.2.2 | Validation against TLD measurements

Although the geometry appeared realistic on visual inspection, the critical test of whether the simulated model replicated the physical setup lay in its quantitative validation against experimental data through the TLD readings. The simulation-experimental ratios in the main study showed a broader spread (0.07 ± 0.09 to 2.67 ± 0.63) compared with the pilot study and a higher weighted mean ($\overline{R}_w^{(\mathrm{sim/exp})} = 1.20 \pm 0.01$), which corresponds to a modest systematic overes-

timation of around 20%. Albeit $\overline{R}_w$ being further away from the ideal unity, in the context of radiation protection, overestimation it is preferable to underestimation as it errs on the side of conservatism. At the same time, it indicated that the more complex facility model could not be validated to the same degree as the simplified pilot setup. It is worth noting, however, that there are no universal standards for what constitutes a "validated" model, nor for the acceptable bounds of agreement. The approach taken here closely followed that of Infantino (2015), who also employed TLDs to benchmark neutron dose rates around a PET cyclotron FLUKA MC model. In their study, the TLDs overestimated by 55%, whereas the present study achieved a substantially lower bias of about 20%. Nevertheless, their model was still considered validated. Infantino further reported that a rem counter yielded far better agreement (0.99 ± 0.04), which underlines that even the choice of dosimeter directly influences the apparent level of validation.

More important is the recognition that while the experimental TLD values were treated as the ground truth for validation, they are themselves subject to error. The Ishikawa diagram in Figure 5.1 illustrates numerous potential sources of uncertainty in obtaining the final experimental $H^*(10)$ values from the TLDs, from radionuclide impurities to phantom positioning on the couch, which could have shifted the measured $H^*(10)$ away from their true value. However, the pilot study suggested that most such issues were controlled. Still, a key difference between the two validations lay in the timing of TLD calibration. The pilot was conducted one day after calibration, whereas the main study was carried out 19 weeks later. Kry et al. (2020) note day-to-day sensitivity variations of TLD readers can exceed 10%. Ademoh (2008) further asserted that the collective sensitivity of TLDs degrades measurably with time, reporting a 3% decrease after six weeks. This deterioration is exacerbated by high humidity and temperature, particularly when dosimeters are stored unsealed (da Rosa, 1989). Given Malta's summer climate and storage conditions, such effects are highly plausible here. Ideally, the TLD batch should have been stored in a dedicated room and recalibrated immediately prior to the main study. However, resource and time constraints made these impractical.

Despite these caveats, the overall validation outcome remained strong as $\overline{R}_w^{(\mathrm{sim/exp})} = 1.20 \pm 0.01$ was supported by the absence of a statistically significant difference in means ($p = 0.1040$) and an almost perfect correlation ($r = 0.9992$), even exceeding that of the pilot study ($r = 0.9977$). Together, these demonstrated that the simulation reproduced not only the overall dose levels but also the spatial pattern of attenuation across the facility, similar to what was observed

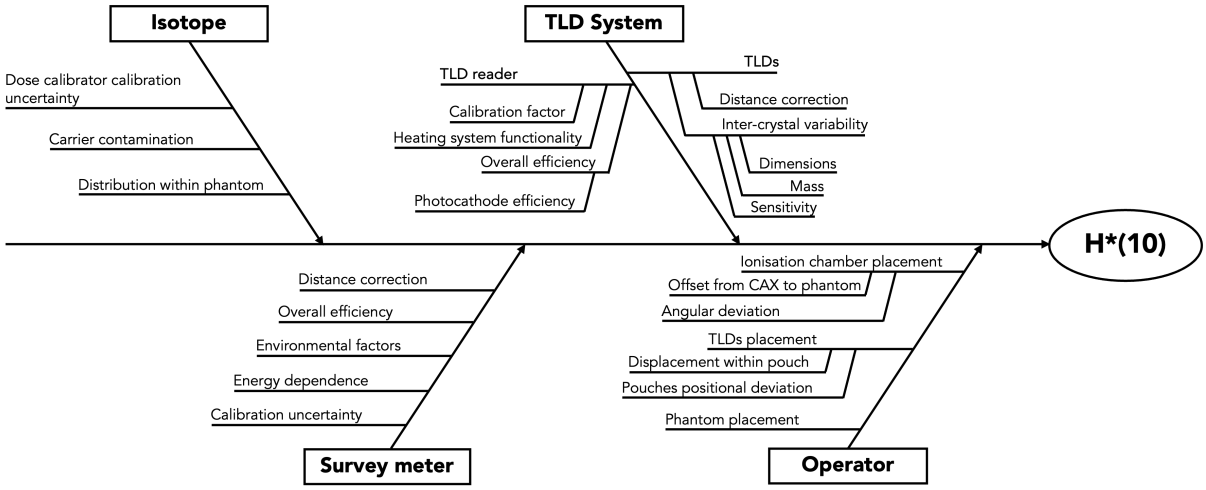

Figure 5.1: Ishikawa diagram summarising potential sources of error in experimental TLD $H^*(10)$ measurements.

in the pilot study. On this basis, the facility model could be considered validated, thereby fulfilling yet another of the study's central objectives.

5.3 | Comparing shielding analysis methods: analytical, simulation, and experiment

In clinical NM practice in Malta, shielding calculations are performed analytically, so it was important to compare this approach against both experimental and simulation results. On average, the analytical method showed a 3% smaller bias relative to experiment than the simulation. However, as the ranges overlap (1.20 ± 0.01 vs. 1.17 ± 0.02), both ratios could be considered equivalent within uncertainty. Moreover, the variability across locations was much larger, with individual ratios that ranged from < 0.01 to 33.90 ± 7.99.

At one extreme, $R^{(\mathrm{ana/exp})} < 0.01$ was observed at location 'C2', reflecting the analytical estimate $H^*(10)^{(\mathrm{ana})} < 0.01$. This very low ambient dose equivalent resulted from Beer–Lambert attenuation (the measurement point being shielded by 2 mm of lead) combined with the inverse-square law (a distance of 3.79 m from the assumed point source). At the opposite end, the highest ratio ($R^{(\mathrm{ana/exp})} = 33.90 \pm 7.99$) was at 'E4'. This discrepancy is attributed to two factors: (i) near-field geometry and (ii) partial shadowing by the CT gantry. For the near-field

effect, the measurement point was only 1.64 m from the phantom, such that the point-source approximation breaks down. This was similarly the case for 'E3' ($R^{(\text{ana/exp})} = 26.55 \pm 5.01$), also at a distance of 1.64 m, and even more pronounced at 'E1' and 'E2' (0.74 m), although their $R^{(\text{ana/exp})}$ was not particularly influenced ($R^{(\text{ana/exp})} = 1.24 \pm 0.07$ and $R^{(\text{ana/exp})} = 1.16 \pm 0.02$, respectively). For the shielding effect, this was due to the analytical method completely disregarding the scanner geometry. Conversely, both of these effect were captured by the MC model ($R^{(\text{sim/exp})} = 2.75 \pm 0.65$). This illustrates the greater realism of the MC approach.

Statistical testing reinforced these deviations. Analytical and experimental means differed significantly ($p = 0.0284$), and their correlation was poorer than between simulation and experiment ($r = 0.9781$). This explains why, although $\overline{R}_w^{(\text{ana/exp})}$ was marginally closer to unity than $\overline{R}_w^{(\text{sim/exp})}$, the large individual $R^{(\text{ana/exp})}$ ratios discrepancies at certain locations led to an overall statistically significant between the two methods, even though, excluding 'E3' and 'E4', five of the remaining nine ratios were closer for the analytical method than for the simulation. Thus, while analytical methods remain appealing for their efficiency and adequate results for pre-installation shielding design, where inputs are assumed and deliberately conservative, they cannot reproduce the complex dose pathways evident in the real facility. Conversely, MC techniques provide substantially greater fidelity and reliability in reproducing measured dose distributions, however, at a computational and effort cost.

Taken together, the three methods yielded physically consistent ambient dose equivalent patterns across the TLD positions:

- **A1, B1, C1, D**: These internal imaging room positions showed intermediate exposures. 'D' gave the highest dose among them due to its shorter distance from the source and unobstructed line-of-sight. This was the opposite for 'A1' and 'C1'.

- **A2, B2, C2**: These recorded the lowest doses, in line with the expected attenuation from their effective shielding capabilities ('A2': 2 mm lead-glass; 'B2': 4 mm lead; 'C2': 2 mm lead + obstruction from the scanner). Discrepancies with experimental values likely arose because the TLDs also captured background or incidental radiation (e.g. nearby patients), whereas the simulation and analytical methods reflected only the primary source.

- **E1, E2, E3, E4**: The SPECT gantry front exhibited the highest exposures overall, as expected from direct line-of-sight to the source with minimal shielding. By contrast, 'E3'

and 'E4' were positioned at the CT gantry sides such that structural attenuation substantially reduced the physical and simulated doses.

Simulation estimates carried consistently lower uncertainties than the experimental measurements, with most below 3%, owing to the large number of particle histories run. This provides confidence that the reported simulation values faithfully represented what was modelled and illustrates yet another key advantage of MC, that is, statistical precision can be driven arbitrarily low, provided that sufficient computing power is available. Notwithstanding, such statistical precision does not itself guarantee physical accuracy as confidence in the modelled geometry and assumptions still depends on external validation.

5.3.1 | Time and workload considerations across methods

In clinical settings, turnaround time and staff effort matter alongside numerical accuracy. The three methodologies distributed workload differently. Analytical calculations provided the shortest time-to-result: once inputs were specified, outputs were available almost immediately, especially using Python scripts. In practice, however, several formulae and barrier thicknesses are trialled during optimisation, so staff time increases with the number of design variants. Experimental measurement was more labour-intensive: TLD and phantom preparation (including for calibration), set-up in the imaging room and dose readouts required effort. As a post-installation activity, its chief role is verification of the realised design. Lastly, simulation entailed the greatest up-front investment: compilation of geometry, materials and sources, implementation, and validation, followed by non-negligible compute time. However, once a baseline model is validated, marginal staff time for alternative designs (e.g., wall thickness/material changes, workload variations) is low and runs can be simulated unattended. An instance of this was the ^{177}Lu extension, which required only a source change before the simulation could run unsupervised. In summary, analytical methods are fastest for initial estimates, experimental measurements allow for verification of the effective installation of shielding but are slow to iterate, and simulation is slower initially, yet most efficient for systematic exploration of design options.

5.4 | Insights from the ^{99m}Tc main study

Whereas experimental and analytical approaches are mostly restricted to single point-dose estimates, an MC simulation yields a far richer set of quantities that in practice would require multiple detectors or separate analytical models to obtain. This further underscores the versatility of MC. With the facility model validated, attention can now turn to the additional observables derived from applying the MC approach to the ^{99m}Tc case.

5.4.1 | Annual dose estimates – TLDs vs 2D maps

The results in Table 4.3 show that, in three of the four areas immediately surrounding the scanner room, annual doses from a typical ^{99m}Tc protocol yielded $H^*(10)$ values below both occupational and public dose limits, and even dose constraints. While these values are equivalent rather than effective doses, equivalent dose is deliberately defined as a conservative quantity that, by design, exceeds effective dose (Pelliccioni, 2000). Thus, given that all equivalent doses lay below regulatory thresholds, the corresponding effective doses can be inferred to do so as well. It is worth mentioning that effective doses were also scored in the simulations, but these results were not retained. To be physically meaningful, effective dose requires the use of anthropomorphic phantoms that account for tissue-specific weighting factors. Without such implementations, the values would have been misleading. The key outcome, therefore, is that the currently installed shielding provides adequate protection for ^{99m}Tc imaging.

At the east wall, no TLD could be placed in the public corridor outside the scanner room due to ethical and practical constraints. This highlights a limitation of relying solely on experimental point-dose measurements: only a small number of locations can be sampled, and gaps in coverage are inevitable. In contrast, MC simulations enable a comprehensive three-dimensional representation of the dose distribution throughout the facility, thereby providing insight that extends far beyond what sparse point measurements can capture. The maps in Figures 4.5–4.7 (and those in Appendix E) exemplify this advantage by visualising how radiation interacts with both the scanner and the surrounding environment.

Several key features emerge from these maps. For instance, the bird's-eye view in Figure 4.5 shows dose spreading outward from the phantom, with the front and rear distributions asymmetrically shaped by the presence of the patient couch and gantry. The concrete support pillars

display a clear attenuation effect as the magnitudes visibly decrease at their centres. Furthermore, in the NM corridor leading to the waiting area, scattered radiation can be seen deflecting around the entryway. Most prominently, the 0.25 mSv public dose constraint and the 1 mSv public dose limit contours demonstrate the immediate drop in dose magnitude at the lead sheets within the walls, which effectively contain both within the scanner room. Figures 4.6 and 4.7 further reinforce these observations. Furthermore, the top and bottom collimators substantially reduce dose levels above and below them, respectively, with contour lines for all four regulatory thresholds contained within their extent, whereas the detector head components are scarcely exposed by comparison.

One feature of note is a narrow contour of 0.25 mSv escaping above the shielding at the top of the wall. This corresponds to the termination of the lead sheeting at 2 m height. Although this represents a potential leakage pathway into adjacent rooms, its height lies well above typical occupancy levels, that is, it is above average adult head height and therefore, its radiological impact is negligible in practice. Moreover, a slight increase in dose is observed close to some of the walls opposite those directly surrounding the scanner. This arises from escaping radiation scattering off the ceiling, and depositing dose in these areas.

Across all maps, statistical uncertainties in the regions of interest were generally low. This is evident in the slices shown in Figures 4.5–4.7, where practically the entire geometry falls within a 10% relative error. This provided confidence that the patterns observed genuinely reflected the behaviour of the modelled geometry.

Finally, it should be acknowledged that these results are inherently site-specific and shaped by the clinical workload in national NM practice. For this reason, direct comparison with the literature is limited, as dose distributions will vary with facility design, scanner model, and local patient throughput. Nonetheless, these maps clearly demonstrated the value of simulation in capturing complex dose pathways and validated the effectiveness of the existing shielding.

5.4.2 | Fluence distributions, spectral characteristics, and secondary particles

The fluence maps in Figure 4.8 show that the dominant contribution to the dose distribution across the facility arises from photons, whose distribution closely mirrors that of the dose maps

(Figure 4.7). Particularly, photons escaping into the floor and ceiling show identical spatial patterns on the dose maps, differing only in magnitude. This reflects the fact that dose deposition was largely governed by photon interactions. In contrast, panel (b) of Figure 4.8 highlights that electron fluence is almost entirely confined to the phantom, which is consistent with the short ranges of secondary electrons in tissue and their rapid self-absorption (Holm, 2022).

The fluence-energy spectra in Figure 4.13 reinforce these observations. Photon fluence generally dominated over electrons in both air and phantom. The sharp peak at 140.5 keV corresponds to the principal γ emission of ^{99m}Tc, with the minor 142.6 keV line not visible due to its much lower branching ratio (Crișan et al., 2022). The pronounced drop beyond 140 keV arises because no higher-energy primary γ lines are emitted, so the spectrum above this energy contains only scattered radiation. Additional features can be observed, such as the smaller peaks near 2 and 18–20 keV, corresponding to characteristic X-rays and Auger electrons, and the broad continuum below the main peak attributable to Compton scattering (Cherry et al., 2013).

The apparent continuous electron spectrum does not arise from true β^- decay of ^{99m}Tc, but from secondary interactions following the isomeric transition. These short-range electrons deposit energy within the phantom and are almost entirely absorbed there, so the sharp drop in air above 140 keV reflects only secondaries from rare photon–matter interactions. Within the phantom, the electron spectrum extends up to about 294 keV, coinciding with the known β^- endpoint of ground-state ^{99}Tc (Grate et al., 2020). While this might suggest that ^{99}Tc β^- decay is being sampled, in reality its half-life (~2.1×10^5 y) is far too long to contribute on clinical timescales. The presence of this feature, along with the associated antineutrinos recorded in the output, is best understood as a consequence of running the simulation in *semi-analogue* mode, that is, the full decay scheme of the isotope is represented in the physics database, even if the probability of occurrence within the simulated time-frame is effectively zero (Marengo and Infantino, 2022). Thus, although the spectrum includes the ^{99}Tc β^- branch, its contribution to dose is negligible in practice.

While such spectral analysis is not, in itself, determinative for routine shielding decisions, it illustrates a strength of the MC approach: the inherent transport physics can be probed at energy-by-particle level whenever needed. Demonstrating that these spectra can be generated, interpreted, and linked to observed dose patterns further meets the first objective of this work of developing proficiency in MC techniques.

5.4.3 | Energy deposition across the model

A quantity which is certainly inaccessible to physical measurement is the total energy released per disintegration and its distribution across the various components, yet these were readily extracted in FLUKA. More so, to reduce computation time, these were not scored directly with `USRBIN`, but rather, they were recovered from the `.out` file, which contains this information by default. This approach also deepened understanding of how FLUKA aggregates results and thus contributed directly to the objective of becoming proficient with the code.

The largest share of the total 224.96 keV energy generated, 61.75%, being absorbed within the phantom reflects the substantial self-attenuation by the patient surrogate. This finding highlighted that more than half of the emitted energy is deposited within the body itself. This agrees closely with the NEMA benchmark of 63% self-absorption for ^{99m}Tc in a similar phantom (National Electrical Manufacturers Association, 2023). Comparable behaviour has also been reported in PET, where Elschot et al. (2010) determined a reduction factor of 0.34 when accounting for patient self-absorption, which, when applying it into shielding calculations considerably reduced lead shielding requirements. Together, these observations imply that incorporating self-attenuation into analytical shielding calculations can improve cost-effectiveness while still maintaining regulatory compliance.

A further 20.45% of the energy was absorbed within the scanner, with 51.74% of that concentrated in the collimator. This reinforces the need to account for attenuation also within the scanner when considering shielding, and highlights the collimator's dual role: while it improves image quality, it also absorbs a large fraction of radiation that never contributes to detection, but does add to patient dose. The contrast between the collimator (10.58%) and the crystals (0.11%) quantifies this inefficiency clearly.

The remaining 17.79% of energy was deposited in the facility structures in a pattern that reflected the geometry and shielding effectiveness. The ceiling (2.83%) and floor (2.68%) absorbed fractions consistent with their large footprint and thickness. Although farther away from the phantom, the ceiling showed slightly higher absorption because the scanner preferentially attenuates downward-directed radiation. This suggests marginally greater leakage to the rooms above than below, although the difference is negligible. The east and west walls followed (2% each), and both of which were longer and more directly exposed to the phantom than the north and south walls ($<$ 1% each). By contrast, openings such as the observation

window and doors contributed only marginally as their smaller surface area outweighed their reduced attenuation. Across all walls, doors, and window, the lead component was the dominant absorber. These distributions reinforce the central role of structural shielding materials, namely lead and concrete, in providing effective shielding.

5.5 | Implications for ^{177}Lu imaging

The ^{177}Lu case illustrates several important contrasts with the ^{99m}Tc study. Firstly, the larger fraction of energy absorbed within the phantom (87.44%) indicated a stronger self-attenuation of ^{177}Lu emissions within the patient being imaged, such that external shielding contributed less (5.81%) compared with ^{99m}Tc (17.79%). The greater self-absorption in ^{177}Lu can be attributed to the local deposition of electrons from β^- decay. Moreover, the scanner absorbed 6.75% of the total generated energy, with 53.04% of the scanner deposition occurring in the collimator (i.e. 3.58% of the total). Two salient points follow from this outcome. Firstly, in both the LEHRS (^{99m}Tc) and HEGP (^{177}Lu) configurations, the collimators are the scanner's principal energy sink, taking roughly half of its deposition. Secondly, the slightly higher fraction for HEGP suggests that this thicker-septa collimator, which was represented as a solid air-lead block with greater lead content than the LEHRS, captures a marginally larger share of energy, despite the pairing with a harder ^{177}Lu spectrum (208 keV photopeak vs 140 keV for ^{99m}Tc).

The photon spectra of ^{177}Lu displayed a richer structure than for ^{99m}Tc, with multiple peaks between 8 and 321 keV that match known nuclear transitions (Liu et al., 2021). Together with the continuous electron component, this pattern reflects the underlying β^- decay of ^{177}Lu. Furthermore, although the ^{177}Lu spectra (Figure 4.15) appear higher than the ^{99m}Tc spectra (Figure 4.13), this is not evidence of greater total energy deposition on a strictly comparable basis. Only the phantom and room-air regions are plotted, whereas total energy deposition is obtained by integrating over energy and summing across all regions, including the scanner and facility components. In those components, the differential fluence is much smaller for ^{177}Lu, since most of the deposition occurs within the phantom itself. Consequently, the total deposited energy per disintegration is lower for ^{177}Lu (181.02 keV) than for ^{99m}Tc (224.96 keV).

A final point concerns applicability. The ^{177}Lu simulation framework is already in place and could be scaled to realistic clinical scenarios. With sufficient literature review to establish ad-

ministered activities and workload data relevant to the Maltese population, the results could be extrapolated to estimate annual doses and verify compliance with regulatory limits. Such extrapolation, however, depends critically on assumptions about workload and clinical practice, and thus sits at the boundary between methodological capability and local implementation.

5.6 | Further practical limitations

Beyond the methodological constraints already discussed, several additional limitations were identified:

- At low-dose locations ('A2', 'B2', 'C2'), measurements exhibited very large relative uncertainties ($> 200\%$). The corresponding simulation points also showed higher relative uncertainties in these regions, although of a lesser magnitude. Together, these effects reduced confidence in the agreement between experiment and model at the most shielded locations. Using a higher ^{99m}Tc activity and increasing the number of primary histories would have reduced experimental and simulation errors, respectively. However, a higher activity was not feasibly attainable because the available eluate had to be reserved for patients. As for the simulation, since relative error scales as $1/\sqrt{N}$ (N =primaries), substantial improvements require a power-law increase in primaries (e.g., halving the error needs ~4 times more primaries and ~4 times runtime). Alternatively, variance reduction techniques could have offered a more practical route to lower uncertainty at similar computational cost. Furthermore, the limited number of TLD positions, particularly around the scanner, restricted the ability to probe finer details of the geometry and its influence on dose distribution.

- The scanner room doors were assumed to remain closed at all times. While this reflects standard radiation protection practice, it may not always hold in reality, introducing a possible source of discrepancy.

- Finally, and as previously noted, several construction features could not be incorporated due to lack of reliable information. Small penetrations, fixtures, and irregularities in shielding structures were excluded, yet these can sometimes act as leakage pathways. For example, reports following scanner installation indicated measurable dose leakage

through door keyholes, which were subsequently mitigated with additional shielding. Such details highlight a level of uncertainty that cannot readily be captured in the model but may nonetheless influence real-world measurements.

5.7 | Conclusion

In summary, the discussion has established that the facility model constructed successfully replicated measured values within tolerable limits. In addition, the observations presented indicated both the applicability and limitations of the MC method for shielding assessment in NM. The following chapter threads all these together to give overall conclusions of this research.

6

Conclusions and recommendations

6.1 | Introduction

This final chapter brings together the main findings of the study and reflects on their broader significance. Having examined the validation, results, and limitations of the facility model in the preceding discussion, the focus now shifts to drawing out the key conclusions in direct relation to the study's objectives. These conclusions are followed by recommendations for both professional practice and future research.

6.2 | Summary of conclusions from the study

The main conclusions of this study were:

- A high-fidelity FLUKA model of the SPECT/CT facility in Malta's national public hospital was built and matched to site drawings. The scanner was modelled at component level with dual SPECT detector heads in H-mode with the installed collimators, full patient couch, the CT gantry with its main components, support framework, and housing. The room envelope included concrete floor/ceiling, lead-lined walls, the lead-glass window and two lead-lined doors with frames/jambs, plus adjacent areas and doorways to capture dose pathways. For a representative ^{99m}Tc protocol, validation against calibrated TLDs showed no significant difference in means for $H^*(10)$ between simulation and ex-

periment ($p = 0.1045$) and an excellent correlation ($r = 0.9992$), with a conservative weighted ratio $\overline{R}_w^{(\mathrm{sim/exp})} = 1.20 \pm 0.01$.

- A three-way comparison between analytical, experimental, and simulation clarified the strengths and limits of each approach. While fast and straightforward for clinical use, analytical methods differed significantly from experiment ($p = 0.0284$) and could not resolve local shielding effects. Experimental TLDs provided the closest representation of reality. However, their accuracy is bounded by intrinsic uncertainties, limited spatial coverage, and the fact that such measurements cannot be performed before installation. In contrast, MC simulations, although demanding in terms of data gathering, model development, and the steep learning curve of FLUKA, once validated, delivered a far richer characterisation of the radiation field, including point doses, 2D maps, fluence distributions, energy deposition by region, and secondary-particle yields. This made possible analyses not feasible with the other methods.

- Annual dose estimates derived with clinically used workloads, activities and scan times confirmed that barrier doses in controlled and public areas remain within applicable constraints and limits. The 2D maps also provided coverage at locations where TLDs could not be sited. Taken together, these findings confirmed that the currently installed shielding is adequate for ^{99m}Tc imaging under existing clinical practices.

- Energy accounting per disintegration showed where radiation is actually absorbed: approximately 62% of the total energy generated is absorbed within the phantom itself due to self-attenuation, about one-fifth within the scanner, notably approximately half of it in the collimator, and the remainder in room structures. This quantifies both patient and scanner self-shielding and explains why simple point-source analytics tend to overpredict external exposure if self-absorption is ignored.

- The framework was extended to ^{177}Lu, demonstrating readiness to support future shielding assessments for therapy-related imaging. Once realistic national workload and activity data are specified via a focused literature/clinical review, the existing results can be scaled to verify regulatory compliance for ^{177}Lu practice. In other words, the underlying MC data are in place — only the application of appropriate scaling factors remains.

- As a practical output, the study not only established a validated, documented MC shielding workflow, including, model development, normalisation, validation metrics, and reporting, but also fulfilled the first objective of gaining proficiency in FLUKA. This workflow now serves as a tool that can be reused and adapted locally.

6.3 | Recommendations for professional practice

The following are recommendations for professional medical physics and radiation protection practice:

- The validated FLUKA MC workflow should be embedded in the early stages of facility planning and equipment installation. Using high-fidelity simulations during the design phase such as this one allows optimisation of shielding layouts, such as minimisation of material costs and maximisation of available space, all while still ensuring compliance with occupational and public dose limits.
- One of the main findings was that a significant fraction of the emitted radiation is self-absorbed within the patient. Incorporating this attenuation into conventional analytical shielding assessments, even if obtained with much simpler simulations that take much less time to model and run, can reduce overly conservative estimates and allow for more cost-effective shielding designs.
- As radionuclides like ^{177}Lu or ^{225}Ac gain wider clinical use, the validated model can be adapted by scaling dose outputs according to radionuclide characteristics and local workload data. It can also support scenario testing, such as workload changes, changes in imaging protocols or alterations in room configuration, provided that any substantial modifications are followed by a re-validation step to maintain credibility.
- The study developed a practical workflow that can serve as a foundation for structured training programmes for medical physicists and radiation protection professionals and trainees that would gradually foster the development of in-house expertise in the MC technique. This expertise can also be leveraged to explore other applications, even those beyond radiation protection or fully-detailed facility models.

- Detailed simulation data provide a strong foundation for transparent reports to regulatory bodies, such as the RPC. Moreover, aligning the results with international standards such as ICRP recommendations and IAEA Safety Reports will strengthen confidence in compliance evaluations. Beyond regulatory approval, simulation-informed data can function as a quality assurance tool that support verification of shielding effectiveness.
- International guidelines provide general recommendations for shielding, but simulation data allow the development of local protocols tailored to national clinical practices, such as accounting for specific facility layouts and scanner types.

6.4 | Recommendations for future research

Suggestions for future research are:

- The current work relied solely on FLUKA. Validating the model against another well-established code such as GEANT4 or MCNP would strengthen confidence in the results and highlight any code-specific biases or methodological limitations. Such cross-code benchmarking is considered best practice, particularly for shielding assessments that inform regulatory compliance and facility planning. This exercise would also build transferable skills across platforms.
- Applying the same methodology to other parts of the NM facility, for example, the two upcoming PET/CT suites or the new cyclotron installation, would provide valuable insight into areas where higher energy photons and secondary neutrons interact differently with shielding materials. For instance, cyclotron fields are highly like to induce material activation, which must be managed under distinct radiation-protection procedures (Infantino et al., 2016).
- A major refinement would be to explicitly model and simulate the CT X-ray source. This would require replicating its polyenergetic X-ray spectrum, incorporating the heel effect, bow-tie filter profiles, and beam collimation geometry, as well as simulating realistic scanning parameters such as rotation speed and tube current modulation. The inclusion of these elements would allow for more accurate estimation of combined SPECT/CT exposures.

- The current model represents a static geometry. Extending the framework to incorporate patient couch motion (e.g., through snapshots at key positions during a scan) and rotating detector heads or CT tubes would better replicate actual clinical conditions.
- While this study focused on a single, typical ^{99m}Tc protocol, future work should simulate all major clinical protocols, varying parameters such as administered activity, scan duration, detector positioning, and collimator types. These would be informed by retrospective data from past patient imaging procedures to provide realistic parameters for the simulations. This approach would provide the most representative estimates, however, at the cost of computational resources, as each model variation would have to be simulated separately.

6.5 | Conclusion

This work developed and validated an MC model of Malta's SPECT/CT facility that demonstrated strong agreement with experimental data and built confidence in its use for dose assessment and shielding optimisation. It also confirmed that existing shielding is compliant with occupational and public dose limits.

All objectives of the study were successfully achieved: proficiency in FLUKA was developed; a realistic and comprehensive facility model was built; simulation results were benchmarked against experimental and analytical methods; annual dose estimates were derived using clinically representative workloads; and the framework was extended to support preliminary evaluations for ^{177}Lu imaging.

Although no simulation can perfectly mirror a physical system, this study demonstrates that, once validated, such models deliver actionable insights that can potentially form a robust foundation for workflow transfer to future shielding studies, as well as for training, scenario testing, and broader applications across the field. This work represents a significant step toward embedding the MC method in routine medical physics and radiation protection practice in Malta.

References

Abdallah, I. I. (2007). *Shielding design for positron emission tomography facility*. Master dissertation, University of Limpopo, Pretoria (South Africa). INIS.

Ademoh, B. A. (2008). *Assessment of characteristics of thermoluminescence dosimetry (TLD) system used in Centre for Energy Research and Training, (CERT), Ahmadu Bello university, Zaria*. Master dissertation, Ahmadu Bello University, Zaria, Nigeria.

Ahdida, C., Bozzato, D., Calzolari, D., Cerutti, F., Charitonidis, N., Cimmino, A., Coronetti, A., D'alessandro, G., Donadon Servelle, A., Esposito, L., et al. (2022). New capabilities of the fluka multi-purpose code. *Frontiers in Physics*, 9:788253.

Allen, M. P. and Tildesley, D. J. (2017). *Computer simulation of liquids*. Oxford university press.

Atanassov, E., Gurov, T., Karaivanova, A., Ivanovska, S., Durchova, M., and Dimitrov, D. (2016). On the parallelization approaches for intel mic architecture. In *AIP Conference Proceedings*, volume 1773, page 070001. AIP Publishing LLC.

Behling, R. (2021). *Modern diagnostic x-ray sources: technology, manufacturing, reliability*. CRC Press.

Belinato, W., Santos, W., Paschoal, C., and Souza, D. (2015). Monte Carlo simulations in multi-detector CT (MDCT) for two PET/CT scanner models using MASH and FASH adult phantoms. *Nuclear Instruments and Methods in Physics Research Section A: Accelerators, Spectrometers, Detectors and Associated Equipment*, 784:524–530.

Bezzina, P. (2015). *Monte Carlo evaluation of small field dosimetry for low KV beams*. Master dissertation, University of Malta, Malta. OAR@UM.

Bilski, P. (2002). Lithium fluoride: from LiF: Mg, Ti to LiF: Mg, Cu, P. *Radiation protection dosimetry*, 100(1-4):199–205.

Bjerke, H., Sigurdsson, T., Meier Pedersen, K., Grindborg, J.-E., Persson, L., Siiskonen, T., Hakanen, A., and Kosunen, A. (2012). Radiation survey meters used for environmental monitoring.

Borlandelli, C. M. and Mahltig, B. (2022). Leather types and fiber-based leather alternatives-an overview on selected materials, properties, microscopy, electron dispersive spectroscopy eds and infrared spectroscopy. *Annals of Textile Engineering and Fashion Technology*, 1(1):1001.

Bouchareb, Y., AlSaadi, A., Zabah, J., Jain, A., Al-Jabri, A., Phiri, P., Shi, J. Q., Delanerolle, G., and Sirasanagandla, S. R. (2024). Technological advances in SPECT and SPECT/CT imaging. *Diagnostics*, 14(13):1431.

Brígido Flores, O., Hernández García, J., Fabelo Bonet, O., Montalván Estrada, A., Aparicio, Y., and Mantecón, R. (2019). Design shielding assessment for a nuclear medicine service. *Nucleus*, (65).

Business Insider (2025). Lead price - YCharts & market data. https://markets.businessinsider.com/commodities/lead-price.

Capintec (2023). *CRC®-55tR dose calibrator*. Capintec. [Data Sheet]. https://assets-mirion.mirion.com/prod-20220822/cms4_mirion/files/pdf/spec-sheets/spc-400-c-crc-55tr-dose-calibrator-data-sheet.pdf.

Carlsson, S. and Le Heron, J. (2014). Radiation protection. In Bailey, D. L., Humm, J., Todd-Pokropek, A., and van Aswegen, A., editors, *Nuclear medicine physics: A handbook for teachers and students*, pages 73–116. International Atomic Energy Agency, Vienna.

Cherry, S. R., Sorenson, J. A., and Phelps, M. E. (2013). *Physics in nuclear medicine*. Saunders.

Commission for the Protection from Ionising and Non-Ionising Radiation (2022). Guidance on the use of diagnostic reference levels for medical exposures. Revised 26 January 2022.

Crișan, G., Moldovean-Cioroianu, N. S., Timaru, D.-G., Andrieș, G., Căinap, C., and Chiș, V. (2022). Radiopharmaceuticals for pet and spect imaging: a literature review over the last decade. *International journal of molecular sciences*, 23(9):5023.

da Rosa, L. (1989). The influence of temperature and humidity on the stability of the response of different thermoluminescent detectors. *International Journal of Radiation Applications and Instrumentation. Part A. Applied Radiation and Isotopes*, 40(2):139–145.

DataSpectrum (n.d.). Flanged jaszczak ECT phantoms: Specifications and applications. Technical brochure [PDF]. https://www.spect.com/pdf/Flanged-Jaszczak-Phantoms.pdf.

Delacroix, D., P. Guerre, J., Leblanc, P., and Hickman, C. (2002). Radionuclide and radiation protection data handbook 2002. *Radiation protection dosimetry*, 98(1):1–168.

Detwiler, R. S., McConn, R. J., Grimes, T. F., Upton, S. A., and Engel, E. J. (2021). Compendium of material composition data for radiation transport modeling. Technical report, Pacific Northwest National Lab.(PNNL), Richland, WA (United States).

Deutsches Institut für Normung (2003). *DIN 6871-1. Cyclotron systems for positron emission tomography part 1: Requirements for constructional radiation protection*. DIN, Berlin, Germany.

Donadon, A., Hugo, G., Theis, C., and Vlachoudis, V. (2024). Flair3–recasting simulation experiences with the advanced interface for fluka and other monte carlo codes. In *EPJ Web of Conferences*, volume 302, page 11005. EDP Sciences.

El-Sadieque, A. (2022). *Final report on the interest programme: Study of some aspects of radiation shielding in a preclinical SPECT/CT scanner prototype using based on Monte Carlo code systems*.

Elschot, M., De Wit, T., and De Jong, H. (2010). The influence of self-absorption on pet and pet/ct shielding requirements. *Medical physics*, 37(6Part1):2999–3007.

ELSE Solutions (n.d.). *Flanged Jaszczak*. Retrieved from https://www.elsesolutions.com/en/prodotti/nuclear-medicine/quality-control/phantoms/deluxe-jaszczak/.

European Organisation for Nuclear Research (2020). *FLUKA Manual*. [User Manual]. Version: 4-5.0. https://flukafiles.web.cern.ch/manual/.

European Organisation for Nuclear Research (2024). Introduction to the Monte Carlo simulation of radiation transport. [PowerPoint presentation]. Indico. https://indico.cern.ch/event/1444491/contributions/6234937/attachments/2977549/5241984/02_Monte_Carlo_Basics_2024_CERN.pdf.

European Union (2014). Council Directive 2013/59/Euratom of 5 December 2013 laying down basic safety standards for protection against the dangers arising from exposure to ionising radiation, and repealing Directives 89/618/Euratom, 90/641/Euratom, 96/29/Euratom, 97/43/Euratom and 2003/122/Euratom. *Official Journal of the European Union*, L(13):1–73.

Garcia, M.-P., Villoing, D., McKay, E., Ferrer, L., Cremonesi, M., Botta, F., Ferrari, M., and Bardiès, M. (2015). Testdose: A nuclear medicine software based on monte carlo modeling for generating gamma camera acquisitions and dosimetry. *Medical Physics*, 42(12):6885–6894.

General Electric (2018). NM800 & NM600 series system description and safety manual for operators. [Instruction Manual].

General Electric (2020). NM/CT 870 CZT — A digital SPECT/CT. [Data sheet]. https://promed-sa.com/wp-content/uploads/2020/08/DOC2109131-NMCT-870-CZT-PDS.pdf.

General Electric (2023). OptimaTM CT540 technical reference manual. 5842611-1EN. https://www.scribd.com/document/748875727/Optima-CT540-Technical-Reference-Manual-UM-5842611-1EN-4.

General Electric (2024). NM/CT 870 final study. [Technical document].

General Electric (2025). NM/CT870 & DiscoveryNM/CT670 nclear medicine imaging system installation manual. 5661545-1EN Rev. 13. [Technical manual]. https://www.gehealthcare.com/support/manuals.

Ghanad, A. (2023). An overview of quantitative research methods. *International journal of multidisciplinary research and analysis*, 6(08):3794–3803.

Grate, J. W., O'Hara, M. J., and Egorov, O. B. (2020). Automated radiochemical separation, analysis, and sensing. In *Handbook of Radioactivity Analysis: Volume 2*, pages 821–872. Elsevier.

Grima, S. (2024). *Setup and operation of a thermoluminescent dosimetry system for patient organ dosimetry*. Bachelor dissertation, University of Malta, Malta. OAR@UM.

Grinstead, C. M. and Snell, J. L. (2006). *Grinstead and Snell's introduction to probability*. Chance Project.

Grove Software (2024). *MicroShield Pro User's Manual*. Grove Software, Colorado Springs, CO, USA. Version 13.

Hacking, C. (2024). Half-life time. https://radiopaedia.org/articles/half-life-time-1.

Hamatsu (1998). Photomultiplier tubes R1307, R1307-01. Technical specifications [PDF]. https://www.hamamatsu.com/content/dam/hamamatsu-photonics/sites/documents/99_SALES_LIBRARY/etd/R1307_TPMH1214E.pdf.

Holm, S. (2022). Radiation protection. In Terwinghe, C., Santos, A., and Pietrzak, A., editors, *Radionuclide therapy management*. European Association of Nuclear Medicine.

Hubbell, J. and Seltzer, S. (2004). Tables of X-ray mass attenuation coefficients and mass energy-absorption coefficients (version 1.4). National Institute of Standards and Technology, Gaithersburg, MD. [Online]. http://physics.nist.gov/xaamdi.

Ibitoye, Z., Adedokun, M., Orotoye, T., and Udo, G. (2022). Design and evaluation of structural shielding of a typical radiotherapy facility using egsnrc monte carlo code. *Journal of Medical Physics*, 47(1):27.

Infantino, A. (2015). *Advanced aspects of radiation protection in the use of particle accelerators in the medical field*. Doctoral dissertation, Alma Mater Studiorum University of Bologna, Italy. AlmaDL.

Infantino, A., Cicoria, G., Lucconi, G., Pancaldi, D., Vichi, S., Zagni, F., Mostacci, D., and Marengo, M. (2016). Radiation protection studies for medical particle accelerators using FLUKA Monte Carlo code. *Radiation protection dosimetry*, 173.

International Atomic Energy Agency (2008). *Radiation protection in newer medical imaging techniques-PET/CT*. International Atomic Energy Agency.

International Atomic Energy Agency (2014). Radiation protection and safety of radiation sources: International basic safety standards. *General Safety Requirements*. GSR Part 3.

International Atomic Energy Agency (2018a). Occupational radiation protection. *General Safety Guide*. GSG-7.

International Atomic Energy Agency (2018b). Radiation protection and safety in medical uses of ionizing radiation. *Specific Safety Guide SSG-46, IAEA, Vienna*.

International Atomic Energy Agency (2018c). Radiation protection of the public and the environment. *General Safety Guide*. GSG-8.

International Commission on Radiation Units and Measurements (1993). Quantities and units in radiation protection dosimetry. Technical Report Report 51, ICRU, Bethesda, MD.

International Commission on Radiological Protection (2007a). The 2007 recommendations of the International Commission on Radiological Protection. ICRP publication 103. *Annals of the ICRP*, 37(2-4):1–332.

International Commission on Radiological Protection (2007b). Radiological protection in medicine. *Annals of the ICRP*, 37(6):1–63. ICRP Publication 105.

Kawrakow, I., Rogers, D., Mainegra-Hing, E., Tessier, F., Townson, R., and Walters, B. (2000). Egsnrc: software for monte carlo simulation of ionizing radiation. *National Research Council of Canada*.

Kim, J. H. (2018). Three principles for radiation safety: time, distance, and shielding. *The Korean journal of pain*, 31(3):145.

Kiran, K., Ravindraswami, K., Eshwarappa, K., and Somashekarappa, H. (2015). Effective atomic number of selected construction materials using gamma backscattering technique. *Annals of Nuclear Energy*, 85:1077–1084.

Kry, S. F., Alvarez, P., Cygler, J. E., DeWerd, L. A., Howell, R. M., Meeks, S., O'Daniel, J., Reft, C., Sawakuchi, G., Yukihara, E. G., et al. (2020). AAPM TG 191: Clinical use of luminescent dosimeters: TLDs and OSLDs. *Medical physics*, 47(2):e19–e51.

Ladrière, T., Faudemer, J., Levigoureux, E., Peyronnet, D., Desmonts, C., and Vigne, J. (2023). Safety and therapeutic optimization of lutetium-177 based radiopharmaceuticals. *Pharmaceutics*, 15(4):1240.

Le, Y., Weng, J.-H., Lee, T.-M., Lee, Y.-C., Kao, P.-F., Pan, L.-K., and Chen, C.-Y. (2020). Tld environmental monitoring of new scanner facilities at the nuclear medicine department of the taiwan medical university hospital. *Technology and Health Care*, 28(1_suppl):151–160.

Liu, X., Liu, H., Cheng, L., Wu, J., Bao, T., Yao, R., and Liu, Y. (2021). A 3-dimensional stationary cascade gamma-ray coincidence imager. *Physics in Medicine Biology*, 66:225001.

Ljungberg, M. (2021). *Handbook of Nuclear Medicine and Molecular Imaging for Physicists: Modelling, Dosimetry and Radiation Protection, Volume II*. CRC Press.

Ljungberg, M., Strand, S., and King, M. (1998). The simind monte carlo program. *Monte Carlo calculation in nuclear medicine: Applications in diagnostic imaging*, pages 145–163.

Madero Ramirez, D. A., Orejuela, D. M., and Plazas De Pinzon, M. C. (2017). Shielding calculation for nuclear medicine services. *TECCIENCIA*, 12(23):7–16.

Madsen, M. T., Anderson, J. A., Halama, J. R., Kleck, J., Simpkin, D. J., Votaw, J. R., Wendt III, R. E., Williams, L. E., and Yester, M. V. (2006). Aapm task group 108: Pet and pet/ct shielding requirements. *Medical physics*, 33(1):4–15.

MaltaToday (n.d.). Bills of quantities. https://content.maltatoday.com.mt/ui/files/2.%20Bills%20of%20Quantities.pdf.

Marengo, M. and Infantino, A. (2022). Assessment of emission data and transmission factors supporting radiation protection in the use of 225ac. *Physica Medica*, 103:59–65.

Marshall, S. K., Hayeeabdunromae, A., Noomad, N., Durawee, W., Sirieak, N., Karnkorn, P., and Keawtong, V. (2024). Evaluation of environmental radiation exposure and algorithms for determining the occupational effective dose during 99mtc-mdp bone scintigraphy: A comprehensive analysis. *Applied Sciences*, 14(23):11211.

Metropolis, N. and Ulam, S. (1949). The monte carlo method. *Journal of the American statistical association*, 44(247):335–341.

Mott, J. and Daniel, J. (2021a). Interactions of electromagnetic radiation and subatomic particles with matter–part 2. *Clinical Oncology*, 33(7):455–460.

Mott, J. and Daniel, J. (2021b). Interactions of electromagnetic radiation and subatomic particles with matter-part 1.

National Council on Radiation Protection and Measurements (2004). *NCRP Report No. 144. Structural Shielding Design for Medical X-Ray Imaging Facilities*. NCRP, Bethesda, USA.

National Council on Radiation Protection and Measurements (2005). *NCRP Report No. 144. Radiation Protection for Particle Accelerator Facilities*. NCRP, Bethesda, USA.

National Electrical Manufacturers Association (2023). Nema nu 1-2023: Performance measurements of gamma cameras. Technical report, National Electrical Manufacturers Association. Virgina, USA.

Oliveira, A. D. and Oliveira, C. (2005). Comparison of deterministic and monte carlo methods in shielding design. *Radiation protection dosimetry*, 115(1-4):254–257.

Oumano, M., Wendt, R., Botti, J., Busse, N., Hintenlang, D., Leon, S., Little, K., Martin, M., Massoth, R., Matthews, K., et al. (2025). Shielding resources for four common radiopharmaceuticals utilized for imaging and therapy: Tc-99m, F-18, I-131, and Lu-177. *Journal of applied clinical medical physics*, 26(5):e70084.

Parliament of Malta (2018). Basic safety standards for ionising radiation regulations. *Gazzetta tal-Gvern ta' Malta Nru. 20,020*, (585.1):2029–2154.

Parodi, K., Ferrari, A., Sommerer, F., and Paganetti, H. (2007). Clinical CT-based calculations of dose and positron emitter distributions in proton therapy using the FLUKA Monte Carlo code. *Physics in Medicine & Biology*, 52(12):3369.

Pelliccioni, M. (2000). Overview of fluence-to-effective dose and fluence-to-ambient dose equivalent conversion coefficients for high energy radiation calculated using the fluka code. *Radiation Protection Dosimetry*, 88(4):279–297.

Pells, S., Cullen, D. M., Deidda, D., Denis-Bacelar, A. M., Fenwick, A., Ferreira, K. M., Hamilton, D., Heetun, W., Julyan, P., Needham, G., et al. (2023). Quantitative validation of monte carlo spect simulation: application to a mediso anyscan gate simulation. *EJNMMI physics*, 10(1):60.

Peterson, T. E. and Furenlid, L. R. (2011). Spect detectors: the anger camera and beyond. *Physics in Medicine & Biology*, 56(17):R145.

Pious, C. and Thomas, S. (2016). 2 - polymeric materials—structure, properties, and applications. In Izdebska, J. and Thomas, S., editors, *Printing on Polymers*, pages 21–39. William Andrew Publishing.

Podgorsak, E., Kesner, A., and Soni, P. (2014). Basic physics for nuclear medicine. In *Nuclear Medicine Physics: A Handbook for Teachers and Students*. IAEA.

Pommranz, C. M., Elmoujarkach, E. A., Lan, W., Cabello, J., Linder, P. M., Vo, H. P., Mannheim, J. G., Santangelo, A., Conti, M., la Fougère, C., et al. (2025). A digital twin of the biograph vision quadra long axial field of view pet/ct: Monte carlo simulation and image reconstruction framework. *EJNMMI physics*, 12(1):31.

Pretorius, P. H., Liu, C., Fan, P., Peterson, M., and Ljungberg, M. (2015). Monte carlo simulations of the ge discovery alcyone czt spect systems. *IEEE Transactions on Nuclear Science*, 62(3):832–839.

Radcard (2013). *Specification for thermoluminescent detectors MCP type*. [Specifications Document]. Radcard, Kraków, Poland.

Rault, E., Staelens, S., Van Holen, R., De Beenhouwer, J., and Vandenberghe, S. (2010). Accurate monte carlo modelling of the back compartments of spect cameras. *Physics in Medicine & Biology*, 56(1):87.

Rising, M. E., Armstrong, J. C., Bolding, S. R., Bull, J. S., Casswell, L., Clark, A. R., Forster, R. A., Frederick, C. S., Giron, J. F., Jones, F. B., et al. (2025). The mcnp® 6 code: A decade of progress. *EPJ Nuclear Sciences and Technologies*, 11(LA-UR-24-28294).

Rizk, T. and Nagalli, S. (2025). Technetium 99m sestamibi. In *StatPearls [Internet]*. StatPearls Publishing, Treasure Island (FL). `https://www.ncbi.nlm.nih.gov/books/NBK553148/`.

Romanets, Y., Bernardes, A., Dorsival, A., Goncalves, I., Kadi, Y., Di Maria, S., Vaz, P., Vlachoudis, V., and Vollaire, J. (2013). Radiation protection, radiation safety and radiation shielding assessment of hie-isolde. *Radiation protection dosimetry*, 155(3):351–363.

Rosato, D. V., Rosato, D. V., and v Rosato, M. (2004). *Plastic product material and process selection handbook*. Elsevier.

Sadek, A., Khamis, F., Polymeris, G. S., Carinou, E., and Kitis, G. (2017). Similarities and differences between two different types of the thermoluminescence dosimeters belonging to the lif family. *physica status solidi c*, 14(1-2):1600220.

Saha, G. B. (2013). *Gamma Cameras*, pages 117–126. Springer New York, New York, NY.

Salehzahi, F. and Tse, J. (2020). Shielding commissioning factors in nuclear medicine facilities. *Journal of Radiological Protection*, 40(1):165.

Sarrut, D. (2025). Monte Carlo simulations: The virtual sandbox for medical physics. https://bioemtech.com/science-letter/monte-carlo-simulations-the-virtual-sandbox-for-medical-physics/.

Sekaran, U. and Bougie, R. (2016). *Research methods for business: A skill building approach*. John Wiley & Sons.

Shibutani, T., Onoguchi, M., Naoi, Y., Yoneyama, H., Konishi, T., Tatami, R., and Nakajima, K. (2021). The usefulness of swiftscan technology for bone scintigraphy using a novel anthropomorphic phantom. *Scientific Reports*, 11(1):2644.

Soliman, A. M. (2024). Monte Carlo simulation of radiation-matter interaction for shielding evaluation in medical imaging applications. Technical report, Joint Institute for Nuclear Research, Laboratory of Nuclear Problems, Dubna, Russia. Final report on the INTEREST Programme, Wave 11. Supervisor: Antonio Leyva Fabelo.

Somasundaram, E., Artz, N. S., and Brady, S. L. (2019). Development and validation of an open source monte carlo dosimetry model for wide-beam ct scanners using fluka. *Journal of Applied Clinical Medical Physics*, 20(4):132–147.

Soo, G., Cain, T., and Chang, C. A. (2019). Spect-ct scan. https://www.insideradiology.com.au/spect-ct-scan/.

SpecialChem (2025). Density of plastics. https://www.specialchem.com/plastics/guide/density.

Strulab, D., Santin, G., Lazaro, D., Breton, V., and Morel, C. (2003). Gate (geant4 application for tomographic emission): a pet/spect general-purpose simulation platform. *Nuclear Physics B-Proceedings Supplements*, 125:75–79.

Sutton, D., Martin, C., Williams, J., and Peet, D. (2012). *Radiation shielding for diagnostic radiology, 2nd Edition*.

Tajudin, S. M. (2020). Basic quantities for photon shielding calculations. In Mann, K. S. and Singh, V. P., editors, *Computational methods in nuclear radiation shielding and dosimetry*, Physics research and technology, pages 65–86. Nova Science Publishers.

Tassé, A. E. L. (2025). Monte Carlo simulation of radiation-matter interaction for shielding evaluation in a preclinical SPECT/CT scanner. Technical report, Joint Institute for Nuclear Research, Laboratory of Nuclear Problems, Dubna, Russia. Final report on the INTEREST Programme, Wave 12. Supervisor: Antonio Leyva Fabelo.

Texonic (n.d.). Fiber properties your guide to structural fibres fiber selection, a key component in our reinforcements. https://texonic.net/en/tableau/technical/.

Thermo Scientific (2018). *Smart Ion Survey Meter (including Mini-ION): Dose, Dose-rate & Bar-code Versions, Instruction Manual*, issue 7 edition. Models: MINI 2100 S, R & G; MINI 2120 S, R & G; MINI 2130 S, R & G; MINI 2140 S, R & G. Document No. 53459.

Toray CFE (n.d.). What is carbon fiber? https://toray-cfe.com/en/what-is-carbon-fiber/.

Vassiliev, O. N. (2017). *Monte Carlo methods for radiation transport*. Biological and Medical Physics, Biomedical Engineering. Springer International Publishing, Cham.

Widorski, M., Bozzato, D., Froeschl, R., and Kouskoura, V. (2023). Flukaval–a validation framework for the fluka radiation transport monte carlo code. In *EPJ Web of Conferences*, volume 284, page 16006. EDP Sciences.

Wong, K. K., Hu, E., Akhavanallaf, A., Dewaraja, Y. K., and Roseland, M. E. (2025). Lutetium-177 theranostics and dosimetry for neuroendocrine neoplasms and prostate cancer. In *Seminars in Roentgenology*. Elsevier.

Xu, S., Yan, Z., and Wei, Q. (2024). A survey of crystals for spect imaging. *Crystals*, 14(12):1039.

Yin, W.-W., Zheng, X.-W., Wang, Z.-Q., Chen, W.-J., Tyan, Y.-S., and Chen, T.-R. (2021). Ambient and personnel occupational dose assessment in a hospital's pet/ct center. *Applied Radiation and Isotopes*, 169:109466.

Zanzonico, P., Dauer, L., and Germain, J. S. (2008). Operational radiation safety for pet-ct, spect-ct, and cyclotron facilities. *Health physics*, 95(5):554–570.

A

Ethics Approval

To get approval from the University Research Ethics Committee at the University of Malta, permission was needed first from the Chair of the Medical Imaging Department, the MDH data protection officer, and the CEO of MDH. Since the Committee's approval below demonstrates that these permissions were obtained, they are not included here.

Samuel Grima <samuel.grima.20@um.edu.mt>

The status of your REDP form (FHS-2025-00006) has been updated to Acknowledged

1 message

form.urec@um.edu.mt <form.urec@um.edu.mt> 7 January 2025 at 10:45
To: samuel.grima.20@um.edu.mt

Dear Samuel Grima,

Please note that the status of your REDP form (FHS-2025-00006) has been set to *Acknowledged*.

You can keep track of your applications by visiting: https://www.um.edu.mt/research/ethics/redp-form/frontEnd/.

This email has been automatically generated by URECA. Please do not reply. If you wish to communicate with your F/REC please use the respective email address.

B

Calibration of TLDs in $H^*(10)$

B.1 | Aim & Objective

The aim of this procedure was to calibrate a set of 33 LiF:Mg,Cu,P TLD crystals in terms of the ambient dose equivalent $H^*(10)$, by reference to a pre-calibrated survey meter operating in the same quantity, for ^{99m}Tc exposures. Calibration was performed by placing the TLDs at set distances from a ^{99m}Tc-injected Jaszczak phantom under controlled conditions.

B.2 | Methodology

B.2.1 | Setup

The setup reproduced the wall conditions of the pilot study. This was achieved by mounting the TLD pouches on a wall constructed with the same layers and thicknesses as used in the actual study settings (Figure B.1). The water and ^{99m}Tc-filled Jaszczak phantom can be seen placed at one end of a wooden table, with its front surface located exactly 100 cm from the wall facing it. On the wall, the survey meter was mounted centrally, with the TLDs pouches placed immediately adjacent to it.

Due to the survey meter's size, its chamber centre did not coincide with the wall plane. In addition, the TLDs could not be placed directly behind it without attenuation. The approaches adopted to address these two issues are detailed in the following section.

B.2.2 | Distance correction factor

Because the survey meter chamber centre was recessed from the wall, a correction factor was required to match the phantom-to-meter and phantom-to-TLD distances of 100 cm. Dose rates were therefore measured at the study position (Figure B.1a) and at the true 100 cm position. The latter was obtained by shifting the table until the chamber centre aligned with the wall edge. Each measurement was repeated three times. These results are presented in Table B.1.

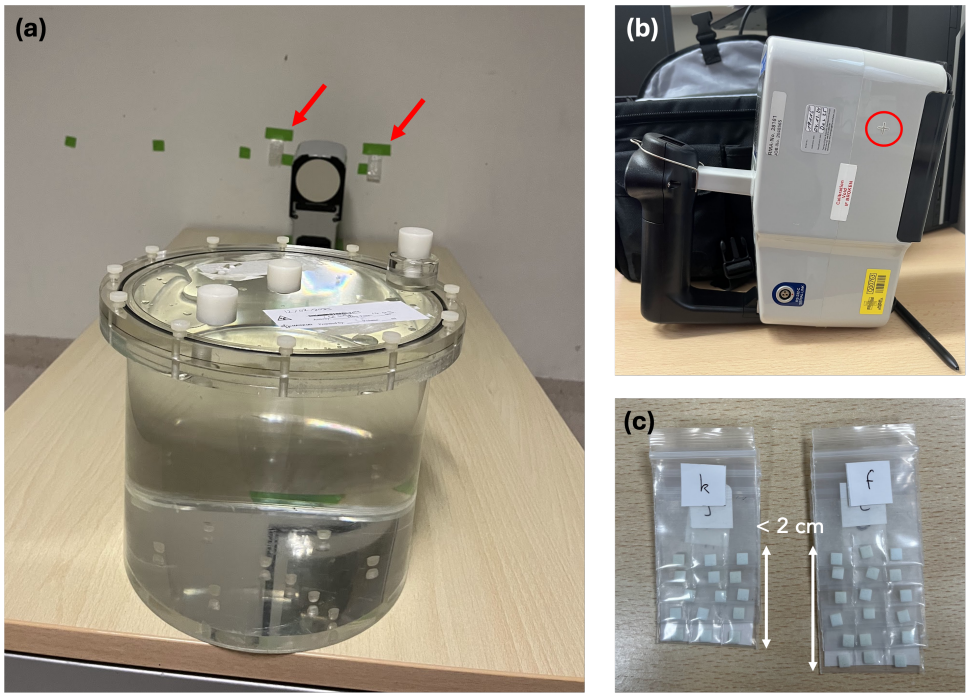

Figure B.1: Experimental setup of the calibration procedure. (a) Phantom placed on a table aligned with the survey meter and TLD pouches (marked with red arrows). (b) Side view of the detector showing the central point of the chamber (the cross in the red circle). (c) Close-up of the TLD pouches, each marked with a mapping letter and containing three TLDs.

Position setting	$\dot{H}_1$ μSv s^{-1}	$\dot{H}_2$ μSv s^{-1}	$\dot{H}_3$ μSv s^{-1}	$\overline{\dot{H}}$ μSv s^{-1}
Study position	16.7	16.5	16.5	16.6 ± 0.1
Corrected position	11.9	11.9	11.9	11.9 ± 0.0

Table B.1: Ambient dose equivalent rates $\dot{H}_i$ (for $i = 1, 2, 3$) measured with the survey meter for distance correction at the study position (the location used in the pilot and main studies) and the corrected position (the meter's centre at 100 cm away from the phantom). $\overline{\dot{H}}$ are reported as mean ± 1σ (standard deviation) from repeated measurements.

The resulting correction factor was,

$$k_d = \frac{\overline{\dot{H}}_{\text{corr}}}{\overline{\dot{H}}_{\text{study}}} = \frac{11.9}{16.6} = 0.7183. \tag{B.1}$$

B.2.3 | Positioning of TLD pouches

To avoid attenuation by the survey meter, the pouches were placed just outside its projected shadow on the wall (Figure B.2). The required lateral offset X was obtained geometrically. From Figure B.2, two

similar triangles are formed with equal vertical angles θ. From the larger triangle, θ was obtained using the tangent ratio,

$$\tan\theta = \frac{\text{opposite}}{\text{adjacent}} \quad \Rightarrow \quad \theta = \tan^{-1}\left(\frac{\frac{B+C}{2}}{D-A}\right) = \tan^{-1}\left(\frac{\frac{10.5+22.24}{2}}{111.12-23.5}\right) = 10.58^\circ. \tag{B.2}$$

For the smaller triangle, X was then calculated as:

$$X = A \cdot \tan\theta = 23.5 \cdot \tan(10.58) = 4.39 \text{ cm}. \tag{B.3}$$

A clearance of 5 cm was adopted to account for pouch size. This small lateral offset was negligible compared to the 100 cm source-to-detector distance. Vertically, the pouches spanned less than 2 cm (Figure B.1c), which was likewise negligible relative to the 100 cm separation.

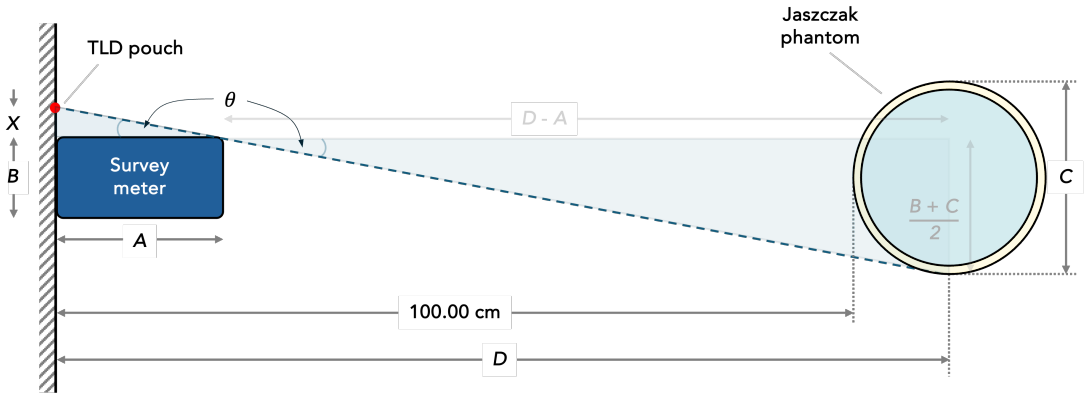

Figure B.2: Schematic diagram of the calibration setup. Drawing is not to scale. $A = 23.50$ cm; $B = 10.50$ cm; $C = 22.24$ cm; $D = 111.12$ cm; $X =$ unknown variable; $\theta = \theta(A, B, C, D)$.

B.2.4 | Calibration process

Calibration involved three standard stages: (i) subtraction of background/reader noise (*zero counts*), (ii) conversion from counts to dose (*device sensitivity*), and (iii) correction for inter-crystal variation (*crystal sensitivity*). The annealing and readout parameters are summarised in Table B.2 and were consistently applied throughout the pilot and main studies. These were sourced from Grima (2024).

After pre-irradiation annealing, crystals were read out to establish zero counts, re-annealed, and sorted into labelled pouches. Meanwhile, the phantom was prepared by filling it with water and injecting it with approximately 1 GBq of ^{99m}Tc activity. The TLD pouches were then mounted on the wall and an overnight exposure was performed with the survey meter in integrating mode. The next day, the integrated meter dose was recorded and the crystals were post-irradiation annealed and then read out to obtain study counts.

Table B.2: Annealing and readout parameters used for the LiF:Mg,Cu,P TLDs in the calibration, pilot, and main study exposures.

Stage	**Temperature** °C	**Duration** s	**Heating rate** °C s^{-1}
Annealing			
Pre-irradiation	240	600	–
Post-irradiation	100	600	–
Readout	25–240	10	10

To determine the final, corrected ambient dose equivalent for each TLD crystal, the following expression was used (Kry et al., 2020):

$$\begin{aligned} H_{\text{corr},i} &= \left(M^{\text{study}}_{\text{raw},i} - M^{\text{cal}}_{\text{bg},i}\right) \cdot \frac{\overline{M}^{\text{cal}}_{\text{net}}}{M^{\text{cal}}_{\text{net},i}} \cdot \frac{H^{\text{cal}}_{\text{SM}}}{\overline{M}^{\text{cal}}_{\text{net}}} \cdot k_d \cdot k_E \\ &= M^{\text{study}}_{\text{net},i} \cdot k_{\text{ECC},i} \cdot k_c \cdot k_d \cdot k_E, \end{aligned} \tag{B.4}$$

where

- $H_{\text{corr},i}$: corrected ambient dose equivalent for the i^{th} TLD,
- $M^{\text{study}}_{\text{raw},i}$: raw *study* counts for the i^{th} TLD,
- $M^{\text{cal}}_{\text{bg},i}$: background *calibration* counts for the i^{th} TLD,
- $M^{\text{study}}_{\text{net},i} \equiv M^{\text{study}}_{\text{raw},i} - M^{\text{cal}}_{\text{bg},i}$: net *study* counts for the i^{th} TLD,
- $M^{\text{cal}}_{\text{net},i} \equiv M^{\text{cal}}_{\text{raw},i} - M^{\text{cal}}_{\text{bg},i}$: net *calibration* counts for the i^{th} TLD,
  - where $M^{\text{cal}}_{\text{raw},i}$: raw *calibration* counts for the i^{th} TLD,
- $\overline{M}^{\text{cal}}_{\text{net}} \equiv \frac{1}{33}\sum_{i=1}^{33} M^{\text{cal}}_{\text{net},i}$: batch mean net *calibration* counts,
- $H^{\text{cal}}_{\text{SM}}$: survey-meter ambient dose equivalent in the *calibration* exposure,
- $k_{\text{ECC},i} \equiv \dfrac{\overline{M}^{\text{cal}}_{\text{net}}}{M^{\text{cal}}_{\text{net},i}}$: element correction coefficient (inter-crystal normalisation, dimensionless),
- $k_c \equiv \dfrac{H^{\text{cal}}_{\text{SM}}}{\overline{M}^{\text{cal}}_{\text{net}}}$: calibration factor (dose [µSv] per count),
- k_d: distance correction factor (dimensionless),
- k_E: energy correction factor (dimensionless).

An energy correction was applied to account for the survey meter's energy dependence. From the manufacturer's response curve (Figure B.3), the relative response at 140 keV was 0.8601, giving,

$$k_E = \frac{1}{0.8601} = 1.1627. \tag{B.5}$$

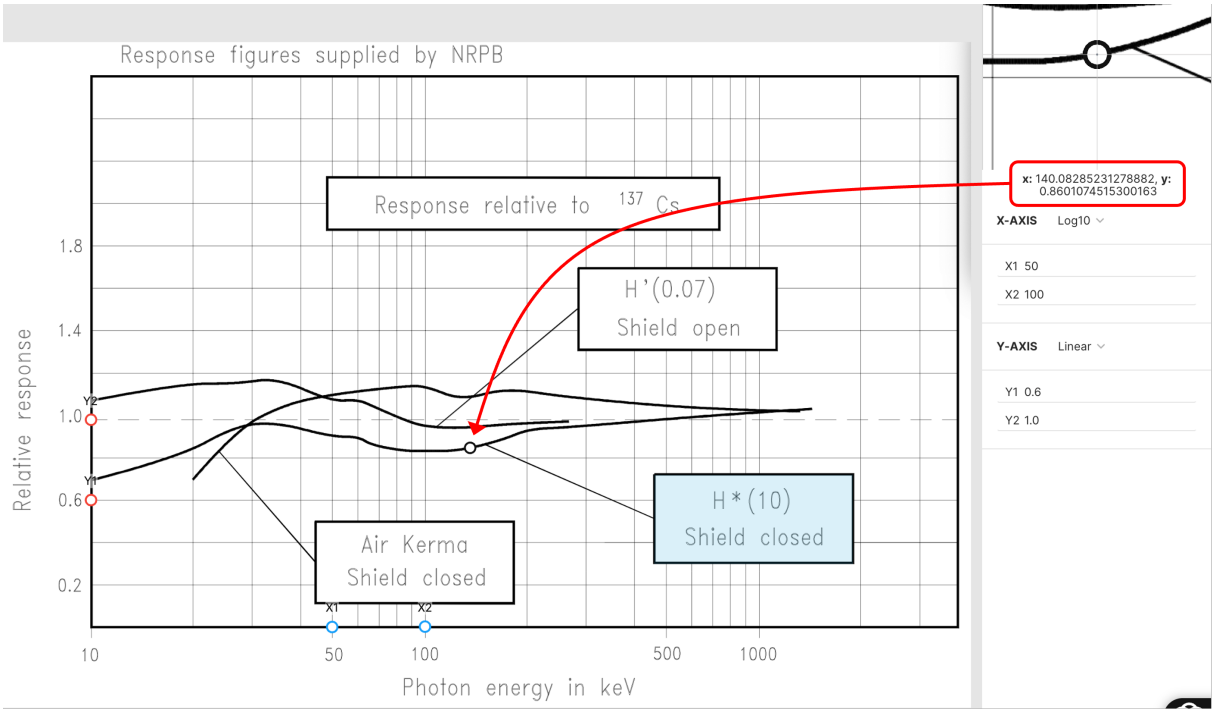

Figure B.3: Relative energy response of the Smart-ION survey meter Thermo Scientific (2018). Data digitised via `https://plotdigitizer.com/app`.

B.3 | Results & Discussion

The results of the calibration procedure for the 33 calibrated LiF:Mg,Cu,P TLDs are summarised in Table B.3. Zero counts ranged from 3,342 to 15,205, with a mean of 9,178 counts. Device sensitivity counts varied between 202,968 and 283,672, with a mean of 243,192 counts. The crystal sensitivity correction factors lay between 0.8445 and 1.2127, with a mean of 1.0116. The survey meter recorded an ambient dose equivalent of 166 µSv, which yielded a calibration factor of:

$$k_c = \frac{166}{243,192 - 9,178} = 7.09 \times 10^{-4}\ \mu\text{Sv count}^{-1} \tag{B.6}$$

This means that, on average, $\frac{1}{7.09 \times 10^{-4}} = 1,409.73$ counts correspond to 1 µSv of $H^*(10)$.

B.4 | Conclusion

The TLDs were successfully calibrated, with all relevant parameters in Equation B.4 determined. The resulting calibration framework was therefore ready to be applied in both the pilot and main studies.

Table B.3: Calibration results from the zero count, device sensitivity and crystal sensitivity stages. The values correspond to $M^{\text{cal}}_{\text{bg},i}$, $M^{\text{cal}}_{\text{raw},i}$ and $k_{\text{ECC},i}$, respectively. For label mapping, see D.1.

TLD	Zero Counts counts	Device Sensitivity counts	Crystal Sensitivity
a4	8,733	234,865	1.0349
a5	9,997	202,968	1.2127
a6	6,194	249,604	0.9614
b4	10,258	222,481	1.1027
b5	8,616	240,121	1.0108
b6	7,639	266,755	0.9031
c4	12,422	283,672	0.8627
c5	7,214	240,938	1.0012
c6	11,310	235,432	1.0441
d4	14,697	254,763	0.9748
d5	11,622	283,327	0.8613
d6	9,440	227,700	1.0722
e4	15,205	252,617	0.9857
e5	6,692	238,124	1.0112
e6	10,512	204,390	1.2070
f4	9,426	263,751	0.9201
f5	9,632	210,395	1.1656
f6	10,356	258,320	0.9437
g4	8,311	232,184	1.0453
g5	10,247	273,843	0.8878
g6	10,059	215,729	1.1378
h4	3,342	272,730	0.8687
h5	8,226	256,934	0.9409
h6	9,562	220,238	1.1108
i4	9,721	250,145	0.9733
i5	4,391	281,496	0.8445
i6	12,497	259,661	0.9468
k4	9,150	214,597	1.1391
k5	8,286	249,999	0.9682
k6	8,699	203,750	1.1998
l4	9,220	203,287	1.2058
l5	7,462	254,877	0.9458
l6	3,729	265,657	0.8934

C

Complete inventory of modelled geometry

This appendix provides a comprehensive description of all regions and their materials as modelled in the MC FLUKA model used for the main study simulation. This information is intended to provide full transparency of the modelling process and reproducibility of the simulation setup.

For each region, Table C.1 includes the name of the region as it appears in the input file, its descriptive name, a brief description of function in the model, the material assigned to it, a summary of how it was geometrically defined, and the reference for its dimensions or material properties. Figures C.1–C.4 provide snapshots of the viewports from the Geometry tab in Flair for visual support for understanding certain geometric configurations. For the references, the following abbreviations apply:

- Technical drawings / data sheet – Specifications provided in General Electric (2024).
- Manuals – Specifications and images provided in General Electric (2018, 2020, 2025).
- Informal peer communication – Information obtained through discussions with peers.
- Physical measurements – Dimensions obtained directly from the actual setup using standard measuring instruments (e.g., measuring tape, ruler, Vernier caliper).
- Assumed – Parameters estimated based on reasonable assumptions.
- N/A – Not applicable.

Other references are listed in full. Also, it should be noted that the absence of a superscript in the Reference entry indicates that the same source was used for both the material and geometric definitions.

Furthermore, Table C.2 details the properties of all compound materials used in the model. Data for individual elements are excluded, as they can be readily obtained from standard databases and literature sources. It should be noted that for materials without a directly defined elemental composition from the available literature, particularly those marked as 'Assumed' under References, their properties were still carefully considered. Approaches such as reverse-engineering by known weight and weight-averaging to estimate effective densities were used. Detailing each case individually would add unnecessary length and falls outside the focus of this work.

Table C.1: Complete list of modelled regions used in the FLUKA main study model.

Region ID	Full name	Description	Material	Geometry	Source
			FACILITY		
BLKBODY	Blackbody	All-absorbing body surrounding the entire geometry to prevent tracking particles to infinity. (See Figure C.1)	Blackhole*	$X = [-1400 : 1300]$ cm $Y = [-600 : 900]$ cm $Z = [-1450 : 1100]$ cm	N/A
AIRt	Air – Top	Air region above the ceiling; occupies entire volume.	Air	Volume above ceiling.	N/A
AIRr	Air – Room	Air region within the scanner room; occupies free space.	Air	Free volume within scanner room Height[a] = 328.0 cm	Technical data sheet
AIRb	Air – Bottom	Air region below the floor; occupies entire volume.	Air	Volume below floor.	N/A
EXTa	Air – Extra	Air outside the scanner room between floor and ceiling.	Air	Volume between floor and ceiling, excluding scanner room.	N/A
W1A	Wall 1 – Air	Air gap between plywood and outer gypsum layers.	Air	Thickness = 9.3 cm – filled the leftover space between the other layers.	N/A
W1G	Wall 1 – Gypsum	Gypsum layers (front & back) of wall 1.	Gypsum	Thickness[a] = 24 mm ($\times$2)	[a]Informal peer communication
W1L	Wall 1 – Lead	Lead sheet within wall 1 for radiation shielding.	Lead	Thickness[a] = 2 mm Height[a] = 200.0 cm	[a]Informal peer communication
W1P	Wall 1 – Plywood	Plywood layer holding the lead sheet in place in wall 1.	Plywood	Thickness[a] = 12 mm	[a]Informal peer communication
W2A	Wall 2 – Air	Air gap between plywood and outer gypsum layers in wall 2.	Air	Thickness = 8.7 cm – filled the leftover space between the other layers.	N/A
W2G	Wall 2 – Gypsum	Gypsum layers (front & back) of wall 2.	Gypsum	Thickness[a] = 24 mm ($\times$2)	[a]Informal peer communication
W2L	Wall 2 – Lead	Lead sheet within wall 2 for radiation shielding.	Lead	Thickness[a] = 4 mm Height[a] = 200.0 cm	[a]Informal peer communication
W2P	Wall 2 – Plywood	Plywood layer holding the lead sheet in place in wall 2.	Plywood	Thickness[a] = 12 mm	[a]Informal peer communication
W3A	Wall 3 – Air	Air gap between plywood and outer gypsum layers in wall 3.	Air	Thickness = 10.1 cm – filled the leftover space between the other layers.	N/A

Continued on next page

*Perfect absorber.

Continued from previous page

Region ID	Full name	Description	Material	Geometry	Source
W3G	Wall 3 – Gypsum	Gypsum layers (front & back) of wall 3.	Gypsum	Thickness[a] = 24 m (×2)	[a]Informal peer communication
W3L	Wall 3 – Lead	Lead sheet within wall 3 for radiation shielding.	Lead	Thickness[a] = 2 mm Height[a] = 200.0 cm	[a]Informal peer communication
W3P	Wall 3 – Plywood	Plywood layer holding the lead sheet in place in wall 3.	Plywood	Thickness[a] = 12 mm	[a]Informal peer communication
W4A	Wall 4 – Air	Air gap between plywood and outer gypsum layers in wall 4.	Air	Thickness = 8.7 cm – filled the leftover space between the other layers.	N/A
W4G	Wall 4 – Gypsum	Gypsum layers (front & back) of wall 4.	Gypsum	Thickness[a] = 24 mm (×2)	[a]Informal peer communication
W4L	Wall 4 – Lead	Lead sheet within wall 4 for radiation shielding.	Lead	Thickness[a] = 2 mm Height[a] = 200.0 cm	[a]Informal peer communication
W4P	Wall 4 – Plywood	Plywood layer holding the lead sheet in place in wall 4.	Plywood	Thickness[a] = 12 mm	[a]Informal peer communication
WEG	Extra Walls – Gypsum	Walls of the areas adjacent to the scanner room.	Gypsum	Thickness[a] = 12 mm	Layout: Technical drawings [a]Informal peer communication
FLOOR	Floor	Floor layer at the bottom of the facility.	Concrete (Portland)	Thickness[a] = 50 cm	[a]Informal peer communication
CEILING	Ceiling	Ceiling layer at the top of the facility.	Concrete (Portland)	Thickness[a] = 50 cm	[a]Informal peer communication
PILLC	Pillars – Concrete	Support pillars at strategic locations, particularly in the corners of rooms.	Concrete (Portland)	Height[a] = 328.0 cm	Layout: Technical drawings [a]Informal peer communication
PILLP	Pillars – Plywood	Plywood sheet encasing certain pillars.	Plywood	Thickness[a] = 12 mm	[a]Assumed
D1L	Door 1 – Lead	Lead sheet in door 1 sandwiched between plywood layers & lining within jamb.	Lead	Leaf: Length[a] = 71.0 cm Width[a] = 0.2 cm (also for jamb lining)[b] Height[a] = 204.5 cm	[a]Physical measurements [b]Assumed
D1P	Door 1 – Plywood	Two wooden layers of door 1 sandwiching the lead sheet.	Plywood	Length[a] = 71.0 cm Width[a] = 2.0 cm (×2) Height[a] = 204.5 cm	[a]Physical measurements
D1J	Door 1 – Jamb	Frame, including door stop, around door 1. (see Figure C.2)	Aluminium	Thickness[a] = 2 mm (all around)	[a]Assumed

Continued on next page

Continued from previous page

Region ID	Full name	Description	Material	Geometry	Source
D2L	Door 2 – Lead	Lead sheet in door 2 sandwiched between plywood layers, lining within jamb & within astragal. (see Figure C.2)	Lead	Leaves† / astragal: Length[a] = 44.5 + 96.0 / 6 cm Width[a] = 0.2 cm (also for jamb lining)[b] Height[a] = 204.5 cm	[a]Physical measurements [b]Assumed
D2P	Door 2 – Plywood	Two wooden layers of door 2 sandwiching the lead sheet & astragal.	Plywood	Leaves† / astragal: Length[a] = 44.5 + 96.0 / 6 cm Width[a] = 2.0 / 0.4 (×2) cm Height[a] = 204.5 cm	[a]Physical measurements
D2J	Door 2 – Jamb	Frame, including door stop, around door 2.	Aluminium	Thickness[a] = 2 mm (all around)	[a]Assumed
WINDOW	Window	Observation lead-glass window.	Lead-glas	Length[a] = 79.9 cm Width[b] = 0.2 cm Height[a] = 106.9 cm	[a]Physical measurements [b]Informal peer communication
WINDL	Window – Lead	Lead lining within jamb of observation window. (see Figure C.2)	Lead	Thickness[a] = 2 mm (front only)	[a]Assumed
WINDJ	Window – Jamb	Jamb frame around observation window.	Aluminium	Thickness[a] = 2 mm (all around)	[a]Assumed
			PHANTOM		
PHANTOM	Phantom – Body	Outer shell of the Jaszczak phantom and top lid, both of which are cylindrical bodies. (see Figure C.3)	PMMA	Body: Height = 19.824 cm Radius = 10.0 cm Thickness = 1.120 (sides); 1.224 (bottom) cm Lid: Height = 2.448 cm Radius = 13.0 cm	Physical measurements and specifications from DataSpectrum (n.d.)
WATER	Phantom – Water	Body of water within the phantom shell. (see Figure C.3)	Water	Height = 18.6 cm Radius = 10.0 cm	N/A
			TLDs		
TLDA1	TLD 'A1'	TLD on the internal side of the observational window	LiF:Mg,Cu,P	$3.2 \times 3.2 \times 0.9$ mm^3	Radcard (2013)
TLDA2	TLD 'A2'	TLD on the external side of the observational window (control room)	LiF:Mg,Cu,P	$3.2 \times 3.2 \times 0.9$ mm^3	Radcard (2013)

Continued on next page

†Contains a 1 mm slit behind astragal (between small and large leaves).

Continued from previous page

Region ID	Full name	Description	Material	Geometry	Source
TLDB1	TLD 'B1'	TLD on the internal side of the west wall	LiF:Mg,Cu,P	$3.2 \times 3.2 \times 0.9$ mm^3	Radcard (2013)
TLDB2	TLD 'B2'	TLD on the external side of the west wall (NM corridor)	LiF:Mg,Cu,P	$3.2 \times 3.2 \times 0.9$ mm^3	Radcard (2013)
TLDC1	TLD 'C1'	TLD on the internal side of the south wall	LiF:Mg,Cu,P	$3.2 \times 3.2 \times 0.9$ mm^3	Radcard (2013)
TLDC2	TLD 'C2'	TLD on the external side of the south wall (store room)	LiF:Mg,Cu,P	$3.2 \times 3.2 \times 0.9$ mm^3	Radcard (2013)
TLDD	TLD 'D'	TLD on the internal side of the east wall	LiF:Mg,Cu,P	$3.2 \times 3.2 \times 0.9$ mm^3	Radcard (2013)
TLDE1	TLD 'E1'	TLD on the left side of the SPECT gantry face	LiF:Mg,Cu,P	$3.2 \times 3.2 \times 0.9$ mm^3	Radcard (2013)
TLDE2	TLD 'E2'	TLD on the right side of the SPECT gantry face	LiF:Mg,Cu,P	$3.2 \times 3.2 \times 0.9$ mm^3	Radcard (2013)
TLDE3	TLD 'E3'	TLD on the left side of the CT gantry	LiF:Mg,Cu,P	$3.2 \times 3.2 \times 0.9$ mm^3	Radcard (2013)
TLDE4	TLD 'E4'	TLD on the right side of the CT gantry	LiF:Mg,Cu,P	$3.2 \times 3.2 \times 0.9$ mm^3	Radcard (2013)
		SCANNER			
PCTT	Patient Couch – Table Top	The outer shell of table top on which the phantom was placed. (see Figure C.3)	Carbon-fibre	Complex	Physical measurements & Somasundaram et al. (2019)
PCTTf	Patient Couch – Table Top (foam)	Internal volume of the patient couch's table top. (see Figure C.3)	Foam	Complex	Somasundaram et al. (2019)
PCTBL	Patient Couch – Table	Main body of the patient couch on which the table top slides.	ALUPCTBL (see Table. C.2)	Complex	Physical measurements & assumed
PCSUPP	Patient Couch – Support	Support frame for the aptient couch	Aluminium	Complex	Assumed (from visual inspection and photographs taken during the installation)
PCCOV	Patient Couch - Cover	Plastic cover encasing the support frame.	Polyurethane[a]	Thickness[b] $= 2$ mm	[a]Borlandelli and Mahltig (2022) [b]Assumed (from visual inspection)
COLL	Collimator	Block-equivalent collimator for both LEHRS and HEGP variants.	See § 3.8.2.2	$54.4 \times 40.4 \times 3.2$ cm^3	N/A
ALCV	Aluminium Cover	Aluminium cover surrounding the crystal.	Aluminium	$54.40 \times 40.40 \times 1.79$ cm^3 Hollow; 0.12 mm thick	Rault et al. (2010)
FOAM	Foam	Foam layer between aluminium cover and crystal.	Foam	$54.16 \times 40.16 \times 1.67$ cm^3 Hollow; 0.08 mm thick	Rault et al. (2010)

Continued on next page

Continued from previous page

Region ID	Full name	Description	Material	Geometry	Source
CRYS	Crystal	Scintillator crystal within detector head.	NaI	$54.0 \times 40.0 \times 1.59$ cm^3	Manuals Garcia et al. (2015) Rault et al. (2010)
LTGD	Light Guide	Light guide layer between crystal and optical coupling.	Glass	$56.4 \times 42.4 \times 0.9525$ cm^3	Rault et al. (2010)
OPTI	Optical Coupling	Very thin layer between the light guide and PMTs.	Visilox	$56.4 \times 42.4 \times 0.02$ cm^3	Rault et al. (2010)
PMTS	Photomultiplier Tubes	Cuboid structure equivalent to PMTs.	PMTs (see Table. C.2)	$56.4 \times 42.4 \times 12.7$ cm^3	Manuals Hamatsu (1998) Rault et al. (2010)
ELEC	Electronics	Electronic board residing behind the PMTs.	ELCTRNCS (see Table. C.2)	$56.4 \times 42.4 \times 0.5$ cm^3	Rault et al. (2010)
VACU	Vacuum	Vacuum inside the detector head.	Vacuum	$57.4 \times 43.4 \times 16.1725$ cm^3	Rault et al. (2010)
PBCS	Lead casing	Dense lead shielding layer forming the inner casing of the detector head.	Lead	$61.0 \times 47.0 \times 19.7625$ cm^3 Hollow; 1.8 cm thick	Rault et al. (2010)
ALCS	Aluminium casing	Outer aluminium shell encasing the detector head structure.	Aluminium	$66.4 \times 52.4 \times 22.4625$ cm^3 Hollow; 2.7 cm thick	Rault et al. (2010)
XRT	X-ray Tube	X-ray tube assembly, made out of 5 cylinders and 4 cuboids.	XRT (see Table. C.2)	Cylinders: [Height, Radius] 1: $[51.2, 13.0]$ cm 2: $[31.6, 6.75]$ cm 3: $[19.4, 4.35]$ cm 4,5: $[17.6, 4.4]$ cm Cuboids: 1: $37.9 \times 40.0 \times 10.0$ cm^3 2: (Merges into cylinder 1)	General Electric (2023) Behling (2021) Assumed
HEX	Heat Exchanger	Cuboid structure made to resemble a CT scanner's heat exchanger.	HEX (see Table. C.2)	$51.2 \times 20.5 \times 20.5$ cm^3	Assumed Behling (2021)
EBD	Electronic Board	Cuboid structure made to resemble a CT scanner's electronic board.	HEX (see Table. C.2)	$40.0 \times 10.0 \times 30.0$ cm^3	Assumed Behling (2021)
HVG	High-Voltage Genrators	Cuboid structures made to resemble a CT scanner's high voltage generators.	HVG (see Table. C.2)	$40.0 \times 20.0 \times 30.0$ cm^3 $(\times 2)$	Assumed Behling (2021)

Continued on next page

Continued from previous page

Region ID	Full name	Description	Material	Geometry	Source
DTS	Detector System	Two overlapping cylindrical bodies made to resemble a CT scanner's detector system.	DTS (see Table. C.2)	Cylinders radii: [Inner, Outer] 1: $[86.5, 100.0]$ cm 2: $[73.0, 86.5]$ cm Thicknesses: 1: 20 cm 2: 10 cm	Assumed Behling (2021)
SUPPORTS	Supports	Structural framework supporting the SPECT and CT gantries and associated components. (see Figure C.4)	Steel	Complex	Manuals Assumed
COVER	Plastic Cover	Plastic housing around scanner (white). (see Figure C.4)	Acrylonitrile Butadiene Styrene[a]	Complex	[a]Pious and Thomas (2016) Technical drawings Assumed
COVERG	Cover – Grey	Plastic housing around scanner, bottom part (grey). (see Figure C.4)	Acrylonitrile Butadiene Styrene[a]	Complex	[a]Pious and Thomas (2016) Technical drawings Assumed
COVERA	Cover – Aluminium	Front facing surfaces on the moving parts of the SPECT scanner.	Aluminium	Complex	Technical drawings Assumed

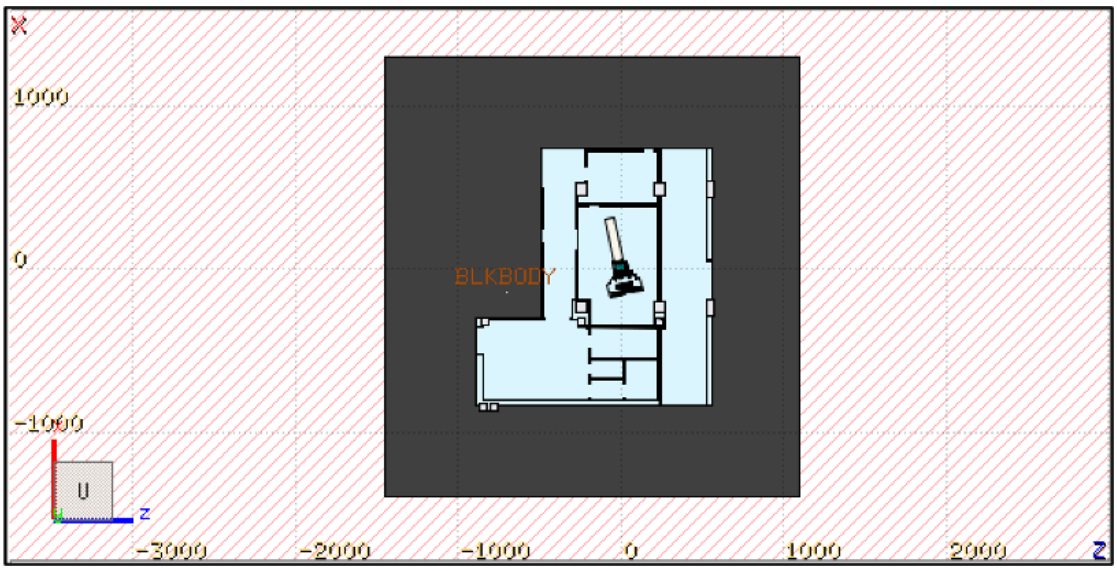

(a)

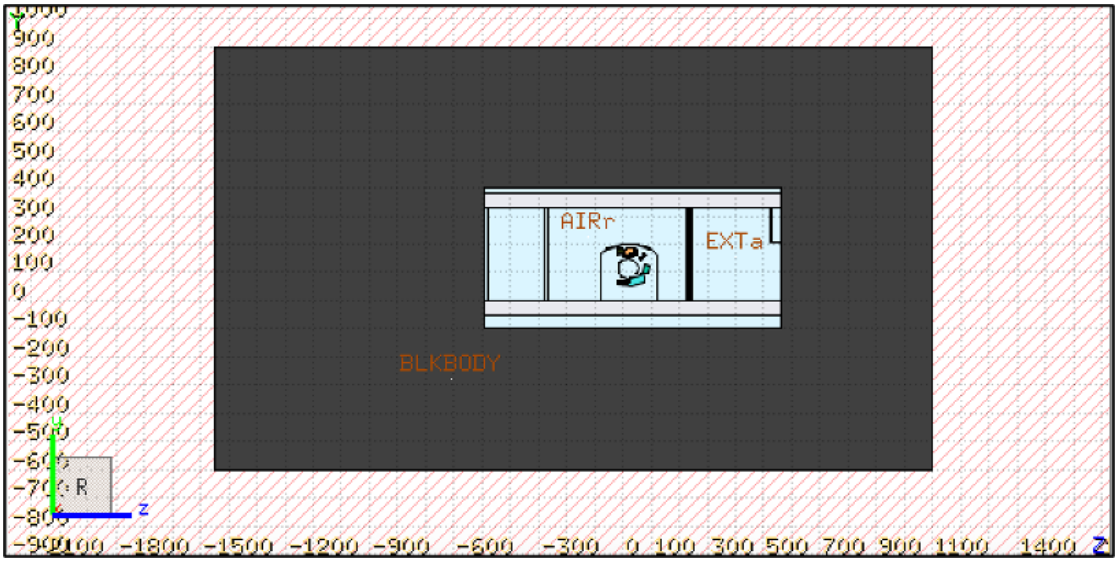

(b)

Figure C.1: Blackbody region as seen from the (a) ZX and (b) ZY viewports in Flair.

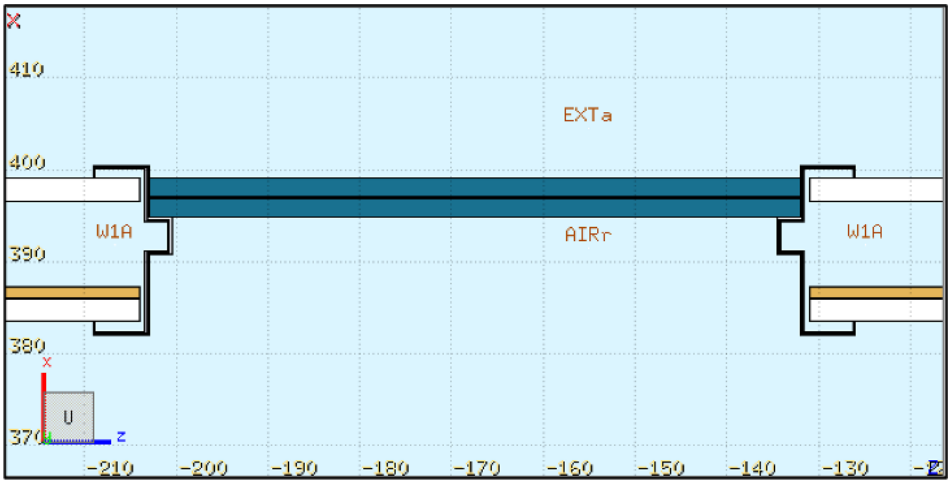

(a)

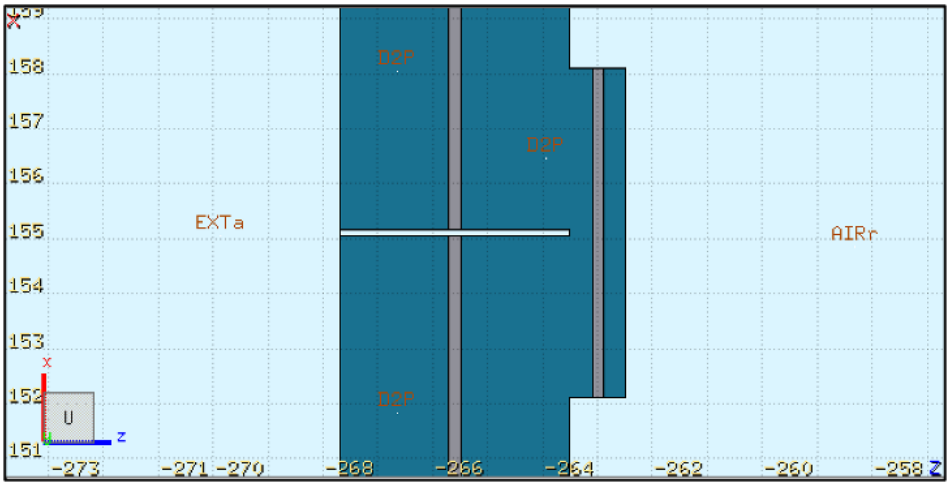

(b)

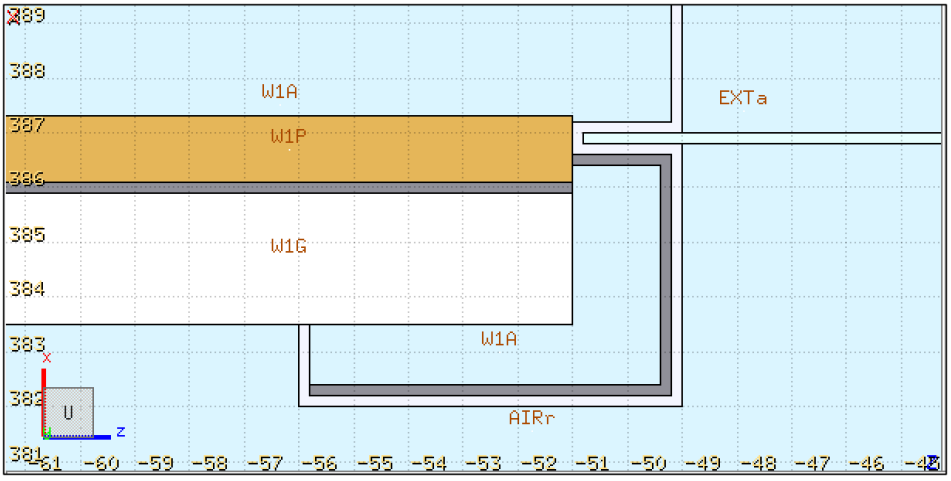

(c)

Figure C.2: (a) Door 1 and its jamb ;(b) Close-up of the astragal and gap of door 2; (c) Front frame of window showing lead-lining. All seen from the ZY viewports in Flair.

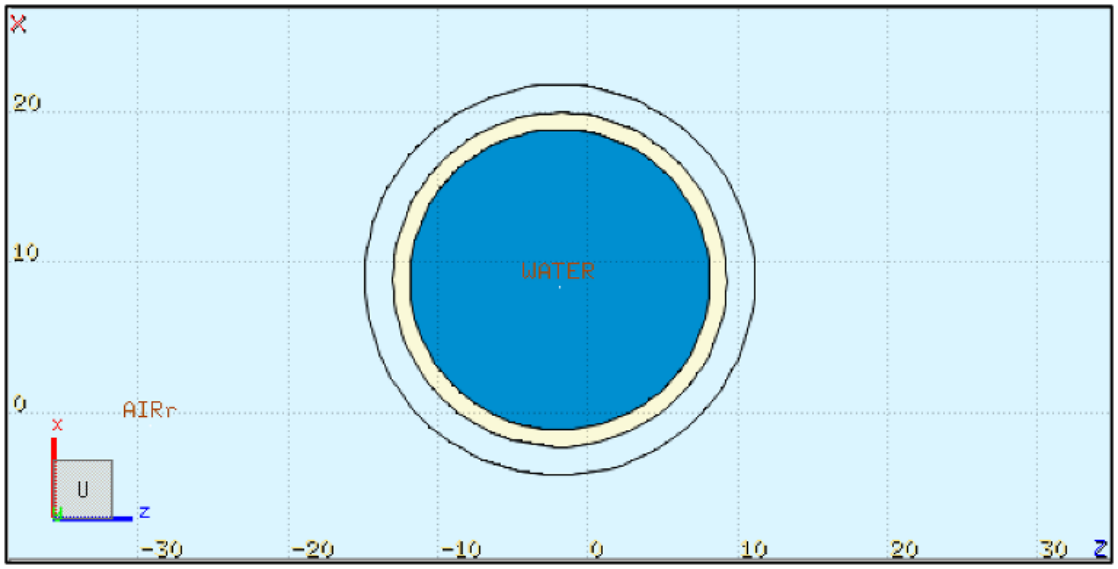

(a)

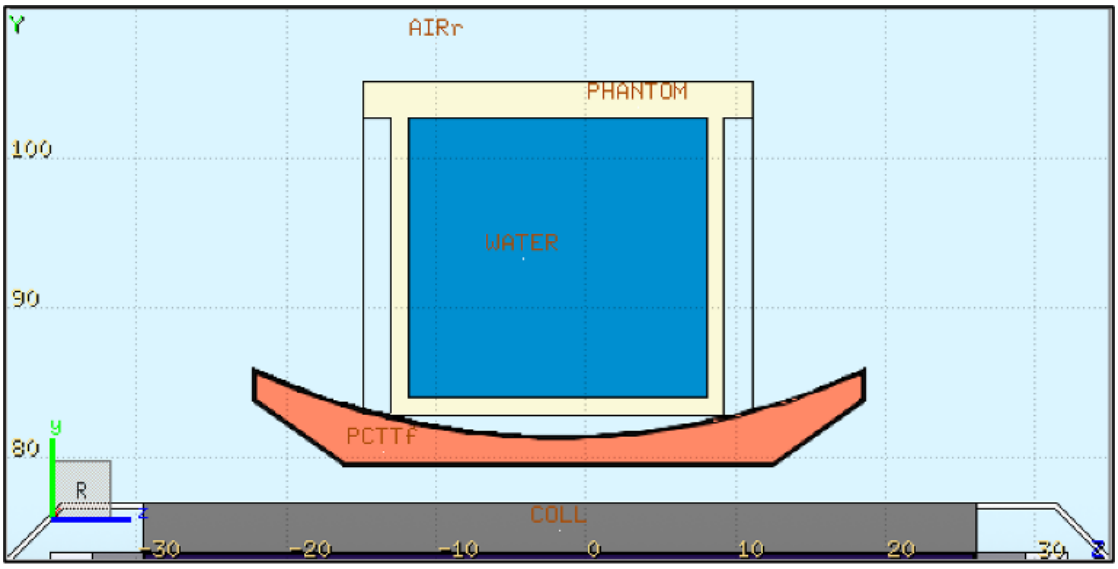

(b)

Figure C.3: Jaszczak phantom as seen from the (a) ZX and (b) ZY viewports in Flair.

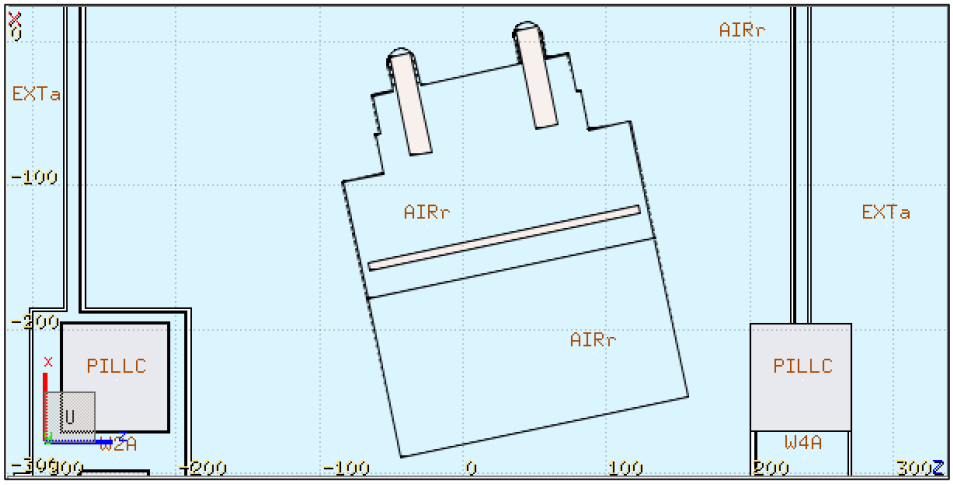

(a)

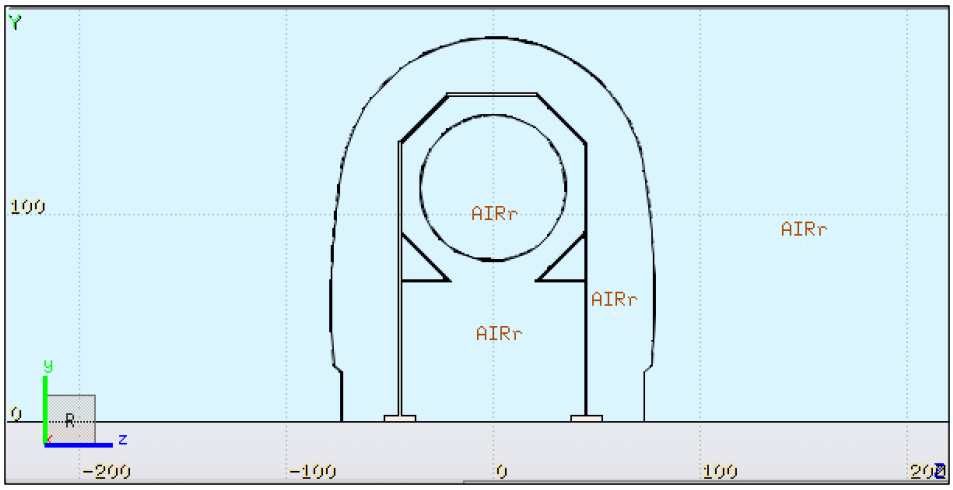

(b)

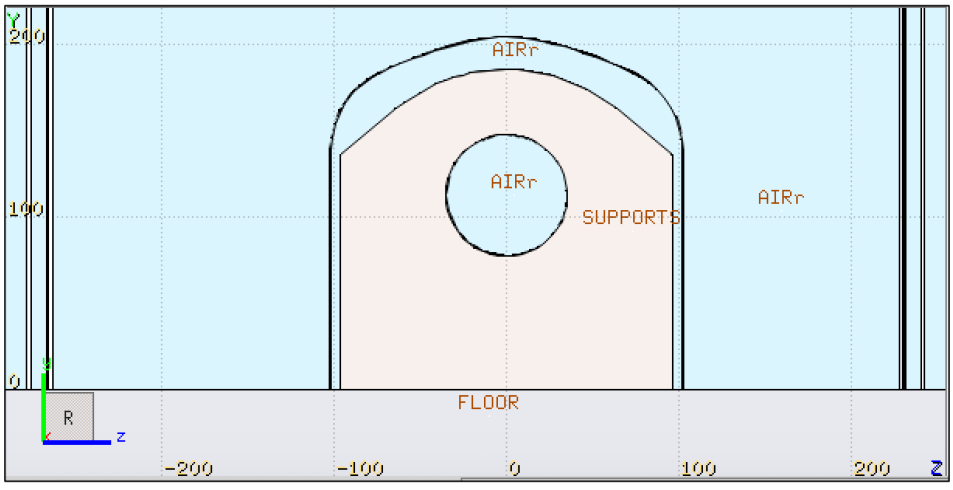

(c)

Figure C.4: (a) Bottom cover (grey) and support legs of the SPECT gantry; (b) SPECT gantry support enclosed by its outer cover; (c) CT gantry support enclosed by its outer cover. Panel (a) is shown from the ZX viewport, while panels (b) and (c) are from the ZY viewports in Flair. The 12° rotation applied to the scanner in the model was removed in panels (b) and (c) for clarity.

Table C.2: Properties of the materials used in the FLUKA main study simulation. For elemental composition (by mass fraction, except those marked with †), each letter denotes the element and the accompanying number indicates its percentage by weight.

Material	Full name	Density	Elemental Composition	Reference
		$g\,cm^{-3}$	%	
ALUPCTBL*	Aluminium patient couch table	0.3769	Al: 100	Assumed
ABS	Acrylonitrile butadiene styrene	1.115	H: 7.92, C: 85.48, N: 6.6	Rosato et al. (2004) & SpecialChem (2025)
AIR	Dry air	0.00120479	C: 0.01, N: 75.53, O: 23.18, Ar: 1.28	Pre-defined FLUKA material
CARBFIB	Carbon fibre	1.8	C: 95, N: 5	Texonic (n.d.) & Toray CFE (n.d.)
CONCRETE	Concrete (Portland)	2.3	H: 1.0, C: 0.1, O: 52.91, Na: 1.6, Mg: 0.2, Al: 3.39, Si: 33.70, K: 1.3, Ca: 4.4, Fe: 1.4	Flair material library (General)
DTS*	Detector system	9.97	W: 40, O: 3, Gd: 6, Y: 6, C: 2, H: 1, Si: 1, Cu: 3, Sn: 3, Al: 35	Assumed
EBD*	Electronic board	5.58	C: 20, H: 10, Si: 10, Cu: 30, Sn: 30	Assumed
ELCTRNCS*	Electronics	1.188	PMMA: 75, Cu: 5, Fe: 20	Rault et al. (2010)
GLASS_So†	Soda-lime glass	2.33	O: 60, Si: 25, Na: 10, Ca: 3, Mg: 1, Al: 1	Flair material library (Implanatation)
GYPSUM	Gypsum plaster of paris	1.428	H: 2.34, O: 55.76, S: 18.62, Ca: 23.28	Flair material library (General)
HEX*	Heat exchanger	3.83	H: 2.2, C: 10.5, O: 11.7, N: 0.6, Al: 50, Cu: 25	Assumed
HVG*	High-voltage generator	3.91	H: 1.7, C: 15.7, N: 0.6, O: 1.5, Al: 50, Fe: 12, Cu: 12.5, Si: 6	Assumed
LEAD-GLA	Lead-glass	6.22	O: 15.65, Si: 8.09, Ti: 0.81, As: 0.27, Pb: 75.19	Flair material library (General)
LEADcoll*	Lead collimator (HEGP/LEHRS)	11.35	Pb: 0.7/1.5, Air: 99.3/98.5	See § 3.8.2.2
MCP	LiF:Mg,Cu,P	2.5	Li: 26.30, F: 72.18, Mg: 0.20, P: 1.25, Cu: 0.05	Bilski (2002) & Sadek et al. (2017)
NaI	Sodium iodide	3.667	Na: 15.34, I: 84.66	Flair material library (General)
PMMA		1.18	Approx. polymer (C: 60, H: 8, O: 32)	
PMTs*		0.3410	Mu-metal (Cr: 2.0, Cu: 5, Fe: 18, Ni: 75): 3.4, Glass_So: 15.3, O: 51.2, Air: 21.9, PMMA: 7.2, Cu: 0.33, Fe: 0.67	Rault et al. (2010)
Polyuret†	Polyurethane (leather substitute)	1.18	H: 16, C: 17, Si: 2, S: 4	Flair material library (Plastic / Polymers)
PUR	Polyurethane (foam)	0.021	H: 4.10, C: 54.40, N: 12.10, O: 29.4	Detwiler et al. (2021)

Continued on next page

Continued from previous page

Material	Full name	Density	Elemental Composition	Reference
		$g\,cm^{-3}$	%	
SS316LN	Stainless steel	7.8	Fe: 67.15, Cr: 18.5, Ni: 11.25, Mn: 2, Si: 1, P: 0.045, S: 0.03, C: 0.03	Flair material library (Metal Alloys)
Visilox†	Branded silicone compound	1.0313	Si: 38.3, O: 23.2, C: 30.8, H: 7.74	N/A
WATER†	Water (liquid)	1.0	H: 2, O: 1	Pre-defined FLUKA material
WOOD	Plywood	0.64	C: 49.70, O: 42.74, H: 5.96, N: 0.50, S: 0.50, Mg: 0.20, K: 0.20, Ca: 0.20	Detwiler et al. (2021)
XRT*	X-ray tube	11.27	W: 17.5, Re: 0.25, Mo: 0.15, C: 2.65, O: 3.22, Na: 0.7, Si: 2.38, Ca: 0.7, Pb: 52.0, H: 0.45, Cu: 20.0	Assumed

* Not real materials, but created for this work.

† Composition provided as atomic fraction, not mass.

D

Individual TLD counts and doses

Throughout this work, a consistent labelling system was applied to track the TLDs and to map each individual dosimeter to its corresponding group of three. This scheme is summarised in Table D.1. Lower-case identifiers (e.g., 'a4') denote individual TLDs, whereas upper-case letters (e.g., 'A') represent the pouch/group labels used in the main study. In the pilot study, rather than using upper-case letters, simple numerical labels were adopted to distinguish those groups from the main study labels and to emphasise that the results associated with the two datasets are not directly comparable. The letter 'j' is not present in the TLD tray and was therefore not included in the labelling scheme presented here.

Table D.1: Mapping between individual (lower-case) TLD identifiers and the labels used in the pilot (numeric groups 1–6) and main study (A1, A2, B1, B2, C1, C2, D, E1–E4).

Individual TLDs	Pilot TLDs	Main TLDs
a4, a5, a6	1	A1
b4, b5, b6	2	A2
c4, c5, c6	3	B1
d4, d5, d6	4	B2
e4, e5, e6	5	C1
f4, f5, f6	6	C2
g4, g5, g6	—	D
h4, h5, h6	—	E1
i4, i5, i6	—	E2
k4, k5, k6	—	E3
l4, l5, l6	—	E4

Table D.2 lists, for each of the 33 individual TLDs used in this work, the raw reader counts $M_{\mathrm{raw},i}^{\mathrm{study}}$ and the calibrated ambient dose equivalent $H^*(10)$. Doses were derived from the read-outs using Equation B.4 from the calibration stage, i.e.,

$$H_{\mathrm{cal},i} = \left(M_{\mathrm{raw},i}^{\mathrm{study}} - M_{\mathrm{bg},i}^{\mathrm{cal}}\right) \cdot k_{\mathrm{ECC},i} \cdot \left(7.0936 \times 10^{-4}\right) \cdot (0.7183) \cdot (1.1627), \tag{D.1}$$

where the numerical factors are the global constants common to all TLDs and the per-TLD terms $M_{\mathrm{bg},i}^{\mathrm{cal}}$ and $k_{\mathrm{ECC},i}$ are the individual entries in Table B.3. Entries reported as 0 µSv indicate that the raw study counts were less than the calibration background counts. In such cases, a zero dose was assigned.

Table D.2: Side-by-side individual TLD raw counts $M_{\text{raw},i}^{\text{study}}$ and calibrated $H^*(10)$ for the pilot and main studies. Zeros in the main column indicate $M_{\text{raw},i}^{\text{study}} \leq M_{\text{bg},i}^{\text{cal}}$.

	Pilot		**Main**	
TLD	$M_{\text{raw},i}^{\text{study}}$ counts	$H^*(10)$ µSv	$M_{\text{raw},i}^{\text{study}}$ counts	$H^*(10)$ µSv
a4	271,419	161.05	57,100	29.65
a5	242,084	166.74	50,420	29.04
a6	297,881	166.13	56,366	28.58
b4	251,041	157.29	13,530	2.14
b5	263,853	152.84	11,537	1.75
b6	293,109	152.73	16,147	4.55
c4	296,971	145.43	134,683	62.48
c5	248,241	142.96	107,988	59.77
c6	248,431	146.67	107,829	59.70
d4	223,633	120.66	12,433	0.00
d5	254,853	124.11	9,970	0.00
d6	202,424	122.58	13,251	2.42
e4	187,529	100.63	55,375	23.46
e5	184,377	106.28	61,360	32.59
e6	153,927	102.55	47,040	26.12
f4	173,877	89.64	14,034	2.51
f5	139,760	89.86	11,006	0.95
f6	176,370	92.81	10,362	0.00
g4	—	—	141,657	82.57
g5	—	—	161,455	79.53
g6	—	—	134,608	83.95
h4	—	—	1,324,083	679.69
h5	—	—	1,323,902	733.36
h6	—	—	1,120,702	731.19
i4	—	—	1,345,533	770.22
i5	—	—	1,532,789	764.64
i6	—	—	1,372,845	763.01
k4	—	—	20,987	7.99
k5	—	—	18,439	5.82
k6	—	—	18,431	6.92
l4	—	—	16,249	5.02
l5	—	—	15,669	4.60
l6	—	—	16,219	6.61

E

Ambient dose equivalent distribution maps

Figures E.1–E.25 are additional transverse projections that complement the dose maps presented in § 4.6.1 to provide a complete set of views across the vertical extent of the facility along the Y projection (bird's eye view). These supplementary slices are included here to allow more detailed inspection of spatial variations in $H^*(10)$ beyond the representative projections shown in the main Results chapter.

The sequence of the projections may be interpreted as a virtual upward sweep through the environment, beginning below the floor and traversing it, then moving progressively upward through the room, and finally extending into and beyond the ceiling space.

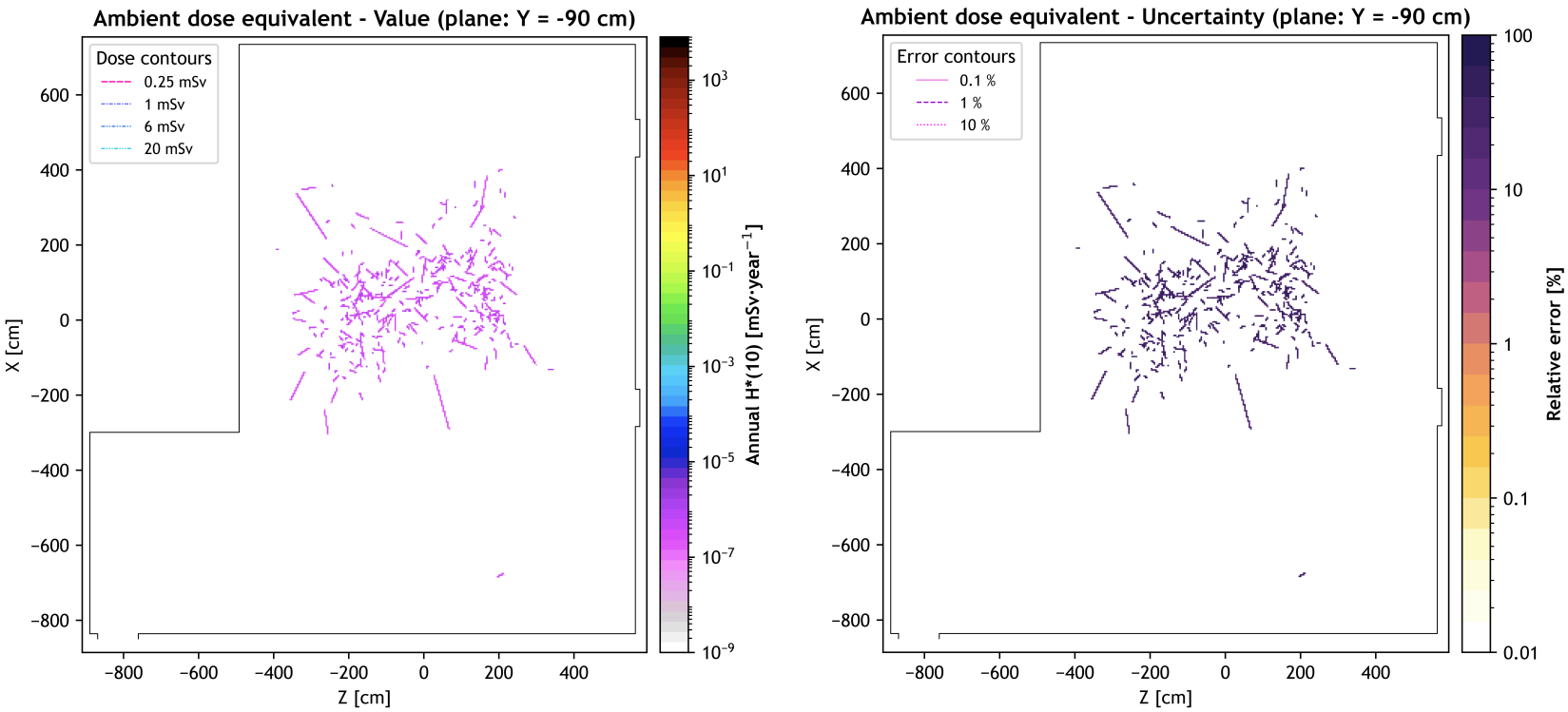

(a) (b)

Figure E.1: Ambient dose equivalent maps obtained from FLUKA USRBIN scoring of $H^*(10)$ distribution, shown for the projection at $Y = -90$ cm, corresponding to the average over the slab $Y \in [-100, -80]$ cm: (a) Value map of the ambient dose equivalent rate $H^*(10)$, scaled to typical annual workloads for ^{99m}Tc; (b) Relative statistical uncertainty of $H^*(10)$ for the same slice.

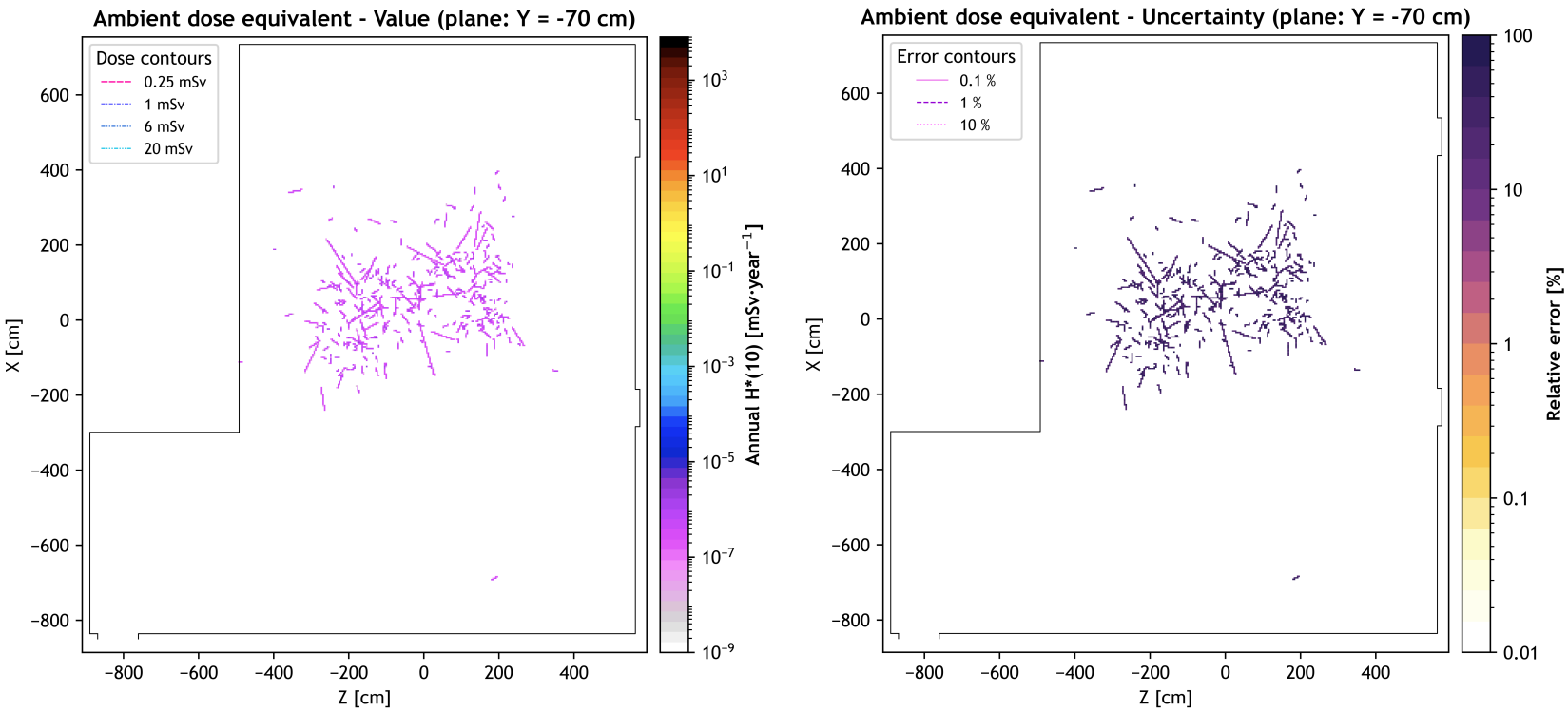

(a) (b)

Figure E.2: Ambient dose equivalent maps obtained from FLUKA USRBIN scoring of $H^*(10)$ distribution, shown for the projection at $Y = -70$ cm, corresponding to the average over the slab $Y \in [-80, -60]$ cm: (a) Value map of the ambient dose equivalent rate $H^*(10)$, scaled to typical annual workloads for ^{99m}Tc; (b) Relative statistical uncertainty of $H^*(10)$ for the same slice.

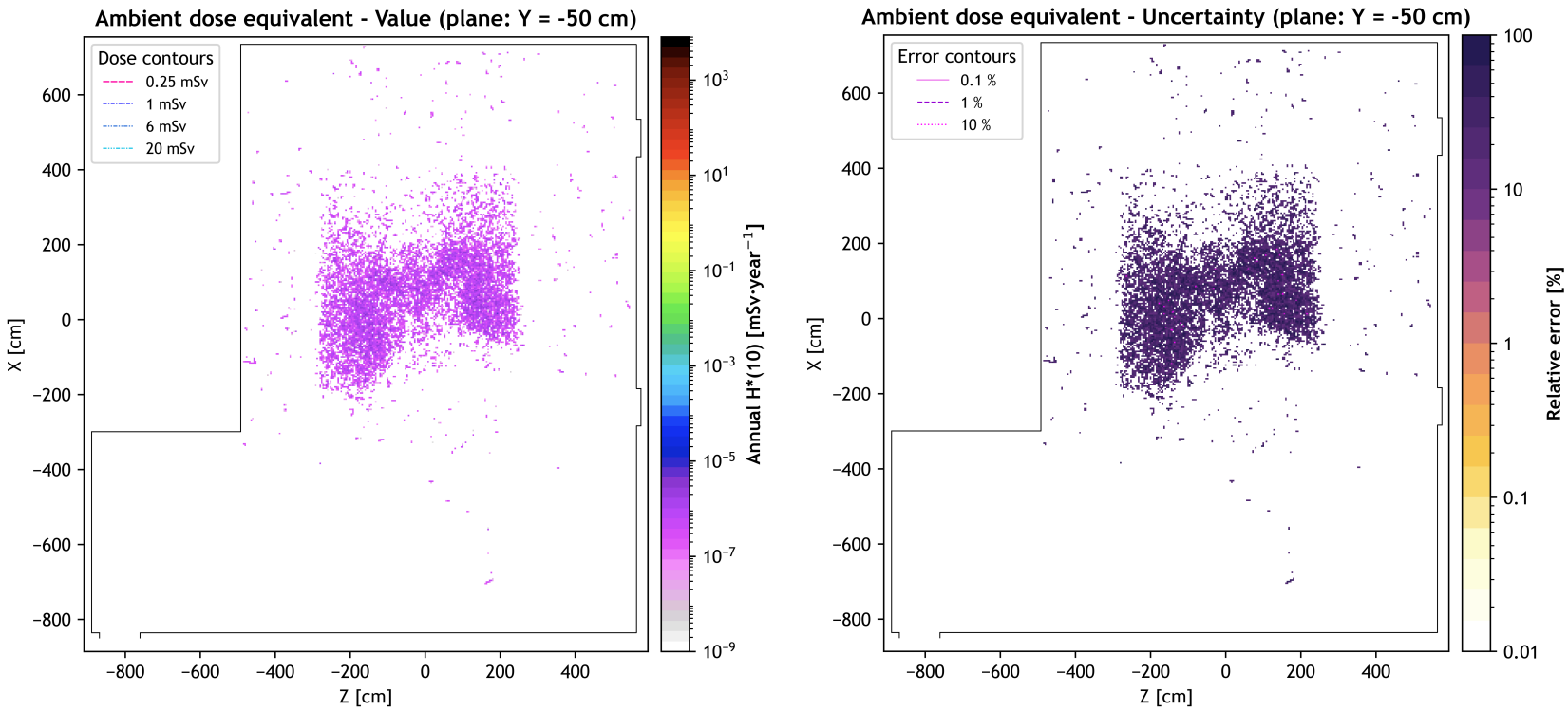

(a) (b)

Figure E.3: Ambient dose equivalent maps obtained from FLUKA USRBIN scoring of $H^*(10)$ distribution, shown for the projection at $Y = -50$ cm, corresponding to the average over the slab $Y \in [-60, -40]$ cm: (a) Value map of the ambient dose equivalent rate $H^*(10)$, scaled to typical annual workloads for ^{99m}Tc; (b) Relative statistical uncertainty of $H^*(10)$ for the same slice.

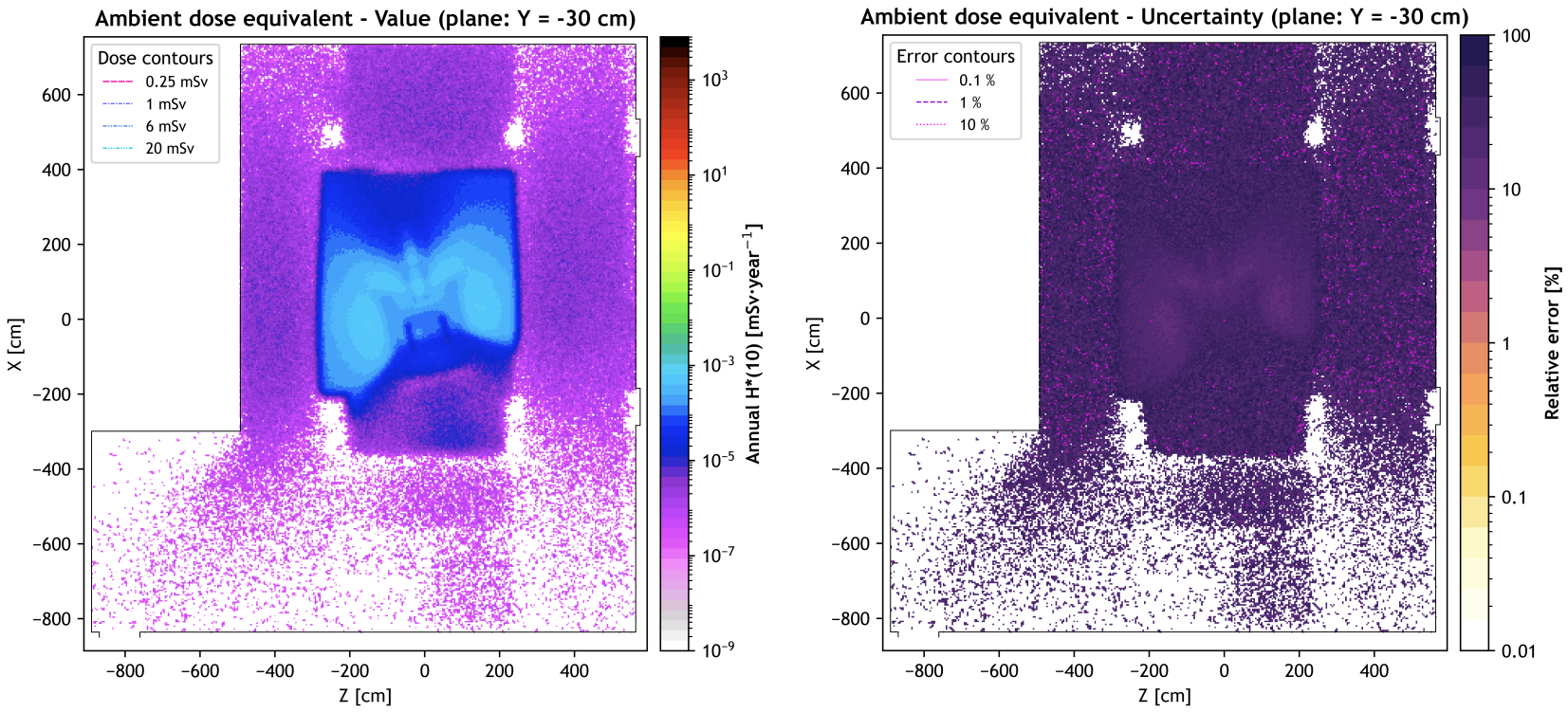

(a) (b)

Figure E.4: Ambient dose equivalent maps obtained from FLUKA USRBIN scoring of $H^*(10)$ distribution, shown for the projection at $Y = -30$ cm, corresponding to the average over the slab $Y \in [-40, -20]$ cm: (a) Value map of the ambient dose equivalent rate $H^*(10)$, scaled to typical annual workloads for ^{99m}Tc; (b) Relative statistical uncertainty of $H^*(10)$ for the same slice.

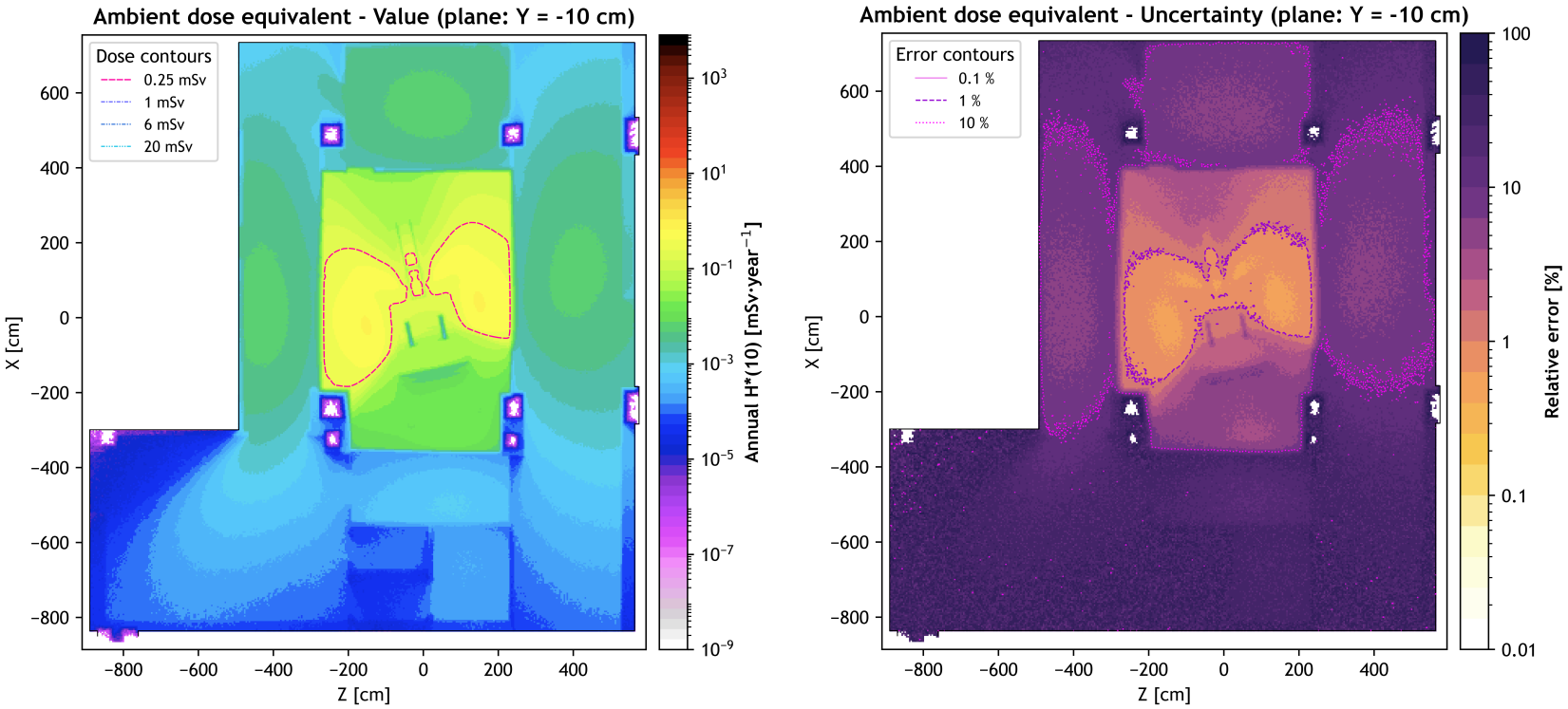

(a) (b)

Figure E.5: Ambient dose equivalent maps obtained from FLUKA USRBIN scoring of $H^*(10)$ distribution, shown for the projection at $Y = -10$ cm, corresponding to the average over the slab $Y \in [-20, 0]$ cm: (a) Value map of the ambient dose equivalent rate $H^*(10)$, scaled to typical annual workloads for ^{99m}Tc; (b) Relative statistical uncertainty of $H^*(10)$ for the same slice.

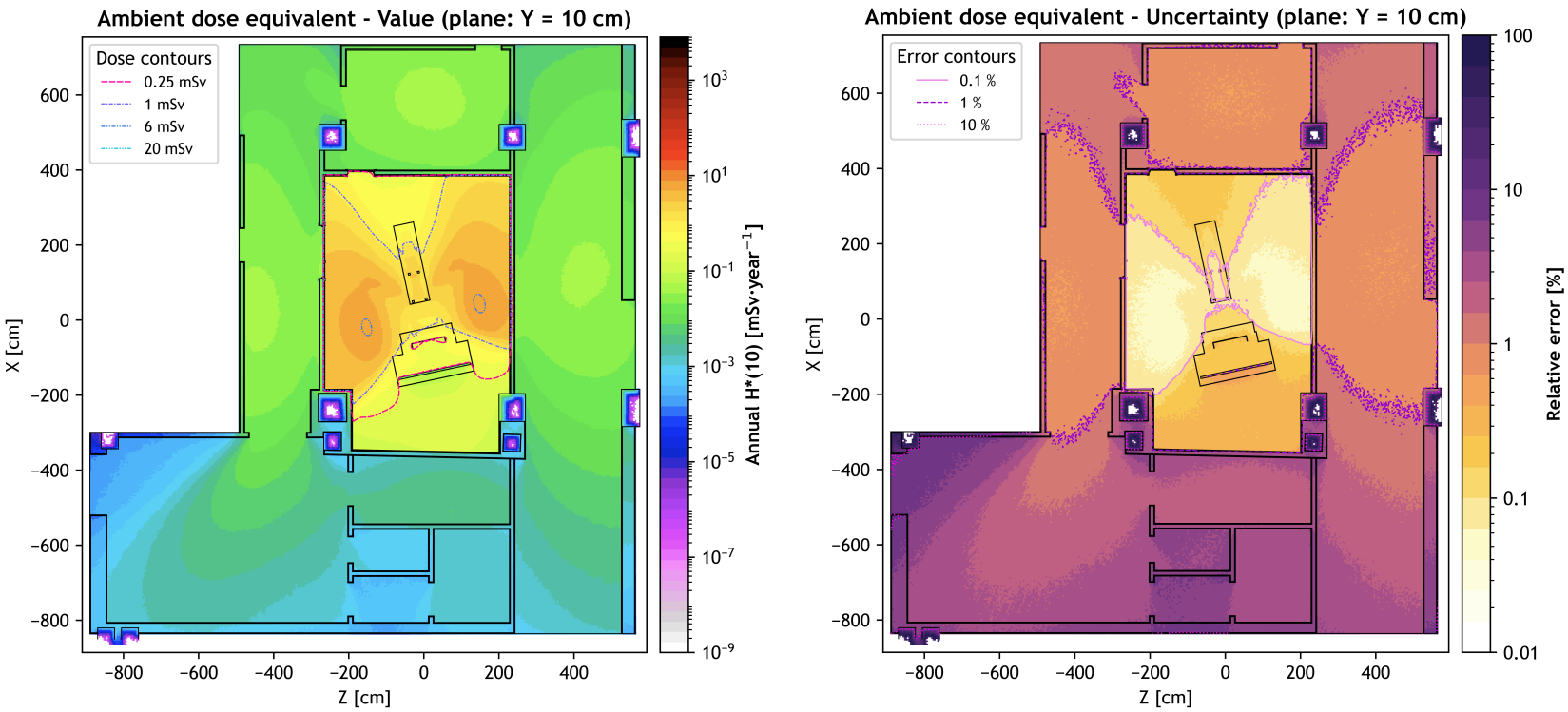

(a) (b)

Figure E.6: Ambient dose equivalent maps obtained from FLUKA USRBIN scoring of $H^*(10)$ distribution, shown for the projection at $Y = 10$ cm, corresponding to the average over the slab $Y \in [0, 20]$ cm: (a) Value map of the ambient dose equivalent rate $H^*(10)$, scaled to typical annual workloads for ^{99m}Tc; (b) Relative statistical uncertainty of $H^*(10)$ for the same slice.

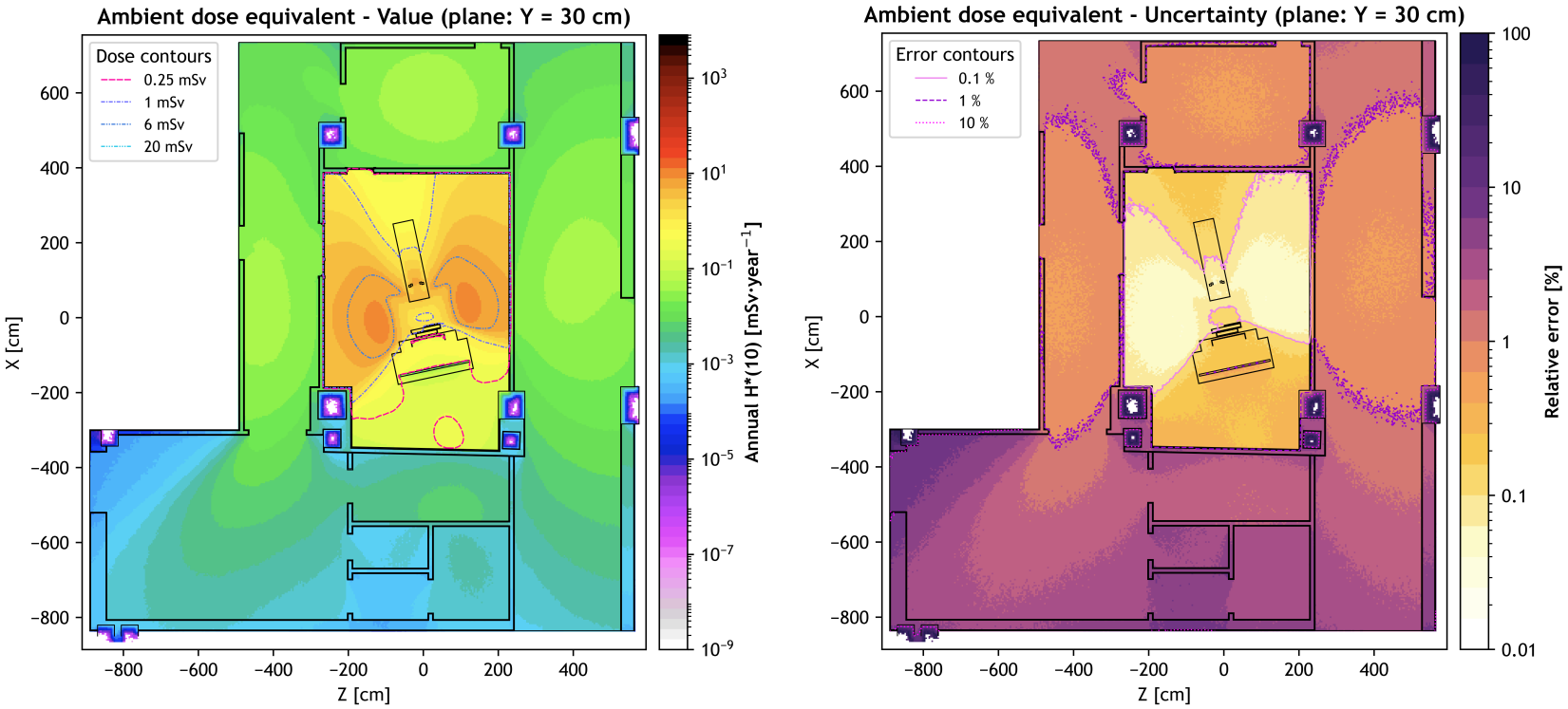

(a) (b)

Figure E.7: Ambient dose equivalent maps obtained from FLUKA USRBIN scoring of $H^*(10)$ distribution, shown for the projection at $Y = 30$ cm, corresponding to the average over the slab $Y \in [20, 40]$ cm: (a) Value map of the ambient dose equivalent rate $H^*(10)$, scaled to typical annual workloads for ^{99m}Tc; (b) Relative statistical uncertainty of $H^*(10)$ for the same slice.

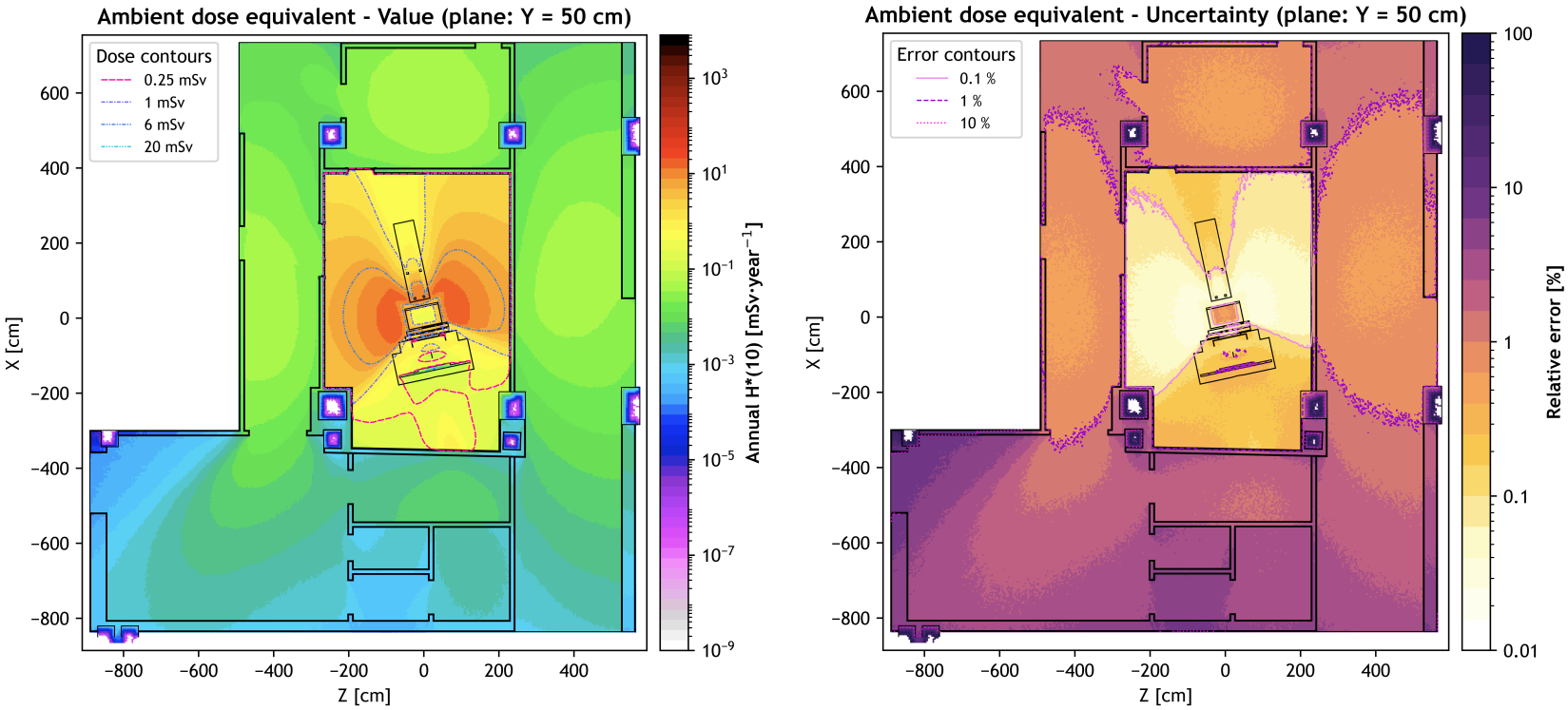

(a) (b)

Figure E.8: Ambient dose equivalent maps obtained from FLUKA USRBIN scoring of $H^*(10)$ distribution, shown for the projection at $Y = 50$ cm, corresponding to the average over the slab $Y \in [40, 60]$ cm: (a) Value map of the ambient dose equivalent rate $H^*(10)$, scaled to typical annual workloads for ^{99m}Tc; (b) Relative statistical uncertainty of $H^*(10)$ for the same slice.

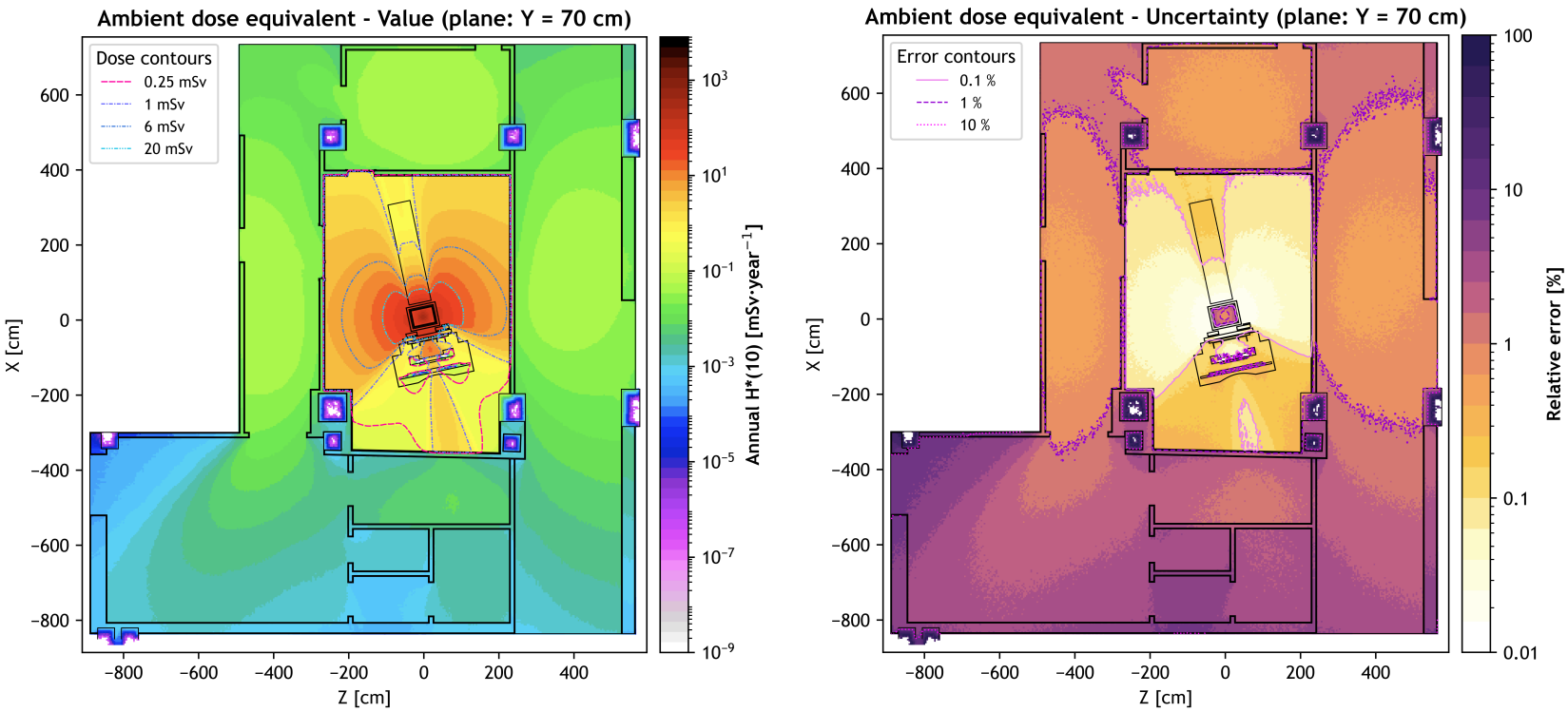

(a) (b)

Figure E.9: Ambient dose equivalent maps obtained from FLUKA USRBIN scoring of $H^*(10)$ distribution, shown for the projection at $Y = 70$ cm, corresponding to the average over the slab $Y \in [60, 80]$ cm: (a) Value map of the ambient dose equivalent rate $H^*(10)$, scaled to typical annual workloads for ^{99m}Tc; (b) Relative statistical uncertainty of $H^*(10)$ for the same slice.

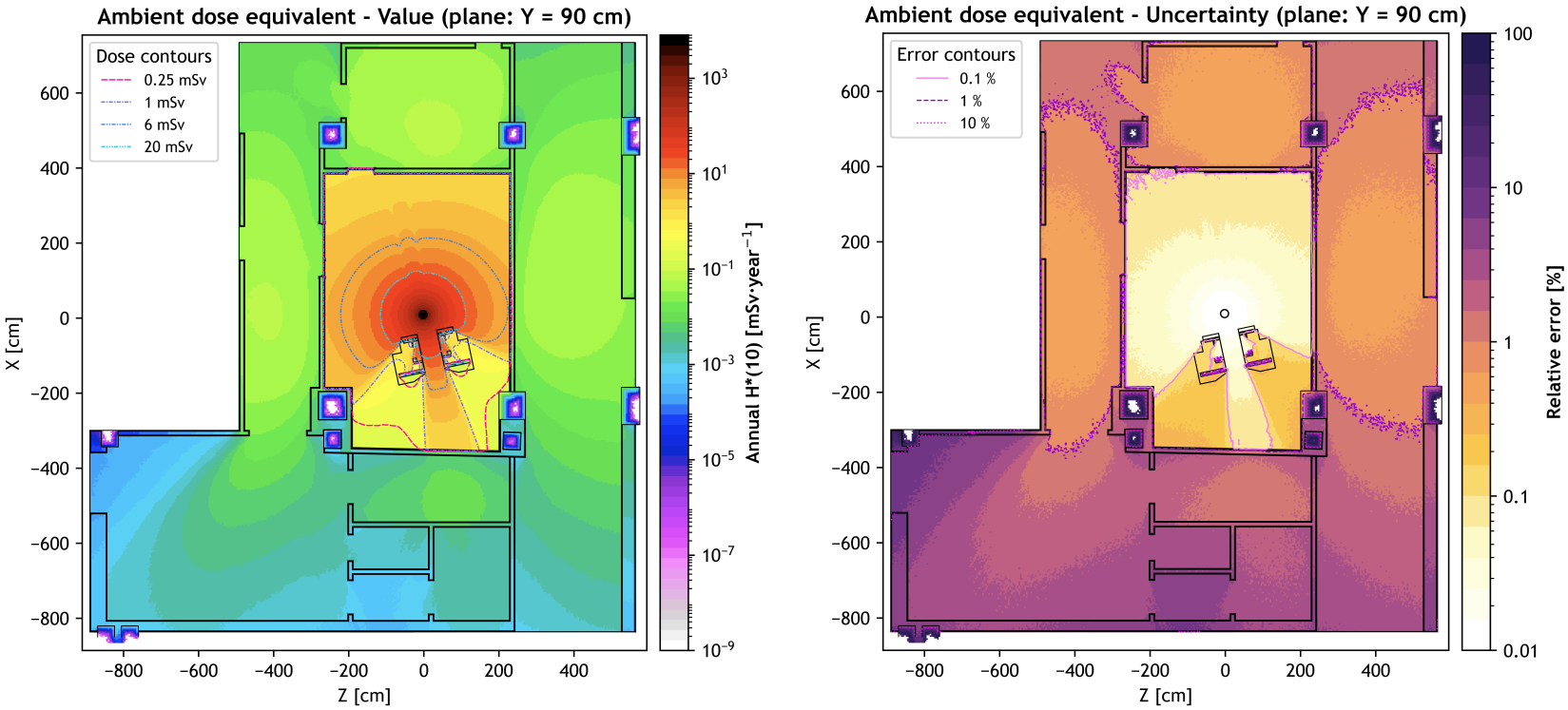

(a) (b)

Figure E.10: Ambient dose equivalent maps obtained from FLUKA USRBIN scoring of $H^*(10)$ distribution, shown for the projection at $Y = 90$ cm, corresponding to the average over the slab $Y \in [80, 100]$ cm: (a) Value map of the ambient dose equivalent rate $H^*(10)$, scaled to typical annual workloads for ^{99m}Tc; (b) Relative statistical uncertainty of $H^*(10)$ for the same slice.

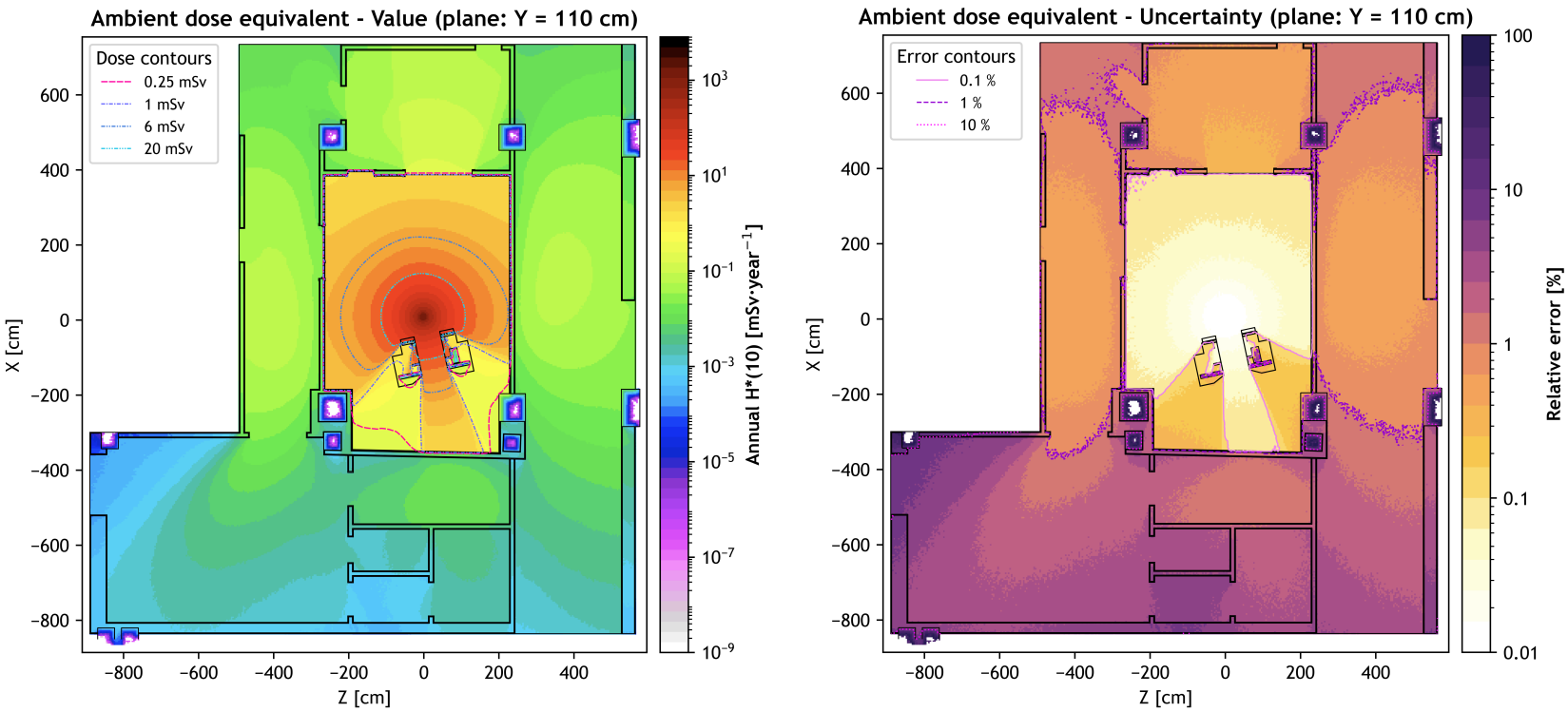

(a) (b)

Figure E.11: Ambient dose equivalent maps obtained from FLUKA USRBIN scoring of $H^*(10)$ distribution, shown for the projection at $Y = 110$ cm, corresponding to the average over the slab $Y \in [100, 120]$ cm: (a) Value map of the ambient dose equivalent rate $H^*(10)$, scaled to typical annual workloads for ^{99m}Tc; (b) Relative statistical uncertainty of $H^*(10)$ for the same slice.

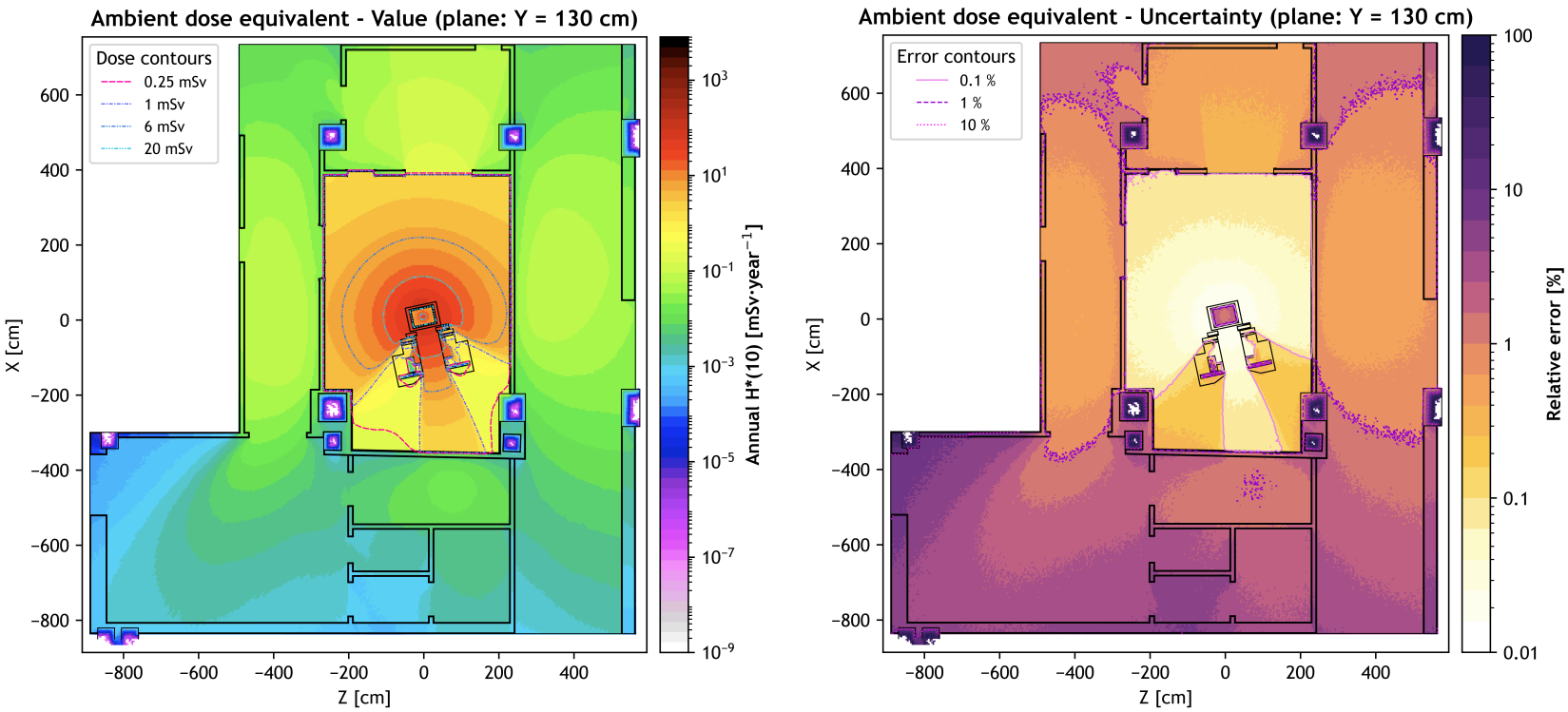

(a) (b)

Figure E.12: Ambient dose equivalent maps obtained from FLUKA USRBIN scoring of $H^*(10)$ distribution, shown for the projection at $Y = 130$ cm, corresponding to the average over the slab $Y \in [120, 140]$ cm: (a) Value map of the ambient dose equivalent rate $H^*(10)$, scaled to typical annual workloads for ^{99m}Tc; (b) Relative statistical uncertainty of $H^*(10)$ for the same slice.

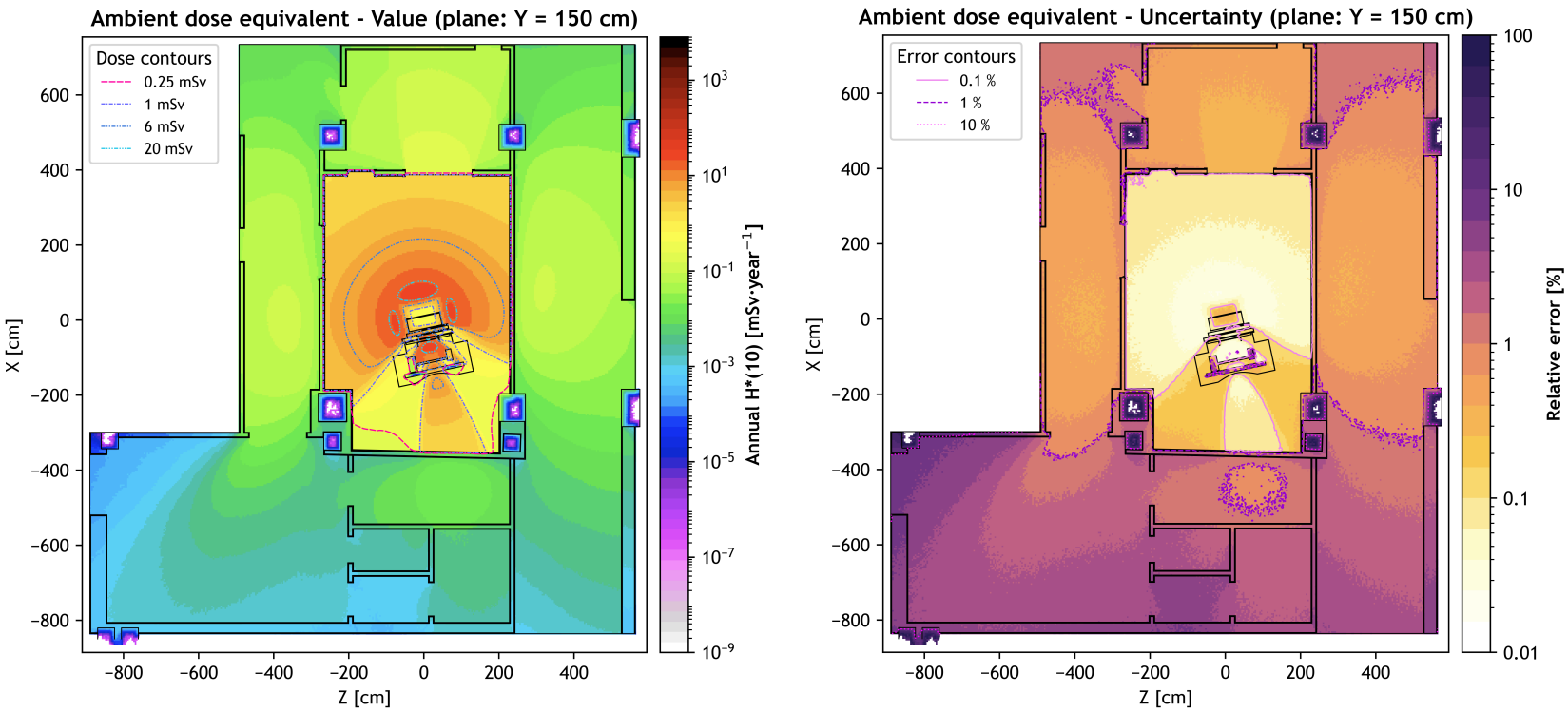

(a) (b)

Figure E.13: Ambient dose equivalent maps obtained from FLUKA USRBIN scoring of $H^*(10)$ distribution, shown for the projection at $Y = 150$ cm, corresponding to the average over the slab $Y \in [140, 160]$ cm: (a) Value map of the ambient dose equivalent rate $H^*(10)$, scaled to typical annual workloads for ^{99m}Tc; (b) Relative statistical uncertainty of $H^*(10)$ for the same slice.

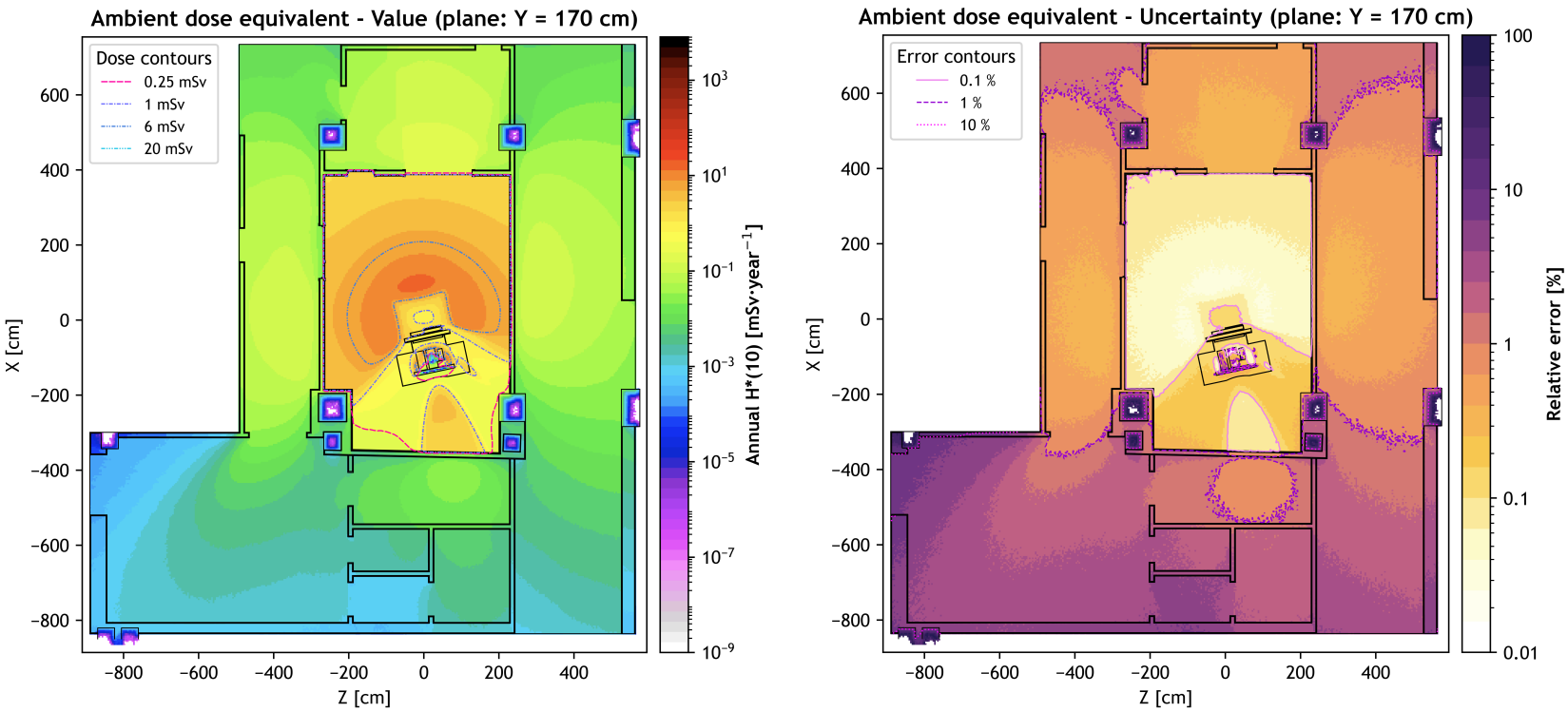

(a) (b)

Figure E.14: Ambient dose equivalent maps obtained from FLUKA USRBIN scoring of $H^*(10)$ distribution, shown for the projection at $Y = 170$ cm, corresponding to the average over the slab $Y \in [160, 180]$ cm: (a) Value map of the ambient dose equivalent rate $H^*(10)$, scaled to typical annual workloads for ^{99m}Tc; (b) Relative statistical uncertainty of $H^*(10)$ for the same slice.

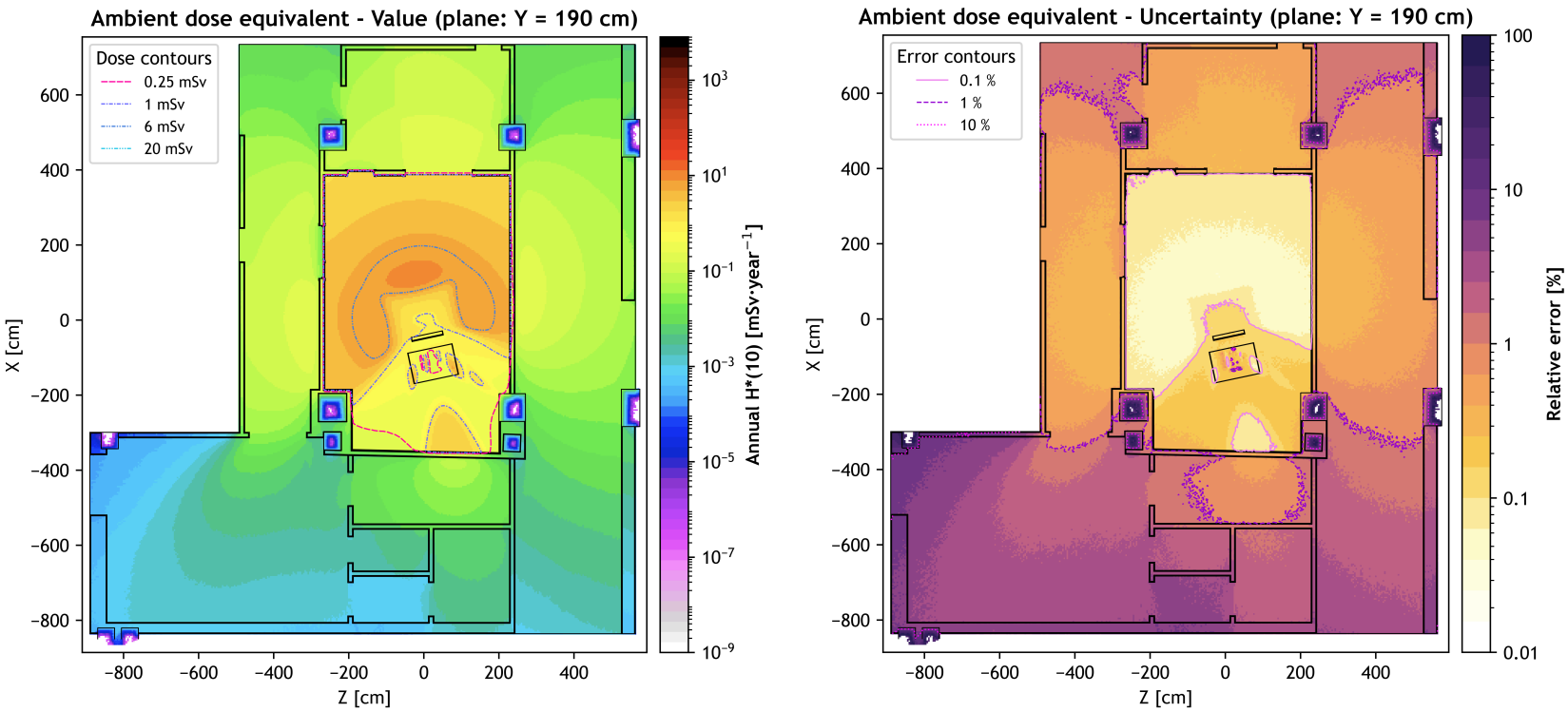

(a) (b)

Figure E.15: Ambient dose equivalent maps obtained from FLUKA USRBIN scoring of $H^*(10)$ distribution, shown for the projection at $Y = 190$ cm, corresponding to the average over the slab $Y \in [180, 200]$ cm: (a) Value map of the ambient dose equivalent rate $H^*(10)$, scaled to typical annual workloads for ^{99m}Tc; (b) Relative statistical uncertainty of $H^*(10)$ for the same slice.

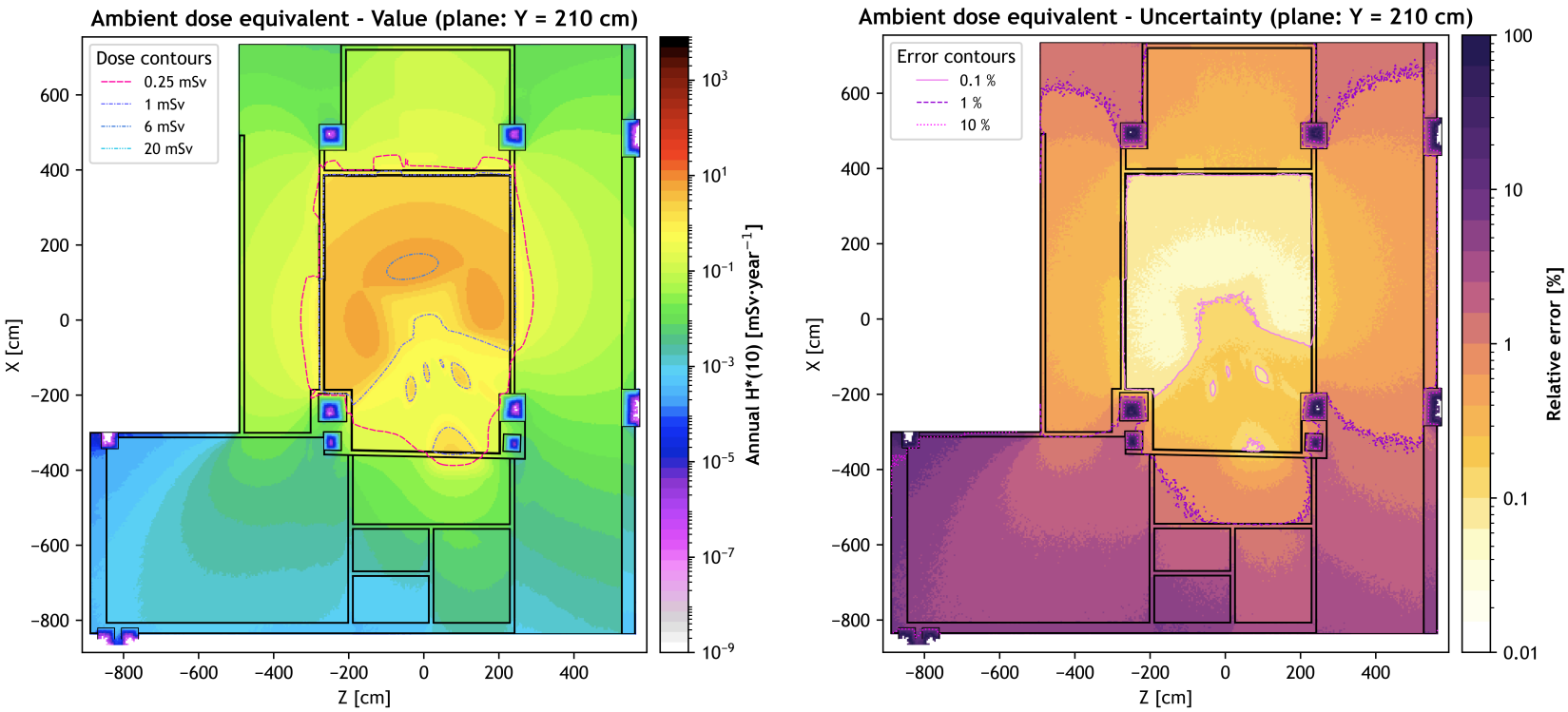

(a) (b)

Figure E.16: Ambient dose equivalent maps obtained from FLUKA USRBIN scoring of $H^*(10)$ distribution, shown for the projection at $Y = 210$ cm, corresponding to the average over the slab $Y \in [200, 220]$ cm: (a) Value map of the ambient dose equivalent rate $H^*(10)$, scaled to typical annual workloads for ^{99m}Tc; (b) Relative statistical uncertainty of $H^*(10)$ for the same slice.

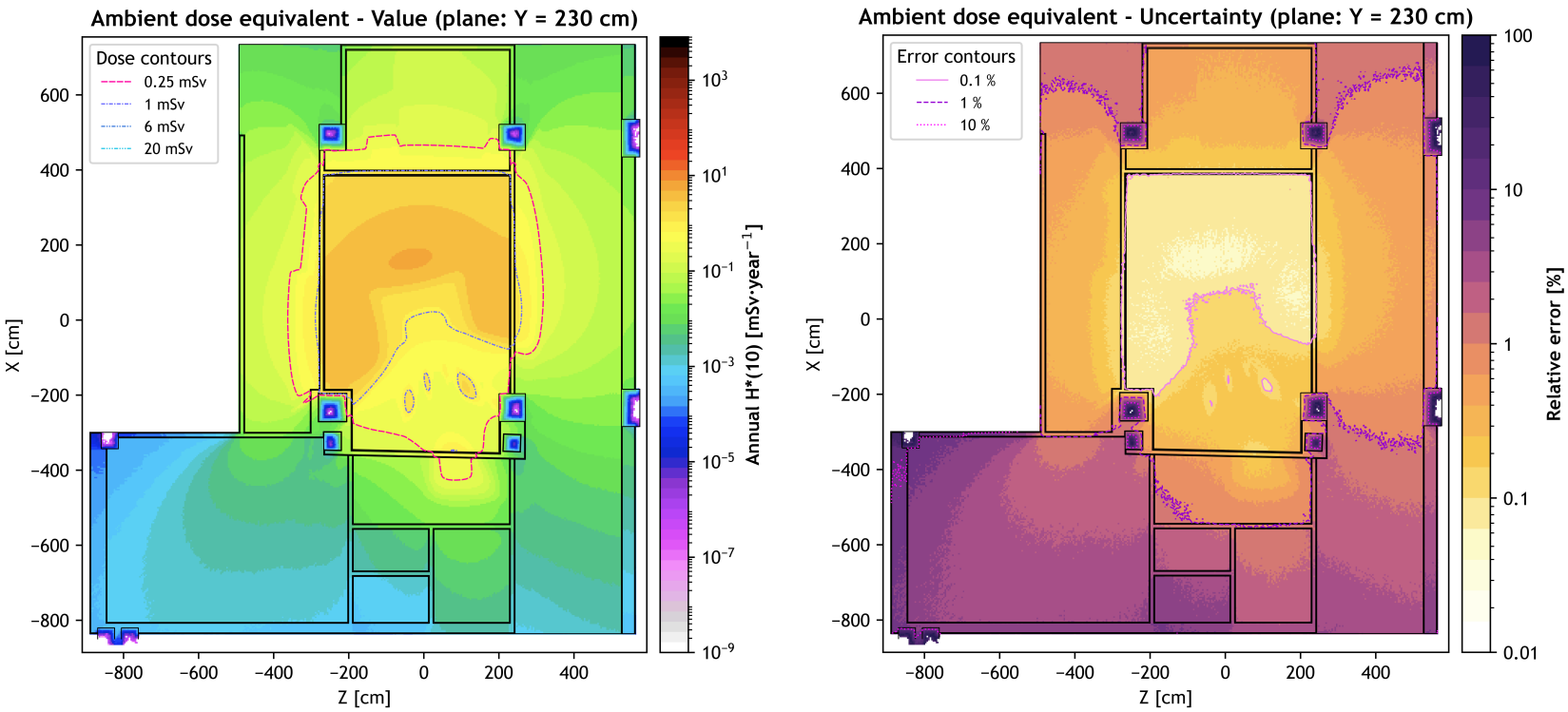

(a) (b)

Figure E.17: Ambient dose equivalent maps obtained from FLUKA USRBIN scoring of $H^*(10)$ distribution, shown for the projection at $Y = 230$ cm, corresponding to the average over the slab $Y \in [220, 240]$ cm: (a) Value map of the ambient dose equivalent rate $H^*(10)$, scaled to typical annual workloads for ^{99m}Tc; (b) Relative statistical uncertainty of $H^*(10)$ for the same slice.

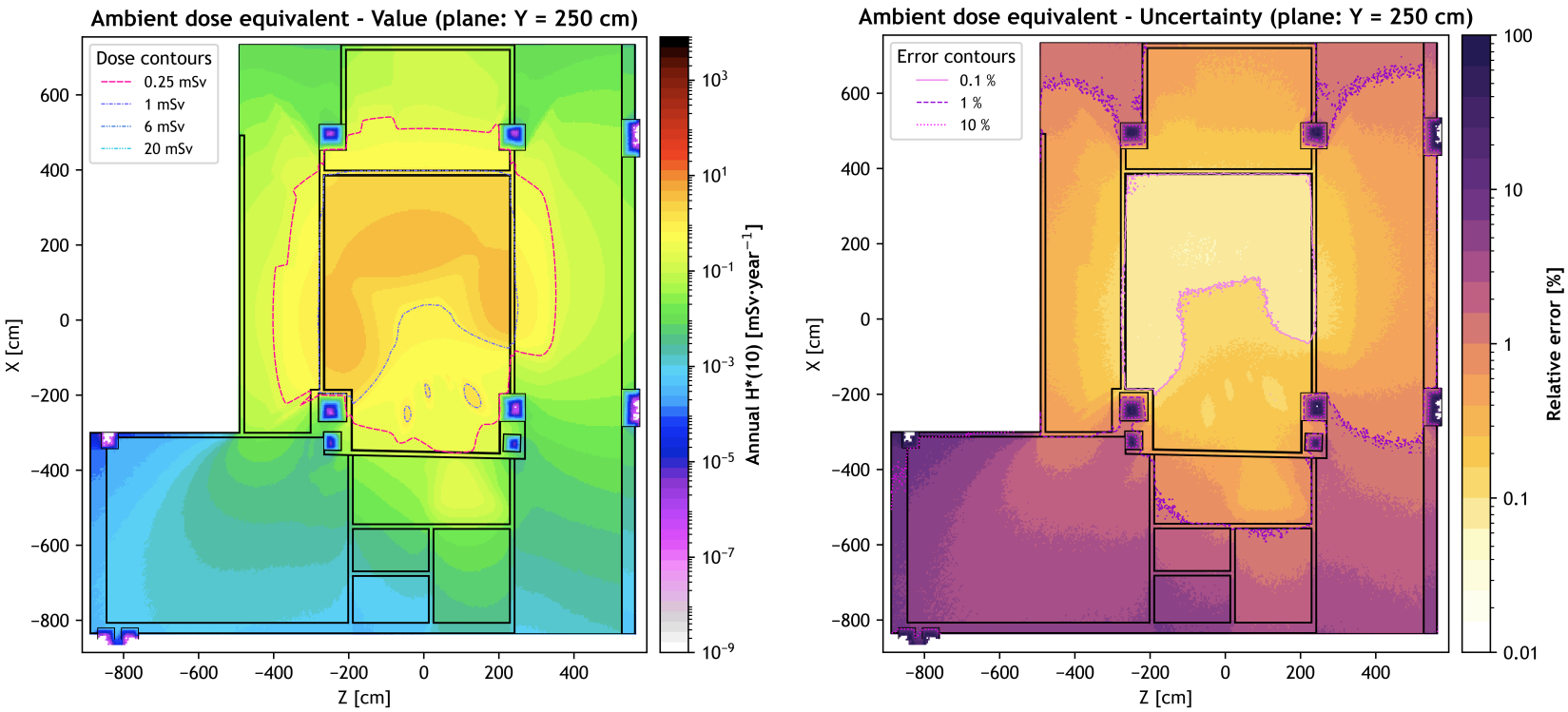

(a) (b)

Figure E.18: Ambient dose equivalent maps obtained from FLUKA USRBIN scoring of $H^*(10)$ distribution, shown for the projection at $Y = 250$ cm, corresponding to the average over the slab $Y \in [240, 260]$ cm: (a) Value map of the ambient dose equivalent rate $H^*(10)$, scaled to typical annual workloads for ^{99m}Tc; (b) Relative statistical uncertainty of $H^*(10)$ for the same slice.

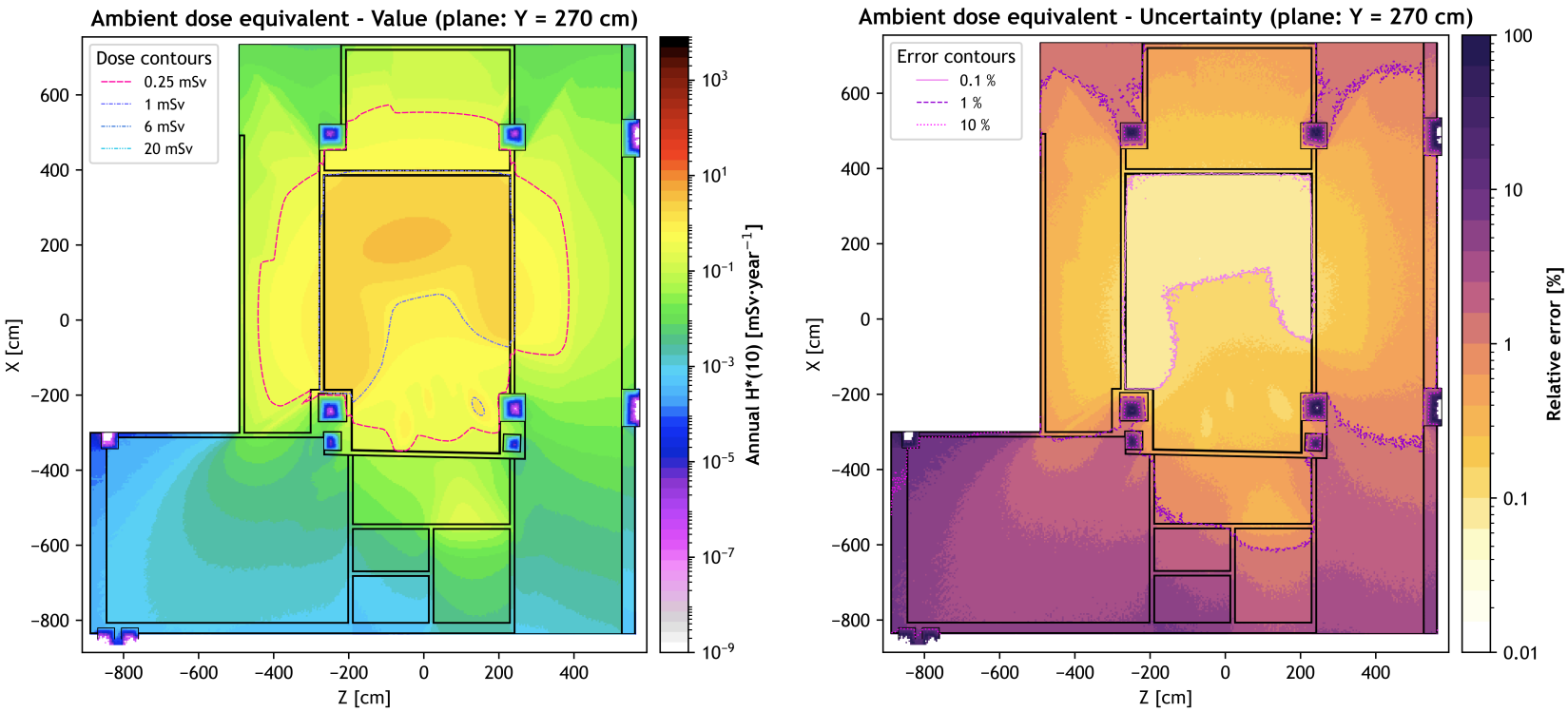

(a) (b)

Figure E.19: Ambient dose equivalent maps obtained from FLUKA USRBIN scoring of $H^*(10)$ distribution, shown for the projection at $Y = 270$ cm, corresponding to the average over the slab $Y \in [260, 280]$ cm: (a) Value map of the ambient dose equivalent rate $H^*(10)$, scaled to typical annual workloads for ^{99m}Tc; (b) Relative statistical uncertainty of $H^*(10)$ for the same slice.

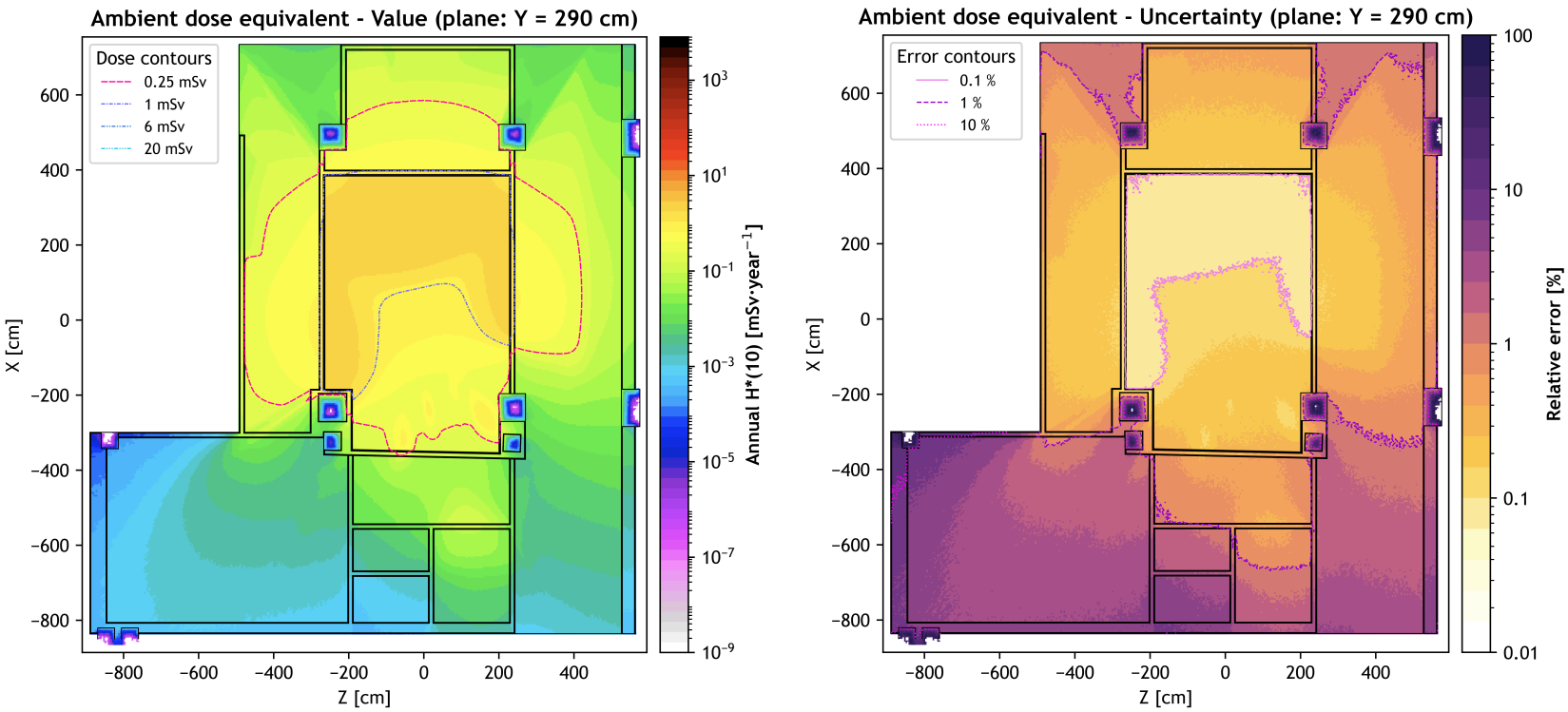

(a) (b)

Figure E.20: Ambient dose equivalent maps obtained from FLUKA USRBIN scoring of $H^*(10)$ distribution, shown for the projection at $Y = 290$ cm, corresponding to the average over the slab $Y \in [280, 300]$ cm: (a) Value map of the ambient dose equivalent rate $H^*(10)$, scaled to typical annual workloads for ^{99m}Tc; (b) Relative statistical uncertainty of $H^*(10)$ for the same slice.

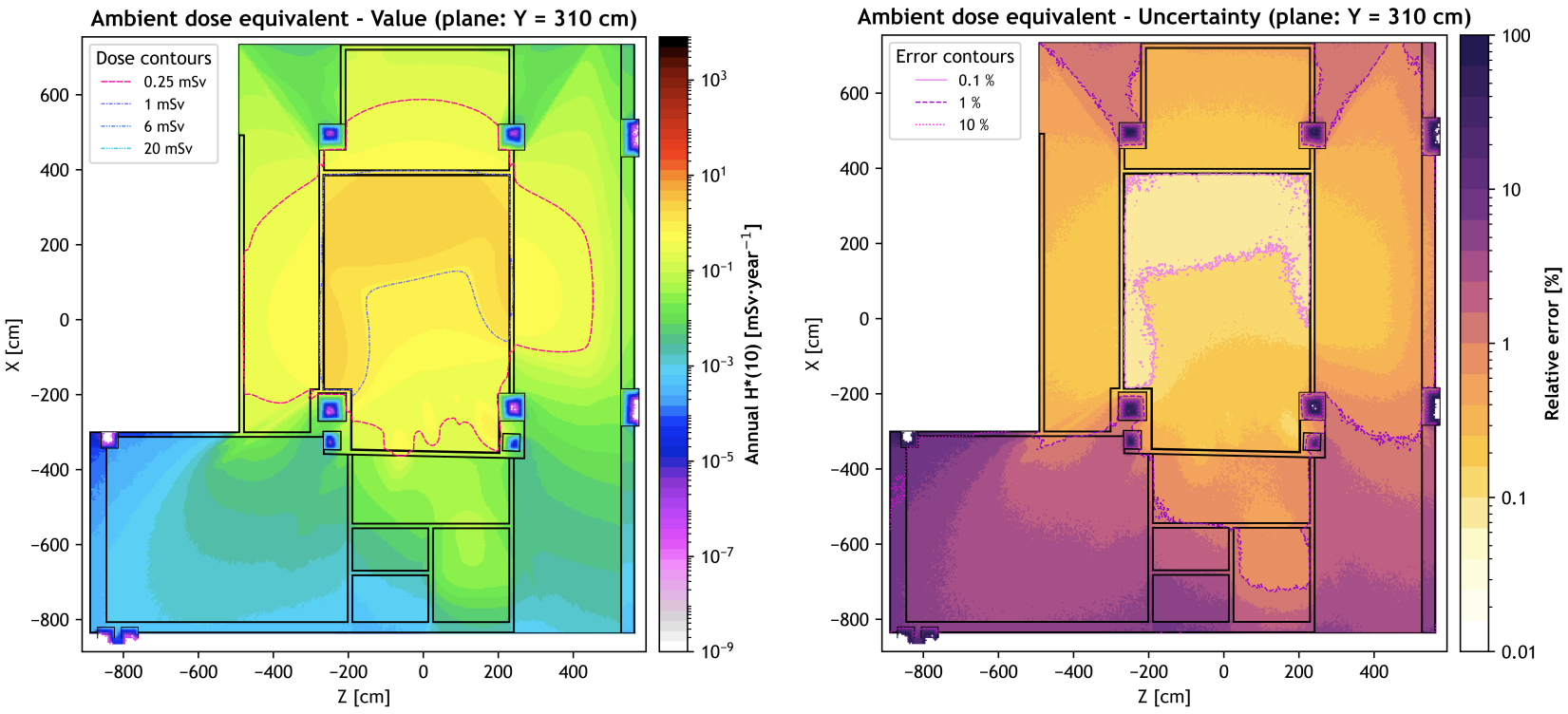

(a) (b)

Figure E.21: Ambient dose equivalent maps obtained from FLUKA USRBIN scoring of $H^*(10)$ distribution, shown for the projection at $Y = 310$ cm, corresponding to the average over the slab $Y \in [300, 320]$ cm: (a) Value map of the ambient dose equivalent rate $H^*(10)$, scaled to typical annual workloads for ^{99m}Tc; (b) Relative statistical uncertainty of $H^*(10)$ for the same slice.

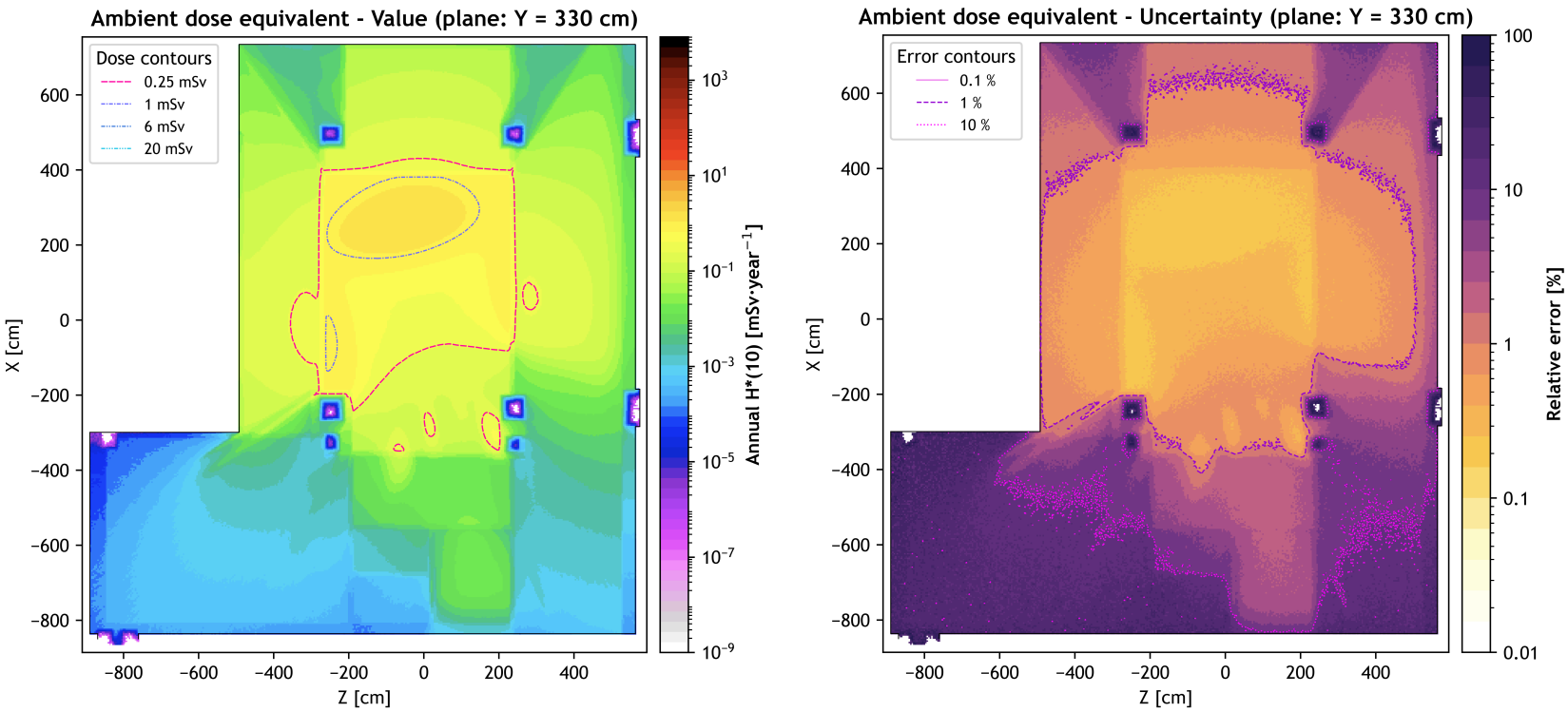

(a) (b)

Figure E.22: Ambient dose equivalent maps obtained from FLUKA USRBIN scoring of $H^*(10)$ distribution, shown for the projection at $Y = 330$ cm, corresponding to the average over the slab $Y \in [320, 340]$ cm: (a) Value map of the ambient dose equivalent rate $H^*(10)$, scaled to typical annual workloads for ^{99m}Tc; (b) Relative statistical uncertainty of $H^*(10)$ for the same slice.

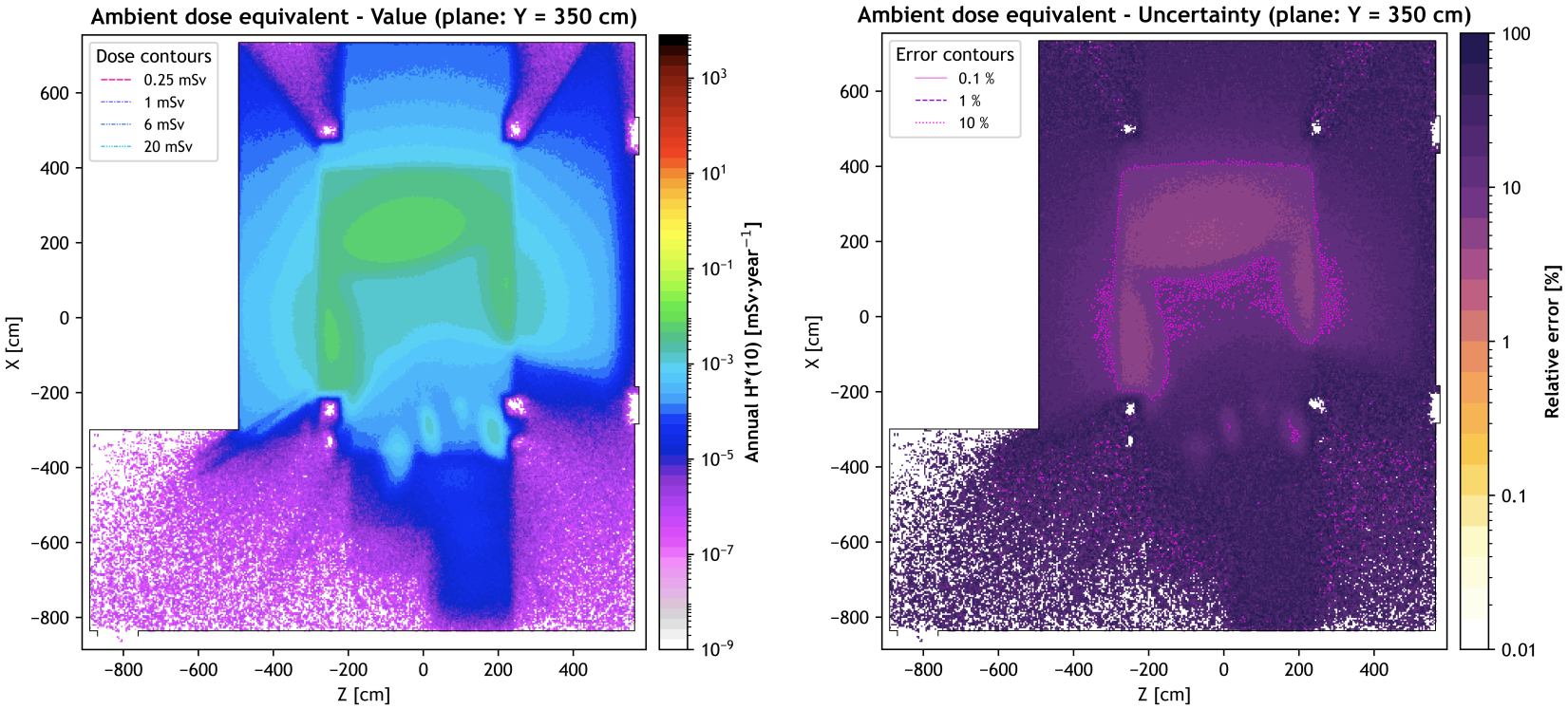

(a) (b)

Figure E.23: Ambient dose equivalent maps obtained from FLUKA USRBIN scoring of $H^*(10)$ distribution, shown for the projection at $Y = 350$ cm, corresponding to the average over the slab $Y \in [340, 360]$ cm: (a) Value map of the ambient dose equivalent rate $H^*(10)$, scaled to typical annual workloads for ^{99m}Tc; (b) Relative statistical uncertainty of $H^*(10)$ for the same slice.

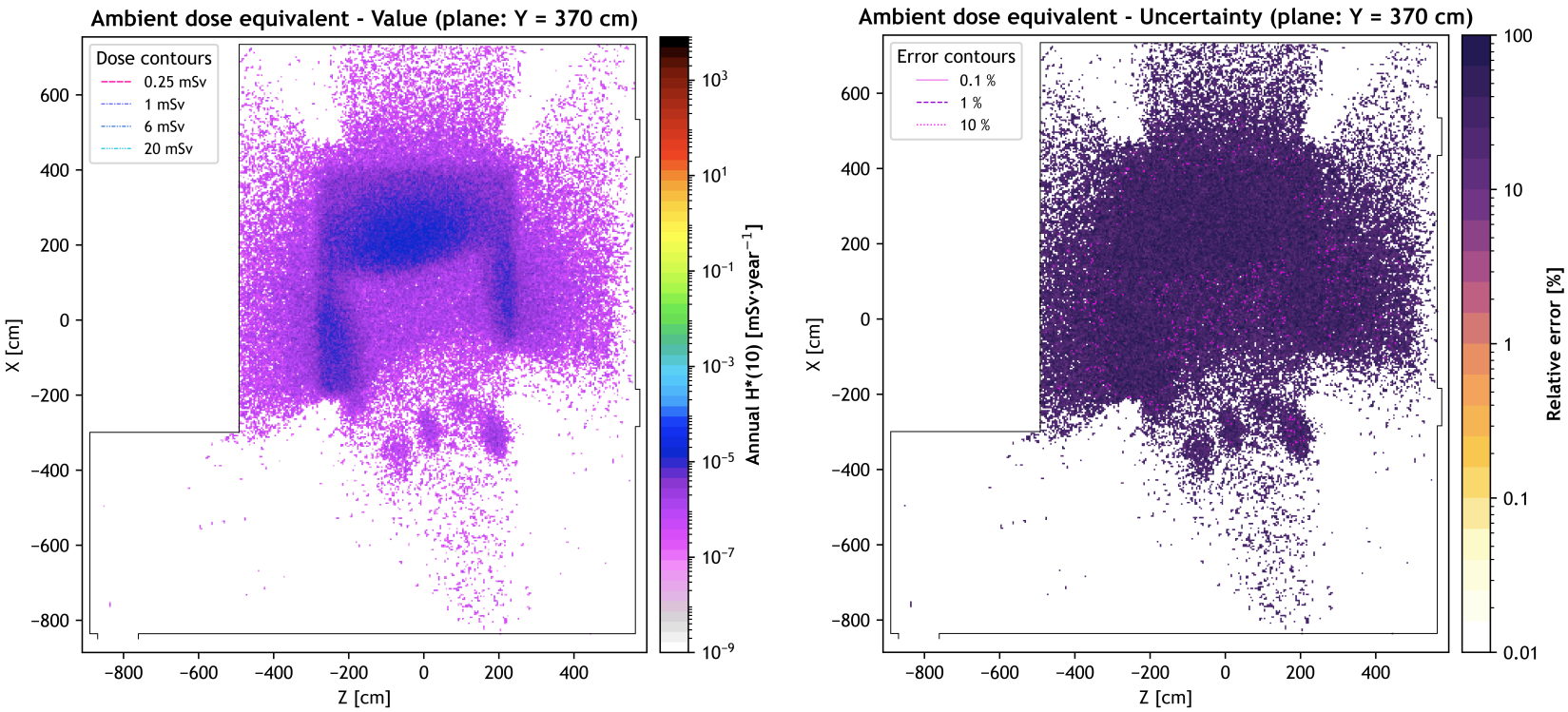

(a) (b)

Figure E.24: Ambient dose equivalent maps obtained from FLUKA USRBIN scoring of $H^*(10)$ distribution, shown for the projection at $Y = 370$ cm, corresponding to the average over the slab $Y \in [360, 380]$ cm: (a) Value map of the ambient dose equivalent rate $H^*(10)$, scaled to typical annual workloads for ^{99m}Tc; (b) Relative statistical uncertainty of $H^*(10)$ for the same slice.

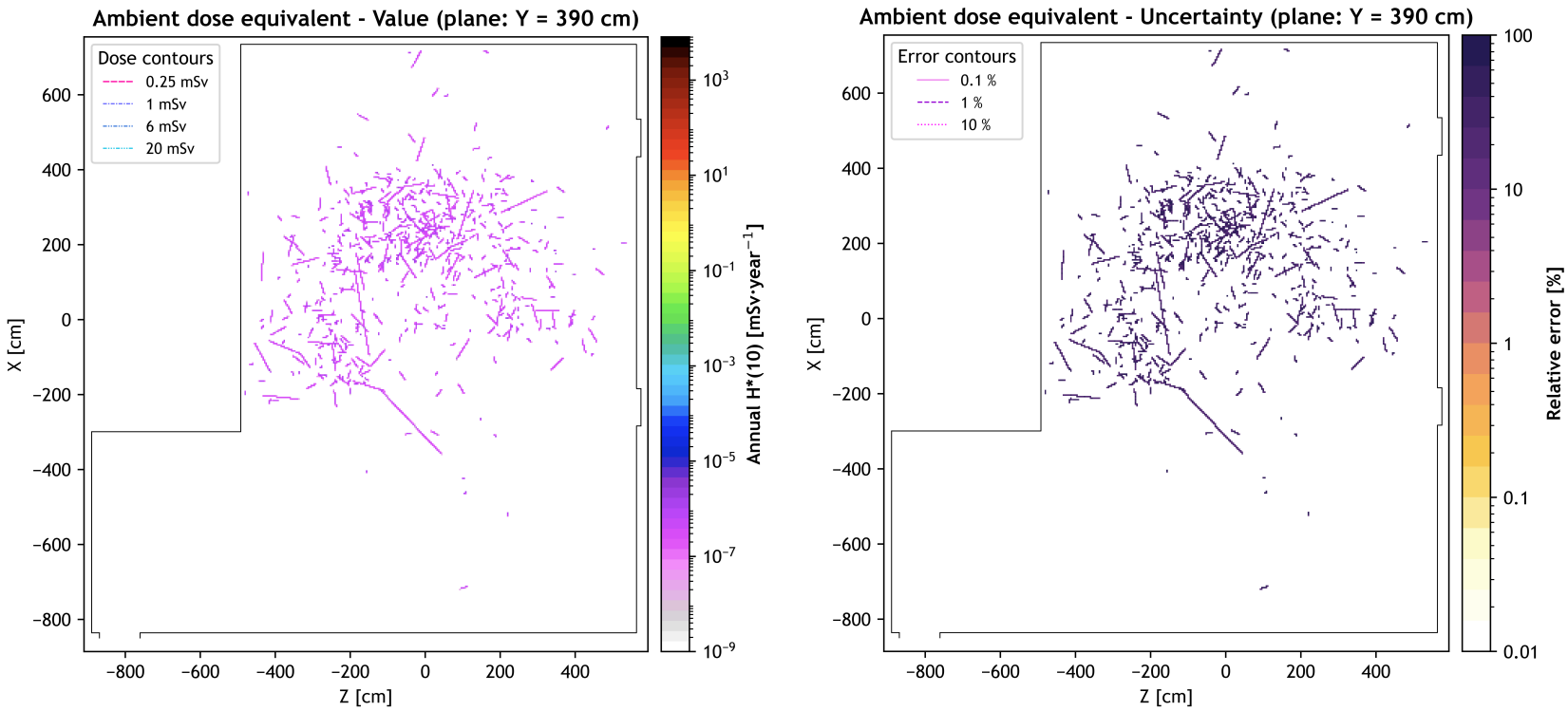

(a) (b)

Figure E.25: Ambient dose equivalent maps obtained from FLUKA USRBIN scoring of $H^*(10)$ distribution, shown for the projection at $Y = 390$ cm, corresponding to the average over the slab $Y \in [380, 400]$ cm: (a) Value map of the ambient dose equivalent rate $H^*(10)$, scaled to typical annual workloads for ^{99m}Tc; (b) Relative statistical uncertainty of $H^*(10)$ for the same slice.

F

Energy deposition in regions

Tables F.1 and F.2 present the energy deposition results by region, given both in absolute units (keV) and as a percentage of the total energy generated, for the ^{99m}Tc and ^{177}Lu main study simulations. Energies are shown in scientific notation as $(X \pm 0.Y) \times 10^{Z}$, where the quoted uncertainty is the (1σ) MC statistical error (rounded to one decimal place in the mantissa). Percentages are reported as values only to four decimal places. Entries reported as < 0.0001 indicate that the reported value is below this threshold. By construction, the percentages sum to 100%. The vacuum region (`VACU`) is identically zero, as no interactions occur there and thus, no energy deposition occurs.

Table F.1: Energy deposition by region, values both in energy (keV) and as a percentage of the total energy, and the associated statistical uncertainty, as produced by FLUKA, for the ^{99m}Tc main study.

Region	**Energy Deposition** keV	**Percentage of Total** %
BLKBODY	$(3963.9 \pm 0.2) \times 10^{-4}$	0.1762
AIRt	$(0.7 \pm 0.7) \times 10^{-9}$	< 0.0001
AIRr	$(5103.6 \pm 0.1) \times 10^{-4}$	0.2269
AIRb	$(0.3 \pm 0.2) \times 10^{-9}$	< 0.0001
EXTa	$(2806.0 \pm 0.4) \times 10^{-5}$	0.0125
W1A	$(740.0 \pm 0.5) \times 10^{-6}$	0.0003
W1G	$(19261.4 \pm 0.4) \times 10^{-4}$	0.8562
W1L	$(12922.1 \pm 0.3) \times 10^{-4}$	0.5744
W1P	$(5009.8 \pm 0.5) \times 10^{-5}$	0.0223
W2A	$(1117.9 \pm 0.6) \times 10^{-6}$	0.0005
W2G	$(43079.8 \pm 0.5) \times 10^{-4}$	1.9150
W2L	$(43235.8 \pm 0.7) \times 10^{-4}$	1.9219
W2P	$(8219.6 \pm 0.5) \times 10^{-5}$	0.0365
W3A	$(97.7 \pm 0.2) \times 10^{-6}$	< 0.0001

Continued on next page

Continued from previous page

Region	**Energy Deposition** keV	**Percentage of Total** %
W3G	$(5714.7 \pm 0.2) \times 10^{-4}$	0.2540
W3L	$(7890.7 \pm 0.3) \times 10^{-4}$	0.3508
W3P	$(631.8 \pm 0.1) \times 10^{-5}$	0.0028
W4A	$(776.6 \pm 0.5) \times 10^{-6}$	0.0003
W4G	$(40102.3 \pm 0.6) \times 10^{-4}$	1.7826
W4L	$(47115.8 \pm 0.7) \times 10^{-4}$	2.0944
W4P	$(6006.3 \pm 0.6) \times 10^{-5}$	0.0267
WEG	$(5324.9 \pm 0.2) \times 10^{-4}$	0.2367
FLOOR	$(60181.1 \pm 0.7) \times 10^{-4}$	2.6752
CEILING	$(63745.4 \pm 0.8) \times 10^{-4}$	2.8336
PILLC	$(4182.9 \pm 0.2) \times 10^{-4}$	0.1859
$PILL_P$	$(1105.3 \pm 0.2) \times 10^{-5}$	0.0049
D1L	$(5239.9 \pm 0.3) \times 10^{-4}$	0.2329
D1P	$(2080.1 \pm 0.3) \times 10^{-5}$	0.0092
D1J	$(1186.1 \pm 0.3) \times 10^{-5}$	0.0053
D2L	$(18290.1 \pm 0.5) \times 10^{-4}$	0.8130
D2P	$(9775.1 \pm 0.6) \times 10^{-5}$	0.0435
D2J	$(1464.4 \pm 0.3) \times 10^{-5}$	0.0065
WINDOW	$(8706.1 \pm 0.3) \times 10^{-4}$	0.3870
WINDL	$(2170.0 \pm 0.2) \times 10^{-4}$	0.0965
WINDJ	$(1491.9 \pm 0.3) \times 10^{-5}$	0.0066
PHANTOM	$(76466.4 \pm 0.5) \times 10^{-4}$	3.3991
WATER	$(131277.8 \pm 0.3) \times 10^{-3}$	58.3558
TLDA1	$(4.2 \pm 0.4) \times 10^{-8}$	< 0.0001
TLDA2	$(0.4 \pm 0.2) \times 10^{-8}$	< 0.0001
TLDB1	$(8.9 \pm 0.6) \times 10^{-8}$	< 0.0001
TLDB2	$(0.3 \pm 0.2) \times 10^{-10}$	< 0.0001
TLDC1	$(3.1 \pm 0.3) \times 10^{-8}$	< 0.0001
TLDC2	$(0.4 \pm 0.4) \times 10^{-9}$	< 0.0001
TLDD	$(10.9 \pm 0.6) \times 10^{-8}$	< 0.0001

Continued on next page

Continued from previous page

Region	**Energy Deposition**	**Percentage of Total**
	keV	%
TLDE1	$(10.3 \pm 0.2) \times 10^{-7}$	< 0.0001
TLDE2	$(10.6 \pm 0.2) \times 10^{-7}$	< 0.0001
TLDE3	$(1.2 \pm 0.2) \times 10^{-8}$	< 0.0001
TLDE4	$(1.5 \pm 0.2) \times 10^{-8}$	< 0.0001
PCTT	$(11382.2 \pm 0.2) \times 10^{-4}$	0.5060
PCTTf	$(7514.0 \pm 0.5) \times 10^{-5}$	0.0334
PCSUPP	$(4499.4 \pm 0.2) \times 10^{-4}$	0.2000
PCTBL	$(14788.0 \pm 0.4) \times 10^{-4}$	0.6574
PCCOV	$(3031.2 \pm 0.4) \times 10^{-5}$	0.0135
COLL	$(23811.8 \pm 0.1) \times 10^{-3}$	10.5849
ALCV	$(1348.9 \pm 0.3) \times 10^{-5}$	0.0060
FOAM	$(23.6 \pm 0.4) \times 10^{-7}$	< 0.0001
CRYS	$(2405.6 \pm 0.2) \times 10^{-4}$	0.1069
LTGD	$(112.3 \pm 0.3) \times 10^{-6}$	< 0.0001
OPTI	$(8.4 \pm 0.2) \times 10^{-7}$	< 0.0001
PMTS	$(130.1 \pm 0.3) \times 10^{-6}$	< 0.0001
ELEC	$(24.5 \pm 0.1) \times 10^{-6}$	< 0.0001
VACU	0	0
PBCS	$(13285.0 \pm 0.4) \times 10^{-4}$	0.5905
ALCS	$(10607.6 \pm 0.3) \times 10^{-4}$	0.4715
XRT	$(5783.6 \pm 0.3) \times 10^{-4}$	0.2571
HEX	$(1413.9 \pm 0.1) \times 10^{-4}$	0.0628
EBD	$(1124.4 \pm 0.1) \times 10^{-4}$	0.0500
HVG	$(4023.4 \pm 0.2) \times 10^{-4}$	0.1788
DTS	$(6145.8 \pm 0.3) \times 10^{-4}$	0.2732
SUPPORTS	$(13240.1 \pm 0.1) \times 10^{-3}$	5.8855
COVER	$(8402.3 \pm 0.2) \times 10^{-4}$	0.3735
COVERG	$(4396.9 \pm 0.5) \times 10^{-5}$	0.0195
COVERA	$(4117.2 \pm 0.2) \times 10^{-4}$	0.1830

Table F.2: Energy deposition by region, values both in energy (keV) and as a percentage of the total energy, and the associated statistical uncertainty, as produced by FLUKA, for the ^{177}Lu main study.

Region	**Energy Deposition** keV	**Percentage of Total** %
BLKBODY	$(1891.1 \pm 0.1) \times 10^{-4}$	0.1045
AIRt	$(0.9 \pm 0.3) \times 10^{-9}$	< 0.0001
AIRr	$(14046.3 \pm 0.6) \times 10^{-5}$	0.0776
AIRb	$(3.6 \pm 0.8) \times 10^{-9}$	< 0.0001
EXTa	$(987.1 \pm 0.1) \times 10^{-5}$	0.0055
W1A	$(221.9 \pm 0.2) \times 10^{-6}$	0.0001
W1G	$(4722.1 \pm 0.1) \times 10^{-4}$	0.2609
W1L	$(3405.2 \pm 0.1) \times 10^{-4}$	0.1881
W1P	$(1455.2 \pm 0.2) \times 10^{-5}$	0.0080
W2A	$(324.3 \pm 0.3) \times 10^{-6}$	0.0002
W2G	$(10557.9 \pm 0.2) \times 10^{-4}$	0.5832
W2L	$(11774.4 \pm 0.3) \times 10^{-4}$	0.6504
W2P	$(2363.5 \pm 0.3) \times 10^{-5}$	0.0131
W3A	$(332.7 \pm 0.9) \times 10^{-7}$	< 0.0001
W3G	$(14143.8 \pm 0.8) \times 10^{-5}$	0.0781
W3L	$(2059.6 \pm 0.1) \times 10^{-4}$	0.1138
W3P	$(2185.6 \pm 0.8) \times 10^{-6}$	0.0012
W4A	$(245.9 \pm 0.3) \times 10^{-6}$	0.0001
W4G	$(9934.8 \pm 0.2) \times 10^{-4}$	0.5488
W4L	$(12335.4 \pm 0.3) \times 10^{-4}$	0.6814
W4P	$(1922.6 \pm 0.3) \times 10^{-5}$	0.0106
WEG	$(16286.2 \pm 1.0) \times 10^{-5}$	0.0900
FLOOR	$(15862.1 \pm 0.3) \times 10^{-4}$	0.8763
CEILING	$(17060.8 \pm 0.3) \times 10^{-4}$	0.9425
PILLC	$(13073.0 \pm 0.8) \times 10^{-5}$	0.0722
PILL_P	$(344.2 \pm 0.1) \times 10^{-5}$	0.0019
D1L	$(13440.8 \pm 0.9) \times 10^{-5}$	0.0742
D1P	$(576.4 \pm 0.1) \times 10^{-5}$	0.0032

Continued on next page

Continued from previous page

Region	**Energy Deposition** keV	**Percentage of Total** %
D1J	$(3061.2 \pm 0.8) \times 10^{-6}$	0.0017
D2L	$(4715.6 \pm 0.2) \times 10^{-4}$	0.2605
D2P	$(2708.8 \pm 0.2) \times 10^{-5}$	0.0150
D2J	$(387.8 \pm 0.1) \times 10^{-5}$	0.0021
WINDOW	$(1977.1 \pm 0.1) \times 10^{-4}$	0.1092
WINDL	$(5495.6 \pm 0.6) \times 10^{-5}$	0.0304
WINDJ	$(404.5 \pm 0.1) \times 10^{-5}$	0.0022
PHANTOM	$(23385.1 \pm 0.1) \times 10^{-3}$	12.9185
WATER	$(134897.4 \pm 0.3) \times 10^{-3}$	74.5204
TLDA1	$(1.2 \pm 0.2) \times 10^{-8}$	< 0.0001
TLDA2	$(2.8 \pm 1.0) \times 10^{-9}$	< 0.0001
TLDB1	$(2.4 \pm 0.3) \times 10^{-8}$	< 0.0001
TLDB2	$(1.2 \pm 0.1) \times 10^{-11}$	< 0.0001
TLDC1	$(0.6 \pm 0.1) \times 10^{-8}$	< 0.0001
TLDC2	$(0.1 \pm 0.1) \times 10^{-9}$	< 0.0001
TLDD	$(3.4 \pm 0.3) \times 10^{-8}$	< 0.0001
TLDE1	$(29.2 \pm 0.7) \times 10^{-8}$	< 0.0001
TLDE2	$(29.1 \pm 0.8) \times 10^{-8}$	< 0.0001
TLDE3	$(3.5 \pm 0.8) \times 10^{-9}$	< 0.0001
TLDE4	$(3.1 \pm 0.7) \times 10^{-9}$	< 0.0001
PCTT	$(30551.4 \pm 1.0) \times 10^{-5}$	0.1688
PCTTf	$(2022.9 \pm 0.2) \times 10^{-5}$	0.0112
PCSUPP	$(11461.1 \pm 0.8) \times 10^{-5}$	0.0633
PCTBL	$(3749.3 \pm 0.1) \times 10^{-4}$	0.2071
PCCOV	$(761.0 \pm 0.1) \times 10^{-5}$	0.0042
COLL	$(64868.1 \pm 0.8) \times 10^{-4}$	3.5835
ALCV	$(2145.9 \pm 0.9) \times 10^{-6}$	0.0012
FOAM	$(10.9 \pm 0.2) \times 10^{-7}$	< 0.0001
CRYS	$(6472.6 \pm 0.6) \times 10^{-5}$	0.0358
LTGD	$(557.6 \pm 0.5) \times 10^{-6}$	0.0003

Continued on next page

Continued from previous page

Region	**Energy Deposition** keV	**Percentage of Total** %
OPTI	$(46.8 \pm 0.4) \times 10^{-7}$	< 0.0001
PMTS	$(751.9 \pm 0.7) \times 10^{-6}$	0.0004
ELEC	$(107.6 \pm 0.2) \times 10^{-6}$	< 0.0001
VACU	0	0
PBCS	$(3607.5 \pm 0.2) \times 10^{-4}$	0.1993
ALCS	$(26598.5 \pm 0.9) \times 10^{-5}$	0.1469
XRT	$(1577.3 \pm 0.1) \times 10^{-4}$	0.0871
HEX	$(3713.7 \pm 0.5) \times 10^{-5}$	0.0205
EBD	$(2968.0 \pm 0.4) \times 10^{-5}$	0.0164
HVG	$(10748.5 \pm 0.8) \times 10^{-5}$	0.0594
DTS	$(1722.9 \pm 0.1) \times 10^{-4}$	0.0952
SUPPORTS	$(33513.4 \pm 0.6) \times 10^{-4}$	1.8514
COVER	$(23979.8 \pm 0.9) \times 10^{-5}$	0.1325
COVERG	$(1094.2 \pm 0.2) \times 10^{-5}$	0.0060
COVERA	$(11513.8 \pm 0.6) \times 10^{-5}$	0.0636